



UNIVERSITÉ PIERRE ET MARIE CURIE

SPECIALITÉ : CHIMIE PHYSIQUE

ED 388 – CHIMIE PHYSIQUE ET CHIMIE ANALYTIQUE DE PARIS CENTRE

THÈSE DE DOCTORAT

---

# Colloidal Interactions in Ionic Liquids

*Interactions Colloïdales Dans Les Liquides Ioniques*

---

*Auteur:*

Marianna MAMUSA

*Directrice de thèse:*

Dr. Véronique PEYRE

*Travail de thèse soumis pour obtenir le grade de*

Docteur de l'Université Pierre et Marie Curie

*et déroulé au*

Laboratoire PHENIX - PHysicochimie des Electrolytes et  
Nanosystèmes Interfaciaux

*Thèse soutenue le*

25 Février 2014

*devant le jury composé de:*

Werner KUNZ, Professeur

André VIOUX, Professeur

Julian OBERDISSE, Directeur de Recherche

Corinne CHANEAC, Professeur

Véronique PEYRE, Maître de Conférences

*Rapporteur*

*Rapporteur*

*Examineur*

*Examinatrice*

*Directrice de thèse*



# Contents

<b>List of Figures</b>	<b>vii</b>
<b>List of Tables</b>	<b>xi</b>
<b>Abbreviations</b>	<b>xiii</b>
<b>Introduction</b>	<b>1</b>
<b>1 Background</b>	<b>5</b>
1.1 Interactions between atoms, molecules, particles . . . . .	6
1.1.1 General Considerations on Electrostatic Forces . . . . .	6
1.1.2 Dipolar Magnetic Interactions . . . . .	11
1.1.3 Van der Waals Forces between Atoms and Molecules . . . . .	12
1.1.4 Steric Contributions and Total Interaction Potential . . . . .	15
1.1.5 DLVO Theory . . . . .	17
1.2 The Colloids: Maghemite Nanoparticles . . . . .	22
1.3 Ionic Liquids . . . . .	28
1.3.1 Ethylammonium Nitrate . . . . .	30
1.4 Ionic Liquids in Colloidal Systems: State of the Art . . . . .	34
1.4.1 Ionic Liquids as a Medium for the Synthesis of Nanoparticles . . . . .	34
1.4.2 Colloidal Dispersions in Ionic Liquids . . . . .	35
1.4.3 ILs at a Surface . . . . .	45
1.4.4 Interparticle Potential in ILs . . . . .	52
1.5 Conclusion . . . . .	55
<b>2 Materials and Methods</b>	<b>57</b>
2.1 Materials . . . . .	58
2.2 Syntheses and Functionalizations . . . . .	58
2.2.1 Synthesis of Maghemite Nanoparticles . . . . .	58
2.2.2 Size Sorting of Maghemite Nanoparticles . . . . .	60
2.2.3 Preparation of Acidic and Alkaline Ferrofluids with Different Counterions . . . . .	62
2.2.4 Surface Functionalization with Citrate Ligands . . . . .	63
2.2.5 Synthesis of the Ionic Liquid Ethylammonium Nitrate . . . . .	64
2.2.6 Synthesis of the Choline-Amino Acid ([Cho][AA]) Ionic Liquids . . . . .	64
2.2.7 Transfer of Nanoparticles from Water to IL . . . . .	65
2.2.8 Lyophilization . . . . .	67

2.3	Characterization Techniques . . . . .	67
2.3.1	Karl Fischer Titration . . . . .	67
2.3.2	pH Measurements in Ethylammonium Nitrate . . . . .	68
2.3.3	Flame Atomic Absorption Spectroscopy . . . . .	69
2.3.4	Small Angle (Neutron and X-Ray) Scattering . . . . .	70
2.3.5	Dynamic Light Scattering . . . . .	71
2.3.6	Magnetization Measurements . . . . .	73
2.3.7	Magneto-Optical Birefringence Experiments . . . . .	74
<b>3</b>	<b>Preliminary Screenings on Polydisperse Nanoparticle/Ethylammonium Nitrate Dispersions</b> . . . . .	<b>75</b>
3.1	pH Measurements in Ethylammonium Nitrate . . . . .	76
3.1.1	Response of the Glass Electrode in EAN . . . . .	77
3.1.2	Dissociation Constants of Citric Acid in EAN . . . . .	78
3.2	Dispersions of Bare Maghemite Nanoparticles in EAN: Effect of pH, Counterion and Water Content . . . . .	80
3.2.1	Neutral Medium – Point of Zero Charge . . . . .	82
3.2.2	Acidic Medium . . . . .	82
3.2.3	Alkaline Medium . . . . .	84
3.3	Dispersions of Citrate-Covered Maghemite Nanoparticles in EAN . . . . .	84
3.4	Microscopic Study of Citrate-Covered Maghemite Nanoparticles in EAN . . . . .	86
3.4.1	Dynamic Light Scattering Experiments . . . . .	88
3.4.2	Small Angle Neutron Scattering (SANS) Experiments . . . . .	90
3.5	Conclusion . . . . .	93
<b>4</b>	<b>Dispersions of Size-Sorted Maghemite Nanoparticles in the IL Ethylammonium Nitrate</b> . . . . .	<b>95</b>
4.1	Introduction . . . . .	96
4.2	Preparation and Chemical Analysis of the Samples . . . . .	97
4.3	Evolution During the Preparation of the Samples: the Special Case of Lithium . . . . .	102
4.4	Effect of NP Size and Concentration . . . . .	104
4.5	Small Particles (7 nm): Effect of the Counterion . . . . .	110
4.5.1	Dilute Regime . . . . .	110
4.5.2	Concentrated Regime . . . . .	111
4.6	Large Particles (11 nm): Effect of the Counterion . . . . .	118
4.6.1	Dilute Regime . . . . .	118
4.6.2	Concentrated Regime . . . . .	119
4.7	Discussion on the Effect of the Counterions on Both Sizes . . . . .	128
4.8	Effect of Water Content . . . . .	131
4.9	Conclusion . . . . .	137
<b>5</b>	<b>Tests with Cholinium-based Ionic Liquids</b> . . . . .	<b>139</b>
5.1	Introduction . . . . .	139
5.2	Dispersion of Maghemite Nanoparticles in Cholinium-Aminoacid ILs . . . . .	142
5.3	Dispersions of Maghemite in Water/[Cho][Gly] Media . . . . .	144
5.4	Conclusion . . . . .	145

---

<b>Conclusions and Perspectives</b>	<b>147</b>
<b>A Dispersions of Different Nanoparticles in Ionic Liquids</b>	<b>151</b>
<b>B Small Angle Scattering Techniques</b>	<b>157</b>
B.1 Theoretical Principles . . . . .	157
B.2 Experimental Intensity and Absolute Intensity . . . . .	159
B.3 Form Factor and Structure Factor . . . . .	160
B.4 Calculation of Scattering Length Densities and Contrast . . . . .	161
B.5 The Scattering Invariant. Calculation of $\Phi$ . . . . .	164
B.6 Guinier Plot . . . . .	165
B.7 Experimental Form Factors, $P(Q)$ . . . . .	165
<b>Bibliography</b>	<b>169</b>



# List of Figures

1.1	Electric Double Layer at a Charged Surface in Water . . . . .	10
1.2	Van der Waals Interaction between Surfaces . . . . .	14
1.3	Full Pair Potentials for Molecules and Particles . . . . .	17
1.4	DLVO Energy <i>vs.</i> Distance Profiles . . . . .	18
1.5	TEM Image of Maghemite Nanoparticles . . . . .	22
1.6	Stability of Maghemite Nanoparticles as a Function of pH . . . . .	24
1.7	Dependence of the Structural Charge of Maghemite NP on the pH . . . . .	25
1.8	Stability of Citrate-Covered Maghemite Nanoparticles as a Function of pH . . . . .	25
1.9	Phase Diagrams for Citrate-Covered Maghemite Nanoparticles in Water . . . . .	26
1.10	Common IL Cations . . . . .	28
1.11	Molecular Formula of Ethylammonium Nitrate . . . . .	31
1.12	H-bond Networks of EAN and Water . . . . .	32
1.13	ZnO nanostructures synthesized in ILs . . . . .	35
1.14	IL Layers at the Bare Maghemite Surface . . . . .	37
1.15	Different Colloidal Stability of Bare and PMMA-Grafted Silica Particles . . . . .	41
1.16	Silica-based Ionogels . . . . .	43
1.17	AFM Force Profile . . . . .	46
1.18	DLVO Interparticle Potential for Silica Particles in ILs . . . . .	53
1.19	DLVO Interparticle Potential for Magnetite Particles in ILs . . . . .	54
2.1	Size Distribution of Unsorted Maghemite Nanoparticles . . . . .	59
2.2	Destabilization of Maghemite Nanoparticles by Ionic Strength . . . . .	60
2.3	Size Sorting of Maghemite Nanoparticles . . . . .	61
2.4	Size Distribution of Size-Sorted Maghemite Nanoparticles . . . . .	62
2.5	Reaction between Choline Hydroxide and an Amino Acid . . . . .	65
2.6	Synthesis of Cho-AA Ionic Liquids . . . . .	66
2.7	Process 1 for the Transfer of NP from Water to IL . . . . .	66
2.8	Process 2 for the Transfer of NP from Water to IL . . . . .	66
2.9	Karl Fischer . . . . .	68
2.10	Sample Preparation for SAXS . . . . .	71
3.1	Response of a Glass Electrode in Basic EAN Solutions . . . . .	78
3.2	Response of a Glass Electrode in EAN . . . . .	79
3.3	Different States of Dispersion . . . . .	82
3.4	Citrate Anion . . . . .	85
3.5	DLS Experiments on Some Citrated NP . . . . .	89
3.6	SANS Experiments on Polydisperse Maghemite Dispersions in EAN and Water . . . . .	90

3.7	Fits of SANS Intensities for Three Representative Cases in Water and EAN	91
4.1	Separation of Particles and Solvent by Centrifugation	97
4.2	UV-Vis Absorption Spectra for FeNSA-5 Complex in EAN	99
4.3	Calibration Curve for the FeNSA-5 Complex in EAN	99
4.4	UV-Vis Absorption Spectra for FeNSA-5 Complex in EAN	100
4.5	Effect of Ageing on Li <sup>+</sup> /EAN Dispersion	103
4.6	Effect of Ageing on Li <sup>+</sup> /EAN Dispersion	103
4.7	Optical Microscopy under Magnetic Field: Reversible Phase Separation	105
4.8	Coexistence of Dilute and Concentrated NP Phases (Large Particles)	106
4.9	Optical Microscopy of the Coexistence of Dilute and Concentrated NP Phases	107
4.10	Schematic Phase Diagram for a Colloidal System	107
4.11	S(Q) Plots for Dilute Dispersions of Small NP in EAN with Different Counterions	111
4.12	I(Q) Plots for Small Particles with Different Counterions	112
4.13	Magneto-Optic Birefringence Relaxation Curves for Small Particles with Different Counterions	112
4.14	Effect of Small NP Concentration of the S(Q) in the Case of Li <sup>+</sup> Counterions	114
4.15	Structure Factors for Dilute Suspensions of Large Particles	118
4.16	Magneto-optic Birefringence Experiments for Dilute Dispersions of Large Particles	120
4.17	Structure Factors of Liquid Phases (Large Particles)	121
4.18	Optical Microscopy under Applied H: NaCC One-Phase Dispersion	121
4.19	SAXS of NaCC One-Phase and Phase-Separated Samples	122
4.20	SAXS of LiCC Gas Phases Showing no Time Evolution	123
4.21	SAXS of LiCC Liquid Phases Showing no Time Evolution	123
4.22	SAXS of LiCC One-Phase and Phase-Separated Samples	124
4.23	SQUID of LiCC One-Phase and Phase-Separated Samples	124
4.24	Magneto-optic Birefringence of LiCC One-Phase and Phase-Separated Samples	125
4.25	Effect of Ageing on EACC Gas Phases	127
4.26	Effect of Ageing on EACC Liquid Phases	127
4.27	Behaviour of Dispersions of Small Particles According to their Counterion	130
4.28	Behaviour of Dispersions of Large Particles According to their Counterion	131
4.29	Structure Factors for EAN/W Dispersions. Small Particles, EA <sup>+</sup> Counterions.	132
4.30	Structure Factors for EAN/W Dispersions. Small Particles, Na <sup>+</sup> Counterions.	133
4.31	Structure Factors for EAN/W Dispersions. Large Particles, EA <sup>+</sup> Counterions.	133
4.32	Structure Factors for EAN/W Dispersions. Large Particles, Na <sup>+</sup> Counterions.	134
4.33	Structure Factors for Aqueous Maghemite Dispersions with Added EAN. Small Particles.	135
4.34	Structure Factors for Aqueous Maghemite Dispersions with Added EAN. Large Particles.	136



---

5.1	Cholinium Cation . . . . .	141
5.2	SAXS Results for Small NP Dispersions in Cholinium Glycinate . . . . .	144
B.1	Principle of Small Angle Scattering . . . . .	157
B.2	Scattered Intensities for Neutron and X-Ray Beams . . . . .	159
B.3	Form Factor and Structure Factor . . . . .	162
B.4	Information in an $I(Q, \Phi)$ curve . . . . .	163
B.5	Experimental $P(Q)$ , Small Particles . . . . .	166
B.6	Experimental $P(Q)$ , Large Particles . . . . .	166
B.7	$P(Q)$ for Small and Large Particles . . . . .	167



# List of Tables

1.1	Physico-chemical Properties of Ethylammonium Nitrate . . . . .	31
3.1	Citric Acid pK in EAN . . . . .	79
3.2	Dispersions of Bare Maghemite in EAN, according to pH, Counterion and Water Content . . . . .	81
3.3	Dispersions of Citrated Maghemite in EAN, according to pH, Counterion and Water Content . . . . .	85
3.4	Some Properties of Dispersions of Citrated Maghemite in EAN . . . . .	88
3.5	Results from SANS on Citrated NP Dispersions in EAN . . . . .	92
4.1	Concentration of NP/EAN Dispersions: Small Particles (SSC) . . . . .	106
4.2	Concentration of NP/EAN Dispersions: Large Particles (CC) . . . . .	109
4.3	Properties of the LiSSC Series . . . . .	115
5.1	Dispersions of Acidic and Citrated Maghemite in Cholinium Glycinate . . . . .	143
5.2	Dispersions of Citrated Maghemite NP in Cholinium Glycinate and its Aqueous Mixtures . . . . .	144
A.1	Dispersions of Several Types of Particles in Ionic Liquids . . . . .	156
B.1	Scattering Length Densities . . . . .	163
B.2	Scattering Length Contrasts . . . . .	163



# Abbreviations

[Cho][AA]	Cholinium-Aminoacid ionic liquids (class)
[Cho][Ala]	Cholinium Alaninate
[Cho][Gly]	Cholinium Glycinate
[EMIM][Ac]	1-ethyl-3-methylimidazolium Acetate
[EMIM][BF <sub>4</sub> ]	1-ethyl-3-methylimidazolium Tetrafluoroborate
[EMIM][EtSO <sub>4</sub> ]	1-ethyl-3-methylimidazolium Ethylsulfate
[EMIM][Et <sub>2</sub> PO <sub>4</sub> ]	1-ethyl-3-methylimidazolium Diethylphosphate
[EMIM][N(CN) <sub>2</sub> ]	1-ethyl-3-methylimidazolium Dicyanamide
[EMIM][NTf <sub>2</sub> ]	1-ethyl-3-methylimidazolium Bis(trifluoromethyl-sulfonyl)imide
[EMIM][SCN]	1-ethyl-3-methylimidazolium Thiocyanate
[EOHMIM][NTf <sub>2</sub> ]	1-(2-hydroxyethyl)-3-methylimidazolium Bis(trifluoromethylsulfonyl)imide
[BMIM][BF <sub>4</sub> ]	1-butyl-3-methylimidazolium Tetrafluoroborate
[BMIM][Cl]	1-butyl-3-methylimidazolium Chloride
[BMIM][NTf <sub>2</sub> ]	1-butyl-3-methylimidazolium Bis(trifluoromethyl-sulfonyl)imide
[BMIM][PF <sub>6</sub> ]	1-butyl-3-methylimidazolium Hexafluorophosphate
[BMMIM][NTf <sub>2</sub> ]	1-butyl-2,3-dimethylimidazolium Bis(trifluoromethyl-sulfonyl)imide
[BMPy][FAP]	<i>N</i> -butyl, <i>N</i> -methylpyrrolidinium Tris(pentafluoroethyl)trifluorophosphate
[BMPy][NTf <sub>2</sub> ]	<i>N</i> -butyl, <i>N</i> -methylpyrrolidinium Bis(trifluoromethyl-sulfonyl)imide

---

<b>[DEME][BF<sub>4</sub>]</b>	<i>N,N</i> -diethyl- <i>N</i> -methyl- <i>N</i> -(2-methoxyethyl)- ammonium Tetrafluoroborate
<b>[HMIM][FAP]</b>	1-hexyl-3-methylimidazolium Tris(pentafluoroethyl)- trifluorophosphate
<b>[PMPy][NTf<sub>2</sub>]</b>	<i>N</i> -methyl, <i>N</i> -propylpyrrolidinium Bis(trifluoromethyl- sulfonyl)imide
<b>AFM</b>	Atomic Force Microscopy
<b>BS</b>	BenzeneSulfonate
<b>BSA</b>	BenzeneSulfonic Acid
<b>Cit</b>	Citrate
<b>DLCA</b>	Diffusion-Limited Colloidal Aggregation
<b>DLS</b>	Dynamic Light Scattering
<b>EC SFA</b>	ElectroChemical Surface Force Apparatus
<b>EA</b>	Ethylammonium
<b>EAN</b>	Ethylammonium Nitrate
<b>FAAS</b>	Flame Atomic Absorption Spectroscopy
<b>FT-IR</b>	Fourier-Transform InfraRed
<b>FT-IRAS</b>	Fourier-Transform Infrared Reflection Absorption Spectroscopy
<b>IL</b>	Ionic Liquid
<b>MRF</b>	Magneto-Rheological Fluid(s)
<b>NMR</b>	Nuclear Magnetic Resonance
<b>NP</b>	Nanoparticle(s)
<b>PBnMA</b>	Poly-Benzyl-MethAcrylate
<b>PMMA</b>	Poly-Methyl-MethAcrylate
<b>PB</b>	Poisson-Boltzmann
<b>PZC</b>	Point of Zero Charge
<b>SANS</b>	Small-Angle Neutron Scattering
<b>SAXS</b>	Small-Angle X-ray Scattering
<b>SEIRA</b>	Surface-Enhanced Infrared Absorption Spectroscopy
<b>SEM</b>	Scanning Electron Microscopy
<b>SERS</b>	Surface-Enhanced Raman Scattering
<b>SFA</b>	Surface Force Apparatus

<b>TEM</b>	Transmission Electron Microscopy
<b>TMA</b>	Tetramethylammonium
<b>TBA</b>	Tetrabutylammonium
<b>VDW</b>	Van der Waals
<b>XPS</b>	X-ray Photoelectron Spectroscopy





# Introduction

Ionic liquids (ILs) are a class of tunable solvents composed exclusively of ions; despite this, they are liquid below 100 °C, sometimes even at ambient conditions, and they show excellent solvent properties. ILs owe their fame of ‘green’ compounds to some interesting properties such as nonflammability, negligible vapour tension and high thermal stability, thanks to which they have been considered for the replacement of classical and more dangerous organic solvents during the last few decades. Potential uses are as reaction media for organic and inorganic synthesis, for the preparation of magneto-rheological fluids, lubricants for ultra-vacuum applications and electrochemical devices [1].

Recently, ILs have been used as synthesis media for several types of metal and non-metal nanoparticles (NP) [2]. However, the state of dispersion or aggregation of the particles obtained in (or transferred to) ionic liquids has not been exhaustively investigated, despite its importance for the ever growing list of industrial and technological applications of chemical systems where the dispersing agent can be an ionic liquid. Indeed, each application requires a different state of dispersion for the composing colloids. For example, fully dispersed particles are necessary for heterogeneous catalysis [3] since a good catalyst must have the largest possible surface area. It is thus desirable for the particles to be well dispersed, as the presence of aggregates would reduce the accessibility to the catalytic sites. Homogeneous dispersions are also preferable for heat-transfer fluids [4], in which ILs can play a central role thanks to their high heat capacities, and the thermal conductivity can be enhanced with the loading of nanoscale metals or metal oxides. On the other hand, when we consider electrochemical devices in which the electrolyte is an IL, one of the major problems is the possible leaching of the carrier fluid; in this case, the formation of gels is evidently the best solution, since they maintain the conductivity of pure ILs while being in the solid state. Ionogels [5] are then better suited for high-temperature stable Dye-Sensitized solar cells [6] or gas sensors based on solid-like composite membranes [7], to cite a few.

In this work, the attention is focused on the mechanisms leading to different states of dispersions, and thus different microstructures, of nanoparticles in ionic liquids. The goal is to understand which physico-chemical parameters control the colloidal stability in

these media, and how this can be tuned depending on the desired final application. Indeed, it is known that the microstructure of colloidal systems is governed by the balance of attractive (van der Waals, depletion, magnetic dipolar) and repulsive (electrostatic, steric) forces, which is well described by classic theories such as the DLVO [8] for typical aqueous systems. However, when the solvent itself is composed solely of ions, the role of electrostatics is not easy to evaluate. The classic theories such as the Poisson-Boltzmann equation fail to explain the behaviour of these new ionic solvents, because even some physical properties (such as the dielectric constant or the very concept of ionic strength, as it will be discussed further) lack a rigorous definition when ionic liquids are concerned.

Up to present, several stable dispersions of nanoparticles or gels in ILs have been reported, based on a large variety of different kinds of NP and ILs. While most of these works involve the adsorption, on the NP surface, of polymers [9–11] or surfactants [12–14] ensuring steric repulsion, in some cases colloidal stability is achieved without any stabilizers [15]. These apparently diverging results make it difficult to outline any general laws describing the origin of colloidal stability in IL media, which is still poorly understood. Some works indirectly show the existence of interactions between ILs and nanoparticles [16, 17], and many authors propose the formation of IL solvation layers at the NP/liquid interface as a source of colloidal stabilization [10, 16]. Despite this, the study of colloidal stability of ionic liquid-based systems is currently only at its dawn, and our understanding of the colloidal phenomena and the relevant physico-chemical parameters in these media is still very limited.

The questions that come spontaneously to mind then are: how do we control the microstructure? Can the classical methods employed in water- or oil-based colloidal systems be applied to ILs with the same results? Are dispersions in ILs stable, and why?

In this Thesis, we try to shed some light on the matter by focusing on a model system, which is based on two components that have been extensively studied separately. The IL chosen as a dispersing phase is ethylammonium nitrate (EAN): this is a Room-Temperature Ionic Liquid (m.p. = 14 °C), and one of the oldest and best characterized ionic liquids, known for its resemblance to water in many aspects. Indeed, EAN is a protic ionic liquid, in which we can define a pH scale going from zero to 10 [18], and it is characterized by the presence of an extensive hydrogen-bond network similarly to water [19]. At the same time, it shows typical behaviours of ILs: some works based on surface

force measurements, for example, have shown that EAN forms solvation layers when it is in contact with charged flat surfaces [20, 21].

The second system consists of maghemite nanoparticles, which are synthesized in water *via* a coprecipitation method. Such particles have either a positively or negatively charged surface (depending on the pH of the aqueous medium) without any adsorbed molecules; alternatively, the surface can be functionalized with citrate ligands which ensure a negative surface charge. In all cases, the properties of the surface and of the aqueous dispersions are well known and thoroughly characterized. Such properties can be tuned by playing with several parameters (such as pH, ionic strength and type of counterions compensating the surface charge) in order to modify the interactions between particles, especially tuning the repulsions by acting on the charge and ionic strength. Also, due to the magnetic properties of maghemite NP, there is the possibility to modify the attractive part of the interaction potential by changing the size of the particles. Maghemite nanoparticles thus offer an interesting chance to study the interparticle interactions in different media. Once their surface features are adequately tuned in water, the solvent in which we are able to control their properties, we transfer the particles to the ionic liquid EAN and proceed with an in-depth investigation of the colloidal systems thereby obtained.

In a first part, we give an overview of the context of this work. Chapter 1 summarizes the basic knowledge on the interaction forces existing in colloidal systems, and recalls the main points of the classic DLVO theory. We show that the classic equations and theories used to describe aqueous colloids are not entirely suitable for systems based on ionic liquids. We present in more detail the properties of the colloids used for this work and the ionic liquid chosen as dispersing phase, and we provide a summary of the recent works representing the state of the art of IL-based colloidal systems, as well as the behaviour of ILs at the solid/liquid interface.

Chapter 2 details the methods used to prepare and characterize our samples. In Chapters 3 and 4, our ionic liquid and our nanoparticles are eventually mixed together, so we first establish a protocol for the transfer of the NP from water to EAN. The resulting suspensions are investigated by varying several parameters: the nanoparticles' size, polydispersity and concentration, the initial pH and therefore the surface charge, the type and valence of counterions, the EAN/water ratio. We assess the colloidal stability by means of visual observation, optical microscopy under magnetic field, and atomic

absorption spectroscopy. We then perform structural analyses by means of DLS, small angle (neutron and X-ray) scattering, and magneto-optic birefringence, in order to learn more about the microstructure of the samples. Finally, we discuss the results obtained and conclude on the possible interparticle interactions arising in such media. Chapter 5 presents the first tests on dispersions of maghemite nanoparticles in choline-based ionic liquids, applying the methods perfected in the first part of the Thesis and opening the way to future work on biocompatible systems. Finally, we draw our conclusion and outline our perspectives.

# Chapter 1

## Background

### Contents

---

<b>1.1 Interactions between atoms, molecules, particles</b> . . . . .	<b>6</b>
1.1.1 General Considerations on Electrostatic Forces . . . . .	6
1.1.2 Dipolar Magnetic Interactions . . . . .	11
1.1.3 Van der Waals Forces between Atoms and Molecules . . . . .	12
1.1.4 Steric Contributions and Total Interaction Potential . . . . .	15
1.1.5 DLVO Theory . . . . .	17
<b>1.2 The Colloids: Maghemite Nanoparticles</b> . . . . .	<b>22</b>
<b>1.3 Ionic Liquids</b> . . . . .	<b>28</b>
1.3.1 Ethylammonium Nitrate . . . . .	30
<b>1.4 Ionic Liquids in Colloidal Systems: State of the Art</b> . . . . .	<b>34</b>
1.4.1 Ionic Liquids as a Medium for the Synthesis of Nanoparticles . . . . .	34
1.4.2 Colloidal Dispersions in Ionic Liquids . . . . .	35
1.4.3 ILs at a Surface . . . . .	45
1.4.4 Interparticle Potential in ILs . . . . .	52
<b>1.5 Conclusion</b> . . . . .	<b>55</b>

---

In this Chapter, we provide the background information necessary to the comprehension of the experimental work described in the following. As stated in its title, this Thesis deals with colloidal interactions in ionic liquids (ILs), hence it is mandatory to introduce (in Section 1.1) the basics of colloidal interactions and the classical theories that describe them. Next, Section 1.2 will depict the nanocolloids used for this work, that is, iron oxide (maghemite) nanoparticles (NP). Section 1.3 will present ionic liquids,

a peculiar class of solvents composed of ions only, with a special focus on ethylammonium nitrate, the IL used in the present work. Finally, Section 1.4 will draw a picture of the current research involving IL-based colloidal systems: we will learn about the role of ionic liquids as media for synthesis and, in particular, for dispersion of nanoparticles, then we will review the studies that have tried to shed light on the behaviour of these compounds when interacting with various surfaces, as well as those works that have made an effort towards the description of the interparticle potential arising when nanoparticles are dispersed in ionic liquids.

## 1.1 Interactions between atoms, molecules, particles

Prior to discussing in detail the colloidal system chosen as a model for this work, we will review the most important interactions existing between the chemical species that will be dealt with in the following: electrostatic, magnetic, steric and van der Waals forces. Subsequently, we will introduce the DLVO theory, which is classically used to describe the overall interaction potential in colloidal systems. This whole section will be mainly based on the classic books “Intermolecular and Surface Forces” by J. Israelachvili [22] and “Theory of the Stability of Lyophobic Colloids” by Verwey and Overbeek [8]. Finally, we will discuss the problems encountered when trying to apply such classical descriptions to ionic liquid-based colloidal systems.

### 1.1.1 General Considerations on Electrostatic Forces

In the present work, not only are the nanocolloids charged, but the very solvent in which they are dispersed is composed of ions (*i.e.*, charges of much smaller size than the macroions represented by the nanoparticles). This means that electrostatic interactions exist between all the species involved in the system in study, ranging from the molecular to the supramolecular scale.

The interactions between charges, ions, dipoles, quadrupoles, and so forth fall into the category of purely electrostatic forces arising from the Coulomb force. The free energy for the Coulomb interaction between two charges  $q_1$  and  $q_2$  found at a distance  $r$  is:

$$w_{Coulomb}(r) = \frac{q_1 q_2}{4\pi\epsilon_0\epsilon r} = \frac{z_1 z_2 e^2}{4\pi\epsilon_0\epsilon r} \quad (1.1)$$

where  $\varepsilon$  is the dielectric permittivity of the medium ( $\varepsilon_0$  for vacuum). The expression on the right of Eqn. 1.1 is commonly used for *ionic interactions* in aqueous solutions, where the magnitude and sign of each ionic charge is given in terms of the elementary electron charge ( $e = 1.602 \cdot 10^{-19}$  C) multiplied by the ionic valency  $z$ . This is the strongest chemical interaction after covalent bonds and, depending on the nature of the charges involved, it can be attractive (like signs) or repulsive (opposite signs). The order of magnitude of the binding energy for a typical ionic couple like  $\text{Na}^+\text{Cl}^-$  is of about  $10^{-19}$  J, corresponding to about  $200 kT$ . In order for the energy to fall below  $kT$ , we have to go to distances  $r$  larger than a few nanometers. In sum, the Coulomb interaction is very strong and of long range.

Electrostatic interactions are not only of ion-ion type, but they exist also between polar molecules, which are characterized by an anisotropic distribution of charges, such that an electric dipole moment  $u$  arises. The free energy of the *ion-dipole* interaction decreases as  $r^{-2}$  and depends on the interaction angle; it is stronger than  $kT$  at typical interatomic separations, even when it is reduced by the high dielectric constant of water. This force is also responsible for the solvation of ions in polar solvents such as water.

The free energy for the *dipole-dipole* interaction depends on the relative orientation of the molecules involved; it is thus of shorter range than the forces described above, and generally not strong enough to induce the alignment of molecules in the liquid state. However, in the case of water, the small size and large dipole moment of the  $\text{H}_2\text{O}$  molecule does lead to short-range association in the liquid *via* the *hydrogen bond*, depicted by the symbol  $-\text{X}^- \cdots \text{H}^+$ , where X is an electronegative atom (O, F, N...). Hydrogen bonds are the origin of water's surprising qualities such as its unexpectedly high melting and boiling points, its low compressibility, and the fact that ice is less dense than liquid water. The H-bond is believed to be purely electrostatic, and it is strongly attractive and more or less directional. Its strength is approximately 5-10  $kT$  at 298 K, which is stronger than typical van der Waals interactions ( $\sim 1 kT$ ) but a lot weaker than covalent and ionic bonds ( $\sim 100 kT$ ). Unfortunately, there is not yet a simple theory or equation describing this complex interaction; it is known, though, that it follows a  $1/r^2$  distance dependence like charge-dipole interactions.

Hydrogen bonds do not concern water alone, but exist between any species implying the presence of electronegative atoms and of hydrogen atoms able to act as "bridges". They are thus responsible for the interactions between water and other molecules – even

nonpolar ones, as long as they carry a H-bond forming atom, such as C=O groups on ketones. As it will be discussed later (Subsection 1.3.1), hydrogen bonds also play a fundamental role in the bulk structure of some ionic liquids.

## Electrostatics in Colloidal Systems

In the majority of real cases, colloids can be pictured as *macroions*: the surfaces of particles suspended in a polar liquid medium are usually charged *via* one of three possible mechanisms (1. dissociation of surface groups; 2. adsorption of ions coming from the solution; 3. charge exchange between two dissimilar surfaces). Such surface charge must be compensated by the presence of *counterions* of opposed charge, in order to respect the condition of electroneutrality: these counterions are in part bound (more or less loosely) to the surface, forming the so-called *Stern* or *Helmholtz layer*, while the rest are further away from the surface, in a sort of ionic atmosphere characterized by continuous thermal motion and known as the *diffuse electric layer*. This scheme applies to most common colloidal systems, such as dispersions of solid nanoparticles, clays, micelles and other surfactant aggregates.

The mathematical relations describing the electrostatic interactions between charged surfaces in a liquid medium are based on the theory developed by Gouy and Chapman, who combined thermal energy and Coulomb interactions into a statistical theory. Since in colloidal dispersions the total area in contact with the solvent is extremely large, the physics of meso- and nanoscopic particles are dominated by “surface” properties and interactions. It is then justified to adopt a model involving surfaces to try and understand the behaviour of charged object in solution. The theory describing the electrostatic potential between two flat surfaces interacting through a medium is known as the Poisson-Boltzmann (PB) equation:

$$\frac{d^2\psi}{dx^2} = \frac{-ze\rho}{\epsilon_0\epsilon} \quad (1.2)$$

where  $\psi$  is the electrostatic potential and  $\rho$  is the number density of ions of valency  $z$  at the point  $x$  ( $\rho_0$  being the ions density at the midplane). Once the appropriate boundary conditions are chosen, the PB equation can be solved to obtain the electric field ( $E = -\partial\psi/\partial x$ ) and the counterion density  $\rho$  at any distance  $x$  between the surfaces. The counterion distribution profile is given by:



$$\rho_x = \rho_0 e^{-ze\psi/kT} \quad (1.3)$$

which shows that the concentration of counterions decreases exponentially with growing distance from the charged surface. The PB equation is only valid in a *mean-field regime*, *i.e.* a system characterized by weakly charged surfaces, low valency counterions and/or high temperature, cases in which counterions form a loosely bound cloud at the surface [23].

Usually, macroions in solution present like-sign surface charges, but the overall interaction is complicated by the presence of the counterions forming the electric double layer, and depends on their distribution around the macroions: both repulsive and attractive effective forces can result from the scheme. Indeed, on one hand the counterions are attracted to the surface, due to the requirement of maintaining electroneutrality, which prevents them from going into the surrounding bulk liquid reservoir. At the same time, the counterions do not fall back onto the surface itself because of the repulsion between like-sign charges that tends to keep them apart from each other. When two similarly charged surfaces (or particles) are pushed against each other, their electric double layers overlap. This act corresponds to forcing the counterions back onto the surface, to which the double layer responds with a repulsion that keeps the particles apart. At large separations, the overall interaction between two similarly charged surfaces is thus repulsive [23].

So far, we have considered a simple model describing an ideal situation in which only the charge on the surface and its counterions are present. However, in most real systems the medium through which the surfaces are interacting already contains an electrolyte solution, *i.e.* there is an “external” source of electrical charges to be taken into account that interacts with the particles (or micelles, etc.) and their counterions. Figure 1.1 depicts an isolated surface in an aqueous solution of a 1:1 electrolyte. Near the surface, there is an accumulation of counterions, either dehydrated or hydrated, and a depletion of coions. The outer Helmholtz plane (OHP) is the plane beyond which the distribution of ions obeys the Poisson-Boltzmann equation.

The *Debye length*  $\kappa^{-1}$  in Figure 1.1 is the characteristic thickness of the diffuse electric double layer, given by:

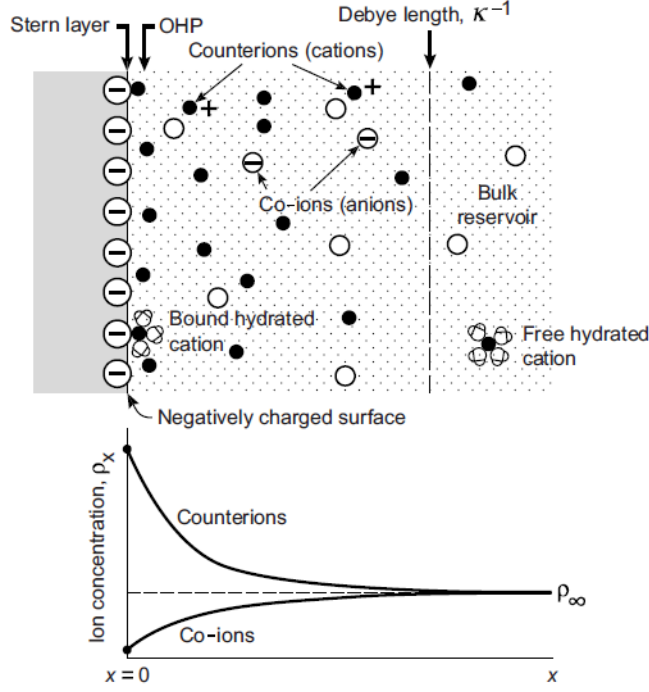


FIGURE 1.1: Distribution of counterions and coions near a negatively charged surface in water (top), and corresponding concentration profiles (bottom). Reproduced from reference [22].

$$\kappa^{-1} = \sqrt{\frac{\epsilon_0 \epsilon k T}{\sum_i \rho_{\infty i} e^2 z_i^2}} \quad (1.4)$$

where  $z_i$  is the charge of the ion  $i$ , and  $\rho_{\infty i}$  is the ionic concentration of ions  $i$  in the bulk (at  $x = \infty$ , where the electric potential is zero). The Debye length thus depends only on the properties of the solution (ionic strength, dielectric constants and temperature) and not on those of the surface. In the simple case of a 1:1 electrolyte (such as NaCl) and for low potentials, the Debye-Hückel equation shows that the potential at any distance  $x$  from the surface is

$$\psi_x \approx \psi_0 e^{-\kappa x} \quad (1.5)$$

so the Debye length can also be defined as the characteristic decay distance of the potential.

As mentioned earlier, the Poisson-Boltzmann theory is only valid in the mean-field

regime approximation, and a number of problems arise in the description of more complex systems. For example, this theory neglects the molecular nature of the solvent by representing it as a continuum dielectric medium [23]: as a consequence, it lacks any fluctuations in the ion concentration profile and does not take into account the local perturbations of the solvent structure around particles. It also neglects any finite-size (steric) effects between the ions, which are considered as point-like.

Also, some experimental conditions that the PB theory fails to account for are the attraction between like-charged particles in the presence of multivalent counterions (due to the correlations between ions, which are missed within the mean-field treatment) and the chemical specificity of ions (which is mainly related to their polarizability and their solvation) [24].

Further in this section, the discussion will turn to the even more dramatic limitations of the PB theory (and the DLVO, relying on it; see Subsection 1.1.5) in the case of ionic liquids.

### 1.1.2 Dipolar Magnetic Interactions

The interactions existing between magnetic dipoles will often be called into question in the present work concerning magnetic nanoparticles. The free energy associated to the magnetic interaction is much weaker than the case of electric dipoles, but it can become important for large molecules or particles, as shown in what follows. In both cases, the interaction between dipoles depends on the inverse cube of the distance; for magnetic dipoles:

$$w_{magn}(r) = -\frac{\mu_0}{4\pi r^3} \left[ \frac{3(\boldsymbol{\mu}_1 \cdot \mathbf{r})(\boldsymbol{\mu}_2 \cdot \mathbf{r})}{r^5} - (\boldsymbol{\mu}_1 \cdot \boldsymbol{\mu}_2) \right] \quad (1.6)$$

where  $\boldsymbol{\mu}_1$  and  $\boldsymbol{\mu}_2$  are the dipole vectors,  $\mu_0$  is the magnetic permeability of vacuum,  $r$  is center-to-center distance between the two dipoles and  $\mathbf{r}$  is the vector between centres. However, while the electric dipole moment values increase in proportion to a length (for example, the diameter of the molecule), magnetic dipole moments increase with the *volume*.

The maximum attraction will occur when the dipoles  $\boldsymbol{\mu}_1$  and  $\boldsymbol{\mu}_2$  lie in line and pointing in the same direction, and as a consequence magnetic particles in an external magnetic field will tend to orient themselves associating into linear strings.

### 1.1.3 Van der Waals Forces between Atoms and Molecules

The van der Waals force exists in all systems, including ionic liquids. In general, this interaction is attractive when experienced by identical objects. It is the sum of three inverse sixth power contributions:

1. The Keesom interaction, also known as the Boltzmann-averaged interaction between two permanent electric dipoles  $u_1$  and  $u_2$ , given by the following equation:

$$w_{Keesom}(r) = -\frac{u_1^2 u_2^2}{3(4\pi\epsilon_0\epsilon)^2 kT r^6} \quad (1.7)$$

2. The Debye interaction, or the net dipole – induced dipole interaction for two molecules possessing permanent dipole moments  $u_1$  and  $u_2$  and electronic polarizabilities  $\alpha_{01}$  and  $\alpha_{02}$ :

$$w_{Debye}(r) = -\frac{[u_1^2 \alpha_{02} + u_2^2 \alpha_{01}]}{(4\pi\epsilon_0\epsilon)^2 r^6} \quad (1.8)$$

where the total polarizability  $\alpha$  is a quantity defined for all atoms and molecules according to the strength of the *induced* dipole moment they acquire in an electric field:  $u_{ind} = \alpha E$ . The electronic polarizability  $\alpha_0$  is one contribution to the total polarizability, and at very high frequencies ( $> 10^{12}$  Hz)  $\alpha = \alpha_0$ . For nonpolar molecules, the electronic polarizability originates from the displacement of their electron cloud under the influence of the external field, and it roughly depends on the molecule's radius:  $\alpha_0 \simeq 4\pi\epsilon_0 R^3$ .

3. London's dispersion forces, which always exist between all atoms and molecules, and whose name originates from their relation to the dispersion of light in the visible and UV regions of the electromagnetic spectrum. The London potential between two dissimilar species interacting in a vacuum is represented by the classic equation:

$$w_{London}(r) = \frac{-C_{London}}{r^6} = -\frac{3}{2} \frac{\alpha_{01}\alpha_{02}}{(4\pi\epsilon_0)^2 r^6} \frac{h\nu_1\nu_2}{(\nu_1 + \nu_2)} = -\frac{3}{2} \frac{\alpha_{01}\alpha_{02}}{(4\pi\epsilon_0)^2 r^6} \frac{I_1 I_2}{(I_1 + I_2)} \quad (1.9)$$

where the London coefficient  $C$  regroups all the constants and  $I_i = h\nu_i$  is the first ionization potential of the species  $i$ . Dispersion forces are quantum-mechanical in

origin and they arise from the instantaneous dipole moments existing in all atoms and molecules as their electron clouds constantly move around the nuclei; the instantaneous electric fields can then induce a dipole moment on the neighbouring species, generating a short-range interaction that may be repulsive or attractive. For two typical, small atoms in contact, the London free energy is of the order of  $kT$ , which is not negligible and gives an idea of how it is possible for high-molecular weight hydrocarbons to be in the solid state at room T and P despite the absence of electrostatic interactions.

The total van der Waals interaction is generally dominated by the dispersion force, except in the case of small and highly polar molecules. Its general equation for two polar molecules 1 and 2 interacting through a vacuum is:

$$\begin{aligned}
 w_{vdW}(r) &= -C_{vdW}/r^6 = -[C_{Keesom} + C_{Debye} + C_{London}]/r^6 \\
 &= - \left[ (u_1^2 \alpha_{02} + u_2^2 \alpha_{01}) + \frac{u_1^2 u_2^2}{3kT} + \frac{3\alpha_{01} \alpha_{02} h \nu_1 \nu_2}{2(\nu_1 + \nu_2)} \right] / (4\pi\epsilon_0)^2 r^6 \quad (1.10)
 \end{aligned}$$

The main disadvantage of London's theory is that it is unable to deal with the interactions of molecules in a solvent. Newer theories have tried to account for this problem: for example, this is done by introducing the polarizabilities of the interacting molecules (or particles) and the dielectric permittivity of the medium; also, the dielectric permittivity can be expressed at absorption frequencies  $\nu > \nu_{n=1}$  as a function of the medium's refraction index  $n$ .

In ionic liquids media, the van der Waals force is held responsible (along with electrostatics) for the formation of the bulk structure. The vdW force also dictates some physical properties of hydrophobic imidazolium ionic liquids [25], such as melting points or viscosities, thanks to the interactions between the alkyl chains often carried by the ionic moieties.

## Van der Waals Forces between Surfaces and Particles

When we consider the van der Waals interaction between flat surfaces or particles, the geometries of the involved bodies must be taken into account. Figure 1.2 lists the form of the van der Waals interaction for some typical geometries.


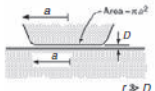
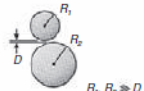
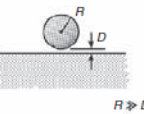
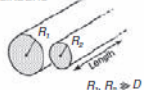
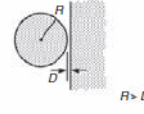
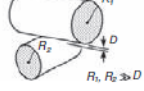
Geometry of bodies with surfaces $D$ apart ( $D \ll R$ )		Van der Waals Interaction*	
		Energy, $W$	Force, $F = -dW/dD$
Two atoms or small molecules	TWO ATOMS or SMALL MOLECULES 	$-C/r^6$	$-6C/r^7$
Two flat surfaces (per unit area)	TWO FLAT SURFACES 	$W_{\text{flat}} = -A/12\pi D^2$	$-A/6\pi D^3$
Two spheres or macromolecules of radii $R_1$ and $R_2$	TWO SPHERES 	$\frac{-A}{6D} \left( \frac{R_1 R_2}{R_1 + R_2} \right)$	$\frac{-A}{6D^2} \left( \frac{R_1 R_2}{R_1 + R_2} \right)$ Also $F = 2\pi \left( \frac{R_1 R_2}{R_1 + R_2} \right) W_{\text{flat}}$
Sphere or macromolecule of radius $R$ near a flat surface	SPHERE ON FLAT 	$-AR/6D$	$-AR/6D^2$ Also $F = 2\pi R W_{\text{flat}}$
Two parallel cylinders or rods of radii $R_1$ and $R_2$ (per unit length)	TWO PARALLEL CYLINDERS 	$\frac{-A}{12\sqrt{2}D^{3/2}} \left( \frac{R_1 R_2}{R_1 + R_2} \right)^{1/2}$	$\frac{-A}{8\sqrt{2}D^{5/2}} \left( \frac{R_1 R_2}{R_1 + R_2} \right)^{1/2}$
Cylinder of radius $R$ near a flat surface (per unit length)	CYLINDER ON FLAT 	$\frac{-A\sqrt{R}}{12\sqrt{2}D^{3/2}}$	$\frac{-A\sqrt{R}}{8\sqrt{2}D^{5/2}}$
Two cylinders or filaments of radii $R_1$ and $R_2$ crossed at $90^\circ$	CROSSED CYLINDERS 	$\frac{-A\sqrt{R_1 R_2}}{6D}$	$\frac{-A\sqrt{R_1 R_2}}{6D^2}$ Also $F = 2\pi\sqrt{R_1 R_2} W_{\text{flat}}$

FIGURE 1.2: Van der Waals interaction energy  $W$  and force  $F$  between macroscopic bodies of different geometries in terms of their Hamaker Constant,  $A$ . Negative  $F$  = positive  $A$  = attraction; positive  $F$  = negative  $A$  = repulsion. Reproduced from reference [22].

In each of these formulae, the constant  $A$  appears as a pre-factor. This is the *Hamaker constant*, whose simple form for two identical phases 1 interacting across medium 3 (the most typical case when nanoparticles of a certain material are dispersed in a solvent) is expressed according to the Lifshitz theory as:

$$A = \frac{3}{4} kT \left( \frac{\varepsilon_1 - \varepsilon_3}{\varepsilon_1 + \varepsilon_3} \right)^2 \frac{3h\nu_e}{16\sqrt{2}} \frac{(n_1^2 - n_3^2)^2}{(n_1^2 + n_3^2)^{3/2}} \quad (1.11)$$

where  $\varepsilon_1$  and  $\varepsilon_3$  are, respectively the static dielectric constants of the identical interacting

phases 1 and the medium 3.  $n$  and  $n$  are the respective refractive indexes in the visible. The interaction medium is also characterized by the frequency of the main electronic absorption in the UV,  $\nu_e$ . Equation 1.11 shows that the van der Waals force between two identical bodies is attractive since  $A$  is always positive (although it may assume negative values in some particular cases that will not be treated here). The Hamaker constants of condensed phases are typically found to lie in the range  $(0.4 - 4) \times 10^{-19}$  J, and the strength of the interaction is quite large (above  $kT$  even for nanoparticles of radius  $R = 20$  nm at a distance  $D = 10$  nm).

In the few works that take into consideration the potentials of species interacting through an ionic liquid [10, 26, 27], the Hamaker constant has been calculated through an adaptation of Equation 1.11. For example, in [10] the global Hamaker constant is  $A_{eff} = (\sqrt{A_m} - \sqrt{A_p})^2$ :  $A_p$  is the contribution of the particles (which is known from the literature and independent from the solvent), while  $A_m$  is the contribution of the IL medium and it is calculated from the Lifschitz theory thanks the reported values of the dielectric constants and the measured refractive indexes of the studied ILs. The values of the effective Hamaker constants for silica nanoparticles interacting through typical imidazolium ILs in [10] are of the order of  $\sim 5 \cdot 10^{-22}$  J. Such values are smaller than those of similar systems of silica particles ( $A_{eff}$  water-silica =  $36.2 \cdot 10^{-22}$  J). This means that the vdW interaction in the ILs is depressed compared to the aqueous system.

#### 1.1.4 Steric Contributions and Total Interaction Potential

The origin of repulsions between atoms and molecules may be not only of electrostatic origin but of steric type as well. In the latter case, the repulsive force arises because of the overlapping of electron clouds at very small interatomic distances. Despite the absence of a general equation to describe steric repulsion, there are several empirical potential functions that are commonly used, among which are for example the *hard sphere potential*, the *inverse power-law potential*, and the *exponential potential*.

In the case of colloidal systems, when the attractive van der Waals force is strong enough as to lead the colloids towards aggregation, a common way to avoid the destabilization of the system is to introduce a source of steric repulsion. Particles of various materials can be coated with surfactants or polymers, forming a “protective” layer on the colloids’ surfaces and sterically hindering their aggregation. Such steric repulsion

arises from the properties of the surfactants or polymers, and it cannot be represented by a simple potential function.

The total intermolecular pair potential is given by the sum of the attractive and the repulsive parts. The most common empiric potential approximating the interaction between a pair of spheres (neutral atoms or molecules) is certainly the *Lennard-Jones* or “6-12” potential:

$$w(r) = 4\epsilon[(\sigma/r)^{12} - (\sigma/r)^6] \quad (1.12)$$

Here,  $\sigma$  is the distance at which the potential becomes zero,  $r$  is the intermolecular distance between the centres of mass, and  $\epsilon$  is the depth of the potential well (*i.e.* the minimum energy). The Lennard-Jones potential results from the sum of an attractive contribution (which scales as  $r^{-6}$  as the vdW force) and a repulsive one (which scales as  $r^{-12}$  and represents the short-range repulsion arising when the interacting spheres are very close to each other). However, despite its common use due to its simplicity, this potential form has some limitations, such as the absence of bonding directionality (the potential is spherically symmetric).

When we move from the atomic sizes up to the particle scale, even though the origin of the interactions is still the same, the situation changes. For particles, the net interaction now arises from the sum of all the pair potentials between the molecules constituting the body, and it is proportional to the particle’s size. The interaction energy can now be larger than  $kT$  even at big separations, and it decays more slowly with separation.

Figure 1.3 shows some typical interaction potentials that can be found both between molecules and between particles in a medium, but sometimes with different consequences. For example, the graph in Fig. 1.3-(a) represents the sum of a long-range attractive interaction and a short-range repulsion: in this case, both molecules and particles are attracted to each other, and the resulting thermodynamic properties and phase diagram will depend on the depth of the minimum. In Fig. 1.3-(b), however, there is an energy barrier. In the case of molecules, this maximum is lower than  $kT$ , so the intrinsic thermal motion will cause the molecules to fall into the potential well anyway, and they will once again attract each other. In the case of particles, though, the barrier is now higher than  $kT$  (since it depends on the size of the objects): this prevents the particles from falling into the minimum, so that they will repel each other in a situation of kinetic



metastability.

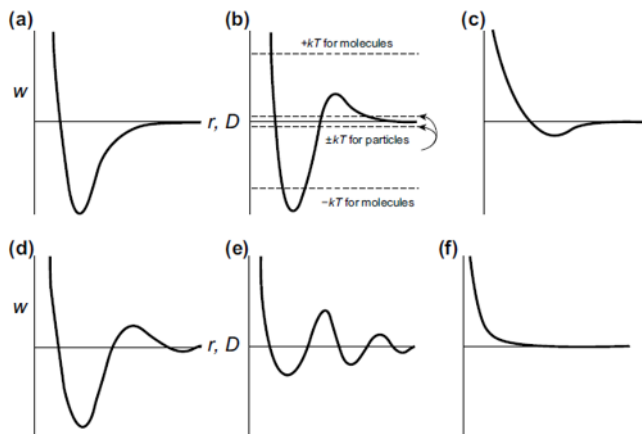


FIGURE 1.3: Examples of full potentials between molecules and particles. (a) and (b), see text. (c) Weak minimum: molecules repel, particles attract. (d) Presence of a secondary minimum: molecules attract strongly, particles attract weakly in the outer minimum. (e) Molecules attract weakly, particles attract strongly. (f) Pure repulsion. Reproduced from reference [22].

### 1.1.5 DLVO Theory

Generally speaking, colloids attract each other due to the ubiquitous van der Waals forces, so that they tend to aggregate and destroy the dispersion. One common way to stabilize dispersions against aggregation, in water or aqueous electrolyte, is to generate long-range repulsive interactions between colloidal particles by charging their surfaces [23]. The sum of the electrostatic and van der Waals interactions existing in a colloidal system leads to a total interaction potential that can be described by the well-known DLVO theory (after Derjaguin and Landau, 1941, and Verwey and Overbeek, 1948). In the case of two interacting particles, the DLVO theory relies on the Poisson-Boltzmann equation for the electrostatic repulsion, while the attractive van der Waals interaction is calculated as an integral of dispersion interactions over the volume of both particles [24]. The free energy (scaled as  $kT$ ) of the interaction between two spheres of radius  $a$  and effective charge  $Z$ , separated by a surface-to-surface distance  $r$  in an aqueous electrolyte medium, is given by:

$$\frac{w_{DLVO}(r)}{kT} = Z^2 L_B \left( \frac{e^{\kappa a}}{1 + \kappa a} \right)^2 \frac{e^{-\kappa r}}{r} \quad (1.13)$$

where  $L_B$  is the Bjerrum length, which measures the distance at which two elementary charges interact with an energy equal to  $kT$  [23], and  $\kappa^{-1}$  the Debye length (Eqn. 1.4). Objects of other than planar geometries can be treated within the Derjaguin approximation, that expresses the force profile acting between finite size bodies in terms of the force profile between two planar semi-infinite walls, provided their size is substantially larger than the Debye length [8]. Figure 1.4 shows the various types of interaction potentials, plotted as a function of interparticle distance, that can occur between two similarly charged surfaces or colloidal particles in a 1:1 electrolyte solution.

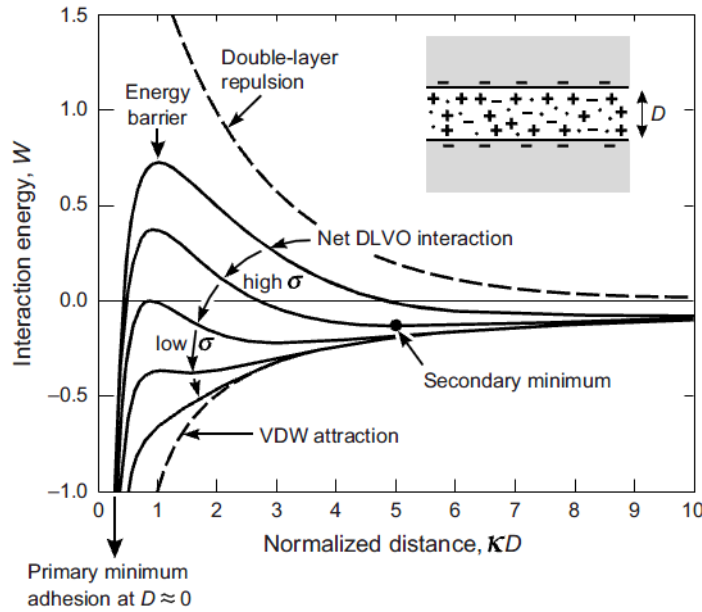


FIGURE 1.4: Energy *vs.* distance profiles of the DLVO interaction. The energy  $W$  is proportional to the interaction area while  $D$  is the distance between the two interacting surfaces. Reproduced from reference [22].

Depending on the system variables, the following different cases are possible for aqueous colloidal systems (in Figure 1.4, from the highest to the lowest curve):

- Surfaces characterized by a high charge density, in contact with a dilute electrolyte solution (*i.e.*, case of a large Debye length): a strong long-range repulsion that peaks at some distance, corresponding to the energy barrier (which can often be several  $kT$  high). The potential energy well at contact represents the “primary” minimum, which is for every system the thermodynamic equilibrium state. Thus, the particles that remain totally dispersed find themselves in a kinetically-driven stable state.

- In more concentrated electrolyte solutions, a significant secondary minimum begins to appear after the energy barrier. However, if the energy barrier is high enough, the particles may sit in the weaker secondary minimum (slight attraction, reversible flocculation), or they may remain dispersed as in the previous case.
- At lower surface charge density, the energy barrier will be lower and thus easily overcome. In this type of systems, the attractive interactions represent the most important contribution to the total potential function, and flocculation is bound to occur more or less slowly.
- When the surface charge density approaches zero, the repulsive contribution is practically non-existent and the two surfaces will strongly attract each other at all separations.

The DLVO theory is extensively used thanks to the fact that it is capable of extracting the essential physics of the problem of lyophobic colloid stability [28], and it represents the starting point for understanding the stability and phase behaviour of colloidal dispersions. When treating simple colloidal systems (low ionic strength, monovalent counterions, solvent with bulk liquid properties up to the interface...), the DLVO gives a good description of the system's interaction potential. However, this model has several limits in the description of complex aqueous systems, mainly because of the several simplifications featured by the Poisson-Boltzmann theory; namely, the representation of the solvent as a continuum dielectric medium, the disregard of finite-size (steric) effects between the ions and their chemical specificity, as well as the effect of multivalent counterions. All these shortcomings are at the origin of the fact that in some cases the DLVO theory is unable to interpret the experimental data: problems are encountered, for example, in aqueous systems characterized by high ionic strength such as biologic media. When the DLVO framework fails to explain certain experimental effects, a series of so-called "non-DLVO" forces are called into cause: hydration, long range hydrophobic, depletion, ion fluctuation, polymer bridging, specific ion effects, etc. [28].

We now turn to considering a colloidal system in which macroions (charged particles) are dispersed in an *ionic liquid* (IL), which will be the case in the present work. We immediately realize that the PB equation (and consequently the DLVO theory) is unlikely to be applicable: indeed, the extremely crowded ionic atmosphere of these media leads

them quite far from the mean-field regime of validity of the PB theory, which neglects the correlations between ions (especially important at such high concentrations as in an IL). A number of problems are thus bound to arise.

First of all, when a charged surface is immersed in a solvent entirely composed of ions, it is difficult to predict whether an electric double layer will be formed as in aqueous electrolyte solutions.

Secondly, we have already mentioned the problems arising from considering an aqueous electrolyte as a continuum dielectric medium; in ionic liquids it gets worse, since the very concept of dielectric constant in the bulk is still unclear: for liquids composed of ions, which would be expected to be very polar (*i.e.*, with a high  $\varepsilon$ ), ILs have surprisingly moderate values of  $\varepsilon$  (see [29] for comparisons between some ILs and typical molecular solvents); moreover, it is not always clear whether the methods used to measure  $\varepsilon$  in classic solvents apply in these media [29]. Since the dielectric constant appears in the expressions describing both the electrostatic (Poisson-Boltzmann) and van der Waals (Hamaker constant) interactions, the total interaction potential computed for an IL-based system will be strongly biased by an uncertain value of  $\varepsilon$ .

Finally, the concept of *ionic force* remains quite ambiguous. Are ionic liquids completely dissociated? If not, does the dissociated ratio count as “ionic strength”? Do the remaining associated cation+anion clusters have a null or negligible electric field? Most authors rely on the definition of “ionicity” deriving from the molar conductivity ratio  $\Lambda_{imp}/\Lambda_{NMR}$  (a parameter used to represent the self-dissociativity of ILs) [30]; while others consider the ILs as entirely dissociated and the molar concentration of the IL’s composing ions as the ionic strength of the system [15, 27]; and yet others treat the IL as a dilute electrolyte, composed of neutral clusters with a low dissociation ratio [31].

The inability to define the ionic force in an unequivocal way leads to a similarly unclear definition of the Debye length (Eqn. 1.4). Attempts at the calculation of a Debye length in ILs have led to contradictory and often unrealistic predictions. If the molar concentration of the ions constituting the IL is taken as the ionic strength of the medium,  $\kappa^{-1}$  is found to be of the order of the ångström [10, 15, 20], which means that the thickness of the diffuse double layer at the solid charged surface is less than the size of a hydrated ion. When the IL is treated as a dilute electrolyte with a low self-dissociation constant, the Debye length resumes more reasonable values around 10 nm [31], but we cannot help wondering whether such description of an IL is intrinsically

realistic. In sum, although many works report stable dispersions of charged particles in ILs (see Subsection 1.4.2), unfortunately the present theories fail to explain these experimental results.

We have shown how the DLVO theory is not fully adapted to the description of colloidal systems in ionic liquids. The aim of this work is to shed some light on the physical properties of such systems and gain a deeper insight in the interactions existing in such media. We will now proceed to present the experimental system used for this goal: the colloids (maghemite nanoparticles) will be described (Section 1.2), and next will be ionic liquids and in particular ethylammonium nitrate (Section 1.3.1).

## 1.2 The Colloids: Maghemite Nanoparticles

The colloids used in this work as a model system for the study of colloidal interactions in ionic liquids are maghemite nanoparticles. Indeed, the simultaneous existence of tunable magnetic dipolar interactions and electrostatic repulsion provides the opportunity to study the influence of the interaction potential's shape on the phase behavior of colloidal suspensions [32].

Maghemite ( $\gamma\text{-Fe}_2\text{O}_3$ ) is a crystalline iron oxide belonging to the class of spinel ferrites. It is most often found as a film coating magnetite, of which it represents the air-oxidised metastable form. Just like magnetite, maghemite is also ferrimagnetic. Maghemite nanoparticles were first obtained *via* the coprecipitation method by René Massart in 1981 [33]: briefly, an aqueous mixture of iron(II) and iron(III) ions is rapidly alkalized to obtain a precipitate composed of magnetite ( $\text{Fe}_3\text{O}_4$ ) particles; these are subsequently oxidized to maghemite (see Subsection 2.2.1 for details of the experimental protocol) and the result is a colloidal dispersion of spheroidal nanoparticles (Fig. 1.5) in water, with an average diameter of 7 nm and characterized by a large size polydispersity. Such polydispersity can be reduced through a size sorting process (see Subsection 2.2.2).

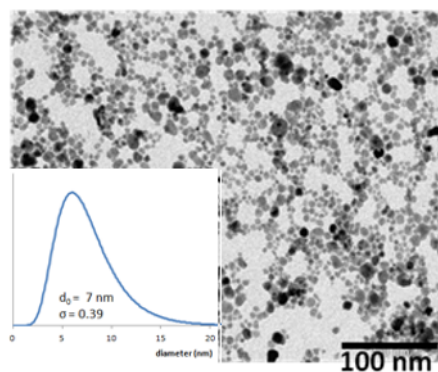


FIGURE 1.5: TEM image of maghemite nanoparticles from a typical polydisperse sample obtained by coprecipitation. The size distribution (lognormal, see Eqn. 2.2) curve shows that the average diameter is 7 nm and the polydispersity is equal to 0.39.

A stable colloidal dispersion of magnetic nanoparticles is known as a *ferrofluid*, a liquid which becomes strongly magnetized in the presence of a magnetic field, but does not retain magnetization otherwise: this property is called *superparamagnetism* and it occurs in small, single-domain magnetic nanoparticles (more information on the magnetic properties of maghemite colloidal solutions is available in reference [34]). Ferrofluids have found numerous applications in technology, industry and in the biomedical domain

[? ]: dispersed in aqueous or oil carriers, they have been used for example in magnetic data storage (hard disks), ink jet printing, catalysis, water depollution, as contrast agents in MRI, and for the treatment of cancer by magnetic hyperthermia.

The maghemite particles obtained by coprecipitation are small enough for the Brownian motion to win over gravity, preventing their sedimentation; also, the attractive interaction between their magnetic dipoles is usually faint at typical sizes and concentrations. This can be shown by writing a  $kT$ -averaged and simplified form for Eqn. 1.6 that depends on the parameter  $\gamma$ :

$$\gamma = -\frac{\mu_0}{kT} \frac{\mu_1 \mu_2}{r^3} \quad (1.14)$$

The magnetic dipole moment of maghemite is  $\mu = m_s \frac{\pi}{6} d^3$ , where the saturation magnetization  $m_s$  has typical values around  $3.1 \cdot 10^5$  A/m, and  $d$  is the diameter of the nanoparticles. Depending on the value of  $\gamma$ , two approximations are possible for the potential  $w_{magn}(r)$  [32]: for  $\gamma/4\pi \ll 1$ , we are in the low coupling regime, the dipoles rotate freely, the mean interaction is isotropic and the potential varies as  $1/r^6$ :

$$\frac{w_{magn}(r)}{kT} = -\frac{\gamma^2}{48\pi^2} \quad (1.15)$$

For  $\gamma/4\pi \gg 1$ , the interaction becomes anisotropic and has a longer range ( $1/r^3$ ):

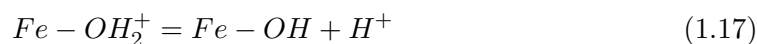
$$\frac{w_{magn}(r)}{kT} = -\frac{\gamma}{2\pi} \quad (1.16)$$

If we consider a typical ferrofluid composed of 10 nm large nanoparticles at a concentration  $\Phi = 0.01$ , the most probable distance between particles can be calculated from the relation  $\Phi = \pi/6 d^3/r^3$ , yielding 37 nm. Then Eqn. 1.14 gives a value  $\gamma$  equal to  $1.5 \cdot 10^{-1}$ , so that the low coupling approximation stands, and the free magnetic interaction energy can be calculated from Eqn. 1.15 to be of the order of  $-5 \cdot 10^{-5} kT$ , which is negligible at room temperature.

The magnetic interaction becomes important for very concentrated systems with particles at contact ( $r \equiv d$ ), where the interaction energy in the high coupling regime overcomes  $kT$ .

However, even in the cases in which the magnetic dipolar attraction is negligible, the van der Waals attraction would eventually lead these particles to flocculation [32] if some source of repulsion was not introduced [35]. This can be represented by the surface

electrostatic charges that iron oxide nanoparticles acquire when dispersed in water as a result of the Brönsted acid-base behavior of the surface sites [36]. Such sites are assumed to behave as weak diacids, and their pH-dependent protonation/deprotonation process can then be described by the following equilibria:



The dispersions issuing from the coprecipitation process have  $\text{pH} \approx 1.5$  and the surface sites on the particles are positively charged, with a surface charge density of approximately  $1.6 \text{ charges/nm}^2$ , *i.e.*, 250 charges/particle for a typical ferrofluid (average diameter of 7 nm and polydispersity around 0.4) [37]. At neutral pH, the surface charge is equal to zero (PZC, Point of Zero Charge), and the absence of electrostatic repulsions leads to the (reversible) aggregation of the particles. The different stability domains of maghemite nanoparticles as a function of the pH of the solution are depicted in Figure 1.6.

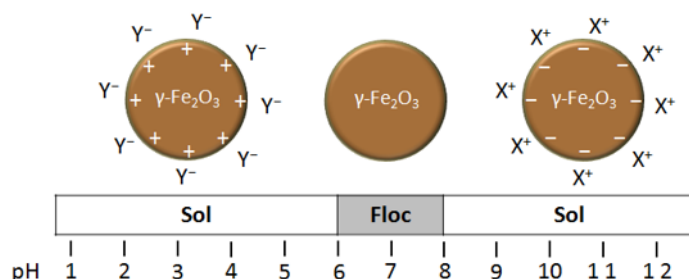


FIGURE 1.6: Stability domains of maghemite nanoparticles as a function of pH. The particles form a stable dispersion (sol) at acidic and basic pH, but they flocculate at neutral pH due to the absence of surface charges.  $Y^-$  and  $X^+$  represent the counterions for each case.

The determination of the surface charge density of larger (12 nm) particles as a function of the pH of the solution has been carried out by means of potentiometric-conductometric acid-base titrations coupled with zetametry measurements (see Fig. 1.7). As shown in Figure 1.7, the experimental results are in good agreement with models using the following parameters:  $[H^+] = 0.01 \text{ mol L}^{-1}$ ; dissociation constants for the surface acidic sites,  $\text{p}K_1 = 5.4$  and  $\text{p}K_2 = 9$ ; surface charge density  $\sigma_s = 2.1 \text{ charges/nm}^2$ . We invite the reader to refer to [36] for further details, and we shall now focus on different systems.



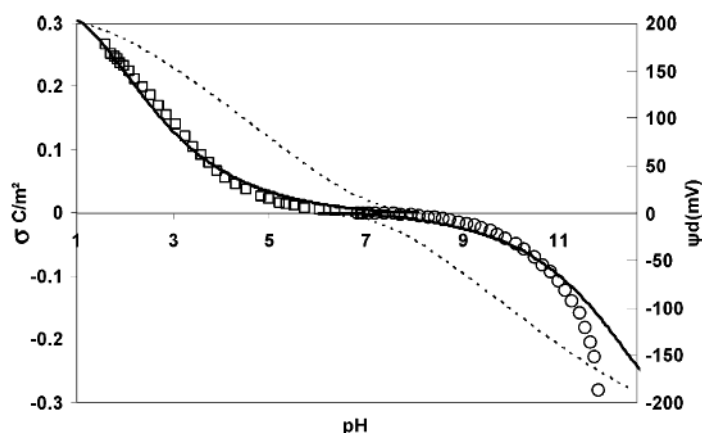


FIGURE 1.7: Dependence of the structural charge  $\sigma_0$  ( $\text{C m}^{-2}$ ) of 12 nm large maghemite NP on the pH. Open symbols:  $\sigma_0$  determined experimentally from potentiometric titrations. Full line: simulation of  $\sigma_0$  during the titration (see text for details). Dashed line:  $\psi_d$  (mV), the surface potential determined from the Poisson-Boltzmann equation for a spherical particle. Reproduced from reference [36].

One way to obtain stable maghemite dispersions in different pH domains is to adsorb various molecules on their surface: for example, the work of N. Fauconnier has focused on the absorption of many different organic ligands, such as  $\alpha$ -hydroxy or thiol polycarboxylic acids and  $\alpha$ -amino hydroxamic acids, capable of complexing the surface iron atoms and forming quite a stable bond with the nanoparticles surface [38]. In particular, citric acid has been a favourite ligand since a long time: not only does it give place to exceptionally stable suspensions, but it is a cost-effective reactant, and it has opened the way to the utilization of ferrofluids in the biomedical domain, thanks to the biocompatibility of its molecule and to the obtention of stable colloidal dispersions at physiologic pH (see Fig. 1.8 for the stability domains of citrate-covered  $\gamma\text{-Fe}_2\text{O}_3$  nanoparticles.).

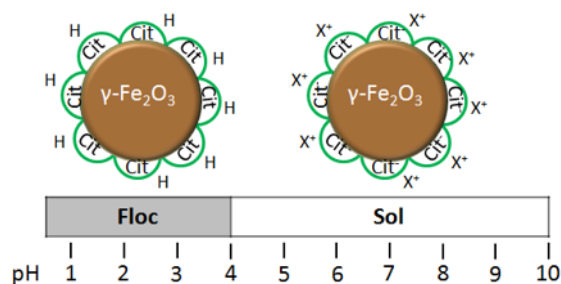


FIGURE 1.8: Stability domains of citrate-covered maghemite nanoparticles as a function of pH. The particles form a stable dispersion (sol) at  $\text{pH} > 4$ , when enough carboxylic functions are deprotonated ( $\text{X}^+$  represent the counterions) to insure an effective repulsion. At  $\text{pH} < 4$ , the particles flocculate due to the absence of surface charges.

The properties of citrate-covered maghemite NP in water have been extensively studied. For example, it is known that the adsorption of citrate reaches the saturation of the maghemite surface sites at a structural charge value of  $2 \pm 0.2$  charges/nm<sup>2</sup> [39]; the remaining citrate is freely dissolved in the bulk solution (in the order of 0.01 mol/L at saturation) and contributes the ionic strength of the system.

The phase diagram for this system [32] has been determined at the beginning of the 2000s thanks to the work of Cousin *et al.*. In order to find the phase boundaries it was necessary to induce a colloidal gas-liquid transition (see [40] for details on phase transitions in colloidal systems): the destabilization of this type of systems can be obtained in different ways, for example by screening the electrostatic repulsion through the addition of an electrolyte, by decreasing the temperature, or by applying a constant magnetic field. In general, the samples were prepared by osmotic compression in order to impose a chosen osmotic pressure  $\Pi$  and a chosen ionic strength  $I$ . Once the volume fraction of the nanoparticle  $\Phi$  was known, the colloidal system was fully characterized by the three parameters  $\Pi$ ,  $\Phi$  and  $I$ . By coupling the visual observation of the samples with nano-scale investigations by means of small angle (neutron and x-ray) scattering, it was possible to obtain the phase diagrams for two distinct regimes: at low ionic strength (when the potential is repulsive and only fluid-solid phase transitions are observed) and at high ionic strength (when the potential is attractive and the phase diagram shows the same regions as an atomic system), as shown in Fig. 1.9.

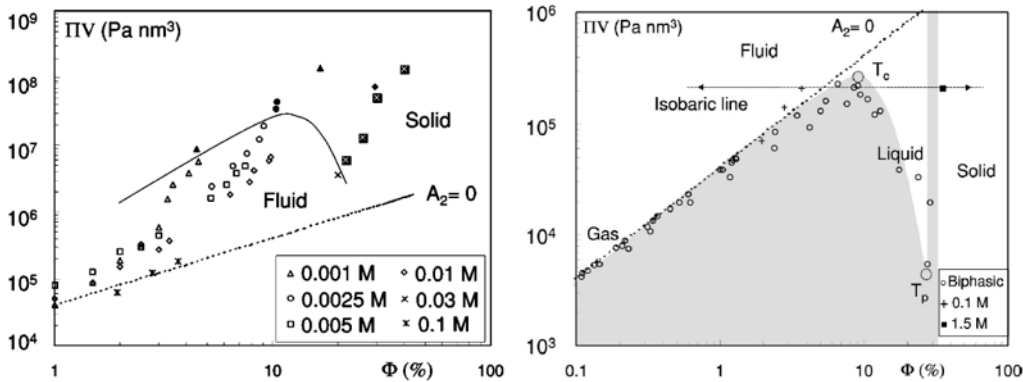


FIGURE 1.9: Phase diagrams for aqueous colloidal dispersions of maghemite NP. Left: low ionic strength regime. The structure of the suspension is ruled by strong electrostatic repulsions; the full line is a guide to the eye, which shows the limit between fluid and solid areas;  $[cit]_{free}$  is given in the caption. Right: high ionic strength regime. The gray part of the diagram is a guide for the eye and represents the biphasic areas;  $[cit]_{free}$  is given in the caption for the different points corresponding to monophasic samples. Reproduced from reference [32].

In conclusion, citrate-covered maghemite NP represent a versatile experimental system. Since the aqueous system has been thoroughly characterized and is mastered in detail, we believe it to be a valid starting point to study the colloidal interactions in ionic liquids.

### 1.3 Ionic Liquids

The solvents used as dispersion media for maghemite nanoparticles in this work are ionic liquids (ILs). Formerly known by the appellation of “molten salts”, they are defined as a class of compounds made up solely of ions and with a melting point  $T_m \leq 100^\circ\text{C}$ . The steric mismatch between the composing ions (generally a bulky organic cation and a smaller organic or inorganic anion) prevents their arrangement in a regular crystal structure, determining the unusually low melting temperatures. ILs that melt at temperatures  $T_m \leq 25^\circ\text{C}$  form the sub-class of Room-Temperature Ionic Liquids (RTILs), and they represent a family of ionic solvents that have been attracting a growing interest in the last few decades.

Ionic liquids are often referred to as “designer solvents”, thanks to their easily tunable design and properties which make it possible to obtain a potentially infinite number of ILs and adapt them to the chemist’s need. Indeed, the association of different types of cations and anions allows not only for the continuous obtention of novel ILs with new qualities, but also for a finer tuning of specific properties such as ionic conductivity or hydrophilicity/hydrophobicity. Even an apparently minor structural modification, such as the substitution of a  $\text{C}_{10}$  chain with a  $\text{C}_{12}$  chain on an alkyylimidazolium moiety, has an impact on the physico-chemical characteristics of the resulting IL. Figure 1.10 lists the most common classes of ILs by cations; anions that are found in most typical ionic liquids are, for example, halide anions,  $\text{BF}_4^-$ ,  $\text{PF}_6^-$ , and bis(trifluoromethylsulfonyl)imide  $\text{NTf}_2^-$ .

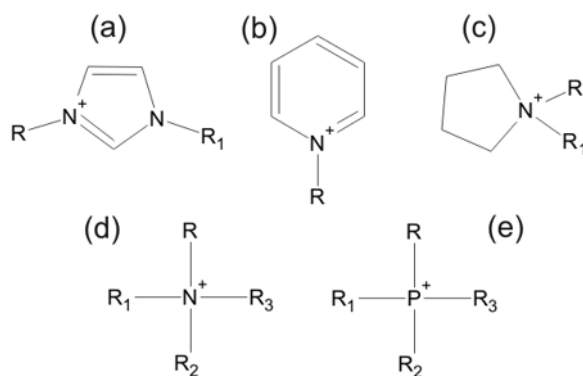


FIGURE 1.10: Common IL families classed by cation: (a)  $N,N$ -dialkylimidazolium; (b)  $N$ -alkylpyridinium; (c)  $N,N$ -dialkylpyrrolidinium; (d) ammonium; (e) phosphonium.

Ionic liquids have been called “green solvents” due to their extremely low vapour

tension and non-flammability, which make them good candidates for the replacement of more dangerous and toxic organic solvents in many cases. In particular, the practically negligible volatility of ILs makes them suitable for low-pressure and vacuum applications. Also, a large number of studies have shown that ILs can stand several cycles of utilization during various processes, such as catalytic reactions, without losing their properties. Though in truth, the real eco-friendliness of ILs in general is in doubt, as their immediate toxicity and environmental fate are often not clear [41]. Other typical properties of ILs are a high viscosity (with values that can range between 15 and 8000 cP) [42], a large electrochemical window, good ionic conductivity and high thermal stability.

An important aspect that should be addressed, since it determines the physico-chemical properties cited above, is the real ionic nature of ILs. Indeed, there is experimental evidence of the formation of ions clusters in bulk ILs. For example, imidazolium-based salts form an extended network of cations and anions connected together by hydrogen bonds: the monomeric unit is always composed of one imidazolium cation surrounded by at least three anions, and in turn, each anion is surrounded by at least three cations [43]. The so-called “ionicity” of ILs then represents the fraction of ionized species that do not form clusters. According to Ueno *et al.* [30], this property depends strongly on the structure of each IL and on the relative Lewis acidity/basicity of the composing ions. Basically, a *good* IL will be constituted of a weakly Lewis-acidic cation and a weakly Lewis-basic anion that do not interact very strongly with each other; as a consequence, the ions can be dissociated at ambient temperature with no need for solvation by a molecular solvent (like water). Hence, the more dissociated is an IL, the more it will be characterized by all the peculiar properties that make this a very special class of solvents.

Despite the fact that they have been known for about a century, ILs and their physico-chemical properties have not received much attention until recently [44]. The number of studies concerning the synthesis and physico-chemical characterization of ILs has been growing exponentially since the 1980s, and their applications are countless:

- as solvents for chemical reactions and liquid/liquid extraction;
- as reaction media for organic and inorganic catalysis, for example in biomass conversion, production of fine chemicals (pharmaceuticals, food additives, pesticides), Friedel-Crafts alkylation of petroleum-derived compounds [3] . . .

- as electrolytes in electrochemical devices such as Dye-Sensitized Solar Cells, with the possibility of forming IL-based gels, to prevent electrolyte leakage and without losing in conductivity. Some examples: SiO<sub>2</sub> nanoparticles dispersed in 1-butyl-3-methylimidazolium tetrafluoroborate ([BMIM][BF<sub>4</sub>]) [6]; TiO<sub>2</sub>, carbon nanotubes, carbon fibers and carbon nanoparticles dispersed in 1-ethyl-3-methylimidazolium bis(trifluoromethylsulfonyl)imide ([EMIM][NTf<sub>2</sub>]) [45]; ceramic materials (TiC) dispersed in 1-ethyl-3-methylimidazolium thiocyanate ([EMIM][SCN]) [46];
- as heat-transfer fluids, alone or as liquid support for various types of nano-sized objects, thanks to a better thermal capacity than commercially available heat-transfer fluids, and the advantage of enduring high temperatures without evaporating or decomposing [47];
- as lubricants, especially alkylimidazolium tetrafluoroborates and trialkylammonium ionic liquids, used to reduce friction in high-vacuum and high-temperature applications thanks to their resistance to evaporation [48];
- as components of membrane systems for CO<sub>2</sub> separation and storage [49].

In the work carried out for this Thesis, the main IL of choice belongs to the class of alkylammoniums (depicted in Figure 1.10-d). These ionic liquids are usually synthesized *via* a simple acid-base reaction involving the appropriate alkylamine and an inorganic or organic acid; the only byproduct of such reactions is water, which is easily eliminated by vacuum pumping or lyophilisation (freeze-drying), allowing the obtention of very pure final products. Detailed information about our IL, ethylammonium nitrate, is given in the next section.

### 1.3.1 Ethylammonium Nitrate

The IL used in this work is ethylammonium nitrate (EAN), one of the first ionic liquids ever discovered, and characterized in 1914 by Paul Walden [50], of which the chemical formula is shown in Figure 1.11. Its similarity with water, and the ease of synthesis and use, make this ionic liquid a very suitable candidate as a dispersion medium for nanoparticles. Thanks to the thorough characterization of EAN carried out in the last century, we can nowadays count on a vast set of data concerning this solvent. Table 1.1 resumes the salient physico-chemical properties of EAN. Details on its synthesis process are given in Chapter 2, subsection 2.2.5.

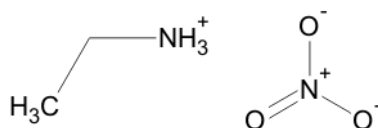
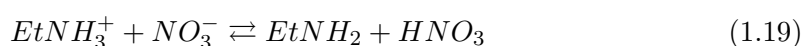


FIGURE 1.11: Molecular formula of ethylammonium nitrate.

Physico-chemical properties of EAN		
Property	Value	Reference
Molecular Weight	108 g mol <sup>-1</sup>	
Melting Point, $T_m$	14 °C	
Density, $\rho$	1.21 g cm <sup>-3</sup>	[51]
Viscosity, $\eta$	35.3 mPa s (at 25 °C)	[52]
	23.1 mPa s (at 30 °C)	[53]
	11.5 mPa s (at 50 °C)	[53]
Surface Tension, $\gamma$	50.6 mN m <sup>-1</sup>	[54]
Vapour Tension	5.33 Pa (at 25 °C)	[55]
Heat Capacity, $C_p$	206 J K <sup>-1</sup> mol <sup>-1</sup>	[51]
Refractive Index, $n$ (at 632.8 nm)	1.4535 (at 25 °C)	[56]
Static Dielectric Constant, $\epsilon$	26.2 (at 25 °C)	[56]
Fraction of eff. ionised ions	92%	[56]
Conductivity, $\Lambda$	49 mS cm <sup>-1</sup> (at 25 °C)	according to [52]
	28 mS cm <sup>-1</sup> (at 25 °C)	according to [56]
Autoprotolysis Constant, $pK_s$	10.1	[57], [18]

TABLE 1.1: Some physico-chemical properties of Ethylammonium Nitrate.

This ionic liquid belongs to the class of Room-Temperature ILs and it is completely miscible with water in all concentration ratios. Additionally, EAN is known to be in many ways similar to water: first of all, it is a protic ionic liquid (PIL), meaning that a labile proton is exchanged between the two species ethylamine and nitrate, according to the following equilibrium:



Here, molecular nitric acid is the strongest acid (solvated proton) and ethylamine is the strongest base. Assimilating activities and concentrations, the pH is defined as  $-\log[HNO_3]$  and the autoprotolysis constant is  $K_s = [EtNH_2][HNO_3]$  ( $pK_s = 10.0 \pm 0.2$ ), as determined independently by Benhlima *et al.* in 1989 [57] and by Kanzaki *et al.* in 2007 [18]. A pH scale can then be defined in this liquid, and the neutral pH in EAN is equal to 5.0. Just like in water, acid-base properties of various species can be

described in EAN: strong acids and bases can be defined, as well as weak acids/bases characterized by an acidity constant [18, 57].

Another important feature that EAN shares with water is the existence of a three-dimensional hydrogen-bond network throughout the bulk liquid. Fumino *et al.* [19] have shown, by means of Far-IR spectroscopy and Density Functional Theory calculations, the presence of intramolecular and intermolecular  $\text{NH}\cdots\text{O}$  bonds possessing comparable strength to those found in water. The geometry of ethylamine and nitrate is nevertheless different from that of water, and the tetrahedral arrangement typical of water's H-bond network cannot be reproduced in EAN (Fig. 1.12); this is reflected in EAN's lower heat capacity.

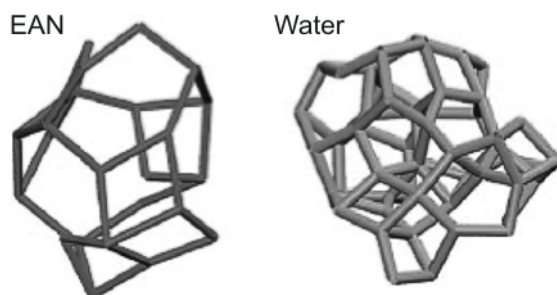


FIGURE 1.12: H-bond network structures of EAN and water obtained from DFT calculations. Reproduced from reference [19].

Further studies have clarified the extent of hydrogen bonding in EAN and its consequences on the bulk structure of this ionic liquid. In a SANS spectrum of pure deuterated EAN (D-EAN), Atkin and Warr [58] detected the presence of a Bragg peak corresponding to a distance approximately twice the ion pair dimension. The spectral data relate with a locally lamellar structure and can be interpreted as originating from an alternation of polar-apolar layers, arising from the H-bonding between ionic moieties and, at the same time, from the solvophobic association of the alkyl groups. EAN, though, is not a birefringent liquid, which rather suggests a wholly disordered sponge-like bulk structure. In a recent paper, [59] Hayes *et al.* went further, comparing EAN with other alkylammonium PILs, all of them forming similar bicontinuous, sponge-like nanostructures, but characterized by hydrogen bonds of different strength depending on the size of the anions. In the final picture, it appears that the very sponge-like nanostructure of the PILs is not a consequence, but actually the origin, of such different H-bond strength: the H-bonds formed are more or less linear (and hence more or less strong, and the resulting



PIL more or less solid-like) depending on the geometry required for the IL molecules to satisfy the amphiphilic balance and be accommodated in the bicontinuous arrangement.

The presence of hydrogen bonds in EAN also seems crucial to promote self-assembly of amphiphilic solutes. In a 1982 study, Evans *et al.* [53] obtained c.m.c. values for several ionic and non-ionic surfactants in EAN, using light scattering experiments and viscosity measurements; the c.m.c.'s are higher than in water, a result obtained for other RTILs as well [60]. Micelle formation is accompanied by the lowering of surface tension just like in water, and more specifically, the final value of surface tension attained by different surfactants in ILs and water are comparable [60]. Other types of structures, namely lamellar and cubic lyotropic liquid crystals, have been found to take place from the self-assembly of non-ionic surfactants in EAN, such as polyoxyethylene [60].

In conclusion, the ionic liquid ethylammonium nitrate was chosen for this work because of three main reasons:

- it is readily synthesized from low-cost reagents, and easy to manipulate;
- it shares many features with water, which makes it easier to compare its system to those already known and well-controlled in water;
- there exists a vast collection of physico-chemical data for it in the literature.

## 1.4 Ionic Liquids in Colloidal Systems: State of the Art

In what follows, we summarize the work that has been done by other authors on the subject area of colloidal systems based on ionic liquids. First, we rapidly present the role of ILs in the synthesis of nanoparticles. Next, we focus on the central topic of this Thesis, the dispersion of nanoparticles in these ionic media, with special interest in magnetic oxides (the main theme of this work) and silica (representing a perspective work to follow). We then review the literature concerning the behaviour of ILs in contact with flat solid surfaces, which offers elements of reflection to better understand the role of such solvents in the stabilization of solid nanoparticles. Finally, we present the few actual studies dealing with the interaction potential in IL-based colloidal systems in an effort to answer the questions, presented in the Introduction to this work, concerning the origin of colloidal stability in ionic liquids.

### 1.4.1 Ionic Liquids as a Medium for the Synthesis of Nanoparticles

Thanks to their many interesting features, ionic liquids (especially imidazolium-derived salts) have been used as “green” synthesis media for quite some time to generate and stabilize metallic nanoparticles. If in some cases the use of toxic and dangerous solvents is still necessary for the synthesis of nanoparticles before the stage involving the IL (for example, in [61] Ni NP are obtained by dispersing the precursor in benzene before transferring the solution to the IL), there is a growing number of works in which the solvent is represented by a pure IL. Indeed, one prominent characteristic of these media is the existence of highly self-organized liquid structures, mainly through hydrogen bonds, providing hydrophobic or hydrophilic domains in which non-polar and polar species can be accommodated. The supramolecular organization of ILs can then act as an entropic driver for the spontaneous, well-defined and extended ordering of nanoscale structures [43]: for example, ILs can facilitate the direct formation of crystals for reactions that, in other media, would need extreme conditions [62], making the procedures less dangerous and more cost-effective.

The low interface tension in ILs results in high nucleation rates, favouring the obtention of very small particles, while the IL used can often be recycled after each synthesis and re-used for several further reaction cycles as in [63], thus reducing the amount of waste.

Moreover, depending on the very composing ions, the final outcome of the synthesis can be tuned. For example, the surface properties of the resulting particles can be modified, as in Itoh *et al.*'s work [64], in which gold nanoparticles have been made hydrophobic or hydrophilic by adsorbing IL anions with different polarities on their surface. The effect of the IL's cationic moiety was studied by Wang *et al.* [65], who were able to prove that the length of the alkyl chain on the imidazolium cation can affect the size of the particles synthesized in the IL.

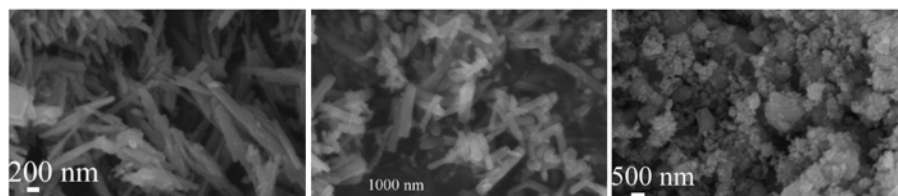


FIGURE 1.13: SEM images of different ZnO nanostructures obtained in  $[\text{BF}_4]$ -based ILs by modifying the imidazolium moiety. Reproduced from reference [65].

Finally, the purity of the ILs used as synthesis media plays an important role, especially for what concerns trace halides and water. Not only do these impurities modify the physico-chemical properties of the ILs (for example their viscosity, and therefore the transport properties), but they can also act as extra ligands and change the kinetics of the NP formation [43]. The role of water, although not very clear so far, is surely important and complex: something certain is that water found in traces in ILs has a different behaviour from that of bulk water, due to the strong interactions with the IL's ionic moieties. Some reactions have showed to depend strongly on the water content of the IL medium, and it was suggested that water may modify the patterns of IL self-organization (which, as said earlier, can be the driving force for the synthesis of NP). On the other hand, when the water content is predominant, the main properties of ILs are lost, but they can still have a role behaving as classical surfactants [62].

### 1.4.2 Colloidal Dispersions in Ionic Liquids

Either synthesized directly in an IL, or in another medium before transfer to the IL, in many cases the nanoparticles need to be stabilized in the ionic liquid in order to be of any use. Many studies have tried to shed some light on the mechanisms leading to the colloidal stabilization of nanoparticles in ILs. Among the first to focus on the transfer of metal nanoparticles from aqueous to IL media, Wei *et al.* [12] propose in 2004

a method to disperse gold NP, synthesized in water, in the ionic liquid [BMIM][PF<sub>6</sub>] without adding capping agents (such as thiols or amines). Unfortunately, the Au nanoparticles flocculate unless a surfactant is previously added to the aqueous phase. The impossibility to stabilize bare Au particles is also reported in a recent work involving the IL [BMIM][NTf<sub>2</sub>] [27].

This kind of evidence is what led Zhao *et al.* [9] to argue that metal nanoparticles cannot form suspensions in ionic liquids unless some sort of stabilizer is used, like polymers or thiol-functionalized ILs. In their work, these authors use a high-molecular weight IL-polymer composed of imidazolium and benzyl units as an additive during the syntheses of gold, platinum and palladium nanoparticles in aqueous medium. The NP thereby obtained can then be readily transferred to the IL phase. The authors try to explain their results by proposing that the synergism of steric, electrostatic and micelle effects be the stabilizing force in this system.

Since the importance of ILs has begun to grow in several applications (such as the preparation of ferrofluids in ionic liquids), fundamental research has been focusing more and more on the understanding of the mechanisms behind the stabilization of nanoparticles in ionic liquids. However the results and attempts at explanations concerning the parameters governing colloidal stability are often contradictory.

For example, in a recent work Oliveira *et al.* [16] prepared stable dispersions of maghemite and cobalt ferrite nanoparticles in the ionic liquid [BMIM][BF<sub>4</sub>]. Following their classical synthesis in water, and with no further functionalization, the nanoparticles are transferred to [BMIM][BF<sub>4</sub>], but the dispersions are not stable unless water is removed by vacuum pumping. The authors propose that the colloidal stabilization occur through the formation of IL layers at the nanoparticles/IL interface, inducing a steric hindrance to the contact between NP. Such layers would present the BF<sub>4</sub><sup>-</sup> anion facing the positive charge on the surface of the particles, inducing a subsequent “... cation ... anion ... cation ...” pattern, as depicted in Figure 1.14. In such a scenario, the presence of water at the interface might screen the surface charges and destroy the protective IL layers, causing flocculation: this is why, according to the authors, elimination of as much water as possible would represent the only path to colloidal stability in their systems.

However, Oliveira *et al.*'s result failed to be replicated by Jain *et al.* [11], who prepared IL-ferrofluids based on maghemite with NP of similar size to those used in [16]. Another point in common with in [16] here is the fact that the NP are synthesized

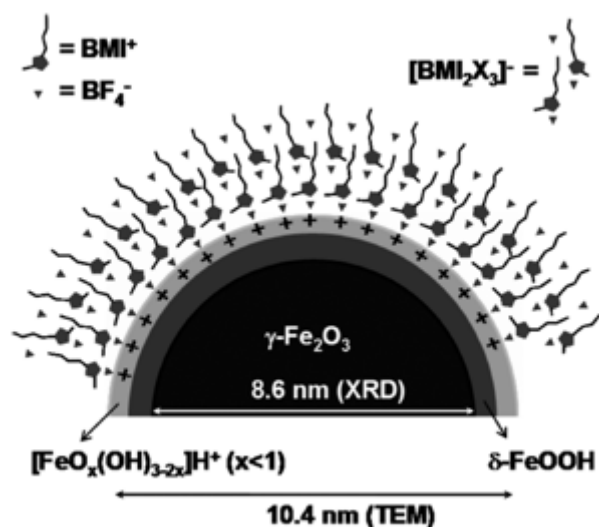


FIGURE 1.14: Schematic proposition of the stabilization mechanism for maghemite NP in  $[\text{BMIM}][\text{BF}_4]$ . The IL forms layers at the NP surface, which are induced by the positive surface charge of the bare maghemite nanoparticle. Reproduced from reference [16].

in water and then transferred to the ionic liquids. After water removal and sonication, the bare nanoparticles give rise to stable dispersions in the two ethyl-methylimidazolium ILs  $[\text{EMIM}][\text{Ac}]$  and  $[\text{EMIM}][\text{SCN}]$ , but only short-lived dispersions in  $[\text{BMIM}][\text{BF}_4]$ . It must be noted, though, that the authors of [11] do not detail the pH conditions occurring before the transfer to the IL, thus nothing is known about the initial surface charge of the NP; moreover, no quantitative determination of the remaining water content is explicitly mentioned. In such a picture, it is difficult to compare this case to Oliveira's work to try and understand the reasons lying behind their different results.

Jain *et al.* also found it impossible to stabilize bare maghemite particles in ethylammonium nitrate (EAN), but once again nothing is known on the surface state of the particles or on the pH of the medium (especially important in a protic IL, as we will show in Chapter 3). On the other hand, they successfully dispersed polymer-coated maghemite nanoparticles in  $[\text{EMIM}][\text{Ac}]$  and EAN, attributing the formation of stable dispersions to the steric effect of the polymer layer. In the other two ILs, such stabilization was not possible, due simply to the insolubility of the polymer in these solvents.

As a final step, the authors of [11] looked into the effect of using a mixed IL-water solvent for bare maghemite nanoparticles. What they found is that as little as 5 wt% ionic liquid (roughly in the order of  $0.5 \text{ mol L}^{-1}$ ) added to water dispersions acts as any

dilute electrolyte and screens the electrostatic forces; the addition of more IL only destabilizes the system further. This result is consistent with the classic effect of electrolytes on electrostatically stabilized colloids. On the “opposite side” of the IL-water mixing ratios line, adding 5-10 wt% water to the IL-ferrofluids also destabilizes the dispersions: just like Oliveira’s team, the authors believe that the mechanism determining the stability of NP in ILs lies in the formation of solvation layers, therefore they infer that the role of water might be the disruption or displacement of the IL’s solvation layers on the particles surface.

Such disruptive role of water is also evidenced in other works. For example, in the case of Ag nanoparticles dispersed in [BMIM][BF<sub>4</sub>] by Rubim *et al.* [66], a very small amount of water is enough to cause aggregation of the NP, followed by their precipitation. Similarly, Vanecht *et al.* [27] studied the effect of water on dispersions of sputtered gold nanoparticles in four common imidazolium ILs. These authors found that the already quite unstable systems show a much faster coagulation rate in the presence of water, even when its concentration is as low as 10 ppm (enough to cover 70% of the NP surface).

As mentioned above, Jain *et al.* could not disperse maghemite NP functionalized with a polymer in [EMIM][Ac] and [EMIM][SCN], due to the insolubility of such polymer in the ILs. One way around this problem is to coat the nanoparticles surface with one of the ions constituting the IL itself, as was done by Medeiros *et al.* [67]: in this work, different types of magnetic nanoparticles undergo a silanization process and are coated with a molecule carrying the cation 1-butyl-3-methylimidazolium. Such particles give rise to stable, concentrated dispersions in [BMIM][NTf<sub>2</sub>], even in the presence of high magnetic fields, thanks to the coating that works as a barrier against flocculation.

Difficulties in the dispersion of bare magnetic nanoparticles are also encountered by Rodríguez-Arco *et al.* In a 2011 work [14], these authors argued that magnetite NP can be dispersed in the ionic liquid [EMIM][EtSO<sub>4</sub>] only when functionalized (in water, before transfer to the IL) with a double layer of oleate, so as to introduce a source of steric hindrance. Therefore, this is yet another work pointing at the fact that some kind of steric repulsion is needed to ensure colloidal stability in ILs. Here, this condition is fulfilled in a classical way by adsorbing a long chain surfactant on the iron oxide surface, which compares well with the study by Jain *et al.* [11] involving steric stabilization by polymer coating. In Rodríguez-Arco *et al.*’s work, though, the role of water is not addressed.

In a similar study, Huang *et al.* [68] also worked with systems based on the IL [EMIM][EtSO<sub>4</sub>], but the dispersed phase in their case is represented by bare and oleate-coated cobalt ferrite nanoparticles. The dispersions are obtained by mixing the dried ferrite powders directly into the ionic liquid (with an excess of oleic acid for the coated nanoparticles, as in [14]). Much like Rodríguez-Arco *et al.*, these authors found that the only way to obtain colloidal stability in this IL is to have an oleate double layer at the cobalt ferrite surface to sterically stabilize the nanoparticles.

In a 2007 study, Guerrero-Sanchez *et al.* [69] successfully prepared magneto-rheological fluids (MRFs, in which the dispersed NP have sizes in the micron range) based on magnetite particles without stabilizing additives dispersed in several ILs, most of which imidazolium-based, some hydrophilic and some hydrophobic. Their results demonstrate the possibility of obtaining MRFs with low rates of sedimentation from bare particles, provided that the proper conditions (type of IL and concentration of dispersed magnetic particles) are chosen.

On the other hand, Gomez-Ramírez *et al.* [70] compared magneto-rheological fluids based on metallic iron particles, bare or coated with silica, prepared in [EMIM][EtSO<sub>4</sub>] and [EMIM][Et<sub>2</sub>PO<sub>4</sub>]. While all samples show a better colloidal stability than the classical suspensions in mineral oil, the authors found that the silica-coated particles in [EMIM][Et<sub>2</sub>PO<sub>4</sub>] give the best results: they are easily, homogeneously dispersed, suggesting that the silica coating somehow allows for the obtainment of less aggregated particles. Once again, no unequivocal information can be extracted on the type of NP surface needed to obtain colloidal stabilization.

Concerning other oxides than those based on iron, Wittmar *et al.* [71] recently tested commercial and laboratory-made TiO<sub>2</sub> nanoparticles of different crystalline structures, dispersed in two RTILs: [EMIM][NTf<sub>2</sub>] (hydrophobic) and [EMIM][BF<sub>4</sub>] (hydrophilic). The authors found that all powders are better dispersed in the hydrophilic ionic liquid; what is more, the powders containing adsorbed water on the surface, or hydroxyl groups, are more efficiently redispersed even at high concentration. The state of surface of the particles is once again of primal importance in determining the colloidal stability. According to the authors, one of the possible reasons for the effects observed could be the formation of hydrogen bonds between the surface-bound water molecules, or –OH groups, and the anions of either IL, NTf<sub>2</sub><sup>–</sup> and BF<sub>4</sub><sup>–</sup>. This is not in contrast with the solvation layers model proposed by other authors, since hydrogen bonds are, just like

pure Colombian interactions, a source of ion-ion correlations.

### **Silica Nanoparticles: Dispersions and Ionogels**

Silica is a very abundant compound on Earth and it is widely used for the preparation of various types of nanomaterials. It is thus not surprising that it has been taken as a model system to study the behaviour of oxide nanoparticles in ionic liquids. For example, Ueno *et al.* have worked extensively, in the latest years, on the preparation and characterization of colloidal silica suspensions in various ILs, with the explicit goal of understanding the mechanisms governing colloidal stability in these media. In one of their first works [72], they used Aerosil 200, a type of fumed silica (composed of 12 nm primary particles) carrying silanol (Si-OH) groups on the surface. While homogeneously dispersed in the ionic liquid [EMIM][NTf<sub>2</sub>] at low NP concentration, Aerosil 200 forms a gel already at 3 wt% in this IL. The authors could confirm the presence of a particulate network structure, and they suggest the formation of fractal aggregates following the RLCA pathway. This mechanism requires moderate repulsions to exist between the particles (*i.e.*, an energy barrier has to be overcome in order to obtain a cluster-forming collision between particles); though, since in ILs the classic electrostatic repulsion is thought to be annihilated, the authors look for a different kind of repulsion. NMR diffusion measurements show that the IL's cation, 1-methyl-3-ethylimidazolium, interacts more strongly with the silica surface than the NTf<sub>2</sub><sup>-</sup> anion. This fact hints once again at the possible induction of solvation layers, probably through the electrostatic interaction between ionized hydroxyl groups (provided the initial pH is basic enough for their deprotonation, which is not mentioned in the paper) and the positive charge on the IL cations. The subsequent "... cation ... anion ... cation ..." pattern would therefore result in the existence of a steric/solvation kind of repulsion.

Later, Ueno *et al.* compared Aerosil silica particles with different surfaces [73]: one hydrophilic, with Si-OH groups, and one hydrophobic, with Si-CH<sub>3</sub> groups. The dispersing media are represented by several different ILs (see Table A.1 for the entire list). The hydrophilic silica forms a stable sol in [BMIM][BF<sub>4</sub>] and [E-OH-MIM][NTf<sub>2</sub>] ionic liquids, chosen for their ability of forming hydrogen bonds. On the other hand, the hydrophobic silica gives place to gels in all of the studied ILs: in this case the silica surface and the ILs are poorly compatible, and the possibility of H-bonding is highly reduced due to the presence of -CH<sub>3</sub> surface groups instead of -OH. It should also be



mentioned that, in the absence of ionizable groups, the surface of the hydrophobic NP is electrically uncharged, which draws off another possible source of interface structuration. This work points out the fact that the surface of the nanoparticles is a crucial parameter for colloidal stability.

Ueno *et al.* seem to be among the first authors to recognise the importance of controlling the NP/IL interface, as evidenced already in [10]. In this work, the authors investigate the stability of monodisperse (120 nm large) silica nanoparticles, either bare or grafted with poly-methyl-methacrylate (PMMA). The dispersing media are the classic imidazolium-based ILs [BMIM][BF<sub>4</sub>], [BMIM][PF<sub>6</sub>], and three [NTf<sub>2</sub>]-based 1-methyl-3-alkylimidazolium ILs with ethyl, butyl and octyl lateral chains. As proven by TEM images (Fig. 1.15), the bare NP aggregate in all of the five ILs used; this represents a difference in stability compared to the smaller Aerosil 200 NP, which proved to be dispersible at low wt% in [EMIM][NTf<sub>2</sub>] [72]. On the other hand, when coated with PMMA, the stability of large silica particles depends on the PMMA-IL compatibility: well dispersed in [BMIM][NTf<sub>2</sub>] (best solvent), the other [NTf<sub>2</sub>] ILs, and [BMIM][PF<sub>6</sub>], but not in [BMIM][BF<sub>4</sub>] since PMMA is insoluble in such IL.

Moreover, in the same work the authors perform some calculations by applying the DLVO theory to discuss the interparticle potential in these systems (see also Subsection 1.1.5). As a result, both the electrostatic and steric contributions are found too weak to be responsible for the colloidal stability experimentally observed. This aspect will be treated in more detail in Subsection 1.4.4.

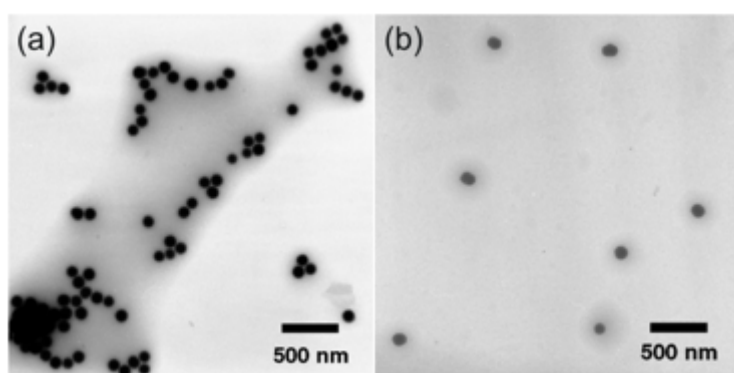


FIGURE 1.15: Different colloidal stability of (a) bare and (b) PMMA-grafted silica particles. Reproduced from reference [10].

The stability of PMMA-grafted silica particles in ILs led Ueno *et al.* to pursue the investigation on such colloids. In a later study [74], the authors focus on colloidal systems

based on the IL [EMIM][NTf<sub>2</sub>]: at low NP concentrations (< 3 wt%) the systems are sols, then, a colloidal glass transition is observed at a volume fraction of approximately 0.70-0.74 (higher than that of the hard sphere system, due to the soft repulsive interaction between the particles). These glassy composites show structural colors, proven to originate from Bragg's diffraction of visible light by short-range ordered glassy colloidal arrays. In [75], the authors use a different polymer, poly-benzyl-methacrylate (PBnMA), to graft silica nanoparticles. Dilute dispersions in [EMIM][NTf<sub>2</sub>] form at low particles concentration, while at higher NP volume fraction, the systems form soft glassy colloidal arrays like for the PMMA coated silica [74], which also show structural colors. In this case though, the PBnMA polymer being thermosensitive, a (reversible) glass-to-gel transition is observed at 95 °C, due to the desolvation of the polymer chains and consequent aggregation of the particles.

Silica is known to form gels in aqueous media, due to a high surface reactivity that leads to strong interparticle interactions. As evidenced in Ueno *et al.*'s work, silica nanoparticles also form gels in ILs even at low particle volume fractions (Fig. 1.16). Gels that take place from the dispersion of solid particles in ionic liquids are denominated *ionogels*, and they are hybrid materials which possess features of the IL and of the gelling agent at the same time. Ionogels can be sorted into two main categories: *physical gels*, characterized by an internal three-dimensional network arising from weak interactions (such as hydrogen bonds) and obtained from the dispersion of small organic molecules, polymers or divided solids (*e.g.*, fumed silica); or *chemical gels*, that show better mechanical properties thanks to the presence of covalent bonds [5].

Despite the fact that the interparticle potential of these systems has never been studied and that, at present, we do not know which properties of silica actually lead to gelation, it is true that silica-based gels can be used for the preparation of promising materials. Their most interesting quality is probably the fact that, despite the solid-like state, they conserve liquid-like dynamics and an ionic conductivity of the same order of magnitude as the pure IL [76]; this is why these materials have been receiving a lot of consideration lately for the fabrication of electrochemical devices such as batteries, fuel cells and photovoltaic systems. Moreover, most silica-based ionogels are transparent, which allows for their utilization in optical devices [76].

Silica-based ionogels are usually obtained through sol-gel preparation or by dispersing silica NP directly in the IL [5]; however, recently a new method has been applied, which

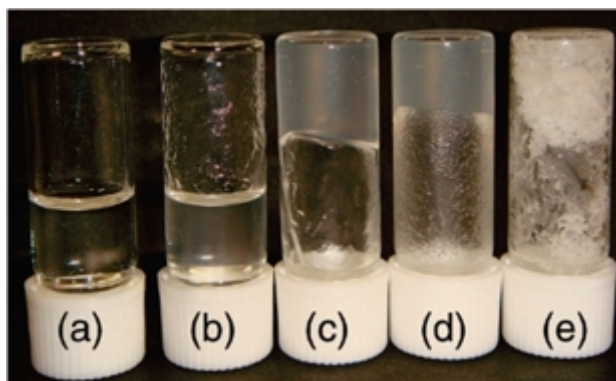


FIGURE 1.16: Dispersions of silica nanoparticles in [EMIM][NTf<sub>2</sub>] with different silica particle concentrations: (a) neat IL, (b) 1 wt%, (c) 3 wt%, (d) 5 wt%, and (e) 15 wt%. Reproduced from reference [72].

involves the functionalization of the particles with the one of the ions as the IL itself (much like in [67]). Moganty *et al.* [77] prepared ionogels based on IL-tethered silica nanoparticles; the IL host being 1-butyl-3-methylpyrrolidinium trifluoromethyl sulfonyl imide ([BMPy][NTf<sub>2</sub>]), the particles are functionalized with 1-trimethoxysilyl propyl-3-methylimidazolium bis(trifluoromethylsulfonyl)imide (SPMIM-NTf<sub>2</sub>). As a result, a true hybrid material is obtained, as demonstrated by thermogravimetric analysis: while the IL host is stable up to 450 °C, and the grafted silica up to 25 °C higher, the ionogel actually shows two degradation steps corresponding to its two basic components.

Ionogels have also been obtained with other materials than pure silica. For example, Ziolkowski *et al.* recently reported on the preparation of interesting magnetic ionogels from a three-component system: silane-modified magnetite nanoparticles dispersed in the hydrophobic IL trihexyl(tetradecyl)phosphonium dicyanamide ([P<sub>14,6,6,6</sub>][N(CN)<sub>2</sub>]), and in the presence of the polymer *N*-isopropylacrylamide [78]. Bare and functionalized nanoparticles are dispersed in the IL, but while the bare magnetite give place to soft gels, those modified with silanes form harder gels, mechanically more robust, thanks to the possibility of forming covalent bonds between the particles and the polymer. The presence of the silica surface appears then fundamental for the obtention of ionogels.

### Other Dispersions

There is yet another type of nanoparticles that have been successfully dispersed in ILs, and it is the case involving carbon-based materials such as carbides and carbon nanotubes.

Carbon nanotubes (CNTs) are hardly soluble in aqueous and organic solvents, but they can be dispersed in ILs, especially the imidazolium-based ones, in which they can form the so-called “bucky gels”. In CNT-IL hybrids, the ionic liquid is usually coated on the outer surface of CNTs via covalent or noncovalent methods. There, the role of ILs can be that of the dispersion medium without any additional dispersing agents, or as a facilitator for the dispersions of CNTs in a matrix or solution, or still, they can act as a binder between CNTs and another component. At present, there are not many systematic studies concerning the non-covalent interactions between CNTs and ILs, and there is a debate over the nature of these interactions. The most widely proposed mechanism explaining the stabilization of carbon nanotubes in ILs involves the binding with CNTs through cation- $\pi$  and/or  $\pi$ - $\pi$  interactions. IL-carbon nanotubes systems have been extensively reviewed by Tunckol *et al.* in [79].

Concerning carbides, Khare *et al.* [80] studied mixtures of  $\text{Fe}_3\text{C}$  nanoparticles in several ILs, based on [EMIM] and [BMIM] cations, with several different anions. As a result, [EMIM][SCN] and [EMIM][N(CN) $_2$ ] prove to be the most efficient dispersing agents: SAXS experiments show that the particles dispersed in [BMIM]-based ILs are a little aggregated compared to the [EMIM] ILs. A UV-vis study of the samples led the authors to suggest the preferred interaction of the ILs’ anions with the carbon atoms on the nanoparticles surface.

Fox *et al.* [4] studied the dispersion of several types of nanoparticles (carbon nanotubes, gold, metal- and non-metal oxides) in [BMMIM][NTf $_2$ ], in order to probe the thermophysical properties of these systems. The IL is chosen because the C2 methylation on the imidazolium moiety increases the thermal stability compared to the more common [BMIM][NTf $_2$ ]. The gold particles give the least stable dispersions, as they immediately precipitate, while carbon black and silica dispersions remain stable for over a month. The IL itself does not have much of a good thermal conductivity, and the only materials that successfully increase it are  $\text{Al}_2\text{O}_3$  (especially in the form of whiskers, although their dispersions were characterized by the presence of clusters about 25  $\mu\text{m}$  large) and multi-walled carbon nanotubes. The shape of the dispersed objects seems thus to be of some importance, since spherical particles have little or no effect on the thermal conductivity, along with a greater tendency to agglomerate, compared to cylindrical materials. Unfortunately, the authors could not discern a clear trend to explain the behaviour of their systems.

What emerges from all the studies cited in this section (and resumed in Table A.1) about dispersions in ILs is that, despite the growing interest in ionic-liquid based nano-material, there is yet no clear explanation for the origin of colloidal stability in ionic liquids. Nonetheless, a few evident factors can be listed:

- Some kind of repulsion is indispensable in order to stabilize nanoparticles in ILs. Steric repulsion arising from polymers or surfactants is usually quite effective if such molecules are compatible with the IL from a solubility point of view.
- When bare nanoparticles are successfully stabilized in ILs, steric repulsion cannot be called in, and neither can electrostatic interaction since it is supposed to be annihilated by the overwhelming ionic force of the medium; in such cases, the origin of the stabilization seems to lie in the formation of IL layers at the nanoparticles surface (a sort of “solvation”-type repulsion).
- The role of water is unclear, but in some cases it seems to disrupt the solvation layers and weaken the interactions that stabilize the dispersions.

In conclusion, despite the presence of some rather clear elements and trends, it must be said that we are far from disclosing a theory that encompasses all possible interactions between ionic liquids and surfaces. This is why more fundamental studies on colloidal stability are necessary. The next section will deal with the efforts that have been made to understand the behaviour of ionic liquids when interacting with surfaces.

### 1.4.3 ILs at a Surface

As it emerges from the previous paragraphs, the structuration of ionic liquids when interacting with a surface is a matter that often comes up in the attempt to explain the stability of colloidal systems. This subject has been extensively explored by different authors through the study of flat-surface model systems, by means of experimental techniques such as Surface Force Apparatus (SFA) and Atomic Force Microscopy (AFM). A Surface Force Apparatus (SFA) is a system that allows direct measurement of the force-laws between surfaces in liquids or vapours at the ångstrom resolution level. Two surfaces (atomically smooth when possible) are immersed in a liquid and brought toward each other. The forces between the two surfaces across the liquid film can be measured. The Atomic Force Microscope (AFM) was originally designed with the scope

of imaging the topology of surfaces. A mechanical probe (“tip”) moves across the surface of the sample thanks to piezoelectric elements electronically controlled, and the forces encountered by the tip are recorded [22].

As explained in [21], the first studies based on the force apparatus date back to the early 80’s, when they first focused on molecular solvents. For many liquids, the structure close to an interface is different from that in the bulk, and the density profile normal to a solid surface oscillates about the bulk density with a periodicity of about one molecular diameter, close to the surface [81]. This region typically extends over a few molecular diameters and is particularly pronounced for a strong liquid–wall interaction. In this range the molecules are ordered in layers. The force recorded by the SFA for a liquid confined between two surfaces is characterized by an oscillatory profile corresponding to alternating regions of attractions and repulsion (Figure 1.17). Such a profile has been interpreted as arising from the formation of solvation layers: every oscillation represents a layer being squeezed out by the approaching surfaces. Such “solvation” force is mainly of geometric origin and can occur even in the absence of attractive interactions between the surface and the confined liquid. An experiment of this kind can then tell how many solvation layers are formed on a solid surface; an atomic force microscope can give the same type of information on a wider range of substrates.

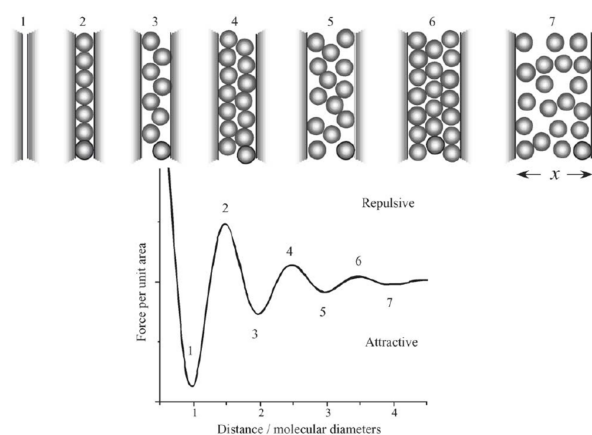


FIGURE 1.17: Schematic structure of a simple liquid confined between two parallel walls. The order changes drastically depending on distance, which results in an oscillatory force. Reproduced from reference [81].

Several other surface-sensitive instrumental techniques (in particular those derived from vibrational spectroscopy) have been used to characterize the behaviour of ionic liquids at the interface, such as surface-enhanced Raman scattering (SERS), Fourier transform infrared reflection absorption spectroscopy (FT-IRAS), surface-enhanced infrared

absorption (SEIRA) spectroscopy, sum-frequency generation [66]. Other techniques are X-ray photoelectron spectroscopy (XPS, that can be conveniently used with ILs, despite the necessary high-vacuum conditions, thanks to their extremely low vapour tension) and X-ray reflectometry. Computer simulation works have also been focusing on the behaviour of ILs at the solid/liquid interface.

### **Studies on Ethylammonium Nitrate**

One of the oldest SFA studies was carried out by Horn *et al.* in 1988 [20] on the ionic liquid ethylammonium nitrate (EAN). The idea for this work took place from the observed swelling of phospholipid lamellar phases in EAN. The authors notice the similarity between EAN and water, especially in the important role of hydrogen bonding, despite the fact that the high ionic force of the IL is supposed to screen all electrostatic interactions: indeed, the calculated Debye length would be less than the molecular size. In this work, the surface force apparatus is constituted of two mica surfaces (atomically smooth, negatively charged) approaching one another through the liquid, and the authors test pure water, pure EAN and EAN/water mixtures. At low concentrations in water, EAN behaves like any dilute electrolyte, with good agreement between measured and theoretical (Poisson-Boltzmann) long-range forces. At very high EAN concentrations, the resulting force is an oscillatory function of the surface separation: in the pure salt, the authors find at least 11 oscillations extending up to 5 nm; at 2 nm separation, the repulsive peaks are so strong that the surfaces cannot come any closer to one another. In order to explain such results, the authors suggest that pure EAN form layers in the confined space between mica sheets, the same way molecular liquids do, and that both cation and anion be present in the layers in equal numbers. However, they infer that the very first layer may be composed of cations only (the mica surface being negatively charged). This hypothesis is supported by a more recent AFM study on the same system [21], confirming the presence of a first layer of cations adsorbed on the mica sheet via Coulombic interaction. This is followed by a non-electrostatically adsorbed EAN ion pair with the ethyl chains pointing towards the surface, as to maximize the solvophobic interaction. The  $\text{NO}_3^-$  anion then follows the cation, in order to quench the charge, and a “... cation ... anion ... cation ...” pattern is subsequently induced. The same type of structure is also observed by Elbourne *et al.*, not only in EAN but also in propylammonium nitrate [82].

Smith *et al.* [15] published an AFM study involving water/EAN mixtures enclosed between a silica colloid probe and a silica surface, giving similar results to [20]. At 100 wt% water they observe long-range repulsions, while in 100 wt% EAN the tip starts to encounter EAN solvation layers 4.5 nm away from the surface. As the tip gets closer and solvation layers are removed, “steps” appear in the force profile. Steps in the force profile are also noted upon retraction due to layer reformation: they are due to the solvophobic attraction between the cations adsorbed to the colloid probe and cations in reformed layers in the confined IL.

The addition of as little as 5 wt% water to EAN reduces the number and resilience of EAN solvation layers, and the solvation structure completely disappears for water content = 50 wt%. According to Horn *et al.* [20], the cations directly bound to the mica surface could become strongly hydrated upon addition of water, disrupting the subsequent layering pattern.

Though, as stated by the authors of [21], silica surfaces are usually less smooth than mica, which leads to smeared peaks in the force profile and a more difficult interpretation of the experimental data. The same authors also studied the behaviour of EAN at a graphite surface by AFM [83], and they found that the force profile is dominated by attractive dispersion interactions between the AFM tip and the graphite substrate; according to the authors, this may be due to the interaction between the ethyl group and the graphite surface, leading to an interfacial excess of EA<sup>+</sup>.

### **Studies on other ILs at different surfaces**

The most widely used type of ILs being the imidazolium- and pyrrolidinium-based ones, especially for electrochemical applications, a lot of studies have made an effort to understand their structure and properties when interacting with a surface that can be representative of an electrode. Many works agree on the fact that the first layer of adsorbed ions is determined by the charge of the surface. This is shown for example in a study on the RTIL/SiO<sub>2</sub> interface, implying a few imidazolium-based ILs with lateral alkyl chains of different length [84]. Sum-frequency vibrational spectra prove here that the imidazolium cations interact with the negative SiO<sub>2</sub> surface, with their alkyl chains arranged in an all-*trans* conformation and pointing perpendicularly to the surface (which is reminiscent of the behaviour of EAN in [21] and [82]). The interfacial structure of 1-butyl-1-methylpyrrolidinium tris(pentafluoroethyl) trifluorophosphate ([BMPy][FAP])



at an Au(111) surface was investigated using AFM and scanning tunnelling microscopy [85], revealing the presence of a cation-rich layer adsorbed on the gold at the open circuit potential. As the potential becomes more negative, the cations are so strongly bound to the surface that the AFM tip is unable to displace them. As the potential becomes more positive, a smooth surface is detected, deriving from an anion-rich layer. Molecular dynamics simulations [86] show that [PMPy][NTf<sub>2</sub>] forms a multilayer structure of 20–30 Å at a graphite surface, equivalent to 4–5 IL layers, and when a potential difference is applied between two graphite electrodes, cations accumulate at the negative electrode and anions at the positive one.

In a study based on X-ray reflectivity, Mezger *et al.* [87] investigate the temperature-dependent interactions of three ionic liquids, based on the tris(pentafluoroethyl) trifluorophosphate anion ([FAP]), at a sapphire (0001) surface; the cations used are 1-butyl-1-methylpyrrolidinium ([BMPy]), 1-hexyl-3-methylimidazolium ([HMIM]), and tetrabutylammonium ([TBA]). The presence of a pronounced interfacial layering is detected, with a layer spacing of  $\sim 8$  Å that increases with increasing temperature. The ions are proven to be arranged in a “double-layer” pattern induced by the negative charge of the sapphire(0001) surface, which attracts the IL cations and repels the anions.

Many other works have proven the existence of an extensive IL layering at the solid/liquid interface. For example, Ueno *et al.* [88] performed surface force measurements on [BMIM][NTf<sub>2</sub>] and [BMIM][BF<sub>4</sub>] confined between silica surfaces, registering some oscillating forces whose step is compatible with the dimension of the ions. As a result, 13 solvation layers can be detected for [BMIM][NTf<sub>2</sub>] and 10 for [BMIM][BF<sub>4</sub>], which is comparable to the number of 9 layers found for EAN [20]. According to the authors, the number of layers depends on the bulk IL nanostructure and reflects the fact that [BMIM][BF<sub>4</sub>] is glass-forming IL at low temperature, hence less structured than [BMIM][NTf<sub>2</sub>], which is a crystal-forming IL. Similar results are reported by Bovio *et al.* [89] on a slightly different system, made of a [BMIM][NTf<sub>2</sub>] film deposited on a fully hydroxylated silica surface (which is not as homogeneous as a liquid confined between two approaching surfaces). Indeed, AFM imaging shows the presence of IL islands randomly distributed on the silica surface. These islands are characterized by an overlayer thickness that in some points exceeds 50 nm; the interlayer separation being  $\sim 0.56$  nm, this means that the IL structure extends for about 100 layers. Comparing the experimental results with molecular dynamics simulations led the authors to suggest

that [BMIM][NTf<sub>2</sub>] be solid-like, maybe crystalline, at the solid/liquid interface due to the presence of the silica surface, even if the bulk IL is liquid at ambient temperature.

The interaction of mica and gold surfaces across [BMIM][NTf<sub>2</sub>] was investigated with an electrochemical surface force apparatus (EC SFA), using different surface potentials [31]. The force profiles are modelled by means of a DLVO-type potential and the repulsion between the two surfaces is interpreted as arising from the interaction between overlapping diffuse layers. Surprisingly, in this work the IL is described as a dilute electrolyte, consisting of a neutral and coordinated cation-anion network in equilibrium with a low quantity of dissociated ions. The authors infer that the reason of their surprisingly original interpretations lies in the sensibility of their SFA, capable of measuring very weak forces that cannot be recorded with currently available AFM instruments. This work will be discussed in more detail in Subsection 1.4.4.

### **Effect of Impurities on the Interfacial Structure of ILs**

The consequences deriving from the presence of salt impurities can strongly alter the interfacial structure of the ionic liquid/electrode interface. Due to the importance of lithium to electrochemical applications, its effects are of concern in several works. For example in [85] the authors show that, while in the pure IL the interfacial layers lead to a repulsive force recorded by the AFM tip, the presence of 10 wt% of dissolved LiCl salt in the IL leads to attractive forces close to the gold surface (*i.e.*, the layering is disrupted). Similarly, Hayes *et al.* [90] perform AFM on [HMIM][FAP] ionic liquid doped with 0.05 wt% LiCl at the Au(111) surface. LiCl reduces the force required to rupture near-surface layers, denoting a weakened IL structure, and at such low concentration it is hard to imagine that LiCl is evenly distributed in the bulk and able to change the IL nanostructure. So, the authors' conclusion is that interfacial LiCl changes the interfacial IL nanostructure either by weakening the electrostatic domains or by modifying the IL's Hamaker constant near the surface so that stronger attraction results.

However, in [91], silica particles are dispersed in [BMIM][BF<sub>4</sub>] doped with LiBF<sub>4</sub>, and the ion-ion and ion-silica interactions are investigated by means of Raman and photon correlation spectroscopy. The presence of Li shifts the gel transition threshold towards higher silica concentration, *i.e.* Li<sup>+</sup> stabilizes the dispersion. The authors propose a model in which the silica surface's silanol groups interact with the solvent *via* hydrogen bonds, while the negatively charged siloxane groups draw the Li<sup>+</sup> cations towards the

surface; the Li cations then coordinate the  $\text{BF}_4^-$  anions, forming ordered solvation layers.

The effect of water on the flat solid/liquid interface is also addressed in a few works. For example, in [84] the authors state that water does not affect the alkyylimidazolium/silica interaction. They propose a structure in which, at low water concentration in the IL, a molecule of water is bridging two fluorinated anions thanks to H-bonds; as the water content is increased, more water molecules are H-bonded to a single anion. On the contrary, Rubim *et al.* [66] witness a highly deleterious effect of water on the IL structure. Thanks to the use of surface-enhanced vibrational spectroscopy, they investigate the  $[\text{BMIM}][\text{BF}_4]/\text{Ag}(0)$  interface, comparing silver nanoparticles dispersed in the IL (explored by means of SEIRA), and the IL deposited as a thin film on a silver island (studied by SERS). In both systems, the interaction of the  $\text{BMIM}^+$  cation with the NP surface is detected, inducing the formation of a first layer of cations; then the  $\text{BF}_4^-$  anions follow, forming a double-layer structure capable of stabilizing the NP in solution. In the case of Ag NP, the presence of water leads the particles to aggregation, and any attempt at studying the system by SERS is useless. In the case of a thin film on the Ag surface, SEIRA experiments show that the IL cations are linked to the metal surface and each  $\text{BF}_4^-$  interacts with water monomers or dimers. This means that water disrupts the double layer structure at the interface, which is why silver nanoparticles flocculate in the presence of water, as the sole source of stability breaks down.

To our knowledge, [66] is the only experimental work allowing a more direct comparison between flat surfaces and nanoparticles. Indeed, despite the fact that studying the behaviour of ILs next to a flat surface surely allows for a better understanding of the structuration of ILs next to any solid surface, the results obtained on flat surfaces do not perfectly compare with nanoparticles. NP are curved surfaces with defects and inhomogeneities, that can engage in different interactions with the ILs and induce different behaviours and structures compared to flat surfaces. Also, a difference between charged flat and curved surfaces is the intensity of the electric field generated by their surface charge, as predicted by Gauss' law (at the same distance from the electrode with the same charge density, the electric field is weaker near cylindrical electrodes than near planar electrodes). This is demonstrated, for example, by molecular dynamics simulations comparing the distribution of  $[\text{BMIM}][\text{PF}_6]$  and  $[\text{BMIM}][\text{Cl}]$  ions at graphite (flat) and carbon nanotube (curved) electrodes [92]. As a result, in [92] the  $\text{BMIM}^+$  cation

is found to adsorb on neutral and negatively charged electrodes, both flat and curved; however, near the cylindrical electrodes the intensity of first counter-ion peak is reduced, while that of first co-ion peak is enhanced. This fact is caused by the reduced electrical field near curved electrodes, leading to an attenuated driving force for the counter-ion adsorption and co-ion desorption on the electrode. Also, still in [92], the position of the anions in the layer following the cations is determined by (i) the packing allowed by the anion's size and (ii) the anion's possibility of forming H-bond with the labile C2 proton on the imidazolium head. The latter effect was also found by Bernardi *et al.*'s *in situ* XPS study on the Ir(0) nanoparticles/[EMIM][EtSO<sub>4</sub>] interface [93], which evidenced a strong interaction between the C2 imidazolium carbon and the EtSO<sub>4</sub><sup>-</sup> anion.

As a conclusion, it is quite evident, from the vast majority of the above cited studies, that despite some general tendencies (of which in particular the layer-by-layer structuration and the role of hydrogen bonds are most often called into cause) there is no general theory able to predict the behaviour of a particular IL at a particular surface. The specific behaviour of an RTIL/surface combination depends on details of the molecular structure of the ions and the ion-substrate interactions [86]. It is however clear that the “electrical double layer” (defined as the region of liquid perturbed by an adjacent charged surface, quoting Susan Perkin in her recent, exhaustive review on nanoconfined ILs [94]) is much larger than a single ion layer thick, which is not compatible with the classical Poisson-Boltzmann theory. As seen earlier [10, 15], if we were to use the DLVO theory to calculate the Debye length for a system characterized by the ionic force corresponding to the molar concentration of ions in an IL, we would obtain values at least one order of magnitude smaller than the experimentally observed thickness of the first ion layer bound to a charged surface. The classical electrical double layer theories are then invalidated. In the next Subsection we see the results of the attempts to apply the DLVO theory on IL-based systems.

#### 1.4.4 Interparticle Potential in ILs

So far, only a few studies have made an effort towards the calculation of the interparticle potential in NP/IL systems, and in each this was done by applying the DLVO theory (or an extension of it), with different interpretations. For example, in [10], [26] and [27] the electrostatic part of the potential is computed through the Poisson-Boltzmann equation, and the Debye length is calculated by using the “effective” ionic concentration

determined by the molar conductivity ratio [30]. It is found of the order of the ångström, which is smaller than the average ionic size. Also, in [10] the effective Hamaker constants for the silica-IL systems are found much smaller than for the silica-water dispersions (meaning that the van der Waals attraction is depressed). Nevertheless, the plot of the interparticle potential contributions (Figure 1.18) shows the sole presence of an attractive force at all separations, in agreement with the experiments in which bare silica particles aggregate in [BMIM][NTf<sub>2</sub>], [BMIM][BF<sub>4</sub>] and [BMIM][PF<sub>6</sub>].

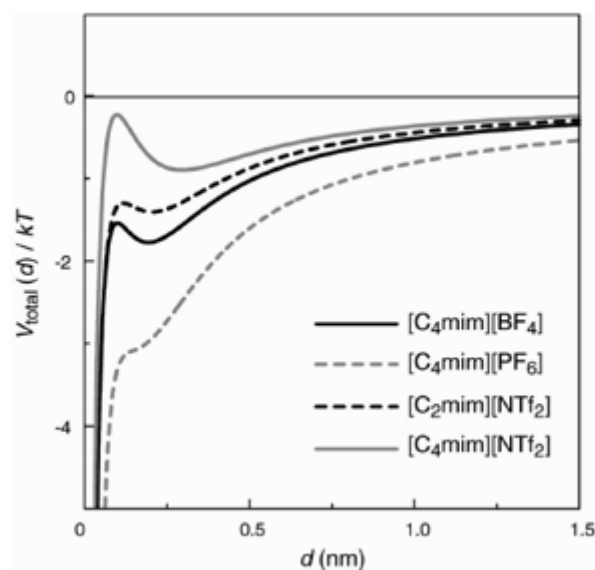


FIGURE 1.18: DLVO interparticle interaction profiles ( $T = 25^\circ\text{C}$ ) for bare silica particles in ILs ( $R = 60\text{ nm}$ ). Reproduced from reference [10].

Similarly, in [27] the electrostatic interaction only appears at a distance  $r = 0.25\text{ nm}$  and never grows above  $1\text{ kT}$ . The total potential is dominated by the attractive van der Waals forces, although they become stronger than  $kT$  only at  $r = 1.5\text{ nm}$ . Still, the gold particles studied in this work do not precipitate immediately, but sometimes after a few days.

In [10], when the silica NP are coated with the polymer PMMA, their stability should depend on the PMMA-IL compatibility. The authors calculate the steric interparticle potential, but in each case the particles are supposed to aggregate (all ILs appear to be poor solvents to the polymer). Nevertheless, the experiments are this time in contradiction with the calculations, since PMMA-coated NP are stable in [BMIM][NTf<sub>2</sub>] and [BMIM][BF<sub>4</sub>]. This leads the authors to state that the reason for the stability should

be found elsewhere, and they propose the formation of stabilizing IL structures at the NP surface.

In another work [26], the application of an extended DLVO theory enables the authors to calculate the interparticle potential for the magnetite/IL system as sum of electrostatic, van der Waals, magnetic and steric interactions. As a result, in the insert of Figure 1.19 the curve representing the electrostatic repulsion begins rising significantly above 0  $kT$  only at a (quite unphysical) distance  $r = 0.01$  nm. The quasi-total screening of the NP surface charge seems to be corroborated by the results of electrophoretic mobility measurements yielding  $0.00 \pm 0.14 \mu\text{m V}^{-1} \text{s}^{-1}$  (this result being however biased by the fact that electrophoresis is a questionable choice to determine the mobility of charged objects in a highly charged solvent). On the other hand, the effective steric repulsion due to an oleate double layer gives rise to a  $400 kT$  high potential barrier against aggregation.

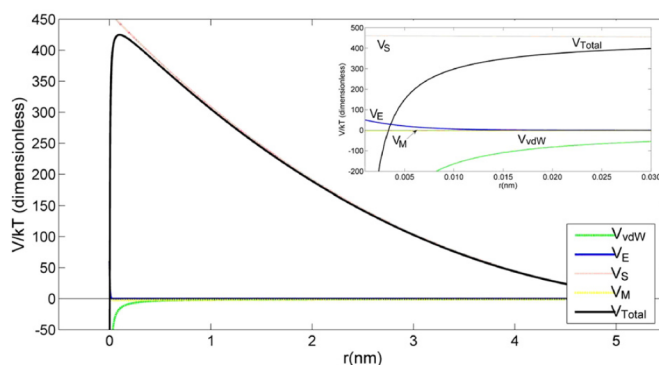


FIGURE 1.19: Total interaction potentials for oleate-covered magnetite particles in [EMIM][EtSO<sub>4</sub>], and the various contributing forces:  $V_{vdW}$ , van der Waals forces;  $V_E$ , electrostatic interaction;  $V_S$ , steric potential;  $V_M$ , magnetic dipolar interaction. Reproduced from reference [26].

The characteristic shared by these three works is the complete annihilation of electrostatics resulting from the values input for the effective ions concentrations using the DLVO theory. In a different work [31], based on the electrochemical surface force study of mica and gold surfaces interacting across [BMIM][NTf<sub>2</sub>], the matter is addressed in an unusual fashion. The force profiles between the two surfaces are modelled by means of a DLVO-type potential with a supplementary steric contribution arising from the absorption of a layer of surface-bound ions. The repulsion between the two surfaces is interpreted as arising from the interaction between overlapping diffuse layers, which allows to treat the system by means of the Poisson-Boltzmann equation. In such

a model, the calculated Debye length is equal to 11 nm, as obtained from the fit of the force–distance profile curves attributed to the electrostatic interactions. Both the method of calculation and the Debye length value itself are in sharp contrast with the work of other authors [10, 15, 26, 27], who found values two orders of magnitude lower by taking into consideration the ionic strength of the IL. From here, using the Boltzmann distribution, the authors of [31] are able to calculate a thermodynamic self-dissociation constant for the studied IL of the order of  $10^{-10}$ : the IL is then described as a dilute electrolyte, consisting of a neutral and coordinated cation-anion network in equilibrium with a low quantity of dissociated ions. Such model is in contrast with the more common (although evidently not perfect, as shown above) “ionicity approach” based on ionic conductivity and ion diffusion measurements [30], and with the generally shared idea that ionic liquids are strong electrolytes with high dissociation ratios. Indeed, computer simulations on probe ion pairs immersed in an IL solvent have shown that the strong electrostatic interactions determine a charge overscreening through the first IL solvation shell surrounding the probe ions [95]. As a consequence, unlike-charged ion pairs are barely stabilised and they readily dissociate, which leads to the appellation of “superdissociating solvents” for ILs. In such a framework, it becomes hard to believe that a Stern and diffuse layer may effectively describe the interaction of ILs with a surface [96].

## 1.5 Conclusion

This chapter attempted to sum up the work that is currently being done in the scientific community on ionic liquids-based colloidal systems, with the goal of elucidating the interactions between ILs and the dispersed phases. Most of the actual literature unfortunately still concerns a matter-of-fact discussion of the synthesis or dispersion of particles in ILs, and only a few works actually try to get a better insight on the experimental results. As we have seen, a deeper understanding of the interaction between ILs and surfaces is not easy to obtain. A great effort in this direction comes from studies based on surface-sensitive techniques. It should be noted, however, that the flat surfaces involved in such studies have different properties than nano-objects, such as particles and rods, characterized by surface curvature, definite forms and high surface-to-volume ratios. Nevertheless, the results thereby obtained are definitely helpful in the constant building of the knowledge on the behaviour of ILs at an interface.

The picture that emerges from what has been discussed so far is that ILs are very complex media, characterized by the simultaneous presence of van der Waals, Coulomb dipole, and in some cases H-bonding interactions. Therefore, the currently available theories are not suited for quantitative calculations and interpretations of colloidal stability in these media. For instance, the classic Poisson-Boltzmann equation does not take into account the correlations between ions; given the strongly ion-correlated nature of ILs, especially when there is no water – or other molecules – to screen the charges, a more general theory is clearly needed [87]. Moreover, the most peculiar feature of ILs, which issues in particular from the surface force studies, is their ability to form the solvation layers in which the origin of colloidal stability is more and more believed to reside. Ultimately, this could be seen as a type of electrostatically-induced steric repulsion, that the DLVO fails to account for.

In conclusion, the scope of this work is to take one step further toward a deeper understanding of colloidal stability in ionic liquids, by focusing on a system whose single composing parts have already been extensively characterized. Indeed, both the dispersed phase, represented by maghemite nanoparticles, and the IL ethylammonium nitrate, have long been known and used in our laboratory, and for both there exists a very large corpus of knowledge available in the literature. In the next chapters we will show what happens when these two systems are mixed together: how they behave, how their properties can be tuned, and what information can be extracted from their thorough characterization *via*, among others, small angle scattering techniques. In particular, we will show the extreme importance of the interface composition in terms of the value and type of the structural charge, something that not all authors take into account (which is particularly evident when “bare” nanoparticles are mentioned, with no further specifications). Finally, we will attempt to give an in-depth interpretation of the experimental data through a more theoretical approach, before applying the newly developed protocols and knowledge to “greener” systems based on the benign choline-amino acid ionic liquids.



# Chapter 2

## Materials and Methods

### Contents

---

<b>2.1</b>	<b>Materials</b>	<b>58</b>
<b>2.2</b>	<b>Syntheses and Functionalizations</b>	<b>58</b>
2.2.1	Synthesis of Maghemite Nanoparticles	58
2.2.2	Size Sorting of Maghemite Nanoparticles	60
2.2.3	Preparation of Acidic and Alkaline Ferrofluids with Different Counterions	62
2.2.4	Surface Functionalization with Citrate Ligands	63
2.2.5	Synthesis of the Ionic Liquid Ethylammonium Nitrate	64
2.2.6	Synthesis of the Choline-Amino Acid ([Cho][AA]) Ionic Liquids	64
2.2.7	Transfer of Nanoparticles from Water to IL	65
2.2.8	Lyophilization	67
<b>2.3</b>	<b>Characterization Techniques</b>	<b>67</b>
2.3.1	Karl Fischer Titration	67
2.3.2	pH Measurements in Ethylammonium Nitrate	68
2.3.3	Flame Atomic Absorption Spectroscopy	69
2.3.4	Small Angle (Neutron and X-Ray) Scattering	70
2.3.5	Dynamic Light Scattering	71
2.3.6	Magnetization Measurements	73
2.3.7	Magneto-Optical Birefringence Experiments	74

---

## 2.1 Materials

The following products were purchased and used as received.

Acids: Nitric acid ( $\text{HNO}_3$ , 69.5% water solution, Carlo Erba). Hydrochloric acid ( $\text{HCl}$ , 37% water solution, AnalaR Normapur). Citric acid ( $\text{H}_3\text{Cit}\cdot\text{H}_2\text{O}$ , Rectapur, Prolabo). Benzenesulphonic acid (BSA, 98% pur., Aldrich). Benzoic acid (pure for analysis, Prolabo).

Bases: Ammonia (20% water solution, Analar Normapur, Prolabo). Ethylamine ( $\text{EtNH}_2$  70% water solution, Acros Organics). Tetramethylammonium hydroxide ( $\text{TMAOH}\cdot 5\text{H}_2\text{O}$ , Sigma). Lithium hydroxide ( $\text{LiOH}\cdot\text{H}_2\text{O}$ , Fluka). Potassium hydroxide (KOH pellets, Prolabo). Cesium hydroxide ( $\text{CsOH}\cdot\text{H}_2\text{O}$ , Acros Organics). Calcium hydroxide ( $\text{Ca}(\text{OH})_2$ , Rectapur, Prolabo). Aluminum hydroxide ( $\text{Al}(\text{OH})_3$ , Prolabo). Choline hydroxide ( $\text{ChoOH}$ , 45% solution in methanol, Aldrich).

Salts: Trisodium citrate ( $\text{Na}_3\text{Cit}\cdot 2\text{H}_2\text{O}$ , Merck). Trilithium citrate ( $\text{Li}_3\text{Cit}$ , Prolabo).

Solvents: Acetone (technical, VWR). Diethyl ether (99.8% pur., AnalaR Normapur). Acetonitrile (99% pur., Acros Organics). Methanol (99.9% pur., AnalaR Normapur).

DL-alanine (98% pur., Janssen-Chimica). Glycine (99% pur., Fluka).

Distilled water was further purified by means of an ELGA LabWater PURELAB UHQ system before use (18  $\text{M}\Omega$  cm).

Iron oxide nanoparticles and the ionic liquids were synthesized in our laboratory (see, respectively, Subsections 2.2.1, 2.2.5 and 2.2.6).

## 2.2 Syntheses and Functionalizations

### 2.2.1 Synthesis of Maghemite Nanoparticles

Bare iron oxide nanoparticles (maghemite,  $\gamma\text{-Fe}_2\text{O}_3$ ) are synthesized via the coprecipitation method [33]. An acidic ( $\text{HCl}$ ) solution of  $\text{FeCl}_2$  is mixed with  $\text{FeCl}_3$ , and ammonia is rapidly added at room temperature in order to precipitate  $\text{Fe}_3\text{O}_4$  (magnetite). After 30 minutes of stirring, this is washed with water and nitric acid, and then reacted with  $\text{Fe}(\text{NO}_3)_3$  at 80 °C for half an hour, in order to be oxidized to  $\text{Fe}_2\text{O}_3$  (maghemite). Such iron oxide particles are subsequently washed with acetone and ether, and finally dispersed in aqueous  $\text{HNO}_3$  solution ( $\text{pH} = 1.5$ ). The stable dispersion of maghemite

nanoparticles thereby obtained is referred to as an acidic aqueous ferrofluid. The presence of a single crystalline  $\gamma$ -Fe<sub>2</sub>O<sub>3</sub> phase is routinely confirmed by X-ray diffraction on the dried NP powder.

The size and polydispersity (typically  $d_0 = 7$  nm,  $\sigma = 0.39$ ) of maghemite NP are obtained through magnetization measurements as a function of the applied magnetic field, using a home-made vibrating sample magnetometer (see 2.3.6) on a dilute dispersion. For such dilute dispersions (*i.e.*, the magnetic interactions between single dispersed objects are negligible) if no aggregation occurs in presence of the magnetic field  $H$ , the classical Langevin formalism for paramagnetism may be used to describe the magnetization  $M$  of the solution [34]. The magnetization curve is then fitted using the first Langevin equation  $L(\xi, d)$ , with  $\xi = \mu_0 \mu H / kT$ :

$$M(H) = m_s \Phi \frac{\int d^3 L(\xi, d) P(d) dd}{\int d^3 P(d) dd} \quad (2.1)$$

where  $m_s$  is the saturation magnetization of the bulk material (for  $H \rightarrow \infty$ ). A lognormal distribution law  $P(d)$  is assumed for the particles:

$$P(d) = \frac{1}{d\sigma\sqrt{2\pi}} \exp\left[-\frac{\ln^2(d/d_0)}{2\sigma^2}\right] \quad (2.2)$$

where  $d$  is the diameter of the spherical magnetic particles,  $\sigma$  is the standard deviation (representative of the size polydispersity) and  $\ln(d_0)$  the average of  $\ln(d)$ . Figure 2.1 shows the lognormal function curve for such size distribution.

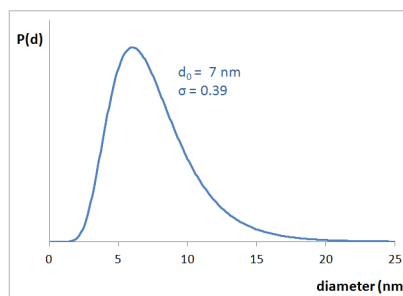


FIGURE 2.1: Lognormal size distribution  $P(d)$  of maghemite nanoparticles for a typical synthesis, before size sorting. Typical values for the distribution are  $d_0 = 7$  nm and  $\sigma = 0.39$ , as determined by magnetization measurements (see 2.3.6)

### 2.2.2 Size Sorting of Maghemite Nanoparticles

The polydispersity of maghemite nanoparticles can be reduced *via* a size sorting procedure based on the destabilization of the suspension by ionic strength: the effect of the added electrolyte is to screen the surface charges and progressively lead the NP to aggregation. This way, a precipitate forms on the bottom of the beaker, containing the largest particles of the sample which are more easily destabilized; at the same time, the volume fraction of dispersed NP is lowered and the supernatant contains the smaller particles. The repartition in two phases is repeated several times until an acceptable polydispersity is reached. This however leads to a reduction of the available volume of dispersion.

The first step to take is a preliminary test on a small volume (20 mL) of unsorted aqueous ferrofluid, so as to decide which concentration of acid must be used in order to obtain the desired repartition of large and small particles. Low quantities of concentrated nitric acid are added, and a portion of the supernatant is sampled after each  $\text{HNO}_3$  addition to evaluate the volume fraction  $\Phi$  of dispersed nanoparticles through a magnetization curve (see 2.3.6). This procedure allows for the obtention of a plot such as Fig. 2.2, with  $\rho\%$  being the ratio of dispersed nanoparticles with respect to the initial total volume fraction.

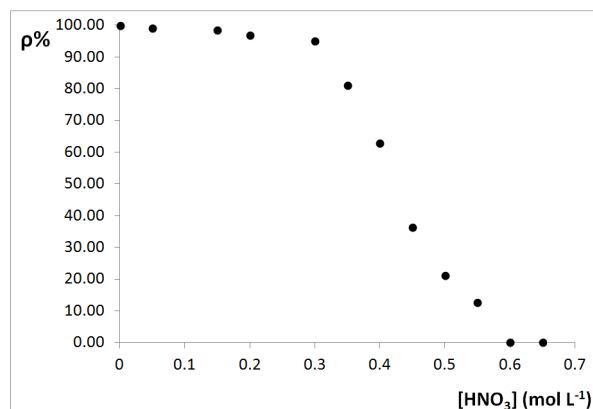


FIGURE 2.2: Fraction of residual dispersed nanoparticles ( $\rho\%$ ) as a function of added electrolyte (in  $\text{mol L}^{-1}$ ).

After this preliminary screening, the method is applied to the entire volume of the ferrofluid:  $0.30 \text{ mol L}^{-1} \text{ HNO}_3$  is added to the dispersion in order to precipitate a first fraction of very large particles, that contribute to the extended “tail” of the lognormal

size distribution. The supernatant is recuperated and transferred in a new beaker, while the precipitate is discarded.

In the second step, the ionic force of the ferrofluid is brought to  $0.42 \text{ mol L}^{-1} \text{ HNO}_3$  to distribute the NP more or less equally between two fractions. From now on, according to the usual definitions used in the laboratory, the fractions are referred to with the letters C for the precipitate and S for the supernatant. The scheme to be followed is depicted in Fig. 2.3.

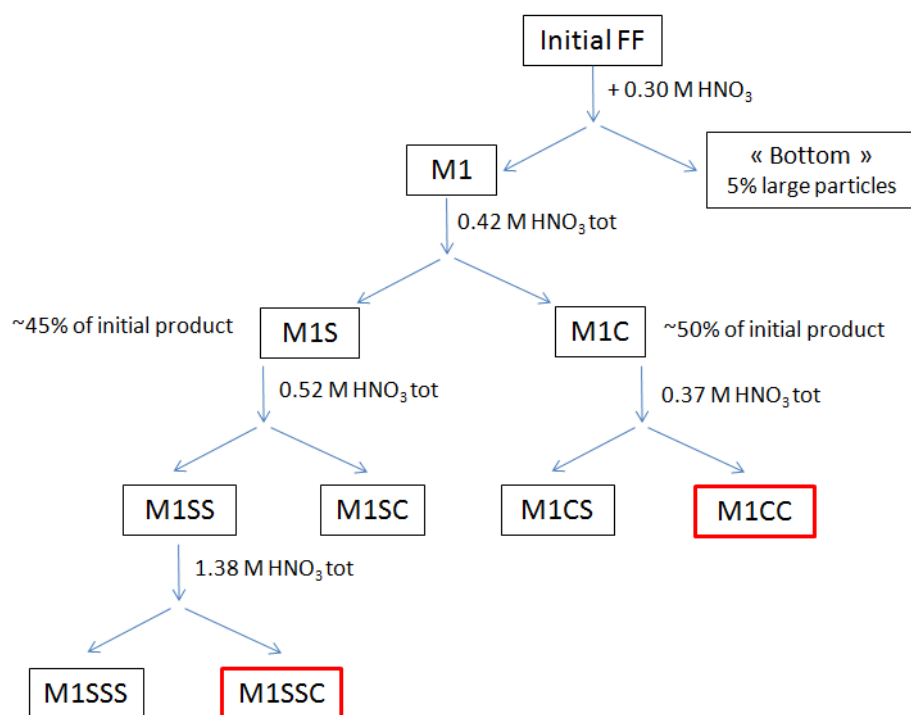


FIGURE 2.3: Tree-like scheme for the size-sorting of maghemite nanoparticles. The letter S indicates a supernatant, while C represents a precipitate.

Continuing down the left path in Figure 2.3, one eventually reaches the fraction of interest, M1SSC, which is washed with acetone and ether and redispersed in 500 mL water. The final pH is 1.95, the volume fraction  $\Phi = 0.92\%$  and the size distribution of the particles is characterized by  $d_0 = 6.9 \text{ nm}$  and  $\sigma = 0.21$  (from magnetization measurements).

The precipitate M1C is redispersed in water, and a screening is repeated through addition of acid and magnetization measurements, in order to evaluate how to divide the product into two fractions, containing respectively  $2/5$  and  $3/5$  of all the particles. This way, the necessary amount of nitric acid is added to reach a total concentration of  $0.37 \text{ M}$ , and the supernatant is recuperated, washed and redispersed in 500 mL water.

The final product, M1CC, is characterized by  $\text{pH} = 2.4$ ,  $\Phi = 0.89\%$ ,  $d_0 = 11.3 \text{ nm}$  and  $\sigma = 0.26$ .

Figure 2.4 shows the lognormal curves for the size distributions of the products M1SSC and M1CC.

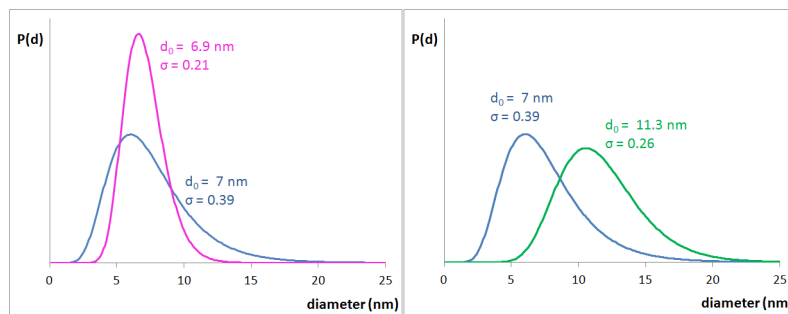


FIGURE 2.4: Lognormal size distribution  $P(d)$  of maghemite nanoparticles after size sorting (left, pink curve: small particles, M1SSC; right, green curve: large particles, M1CC) compared to the size distribution of unsorted particles (blue curve in both graphics) to emphasize the reduction in polydispersity.

### 2.2.3 Preparation of Acidic and Alkaline Ferrofluids with Different Counterions

Starting from these initial acidic dispersions, several kinds of aqueous samples can be easily prepared. The surface charge can be tuned by changing the pH: the positive charge (due to the  $\text{Fe-OH}_2^+$  surface groups) can vary from  $2 \text{ e}^-/\text{nm}^2$  at low pH, down to 0 at the point of zero charge (PZC) located around  $\text{pH} = 7.0$ . The PZC is reached by the titration of the acidic ferrofluid with a base (usually NaOH) until the nanoparticles are completely flocculated and the pH of the supernatant is neutral. The excess ions are eliminated by washing the nanoparticles several times (up to 10) with ultra pure distilled water, until the ionic conductivity of the supernatant is the same as, or very close to, that of distilled water.

The nature of the anion (initially  $\text{NO}_3^-$ ) can be modified in a process that requires passing through the PZC: the particles are flocculated at  $\text{pH} 7.0$ , and after thorough washing with water to remove the undesired ions, an acid with the desired anion (for example perchlorate or benzenesulfonate) is added.

A similar path is followed in order to obtain alkaline ferrofluids. Once the PZC is reached and the undesired ions are washed away, an alkaline solution with the desired pH (leading to the desired surface charge, this time negative due to the dissociation of

the surface groups leading to the species  $\text{Fe-O}^-$ ) is added to the flocculated particles. A typical basic compound used to obtain alkaline ferrofluids is tetramethylammonium hydroxide. Sodium hydroxide is avoided since  $\text{Na}^+$  is known to act as a flocculating counterion, leading to unstable suspensions.

#### 2.2.4 Surface Functionalization with Citrate Ligands

As described in Section 1.2, citrate is a ligand commonly used for the functionalization of iron oxide nanoparticles, thanks to its ability to complex the surface iron atoms with at least one carboxylic function, and the possibility to provide an electrostatic repulsion when the remaining carboxylates are deprotonated.

Citrated nanoparticles are prepared by mixing a chosen volume of acidic aqueous ferrofluid with an amount of citrate salt (typically trisodium citrate,  $\text{Na}_3\text{Cit}$ ) such that the iron to citrate molar ratio is 10:1. This corresponds to the plateau in the adsorption isotherm, *i.e.* the maximum possible surface is covered with citrate whatever the size of the NP. The mixture is stirred and heated at  $80^\circ\text{C}$  for about 20 minutes. Afterwards, the nanoparticles are washed as follows:

- once with acetone, to flocculate the particles
- twice with a water:acetone 1:9 mixture to remove the excess citrate ions
- once again with acetone to remove trace water
- once with diethyl ether to remove trace acetone

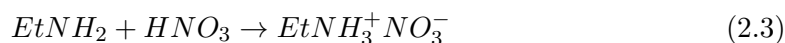
As the last step, an appropriate volume of water is added to obtain the desired concentration of dispersed nanoparticles, and the aqueous citrated ferrofluid is heated at  $60^\circ\text{C}$  in order to remove the remaining organic solvents.

When other citrate salts than sodium are needed but not commercially available, they are prepared by reacting the proper counterion-carrying base (hydroxide or amine) with an aqueous solution of citric acid  $\text{H}_3\text{Cit}$ . For example, potassium citrate ( $\text{K}_3\text{Cit}$ ) is obtained as an aqueous solution by reacting KOH powder with  $\text{H}_3\text{Cit}$  0.5M; similarly, hydroxide powders are used for  $\text{Cs}_3\text{Cit}$ ,  $\text{TMA}_3\text{Cit}$ ,  $\text{Ca}_3\text{Cit}_2$  and  $\text{AlCit}$ ; however, calcium and aluminum citrates precipitate due to poor solubility in water, so they are separated from the solution, washed several times with water and acetone, and dried in an oven at

70 °C. Finally, citrate salts of  $\text{NH}_4^+$  and  $\text{EA}^+$  are obtained by reacting the commercial amine, either in solution or solid, with aqueous citric acid until neutral pH is reached.

### 2.2.5 Synthesis of the Ionic Liquid Ethylammonium Nitrate

Ethylammonium nitrate (EAN) is prepared according to the synthesis protocol described by Evans *et al.* [53]: in a very simple acid-base reaction, equimolar quantities of nitric acid (69.5% water solution) and ethylamine (70% water solution) are reacted in distilled water at  $\sim -10^\circ\text{C}$ . The product is a solution of the ionic liquid in water. The low temperature is necessary to keep this very exothermic reaction under control.



Upon completion of the reaction, the pH of the solution must be verified; if it is acidic (which usually happens), an excess of ethylamine solution is added until the pH becomes plainly basic ( $\sim 10$ ). This ensures a stoichiometric reaction between the two species, and the excess amine is more easily eliminated than  $\text{HNO}_3$ . Amine removal is carried out *via* rotary evaporation, taking care as not to heat the water bath over  $40^\circ\text{C}$ , which helps reduce the risk of degradation of the ammonium moiety. This is followed by overnight lyophilization (see Subsection 2.2.8) to pump most of the remaining water away.

The residual water content is determined via a coulometric Karl Fischer titration (see Subsection 2.3.1), and lyophilization cycles are repeated until the IL contains about 0.3 wt% water. The EAN thereby obtained is a viscous, oily, odourless and transparent fluid, and its pH is slightly above 5.

After its preparation, the ionic liquid is transferred to a clean bottle, which is then filled with anhydrous argon, tightly closed with parafilm, and stored in a fridge at  $4^\circ\text{C}$ . We verified that this procedure reduces the water intake from atmospheric humidity to a minimum.

### 2.2.6 Synthesis of the Choline-Amino Acid ([Cho][AA]) Ionic Liquids

Cholinium glycinate, [Cho][Gly] and cholinium alaninate, [Cho][Ala] are synthesized *via* an acid base reaction (see Figure 2.5).



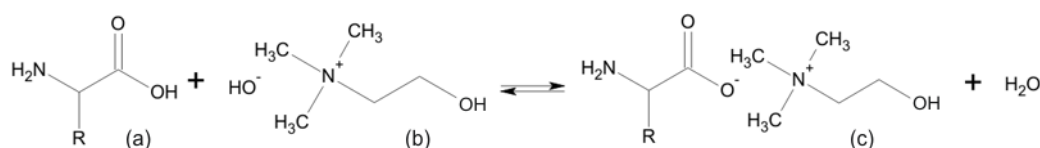


FIGURE 2.5: The figure depicts the reaction between an amino acid ((a), where  $\text{R} = \text{H}$  for glycine and  $\text{R} = -\text{CH}_3$  for alanine) and choline hydroxide, (b). The base  $\text{OH}^-$  removes the acidic proton from the amino acid's carboxylic group to form water; the remaining ions, the amino acid's anion and cholinium, give place to the ionic liquid  $[\text{Cho}][\text{AA}]$ , (c).

The synthesis protocol is adapted from that proposed by Moriel *et al.* [97] to use a choline hydroxide solution in methanol. The amino acid is dissolved in water, and choline hydroxide is added (in the mole ratio  $\text{Cho} : \text{AA} = 1 : 1.1$ ) to this solution at room temperature. The reaction is carried on for 24 hours (Fig. 2.6 shows the typical apparatus).

Upon completion of the reaction, methanol is removed by rotary evaporation at  $40^\circ\text{C}$ . Subsequently, a 3:1 mixture of acetonitrile and methanol is added to the IL solution in order to precipitate the unreacted amino acid. The mixture is stirred overnight, then filtered through Celite powder; the organic solvents are once again evaporated under reduced pressure, and the remaining IL-water mixture is lyophilized (see Subsection 2.2.8) overnight.

The IL thereby obtained is characterized by means of  $^1\text{H-NMR}$  and FT-IR. If some unreacted amino acid is still present, another purification-lyophilization cycle is repeated. The final product is a yellowish, very viscous liquid; it is stored in a clean bottle filled with argon at  $4^\circ\text{C}$ .

### 2.2.7 Transfer of Nanoparticles from Water to IL

Since maghemite NP are synthesized and functionalized in water, it is necessary to find the best conditions to transfer them to an ionic liquid and obtain stable dispersions in this medium. Since the kinetic path followed during the preparation of colloidal dispersions can have a huge impact on their final stability, this is not a straightforward task from a conceptual point of view. For this reason, two protocols have been compared for the transfer of citrated NP from water to EAN:

1. an appropriate volume of pure EAN is added directly into the aqueous citrated ferrofluid (Process 1, Figure 2.7), then lyophilization takes place. This protocol



FIGURE 2.6: Typical apparatus used for the synthesis of Cho-AA ionic liquids.

is used not only for citrated NP but also for the preparation of all the acidic and alkaline dispersions described in Chapter 3;

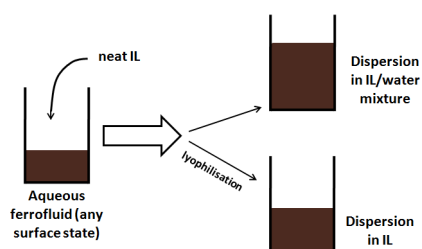


FIGURE 2.7: Schematic representation of Process 1, used for the transfer of maghemite NP from water to ILs.

2. during the surface functionalization with citrate (see Subsection 2.2.4), as a last step, instead of adding water, EAN is added; the product is then lyophilized (Process 2, Figure 2.8). This protocol is only used for citrated NP.

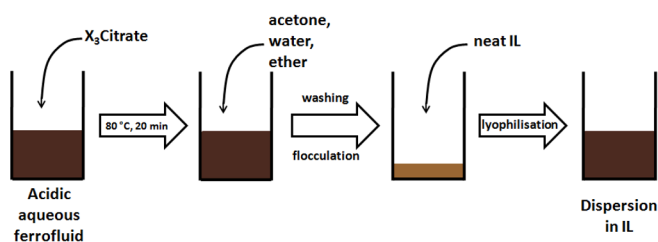


FIGURE 2.8: Schematic representation of Process 2, used for the transfer of citrated maghemite NP from water to ILs.

These two processes are not identical, as in the first case the sample contains much more water, which might prove more difficult to pump away. At the same time, Process 2 avoids the presence of a large quantity of water, but it also brings EAN in contact with the organic solvents remaining after the reaction (acetone and diethyl ether); at this stage, we do not have information on the behaviour of EAN/acetone or EAN/diethyl ether mixtures, but we assume that the volatility of such solvents will make it easy for them to be removed during lyophilization.

To assess the efficacy of each process on the state of dispersion of the citrated NP, the amount of dispersed particles is determined by Flame Atomic Absorption Spectroscopy (FAAS; see 2.3.3). The comparison of processes 1 and 2 on two Na<sub>3</sub>Cit-NP dispersions in EAN (prepared in parallel, keeping all other parameters similar) shows that the amount of dispersed particles is the same with both routes. The more practical process can therefore be chosen depending on the particular working conditions.

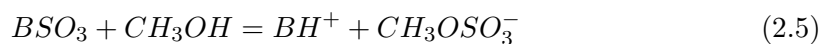
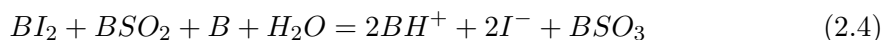
### 2.2.8 Lyophilization

Lyophilization is a “soft” technique for water removal: the sample is first frozen by immersion in liquid nitrogen, and then connected to a vacuum pump which lowers the pressure to about 10<sup>-6</sup> bar. This allows the frozen water to sublime, and the vapour is collected by condensation on a cold serpentine. The IL has such a low vapour tension that it remains liquid at such low pressures; this is therefore a very valuable technique to remove water from an IL. Since it replaces other drying techniques based on heating, lyophilization is particularly useful in the case of EAN, which is easily degraded by heat.

## 2.3 Characterization Techniques

### 2.3.1 Karl Fischer Titration

The water content of EAN and Cho-AA ionic liquids is determined via a Karl Fischer coulometric titration, using a Schott TitroLine KF Trace titration unit. The system is composed as follows: the Pt cathode and anode are immersed in a cell containing *hydranal*<sup>®</sup> solution, which contains iodide ions, sulphur dioxide (SO<sub>2</sub>) and a basic compound (imidazolium or ethanolamine); the reaction at the anode is the oxidation of iodide to iodine, while at the cathode H<sup>+</sup> is reduced to molecular hydrogen. When a sample containing water is injected into the cell, the following reactions take place:



where B is the base. The first of these reactions consumes water, while in the second, the presence of methanol prevents a parasite reaction between water and  $BSO_3$ . Finally, another pair of electrodes detects the abrupt fall in the potential  $\Delta E$  when the point of equivalence is reached (excess of  $I_2$  when all of the water is consumed). This technique allows the determination of trace water quantities (between 1 ppm and  $5 \cdot 10^4$  ppm).

In a typical measurement, 0.1 mL of ionic liquid is injected into the cell by means of a syringe; the mass of the sample, deduced by weighing the syringe before and after injection, is input in the titration unit's computer, which calculates the water content and displays the result in the desired unit (ppm or wt%). The measurement is repeated at least 3 times in order to have a statistically significant value. Figure 2.9 shows the titration apparatus used in this work.



FIGURE 2.9: A Karl Fischer apparatus. All its components are connected to a desiccating material in order to prevent humidity intake from influencing the measurements.

### 2.3.2 pH Measurements in Ethylammonium Nitrate

As explained in Subsection 1.3.1, it is possible to have a pH scale in EAN: pH measurements in the pure IL are performed with a classic glass electrode (Heito BV5ATE), and a saturated calomel electrode as a reference, protected with an agar-agar salt bridge filled with  $KNO_3$  2 M solution. The following solutions in EAN are used for routine calibration:

- pH = 1.0: benzenesulfonic acid (BSA, concentration  $1.0 \cdot 10^{-1}$  mol L<sup>-1</sup>);

- pH = 5.4: equimolar solution of benzoic acid/sodium benzoate (concentration  $2.0 \cdot 10^{-1} \text{ mol L}^{-1}$ );
- pH = 9.0: TMAOH (concentration  $1.0 \cdot 10^{-1} \text{ mol L}^{-1}$ ).

pH/potential measurements are performed on a Tacussel LPH530T pH-meter with a precision of 0.2 mV (in aqueous medium). The glass electrode to be used for measures in EAN is always kept immersed in pure EAN when not in use.

### 2.3.3 Flame Atomic Absorption Spectroscopy

Atomic Absorption Spectroscopy is an analytic technique capable of determining the concentration of trace elements (of the order of the ppm) in adequately prepared samples, based on the selective absorption of light at the element's typical wavelength. A lamp, containing a cathode made of the element to be quantified, is connected to the electric power; an electron current excites the cathode, which emits a light beam at a typical frequency. This light beam is focused to pass through a heating system (commonly a flame burner or a graphite oven) capable of reaching very high temperatures (of the order of  $3000^\circ\text{C}$ ), where the sample is atomized. This way, the atoms of the same element as the lamp's cathode absorb a certain fraction of the light beam's intensity, depending on their quantity. Thanks to a preliminary calibration (Absorbance *vs.* Concentration) with standard solutions of such element, it is possible to determine the element's concentration in the unknown sample.

During the course of this work, Flame Atomic Absorption Spectroscopy (FAAS) is omnipresent: after every synthesis, functionalization or dispersion, the iron concentration [Fe] of the samples is determined by means of FAAS, on a Perkin-Elmer Analyst 100 instrument, after proper dissolution of the NP by concentrated HCl and adequate dilutions in order to fit in the instrument's linearity range for iron's absorbance. The iron concentration, expressed in  $\text{mol L}^{-1}$ , can be converted directly into nanoparticles volume fraction  $\Phi$  using the density and molecular weight of maghemite [36]:

$$\Phi\% = \frac{(2M_{Fe} + 3M_O)[Fe]}{2\rho_{Fe_2O_3}} = 1.577[Fe](\text{molL}^{-1}) \quad (2.6)$$

The FAAS technique has also been used in this work for the determination of the concentrations of other elements than Fe (specifically Na and Li).

### 2.3.4 Small Angle (Neutron and X-Ray) Scattering

Small Angle Scattering techniques based on neutron (SANS) and X-ray (SAXS) incident beams have been used in this work for the characterization of the nanoscale structure of the samples. The information that can be collected with these two techniques is sometimes very similar, but in general the two methods complement each other to give a better picture of the systems. More details on the theoretical principles and the methods of data treatment and interpretation can be found in Appendix B, while an extensive overview is available in reference [98].

SANS experiments have been carried out on the PACE spectrometer at the LLB facility (Laboratoire Léon Brillouin, CEA Saclay, France). The available Q-range  $3.18 \cdot 10^{-3} \text{ \AA}^{-1} < Q < 0.402 \text{ \AA}^{-1}$  is obtained by using three different configurations: neutron wavelength  $\lambda = 13 \text{ \AA}$ , sample to detector distance  $d = 4.7 \text{ m}$ ;  $\lambda = 4.5 \text{ \AA}$ ,  $d = 4.7 \text{ m}$ ;  $\lambda = 4.5 \text{ \AA}$ ,  $d = 1.1 \text{ m}$ .

When dispersions polydisperse particles are studied, all samples are centrifuged at  $6700 \times g$  for 10 minutes prior to SANS experiments, and only the supernatant fraction is studied, in order to avoid scattering by large aggregates. In all cases, the samples are then enclosed in quartz cells of 1 mm inner thickness; the measurements are then performed at atmospheric pressure and room temperature.

The scattered intensities are corrected *in situ* for the detector background by cadmium scattering, for the parasitic intensity scattered by quartz cell by subtraction, and normalized to the water scattered intensity. Standard correction procedures for sample volume, neutron beam transmission, empty cell signal subtraction and detector efficiency are done using the Pasinet software (available free of charge at <http://didier.lairez.fr/>) to obtain the scattered intensity in absolute scale ( $\text{cm}^{-1}$ ).

SAXS experiments have been performed at Soleil Synchrotron (Saclay, France), on the Swing beam line. The beam energy of 7 keV corresponds to  $\lambda = 1.77 \text{ \AA}$ . In order to obtain the working Q-range  $3 \cdot 10^{-3} - 0.4 \text{ \AA}^{-1}$ , three configurations are used by varying the sample-to-detector distance (1.63 m in the high-Q regime, 6.83 m in the intermediate- and low-Q regime) and using different beamstops.

The samples are enclosed between extremely thin mica films, with a spacer ring whose thickness (100  $\mu\text{m}$ , 500  $\mu\text{m}$  or 1 mm) depends on the sample's concentration: indeed, while iron oxide nanoparticles are good X-ray scatterers, iron is a heavy element that

strongly absorbs this type of radiation; hence, when the sample is very concentrated, a minimum amount of matter is used in order to have an acceptable beam transmission, and this is controlled by using a thinner sample cell. See Figure 2.10 for pictures of the experimental setup.

The signal recorded by the 2D detector is circularly averaged; similarly to the SANS treatment described above, the scattered intensity is corrected considering a range of factors (possible detector non-linearity, background noise, x-ray beam transmission) and integrated from the center of the detector in order to obtain a 1D scattering curve. This is done automatically at the Swing beam line using the software *Foxtrot*<sup>®</sup>. Finally, the curves are rescaled by normalization to water in order to obtain the scattered intensity in the absolute scale ( $\text{cm}^{-1}$ ).

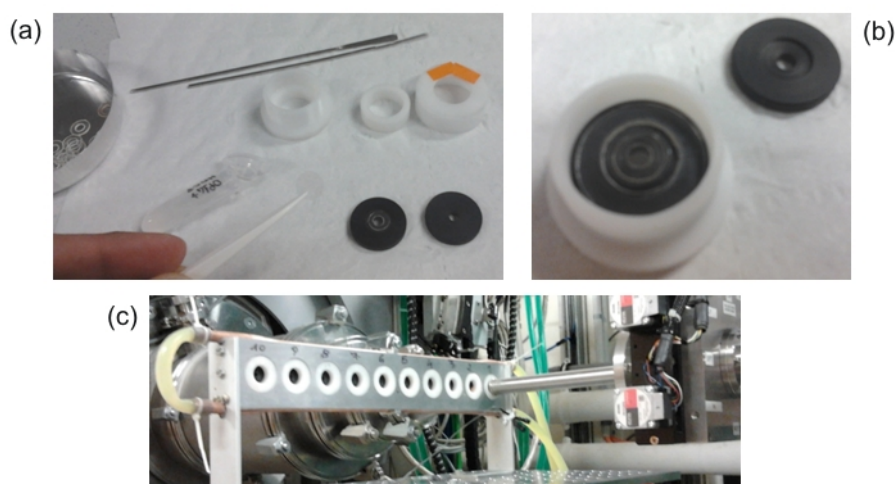


FIGURE 2.10: Sample preparation for SAXS experiments. (a) The sample is enclosed between extremely thin mica films, with a spacer ring made out of different materials depending on the thickness. (b) The sample is then enclosed in a polyoximethylene cell. (c) A mechanic support allows for the study of ten samples per shift.

### 2.3.5 Dynamic Light Scattering

Dynamic Light Scattering (DLS) is a technique in which the sample is irradiated with a laser, and the interference between the light waves scattered by the objects in solution (characterized by Brownian motion) is studied. The intensity  $I$  of the scattered waves is measured at different times, allowing the instrument to determine the autocorrelation function, which describes the variation of the scatterers' position between the instants  $t$  and  $t + \tau$  according to the following time average:

$$F(I, \tau) = \langle I(t)I(t + \tau) \rangle_t \quad (2.7)$$

If  $\tau$  is large, there is no correlation between the positions of the scatterers at different moments, and the function gives the average intensity (base line):

$$F(I, \tau = \infty) = \langle I(t) \rangle_t^2 \quad (2.8)$$

If  $\tau$  is small enough, the positions are entirely correlated:

$$F(I, \tau = 0) = \langle I(t)^2 \rangle_t \quad (2.9)$$

The graph of  $\langle I(t)^2 \rangle$  as a function of  $\tau$  is called a *correlogram*. The study of this function allows to extract the dynamic structure factor  $S(Q, \tau)$  of the solution, which (for monodisperse and non-interacting objects) is related to the movement and the size of the particles through the following equations:

$$S(Q, \tau) = S(Q)e^{-\Gamma\tau} \quad (2.10)$$

$$\Gamma = D_0Q^2 \quad (2.11)$$

where  $Q$  is the scattering vector (depending on the angle between incident and scattered intensity, and on the laser wavelength), and  $D_0$  is the diffusion coefficient of the particles. This quantity can be related to the hydrodynamic radius  $R_H$  of the scatterers *via* the well-known Stokes-Einstein equation:

$$D_0 = \frac{k_B T}{6\pi\eta R_H} \quad (2.12)$$

where  $k_B$  is the Boltzmann constant,  $T$  the absolute temperature, and  $\eta$  the viscosity of the medium.

In this work, the size of the nanoparticles has been determined via Dynamic Light Scattering on a VASCO particle size analyser produced by Cordouan Technologies. This instrument is able to evaluate the diffusion coefficient of particles even in concentrated and dark/turbid media, thanks to an original sample cell design. The viscosities are taken from the literature (0.891 mPa s<sup>-1</sup> for water, 34.3 mPa s<sup>-1</sup> for EAN at 25 °C). Refraction indexes for EAN-Water mixtures and pure EAN have been measured on



an Abbe refractometer at 25 °C. All measurements are run at 25 °C, with the laser operating at  $\lambda = 658$  nm and an analysis angle  $\theta = 135^\circ$ . For each sample, acquisition parameters such as laser power, sampling time and number of channels are adjusted in order to obtain the best autocorrelation curve; each sample is analysed at least 15 times for 60 seconds, and each correlogram is then fitted using the Padé-Laplace method [99]. The size dispersion is then represented as a histogram of the frequency of the Padé-Laplace results. For the sake of comparison with other instruments, the analysis is also carried out through a second order cumulant model, on the averaged correlogram, to give the intensity average size of the particles ( $Z_{ave}$ ) and the associated polydispersity index (PDI).

### 2.3.6 Magnetization Measurements

Magnetization measurements are carried out on two different instruments. For routine measurements, a home-made vibrating sample magnetometer is used, which measures the magnetic moment of a sample when it is vibrated perpendicularly to a uniform magnetizing field [100]. The sample, when magnetized, induces a voltage in the measuring coil which is proportional to the magnetization  $M$  of the material. The instrument is then able to record a curve of  $M$  as a function of the applied magnetic field  $H$ .

In the case of a maghemite-based ferrofluid, the orientation of the particles of size  $d$  under an external magnetic field  $H$  is described by the first Langevin equation (Eqn. 2.1), while their size distribution is characterized by a lognormal law  $P(d)$  (Eqn. 2.2). At high  $H$  values, it is then possible to deduce the volume fraction of nanoparticles from the ratio

$$\frac{M_s}{\Phi} = m_s \quad (2.13)$$

by assuming a standard value for  $m_s$  (for maghemite, a typical value is  $3 \cdot 10^5$  A/m).

For measurements on small volumes, a SQUID (Superconducting QUantum Interference Device) magnetometer is used, which allows to measure even very weak magnetic fields. The particular instrument used for this work is from CRYOGENIC, model S600, with a working temperature range between 1.5 K and 320 K (experiments were carried out at 300 K). The magnetic field ( $B_{max} = 5.5$  T) is generated by a NbTi superconducting coil. The precision on the measurements is around 1%.

### 2.3.7 Magneto-Optical Birefringence Experiments

The rotational relaxation of the nanoparticles can be determined thanks to the magneto-induced birefringence signal. Indeed, each particle bears a magnetic dipole moment and has a uniaxial optical anisotropy [101]. While applying a magnetic field, the magnetic dipole orients along the field, producing a mechanical rotation of the whole nanocrystal and inducing a macroscopic birefringence. Using a weak magnetic field ( $H < 8 \text{ kA m}^{-1}$ ) that can be switched off quickly and a red laser at 650 nm (a wavelength at which the absorption of light by the NP is low), the relaxation of this birefringence after switching off the field can be measured [102]. Such relaxation can be described by a monoexponential decay for an ideal monodisperse sample, however a stretched exponential is necessary for polydisperse samples. The curves are fitted here using the function  $\exp[-(t/\tau_{rot})^\beta]$ , with

$$\tau_{rot} = \frac{1}{6D_{rot}} = \frac{\eta V_H}{k_B T} \quad (2.14)$$

where  $D_{rot}$  is the rotational diffusion coefficient,  $V_H$  is the hydrodynamic volume of each rotating particle,  $\eta$  the viscosity of the solvent,  $k_B$  is the Boltzmann constant,  $T$  the absolute temperature and  $\beta$  the stretching exponent. This is valid if the system is fluid, far from any glass transition.

## Chapter 3

# Preliminary Screenings on Polydisperse Nanoparticle/Ethylammonium Nitrate Dispersions

### Contents

---

<b>3.1</b>	<b>pH Measurements in Ethylammonium Nitrate . . . . .</b>	<b>76</b>
3.1.1	Response of the Glass Electrode in EAN . . . . .	77
3.1.2	Dissociation Constants of Citric Acid in EAN . . . . .	78
<b>3.2</b>	<b>Dispersions of Bare Maghemite Nanoparticles in EAN: Ef- fect of pH, Counterion and Water Content . . . . .</b>	<b>80</b>
3.2.1	Neutral Medium – Point of Zero Charge . . . . .	82
3.2.2	Acidic Medium . . . . .	82
3.2.3	Alkaline Medium . . . . .	84
<b>3.3</b>	<b>Dispersions of Citrate-Covered Maghemite Nanoparticles in EAN . . . . .</b>	<b>84</b>
<b>3.4</b>	<b>Microscopic Study of Citrate-Covered Maghemite Nano- particles in EAN . . . . .</b>	<b>86</b>
3.4.1	Dynamic Light Scattering Experiments . . . . .	88
3.4.2	Small Angle Neutron Scattering (SANS) Experiments . . . . .	90
<b>3.5</b>	<b>Conclusion . . . . .</b>	<b>93</b>

---

This Chapter offers an overview on the preliminary work carried out to probe the main features of the systems composed of maghemite ( $\gamma\text{-Fe}_2\text{O}_3$ ) nanoparticles (NP) dispersed in the ionic liquid ethylammonium nitrate (EAN).

First, a protocol for pH measurements in EAN is established; we will show that a common glass electrode is perfectly suitable for these measurements, and that buffers at different pH can be prepared in EAN. Since the work focuses especially on citrate-covered (“citratated”) nanoparticles, the three dissociation constants of citric acid in EAN are determined, and the solubility of some chemical species in this solvent are probed.

In a second step, we move to the behaviour of bare maghemite nanoparticles. “Bare” here means that these particles do not carry any molecules adsorbed on their surface. However, due to the presence of hydroxyl groups that can be ionized depending on the pH, the particles can bear different surface charge (in sign and value) in EAN. Therefore, acidic, neutral and basic dispersions are prepared in water with different counterions, and are transferred to the ionic liquid (IL); the resulting systems are described and we will conclude on the importance of the surface charge in EAN.

Finally, we will focus on citrated particles as the first qualitative tests show them to have the best colloidal stability in this IL. We compare two different protocols for the transfer of these particles from water to EAN; then, we use a whole set of techniques (visual observation, flame atomic absorption spectroscopy, pH measurements, dynamic light scattering, and small angle neutron scattering) to probe the effect of using different counterions for citrate.

For the work described in this Chapter, a polydisperse ( $d = 7$  nm,  $\sigma = 0.39$ ) ferrofluid is used.

### 3.1 pH Measurements in Ethylammonium Nitrate

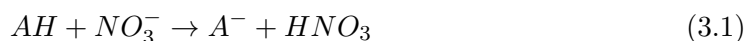
As described earlier (Subsection 1.3.1), EAN is an amphoteric solvent in which an autoprotolysis constant ( $\text{p}K_s = 10$ ) and a pH scale are defined [18, 57]: acid-base properties of various species have been described as in water, defining strong acids and bases, as well as weak acids/bases characterized by an acidity constant. Within this framework, since the constitutive strongest acid and base of EAN (*i.e.*,  $\text{HNO}_3$  and  $\text{EtNH}_2$ ) are not easy to manipulate in a condensed state at room temperature, we chose other compounds in order to control the pH of EAN dispersions. The chosen strong acid is benzenesulfonic

acid (BSA), already described in literature [57], and the chosen bases are tetramethylammonium hydroxide (TMAOH) and sodium hydroxide, which are known to behave as strong bases in water (the next Subsection will show that they do have the same behaviour in EAN). In particular, the choice of  $\text{TMA}^+$  stems from its use as a classical non-flocculating counter-ion for aqueous alkaline ferrofluids [36], and  $\text{Na}^+$  because of its intensive use in water.

### 3.1.1 Response of the Glass Electrode in EAN

In order to test the experimental set up and the response of the glass electrode in neat EAN, we follow the procedure described by Benlhima *et al.* [57]. Growing amounts of a strong base (or acid) solution in EAN (concentration  $C = 0.1 \text{ mol L}^{-1}$ ) are added to the pure ionic liquid, and the electric potentials  $E$  are recorded between a glass electrode and a saturated calomel electrode.

If AH is a strong acid, its reaction in EAN can be expressed as:



with AH and  $A^-$  representing, respectively, the protonated and deprotonated forms of a strong acid (for example, benzenesulfonic acid). The pH of a solution of strong acid of concentration  $C$  is then defined as:

$$pH = -\log[\text{HNO}_3] = -\log C \quad (3.2)$$

Symmetrically, if XOH is a strong base in EAN, the expected reaction with the solvent can be written:



Using the definition of the autoprotolysis constant  $K_s$ , the pH of the strong base of concentration  $C$  in EAN is:

$$pH = pK_s + \log C \quad (3.4)$$

Since the literature has described mainly the behaviour of acids in EAN, let us here focus on the bases TMAOH and NaOH. The expected response of the glass electrode

is  $E = cst + RT/(F \log 10) \log[HNO_3] = cst - RT/F pK_s - RT/(F \log 10) \log C$ , with  $cst$  a constant,  $F$  the Faraday constant and  $RT$  as usual. Here, Fig. 3.1 shows the experimental response and a linear fit that leads to  $E_{NaOH}$  (mV) =  $-132 - 65 \log C_{NaOH}$ , and  $E_{TMAOH}$  (mV) =  $-133 - 63 \log C_{TMAOH}$ , at  $T = 25^\circ C$ .

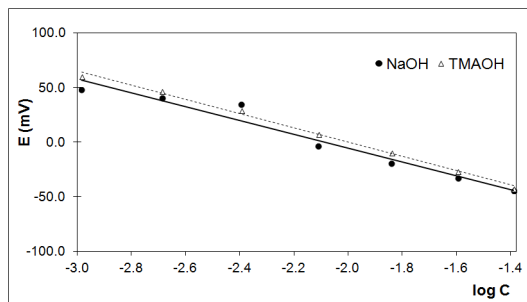


FIGURE 3.1: Response of the glass electrode in NaOH and TMAOH solutions in EAN ( $C$  expressed in  $\text{mol L}^{-1}$ ). See text for details on the protocol.

This result allows us to state that both hydroxides are actually strong bases in EAN, so their pH can be calculated as explained above. In what follows, TMAOH is preferred to NaOH thanks to its better solubility in EAN.

For pH measurements in EAN, we prepare calibration buffers of known pH in order to convert the recorded electric potential into pH values as in water:

- pH = 1.0: a  $1 \cdot 10^{-1} \text{ mol L}^{-1}$  solution of benzenesulfonic acid (BSA);
- pH = 5.4: an equimolar solution of benzoic acid/sodium benzoate (concentration  $2.0 \cdot 10^{-1} \text{ mol L}^{-1}$ );
- pH = 9.0: a  $1.0 \cdot 10^{-1} \text{ mol L}^{-1}$  solution of TMAOH.

The response of the glass electrode is linear in the entire range between pH 1.0 and 9.0, as shown in Figure 3.2. Therefore we can conclude that the experimental set-up properly responds, that the glass electrode can be used even in pure ethylammonium nitrate where the water content is inferior to 0.3 wt%, and that the calibration procedure is appropriate.

### 3.1.2 Dissociation Constants of Citric Acid in EAN

Citric acid ( $H_3\text{Cit}$ ) has three acidity constants in water ( $pK_1 = 3.1$ ;  $pK_2 = 4.8$ ;  $pK_3 = 6.4$ ) [103]. In order to determine their values in EAN, as they are not accessible in literature, we prepared the following solutions: citric acid  $1 \cdot 10^{-2} \text{ mol L}^{-1}$ ; trisodium

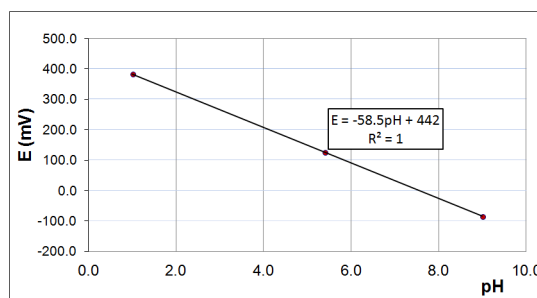


FIGURE 3.2: Potential (in mV) vs. pH response of the glass electrode in the whole pH range in EAN. See text for description of the pH buffers used.

citrate ( $\text{Na}_3\text{Cit}$ )  $1 \cdot 10^{-2} \text{ mol L}^{-1}$ ; finally, 1:1; 1:2 and 2:1 volume mixes of these two solutions. Their pH is measured and reported in Table 3.1.

From these results, the corresponding values for the dissociation constants can be calculated, yielding  $\text{pK}_1 = 4.1$ ;  $\text{pK}_2 = 5.2$ ;  $\text{pK}_3 = 6.6$ . If compared to their homologues in water, an increase of 1 unit can be noticed for  $\text{pK}_1$ , which compares well with the published results for other monocarboxylic acids [57].  $\text{pK}_2$  and  $\text{pK}_3$  are also increased in EAN, however slightly. These results indicate that citric acid can be deprotonated in EAN as in water. In order to validate the use of such simple formulae even for  $\text{pK}_a$  of close values, we calculated *a posteriori* (with the software *Simulwin*, edited by *Chrysis*) the expected pH of the 5 solutions, with the  $\text{pK}_a$  values listed above as input parameters, without any approximation. The values of the exact calculated pH and the measured pH are in very good agreement within 0.2 pH units, as indicated in the last column of Table 3.1.

**Citric Acid and Trisodium Citrate Solutions in EAN**

Composition	pH (meas.)	Approximate Formulae	pH (calc.)
$\text{H}_3\text{Cit}$	3.0	$\text{pH} = \frac{1}{2} (\text{pK}_1 - \log C)$	3.1
$\text{H}_3\text{Cit} : \text{Na}_3\text{Cit} (1:1)$	5.2	$\text{pH} = \text{pK}_2$	5.2
$\text{Na}_3\text{Cit}$	7.3	$\text{pH} = 5.0 + \frac{1}{2} (\text{pK}_3 + \log C)$	7.3
$\text{H}_3\text{Cit} : \text{Na}_3\text{Cit} (1:2)$	5.9	$\text{pH} = \frac{1}{2} (\text{pK}_2 + \text{pK}_3)$	5.9
$\text{H}_3\text{Cit} : \text{Na}_3\text{Cit} (2:1)$	4.5	$\text{pH} = \frac{1}{2} (\text{pK}_1 + \text{pK}_2)$	4.7

TABLE 3.1: Determination of the dissociation constants of citric acid in EAN. All solutions are prepared from  $\text{H}_3\text{Cit}$   $1 \cdot 10^{-2} \text{ M}$  and  $\text{Na}_3\text{Cit}$   $10^{-2} \text{ M}$ .  $\text{pH} (\text{meas.}) = \text{pH}$  measured in the solution;  $\text{pH} (\text{calc.}) = \text{exact calculation of pH}$ .

### 3.2 Dispersions of Bare Maghemite Nanoparticles in EAN: Effect of pH, Counterion and Water Content

The dispersions in EAN are prepared by transferring the particles from the initial aqueous medium. Therefore the first step is the preparation of well-defined aqueous ferrofluids stabilized by electrostatic repulsions for several physico-chemical conditions, *i.e.* different compositions of the interface between water and solid nanoparticles. This allows a precise control of this interface: the sign of the charge and the nature of the counterions can be tuned. Let us emphasize that this latter parameter is indeed crucial in water: some counterions do not allow stabilization, for example  $\text{Na}^+$  at  $\text{pH} = 12$  or  $\text{Cl}^-$  at  $\text{pH} = 2$  [36], which is linked to their condensation on the surface, depending on their size and polarizability.

The well controlled ferrofluids in water are all issued from the home-made maghemite nanoparticles dispersed in acidic medium ( $\text{pH} = 1.5$ ) obtained after the synthesis process. At this stage, the particles' surface is covered with positive charges ( $\text{Fe-OH}_2^+$ ) counterbalanced by  $\text{NO}_3^-$  anions. Starting from these dispersions, several kinds of samples have been prepared by varying the choice of surface charge and counterions (see 2.2.3 for the experimental procedure). In acidic medium, other than nitrate, benzenesulfonate ( $\text{BS}^-$ ) is successfully used here as a counterion for the first time in water. Uncharged flocculated particles without counterions are obtained at  $\text{pH} = 7$  (point of zero charge (PZC)). Alkaline ferrofluids are obtained at  $\text{pH} = 12$  with tetramethylammonium ( $\text{TMA}^+$ ) counterions. In these conditions ( $\text{pH} = 2$  and  $12$ ), the absolute charge of the particles is around  $2 \text{ e}^-/\text{nm}^2$  [36].

All the aforementioned aqueous dispersions are then transferred to EAN or EAN/water mixtures *via* the simple addition of an appropriate volume of IL into the ferrofluid (Process 1 in Subsection 2.2.7), so as to obtain final dispersions with nanoparticles concentration  $\Phi = 0.1\%$ . In the case of 100% EAN sample, this is followed by lyophilization in order to remove as much water as possible. The sample is finally stirred and sonicated, then left standing in a vertical magnetic field ( $H \simeq 160 \text{ kA m}^{-1}$ ) during 24 hours before analysis. Indeed, in the case of unstable dispersions, the presence of a magnetic field accelerates the sedimentation of the particles, while a true, stable ferrofluid is not altered by such field.

Since EAN dispersions are lyophilized in the same way as the pure ionic liquid, we



assume that the water content is similar to that in neat EAN (0.3 wt%, determined by Karl Fischer titration). This assumption though remains, so far, without experimental confirmation due to practical difficulties. Indeed, a Karl Fischer titration (see Subsection 2.3.1) cannot be carried out in a system containing maghemite nanoparticles because of the pollution of the electrodes due to the iron oxide; also, the hydroxyl groups on the surface of the NP can take part into parasitic reactions with the Karl Fischer reactants, thereby interfering with the result of the titration. Therefore, such matter will require deeper consideration and a thorough study in the future.

The colloidal stability of the EAN dispersions is first assessed by simple visual observation, so as to obtain a qualitative indication of the nanoparticles' state of dispersion. Indeed, since maghemite strongly absorbs visible light in the green and blue wavelengths, its stable dispersions appear red, saturating to black with increasing  $\Phi$ . Unstable suspensions, characterized by the formation of large aggregates or flocs, appear brownish and turbid due to the scattering of visible light, and eventually settle down. Table 3.2 summarizes all the samples prepared according to the water content (where the volume fraction of EAN,  $\phi_{EAN}$ , is rather expressed), the measured pH (initial, in water, and final, in 100% EAN) and their stability. In this table, the indication "stable" means that the particles are homogeneously dispersed in the solvent; "floc" indicates total and immediate flocculation of the particles, leaving a clear supernatant; "partial" indicates the coexistence of a well dispersed supernatant with a precipitate (more or less thick) at the bottom; "partial\*" means that the dispersion, partially stable to begin with, is destabilized over a short time (24 hours to a few days) until total flocculation.

**Dispersion State of Maghemite in EAN Depending on Water Content and Counterion**

<b>pH in Water:</b>	<b>Acidic (pH = 1.5)</b>		<b>Neutral (pH = 7)</b>	<b>Basic (pH = 12)</b>
Counterion:	$\text{NO}_3^-$	$\text{BS}^-$	none	$\text{TMA}^+$
$\phi_{EAN} = 0\%$	stable	stable	floc	stable
$\phi_{EAN} = 20\%$ to $60\%$	floc	floc	floc	floc
$\phi_{EAN} = 80\%$ to $90\%$	floc	floc	floc	partial
$\phi_{EAN} = 100\%$	partial*	floc	floc	partial*
pH in 100% EAN:	2.7	3.6	6.0	0.5

TABLE 3.2: Dispersions of bare maghemite NP in EAN, according to pH (in water), counterion and volume fraction of EAN. The pH measured in pure EAN dispersions is given for each counterion. See text for details on the meaning of the stability notations.

All samples have a NP volume fraction of  $\Phi = 0.1\%$ .

The states of dispersion just described can be exemplified by Figure 3.3.

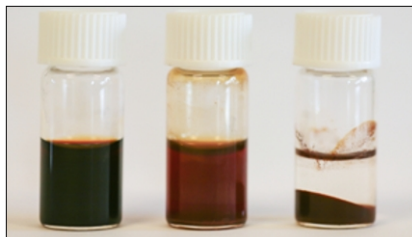


FIGURE 3.3: Different states of dispersion for maghemite nanoparticles. Left: homogeneous dispersion, no precipitate at the bottom. Middle: partial dispersion, with a stable supernatant in equilibrium with a precipitate. Right: total flocculation, leaving a clear supernatant.

After transfer to the new solvent, the samples are left standing one day in a vertical magnetic field before analysis: for such magnetic nanoparticles, flocculation, if occurring, would be enhanced by the presence of magnetic field gradients.

Let us now discuss the experimental results by considering the pH ranges separately.

### 3.2.1 Neutral Medium – Point of Zero Charge

In water, all the samples are homogeneous dispersions except for the particles at PZC, which flocculate due to the uncharged surface near pH 7. This latter sample was nevertheless transferred to EAN and EAN/water mixtures, in order to check for a possible redispersion in the case of a neutral interface without counterions. However, the particles remain totally flocculated whatever the solvent composition, meaning that a charged interface is necessary in order to obtain colloidal stability in neat IL or IL/water mixtures just as well as in pure water.

### 3.2.2 Acidic Medium

For initially acidic aqueous ferrofluids, the water/EAN ratio does not seem to have any effect on the colloidal stability, while a slightly different behaviour can be noticed between the two counterions: indeed, the only case in which the addition of the IL does not lead to immediate flocculation is when nitrate is present. However this latter dispersion is slowly destabilized over the few days following its preparation, yielding the same final result as its benzenesulfonate counterpart.

The final pH in pure EAN (measured in the supernatant) is acidic in both cases, but with different values (namely, 2.7 for nitrate and 3.6 for benzenesulfonate). It should be noted that these two dispersions have been prepared following two different paths

(described hereunder), which may determine a different degree of charge condensation at the surface of the particles, as it has already been proved in similar systems [36].

Indeed, for the  $\text{NO}_3^-$  sample, the particles issued directly from the classical coprecipitation synthesis, during which their surface is immersed in an extremely acidic medium; the surface charge density is therefore very high.

On the other hand, in the case of  $\text{BS}^-$ , the original aqueous ferrofluid is first titrated with base until the point of zero charge (PZC), and only then redispersed in a benzenesulfonic acid solution in EAN; the surface charge density is therefore lower than in the former case, and the surface sites are still able to trap more protons coming from EAN when this is eventually added. Thus, in the  $\text{BS}^-$  sample the concentration of free protons would be reduced, explaining the pH difference between the two dispersions. Also, such initial discrepancy in surface charge, other than the dissimilarity in the two ions' sizes and polarizabilities, may contribute to explain the initial difference in the stability of the two samples after transfer to EAN.

Due to the difficulty of discriminating between an ion-specific effect and a consequence of different pH or preparation paths for the acidic samples, we focus on two sets of products fabricated in exactly the same way and differentiated only by the choice of the surface's counterion: nitrate in one case, and perchlorate in the other. For both counterions, dispersions of particles in pure EAN are prepared starting from different initial pH in water: 0.2, 1.0 and 1.5. As expected, the amount of dispersed particles in EAN is higher for lower pH, corresponding to a higher surface charge density. Also, two important observations follow from these experiments. First, after lyophilization, the pH in EAN is higher than the initial pH in water for both sets of samples. We attribute this fact to the loss of molecular acid ( $\text{HNO}_3$  or  $\text{HClO}_4$ ) during the lyophilization, as confirmed by tests on nitric acid solutions in neat EAN (without particles). Such loss is more important for  $\text{HNO}_3$  than for  $\text{HClO}_4$ , and it also depends on the time of lyophilization. Secondly, at identical conditions of initial pH and preparation path, the particles are better dispersed in the case of  $\text{ClO}_4^-$  counterions. The initial and final pH being practically identical between the two sets of samples, we can confirm the existence of an ion-specific effect leading to a better colloidal stability of positively charged maghemite nanoparticles in EAN when the counterion is perchlorate rather than nitrate.

### 3.2.3 Alkaline Medium

For alkaline samples, the results are quite different: while total flocculation occurs for low  $\phi_{EAN}$  up to 60%, the dispersion is partial for larger  $\phi_{EAN}$ , and homogeneous for 100% EAN immediately after preparation, but evolving towards flocculation in the following days.

However the samples face another kind of evolution over longer periods of time (several months): in 100% EAN, the pH becomes acidic even though TMAOH is a strong base and stable in EAN. This change is accompanied by a slow flocculation of the particles.

In water-containing samples, a similar phenomenon is observed, this time leading to limpid yellow solutions without particles. This can only mean that a slow chemical reaction occurs, involving EAN, water, TMAOH and iron, that leads to the destruction of the nanoparticles. This prevents us from studying the colloidal stability in these media in the long run, and these samples are left aside for future studies.

## 3.3 Dispersions of Citrate-Covered Maghemite Nanoparticles in EAN

In order to stabilize  $\gamma\text{-Fe}_2\text{O}_3$  dispersions in water at  $\text{pH} = 7$ , citrate anions (Figure 3.4) are adsorbed on their surface as described in Subsection 2.2.4; the adsorption takes place thanks to the complexation of iron cations by at least one of the  $\text{COO}^-$  groups, although the exact mechanism is still unclear. At  $\text{pH} = 7$ , most of the carboxyl groups are deprotonated, so that the groups that are not busy complexating the surface iron, are free to ensure a negative charge on the particles. Naturally, this charge is compensated by counterions, which are usually represented by the cation associated to the citrate salt used in the process: the most typical counterion used in water is sodium, and for these preliminary stability tests we also use ammonium ( $\text{NH}_4^+$ ) and tetramethylammonium ( $\text{TMA}^+$ ).

Citrate molecules do not stick permanently onto the iron oxide surface (like a covalently bound polymer would, for example), but there is an adsorption/desorption equilibrium determined by the presence of free citrate salt in the dispersion. The concentration of free citrate controls the ionic strength, which is around  $0.02 \text{ mol L}^{-1}$  in

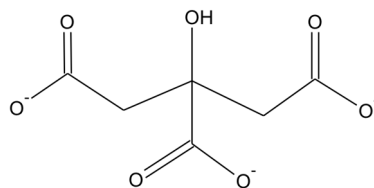


FIGURE 3.4: Chemical structure of the citrate anion.

our case. At such free citrate concentrations, we can be sure to have the maximal charge on the particles, i.e.  $2 e^-/\text{nm}^2$  [39].

Citrated NP are transferred to EAN or EAN/water mixtures according to Process 1 (described in Subsection 2.2.7), so as to obtain dispersions with  $\Phi = 0.1\%$ . The final sample is stirred and sonicated, then left standing one day in a vertical magnetic field before analysis. Table 3.3 summarizes the observations carried out on these samples. Once again, the indication “stable” means that the particles are homogeneously dispersed in the solvent; “partial” indicates the coexistence of a well dispersed supernatant with a precipitate (more or less thick) at the bottom; “partial\*” means that the dispersion, partially stable to begin with, is destabilized over a short time (24 hours to a few days) until total flocculation.

**Dispersion State of Citrated Maghemite in EAN  
Depending on Water Content and Counterion**

Counterion:	Na <sup>+</sup>	NH <sub>4</sub> <sup>+</sup>	TMA <sup>+</sup>
pH in Water:	6.9	6.7	6.7
$\phi_{EAN} = 0\%$	stable	stable	stable
$\phi_{EAN} = 20\%$ to $60\%$	partial	stable	partial*
$\phi_{EAN} = 80\%$ to $90\%$	partial	stable	partial
$\phi_{EAN} = 100\%$	partial	partial	partial
pH in 100% EAN:	7.0	7.0	6.3

TABLE 3.3: Dispersions of citrated maghemite NP in EAN, according to pH (in water), counterion and volume fraction of EAN. The pH measured in pure EAN dispersions is given for each counterion. See text for details on the meaning of the stability notations.

All samples have a NP volume fraction of  $\Phi = 0.1\%$ .

In water, all the samples are homogeneous (stable) dispersions. Partial dispersions are observed when EAN is added; however, among the three counterions used, ammonium seems to impart the mixed water/EAN dispersions with better colloidal stability than the other two cations. Since the structural charge of citrated maghemite NP is the same in all cases, this must represent a true ion-specific effect due to the very properties of each cationic counterion.

Dispersions in 100% EAN are defined partial, but they actually only show a very small quantity of precipitate, probably constituted by the fraction of largest particles that are destabilized. The pH is slightly alkaline as in water, and above the higher  $\text{pK}_a$  of citric acid, thus the citrate anion is the predominant species in these systems. The macroscopic observations are similar for the three counterions used, although their intrinsic properties are different. The small  $\text{Na}^+$  and ammonium, as well as the large  $\text{TMA}^+$ , all enable the dispersion of the particles.

Citrate-covered nanoparticles seem overall the most stable in EAN, and their homogeneity shows the lesser counterion dependency. Moreover, contrary to the case of alkaline dispersions, the samples' appearance is unchanged even after 1 year. In the rest of this work, we will focus on citrated maghemite NP.

### 3.4 Microscopic Study of Citrate-Covered Maghemite Nanoparticles in EAN

In order to go deeper in the understanding of the mechanisms behind colloidal stabilization in IL, we now focus on citrated nanoparticles with several different cationic counterions, and we perform a structural investigation of samples at local scale by coupling Dynamic Light Scattering (DLS) with Small Angle Neutron Scattering (SANS).

In the previous Section, we saw that the cationic counterion introduced with citrate has a slight influence on the macroscopic stability of citrated maghemite dispersions in EAN/water mixtures, as shown by the results of Table 3.3. However, in this first study only three cations were used, and the dispersions had a low nanoparticles concentration. In order to shed more light on this matter, we perform here a study of the influence of the nature of the counterion on the microscopic behaviour of more concentrated suspensions ( $\Phi \approx 1\%$ ). A wide range of counterions are tested: the alkaline series ( $\text{Li}^+$ ,  $\text{Na}^+$ ,  $\text{K}^+$  and  $\text{Cs}^+$ ) allows to probe the influence of the size, as well as the three ammoniums ( $\text{NH}_4^+$ ,  $\text{EA}^+$ ,  $\text{TMA}^+$ ), among which ethylammonium ( $\text{EA}^+$ ) is chosen because it is the same cation as the IL solvent, EAN. The influence of the valence is also checked with divalent  $\text{Ca}^{2+}$  and trivalent  $\text{Al}^{3+}$  counterions.

All systems with monovalent counterions are stable in water; this is the first time that  $\text{Li}^+$ ,  $\text{K}^+$ ,  $\text{Cs}^+$  and  $\text{EA}^+$  are used to prepare stable aqueous ferrofluids from citrated maghemite NP. In the case of calcium citrate, the functionalization reaction takes place

as usual, however the resulting particles are flocculated; this may be explained by the fact that the screening of the surface charges is more effective when the counterion is bivalent. Finally, aluminium citrate does not adsorb on the particles at all: the salt introduced for the functionalization remains unreacted on the bottom of the glass vial.

Next, the flocculated citrated NP with different cationic counterions are transferred to EAN through Process 2 (described in 2.2.7), in order to avoid at most the contact between the particles and water. The transfer is carried out even for the calcium-citrate dispersion, which despite being totally flocculated in water, might encounter different phenomena in the IL. For all samples, the amount of EAN is chosen so that a maximum volume fraction  $\Phi$  of 0.8% would be reached in case of total dispersion.

As a result, all samples except  $\text{Li}^+$  and  $\text{Ca}^{2+}$  give rise to a stable dispersion in EAN immediately after lyophilization: they present a very dark dispersion and a minimum trace of precipitate on the bottom, and we could verify that they remained stable for at least 1 year.

With lithium, while the aqueous dispersion is homogeneous and stable, the EAN sample separates into a flocculated part and a reddish supernatant. During the first days after preparation, the supernatant increasingly darkens with time, indicating a progressive transfer of stable particles from the floc to the dispersed fraction (confirmed by FAAS analysis, showing an increasing content of iron with time in the dispersed fraction). This process reaches an equilibrium in 4–6 weeks, by the end of which the sample presents a dark dispersed fraction coexisting with some precipitate.

Similarly, in the case of calcium, the EAN system is totally flocculated after lyophilization; however the supernatant progressively darkens after several days, corresponding to a slow dispersion of particles in EAN, although there is never a complete redispersion of the precipitate. The redispersion of  $\text{Li}^+$ - and  $\text{Ca}^{2+}$ -citrated NP is a very uncommon behaviour, since colloidal systems often tend to be destabilized and flocculate over time, while the opposite is seldom witnessed.

The concentrations  $\Phi$  in the dispersed fractions (which we will often refer to as “supernatants”), obtained by FAAS analysis after 4 weeks, are given in Table 3.4. The values are close to the maximum possible volume fraction of 0.8% — except for  $\text{Li}^+$  and  $\text{Ca}^{2+}$ . The value for the  $\text{K}^+$  dispersion, superior to  $\Phi = 0.8\%$ , can be explained by taking into account the existing error bar of  $\pm 10\%$  on the iron molar concentration issuing from FAAS determinations.

**Citrated NP Dispersions in EAN with Different Counterions**

Counterion	$\Phi_{FAAS}\%$	pH
Na <sup>+</sup>	0.7	6.7 ± 0.1
Li <sup>+</sup>	0.3	6.0 ± 0.1
K <sup>+</sup>	0.9	6.2 ± 0.1
Cs <sup>+</sup>	0.8	6.1 ± 0.1
NH <sub>4</sub> <sup>+</sup>	0.8	6.5 ± 0.1
EA <sup>+</sup>	0.7	6.1 ± 0.1
TMA <sup>+</sup>	0.7	6.5 ± 0.1
Ca <sup>2+</sup>	0.5	6.2 ± 0.1

TABLE 3.4: Dispersions of citrated maghemite NP in EAN. For each cationic counterion, the table shows the volume fraction determined in the supernatant by FAAS analysis ( $\Phi_{FAAS}$ ) and the measured pH.

### 3.4.1 Dynamic Light Scattering Experiments

DLS measurements are performed 15 days after preparation on all the dispersions in EAN, as well as on some aqueous ferrofluid as a reference. Figure 3.5 presents significant examples from this series of measurements. The average hydrodynamic diameter and polydispersity index of the initial aqueous dispersions are respectively  $Z_{ave} = 19 \pm 2$  nm and  $PDI = 0.22 \pm 0.02$ , which is a typical result for such a stable polydisperse dispersion (the size is large when compared to results from magnetization measurements, since DLS yields a hydrodynamic size and gives more weight to large particles).

For all samples in EAN (except the special cases of Li<sup>+</sup> and Ca<sup>2+</sup>) the mean size and polydispersities are similar in EAN and water, demonstrating that no large aggregates are present. Inversely, the Li<sup>+</sup> and Ca<sup>2+</sup> samples in EAN contains some big aggregates, leading to a large polydispersity index.

For Li<sup>+</sup> in EAN, the DLS measurements are performed repeatedly over time (Figure 3.5). In the first weeks after its preparation, the Li<sup>+</sup> sample shows a very broad distribution of sizes, with an important population having a mean size around 12 nm that coexist with aggregates of larger size. The diameter of the main NP population has a much lower value than the results relative to the suspensions with other counterions, suggesting that in the Li<sup>+</sup> sample the smaller particles are redispersed first.

Two months later (result not shown), the aggregates in the Li<sup>+</sup> sample have vanished and the NP size distribution has become markedly narrower; the overall size of the dispersed objects remains much smaller than for the other suspensions. At the same time, despite a precipitate is still present at the bottom of the vial, the volume fraction of



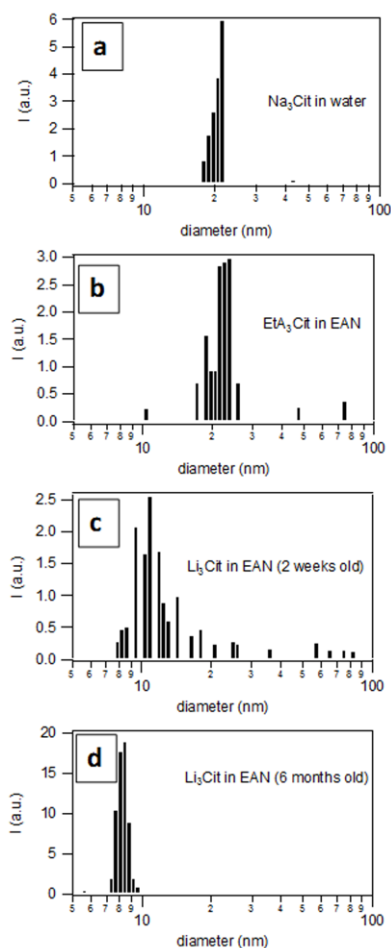


FIGURE 3.5: Size distribution (intensity weighted) obtained from Dynamic Light Scattering (DLS) of several dispersions: (a) initial aqueous dispersion of citrated maghemite nanoparticles with  $\text{Na}^+$  counterions, (b) citrated NP with  $\text{EA}^+$  counterion in EAN, (c) citrated NP with  $\text{Li}^+$  in EAN 15 days after preparation and (d) the same sample 6 months after preparation.

maghemite NP in the upper dispersed fraction has increased. All this is consistent with the redispersion of small particles and with the fact that large clusters, present in the first weeks after the preparation of the sample, are broken down over time. Figure 3.5 shows the strikingly different allure of the  $\text{Li}^+$  sample 6 months after its preparation. As for what concerns the other samples, no temporal evolution whatsoever has been observed.

It must be noted that, due to sample polydispersity, detailed analysis of DLS results is not straightforward. This is why we now concentrate our efforts on Small Angle Neutron Scattering (SANS).

### 3.4.2 Small Angle Neutron Scattering (SANS) Experiments

SANS experiments are performed at the LLB facility in Saclay, France (see Subsection 2.3.4 for the experimental conditions and Appendix B for details on the technique). The experiments are performed on the EAN dispersions of particles carrying all the aforementioned monovalent cationic counterions, plus the two aqueous samples with  $\text{Na}^+$  and  $\text{Li}^+$  as counterions. Figure 3.6 shows the scattered intensities  $I(Q, \Phi)$  for all these samples, normalized by the contrast (see Section B.4) and the volume fraction  $\Phi_{\text{SANS}}$  calculated from the scattering invariant (see Section B.5).

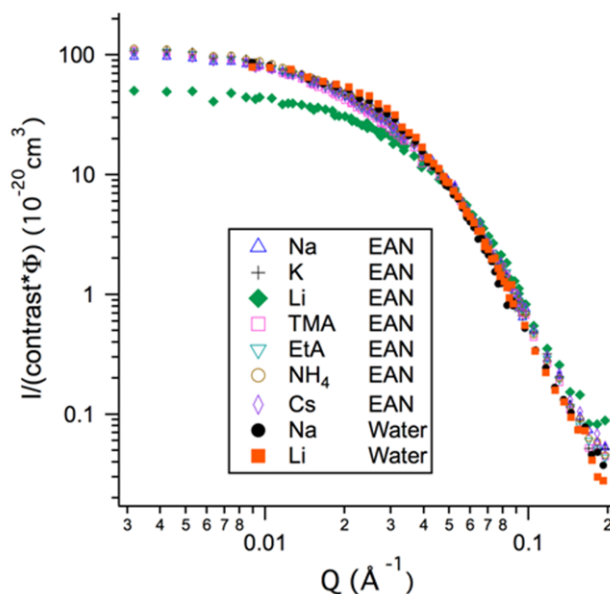


FIGURE 3.6: SANS scattered intensities  $I(Q, \Phi)$ , normalized by the contrast and the volume fraction  $\Phi_{\text{SANS}}$  calculated from the scattering invariant (listed in Table 3.4), for polydisperse maghemite NP dispersions in water and EAN.

It is immediately evident that the scattering curves for all counterions except  $\text{Li}^+$  are superimposed at large  $Q$  values and very close to each other in the low- $Q$  regime. Anyway, the calculated aggregation number being very close to 1 in all cases, there are virtually no aggregates in the samples. We can sort the results into three general cases, that we will review one by one:

1. Aqueous dispersions ( $\text{Na}^+$  and  $\text{Li}^+$  counterions);
2. EAN dispersions (all counterions except  $\text{Li}^+$ );
3. EAN dispersion with  $\text{Li}^+$  counterion.

### Aqueous dispersions

The data are treated with the software *Igor*, containing a vast library of structure and form factor functions provided by the NIST [104]. In water, the volume fraction is low enough and the ionic strength sufficiently high so that interparticle interactions are negligible. Hence, the whole curve is well fitted by the form factor alone, meaning that the systems are dispersions of individual, non-interacting particles. For the aqueous ferrofluids (curves *Na water* and *Li water* in Figure 3.6), the experimental intensity can be fitted by a form factor of polydisperse spheres with a lognormal distribution. Such fit is shown in Figure 3.7, where the sample *Li water* (orange squares) is representative of both aqueous samples.

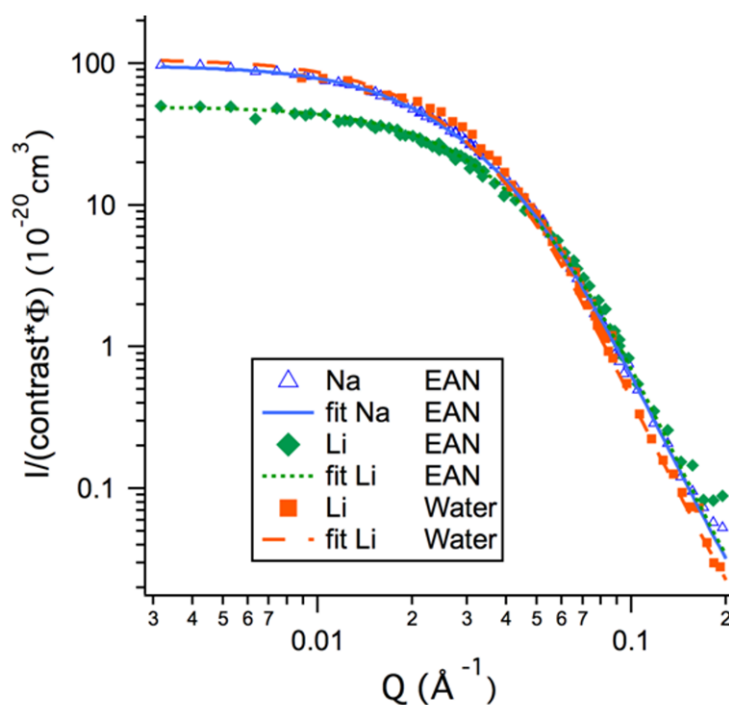


FIGURE 3.7: Fits of SANS experimental intensities for three representative cases: water samples (represented by  $\text{Li}^+$ ), EAN samples (where  $\text{Na}^+$  represents all counterions except  $\text{Li}^+$ ), and EAN samples with  $\text{Li}^+$  counterions.

The fit is performed with several parameters, of which some are imposed and others are free variables. The contrast equals  $5.65 \cdot 10^{-6} \text{ \AA}^{-2}$ , while the volume fraction  $\Phi_{SANS}$  is calculated from the scattering invariant and used as an input parameter for intensity modelling. Therefore the independent fitting parameters are only the median particle diameter  $d_0$  and the polydispersity  $\sigma$ . The values given in Table 3.5 are consistent with

the size distribution extracted from the magnetization measurements ( $d_0 = 7$  nm;  $\sigma = 0.39$ ).

<b>Results from SANS on Citrated NP Dispersions in EAN</b>				
Counterion	$\Phi_{FAAS}\%$	$\Phi_{SANS}\%$	$d_0$ (nm)	$\sigma$
Na <sup>+</sup>	0.7	0.69	$5.2 \pm 0.1$	0.43
Li <sup>+</sup>	0.3	0.32	$4.6 \pm 0.1$	0.40
K <sup>+</sup>	0.9	0.75	$5.2 \pm 0.1$	0.43
Cs <sup>+</sup>	0.8	0.69	$5.2 \pm 0.1$	0.43
NH <sub>4</sub> <sup>+</sup>	0.8	0.73	$5.2 \pm 0.1$	0.43
EA <sup>+</sup>	0.7	0.69	$5.2 \pm 0.1$	0.43
TMA <sup>+</sup>	0.7	0.64	$5.2 \pm 0.1$	0.43
Na <sup>+</sup> (W)	1.3	1.20	$5.6 \pm 0.1$	0.44
Li <sup>+</sup> (W)	1.2	1.20	$5.6 \pm 0.1$	0.44

TABLE 3.5: Results from SANS experiments on dispersions of citrated maghemite NP in EAN (plus two references in water). For each cationic counterion, the table shows: NP volume fraction determined in the supernatant by FAAS analysis ( $\Phi_{FAAS}$ ) and from SANS experiments ( $\Phi_{SANS}$ ); NP median diameter and polydispersity ( $d_0$  and  $\sigma$ ) obtained by fitting the SANS spectra with a lognormal distribution. See text for details.

### EAN dispersions (all counterions except Li<sup>+</sup>)

In Figure 3.7, the fits for all ions except Li<sup>+</sup> are represented by the sample *Na EAN* (blue triangles), since all the other scattering curves are superimposable to this one. These scattering curves are fitted by the same method applied to water samples, only this time the value of the contrast is  $3.19 \cdot 10^{-6} \text{ \AA}^{-2}$ .

The size distributions thereby determined (and shown in Table 3.5) are characterized by values similar to the aqueous samples, meaning that the particles are not modified after transfer to the IL. For all samples, the NP volume fractions obtained from FAAS analysis  $\Phi_{FAAS}$  and from the invariant of diffusion  $\Phi_{SANS}$  are in good agreement. For all counterions, the values compare very well with the maximum expected value for NP, equal to 0.8% in the case of total redispersion.

### EAN dispersion with Li<sup>+</sup> counterion

Finally, for the Li<sup>+</sup> based dispersion, the structure is slightly different. The diameter and the polydispersity extracted from the SANS data are lower than for the other counterions. Such result proves that, upon transfer from water to EAN, in the case of Li<sup>+</sup> the smaller particles are more easily dispersed than larger ones (which remain in the

flocculated fraction). This is consistent with the DLS results, which also showed that the dispersed particles were the smaller ones.

### 3.5 Conclusion

The set of experiments discussed in this Chapter enlightens the huge influence of the nature and structure of the interface between the particles and the solvent. The results from macroscopic observation, DLS and SANS experiments demonstrate that both the charge of the particles and the associated counterions govern the ability to obtain a good colloidal dispersion either in the pure IL or in water/IL mixtures. The important point is that our results demonstrate the possibility to obtain stable colloidal dispersions of maghemite nanoparticles in the ionic liquid EAN even in the absence of steric stabilizers such as polymers or surfactants, despite the fact that other authors reported the impossibility of obtaining such systems [11].

One first conclusion that can be drawn is that it is necessary to have a charged interface in order to obtain colloidal stability in pure IL or IL/water mixtures. This is particularly revealed by the difference of behavior between uncharged particles at the PZC and particles charged thanks to a coating of citrate anions at the same pH. Uncharged particles are not stable in EAN or mixtures, while the dispersion of citrate-coated particles is easily achieved. The fact that citrated NP lead to stable dispersions with a pH around 7 in EAN, whereas particles at the PZC cannot be redispersed, indicates that citric acid remains linked to the surface and is responsible for stabilization. At pH 7, citric acid is indeed deprotonated in EAN.

It should be noted that the EAN/water mixtures cover a wide range of situations. Indeed, at  $\phi_{EAN} = 20\%$ , the solvent can be regarded as a very concentrated aqueous solution of salt (around  $2 \text{ mol L}^{-1}$ ), while symmetrically it becomes an IL containing water for high EAN contents. The IL thus strongly modifies the solid/liquid interface also when it is not pure, and dispersions in mixed solvents are possible in various situations depending on the appropriate choice of surface conditions, despite the high salinity at large water content or the presence of water at large NEA content.

Finally, the structure of the interface (in terms of surface charge and/or ion specificity) has a huge effect on the colloidal stability, as revealed by the difference of behavior depending on the choice of the counterion (reported in acidic medium, with a difference between  $\text{NO}_3^-$  and  $\text{ClO}_4^-$ , and in neutral medium, with the peculiar case of  $\text{Li}^+$ ). The

main remarkable observation is the very slow evolution of some of the samples, over days or weeks after the preparation, either from good dispersions towards flocculated samples, or from flocculated samples towards dispersions. Let us emphasize that the latter situation, *i.e.*, redispersion, is never observed in water. Such slow evolutions indicate that the study of colloidal dispersions in ILs and water/ILs mixtures over a long time is absolutely needed if one wants to properly understand the mechanisms of stabilization.

At this stage, we are aware of the crucial role of the solid/IL interface structuration, but we do not yet know which type of structure we are actually facing and what is its origin. If we assume that the IL forms structured layers in a “... anion ... cation ... anion ...” fashion at the surface of the NP, as most of the current literature hypothesizes, we may be led to believe such structuration to depend on the charge of the surface. The question that arises spontaneously is then whether the charge on the NP surface is represented by citrate, hence negative, or by a first layer of counterions. In water, a first layer of condensed counterions is present in front of the solid charge (the Stern layer); upon transfer to EAN (or its mixtures with water) this could evolve in two distinct ways: (i) the number of charges on the particle’s surface may be modified, or (ii) a substitution of the counterions by the IL ion of same charge (ethylammonium) may occur, depending on the surface/ion interactions. It is clear that, depending on the surface charge, the structuration mechanism of the IL at the interface may differ.

We then finish this Chapter with some new questions:

- Do the counterions of the surface charge stay close to the surface itself, or are they replaced by the IL’s ions, which are much more concentrated?
- Where does the peculiar, ion-specific behaviour of  $\text{Li}^+$  citrate dispersions stem from? Does it originate from the position of the cation at the interface, or from the very properties of the ions (for example, its high charge density leading to a high degree of solvation)?
- What is the role of water on the structuration of the NP/IL interface?
- What are the interactions between particles through an IL medium, and which parameters do they depend on?

In the next Chapter, we will try to get a deeper insight into the maghemite/EAN systems by focusing on citrated NP dispersions with low polydispersity.

## Chapter 4

# Dispersions of Size-Sorted Maghemite Nanoparticles in the IL Ethylammonium Nitrate

### Contents

---

<b>4.1</b>	<b>Introduction</b>	<b>96</b>
<b>4.2</b>	<b>Preparation and Chemical Analysis of the Samples</b>	<b>97</b>
<b>4.3</b>	<b>Evolution During the Preparation of the Samples: the Special Case of Lithium</b>	<b>102</b>
<b>4.4</b>	<b>Effect of NP Size and Concentration</b>	<b>104</b>
<b>4.5</b>	<b>Small Particles (7 nm): Effect of the Counterion</b>	<b>110</b>
4.5.1	Dilute Regime	110
4.5.2	Concentrated Regime	111
<b>4.6</b>	<b>Large Particles (11 nm): Effect of the Counterion</b>	<b>118</b>
4.6.1	Dilute Regime	118
4.6.2	Concentrated Regime	119
<b>4.7</b>	<b>Discussion on the Effect of the Counterions on Both Sizes</b>	<b>128</b>
<b>4.8</b>	<b>Effect of Water Content</b>	<b>131</b>
<b>4.9</b>	<b>Conclusion</b>	<b>137</b>

---

## 4.1 Introduction

The preliminary screenings on the  $\gamma$ -Fe<sub>2</sub>O<sub>3</sub>/EAN colloidal systems described in the previous Chapter have evidenced the importance of the interface's structuration, in terms of structural charge and associated counterions, on the colloidal stability. We are, however, left with many questions concerning the composition of the interface and its role on the interparticle interactions. In the present Chapter, we choose to focus on citrated NP, which appeared to represent the most stable systems in EAN. We now switch to the utilization of NP dispersions with a narrow size distribution, and we compare the behaviour of particles with different diameters (7 nm and 11 nm, respectively; see Subsection 2.2.2 for the experimental size-sorting procedure and the characteristics of the particles it yields). Also, varying the size allows a fine tuning of the attractive part of the interaction potential, since the magnetic dipolar attraction grows with the volume of the particles. For each size, the particles are functionalized with citrate; we compare three cationic counterions for citrate: sodium is chosen because of its common use in water and as a representative of the other monovalent cations (since in the previous study, in Chapter 3, they all appeared to behave in the same way); lithium, for its unusual behaviour observed in the polydisperse  $\gamma$ -Fe<sub>2</sub>O<sub>3</sub>/EAN systems; and finally ethylammonium, which represents the same cation as the IL solvent. The latter counterion is to be used as a sort of reference, since in this case there is only one type of cation that may be found at the solid/liquid interface.

Based on the previous results, we look deeper into the peculiar behaviour of aggregate redispersion in the Li<sup>+</sup> samples. Also, we look into the possibility of obtaining more concentrated dispersions ( $\Phi > 1\%$ ) for each particle size. Therefore, we initially compare the consequences of varying at the same time the size and concentration of the nanoparticles: indeed, we show that the effects due to the different particle sizes become especially evident at high NP volume fraction. Finally, we address the role of water in the EA<sup>+</sup> and Na<sup>+</sup> systems by dispersing the nanoparticles in EAN-water mixtures.

All the samples mentioned so far are studied by means of optical microscopy, FAAS, static SAXS and SANS, and dynamic magneto-optic birefringence experiments. In order to discriminate between the two sizes, from now on we will use the acronyms "SSC" and "CC" to refer to, respectively, small (7 nm) and large (11 nm) nanoparticles.



## 4.2 Preparation and Chemical Analysis of the Samples

For both sets of particles, SSC (small) and CC (large), the starting dispersions in EAN are prepared as described previously (see Protocol 2 described in Subsection 2.2.7), with a NP concentration  $\Phi \approx 1\%$ . Next, for each of the three counterions and each NP size, series of growing NP concentration are prepared by centrifuging the dilute dispersions, as represented in Figure 4.1, in order to reach concentrations in the range  $1\% < \Phi < 8\%$ . In the case of  $\text{Li}^+$ , only the dispersed fraction of the starting suspensions is sampled. Centrifugation is carried out at  $5000\times g$  for 24–48 hours, using 10 kD Amicon Ultra centrifugal filter units by Millipore. The concentrated fraction remains in the filter while the separated solvent is found on the bottom of the tube. This process is quite slow because of EAN's viscosity (for a comparison, let us mention that performing the same procedure on aqueous ferrofluids requires 10–20 minutes). Also, it is sometimes difficult to assess at which point the operations of centrifugation will reach the desired NP volume fraction  $\Phi$ .

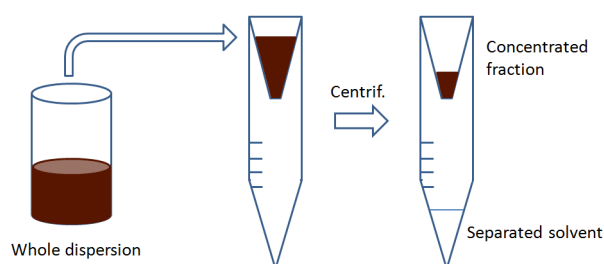


FIGURE 4.1: Separation of the nanoparticles from the IL solvent by centrifugation with filter units. See text for details.

### Analysis of the Free/Bound Equilibrium of Citrate

Dispersions of citrated maghemite NP are characterized by an equilibrium between the citrate molecules that are adsorbed on the surface and those freely dissolved in the bulk dispersing phase. In aqueous ferrofluids, the concentration of free citrate can be determined by means of conductivity measurements in the whole dispersion, since the contribution of the charged nanoparticles to the total conductivity of the system is considered negligible because of their comparatively large size. Unfortunately, this method cannot be transposed to the EAN-based systems due to the ionic and conducting nature of the solvent. Other common techniques used in water are variants of chromatography

with different detection systems; however, conductivity-based detection is not applicable for the above mentioned reason, while indirect UV detection is not applicable in the presence of EAN due to the very strong absorption of this IL at such wavelength. Also, detection by refractive index measurement is hindered by the very similar indexes of citrate and EAN (1.374 for sodium citrate, 1.454 for EAN [56]).

Nevertheless, since the process of concentrating described above yields the separation of the IL solvent from the particles, this enables us to analyse the two phases separately. The concentration of several carboxylic acids in aqueous solutions can be determined by a spectrophotometric method involving the ferric 5-nitrosalicylate (Fe-5NSA) complex [105]. At pH values between 2.6 and 2.8, this complex has an absorption maximum in the visible range at 492 nm. The addition of organic acids, among which citrate, destroys the (Fe-5NSA) complex due to the higher complexation constant of Fe(III) with carboxylates. The absorbance at 492 nm thus decreases linearly with the concentration of citrate in the sample. Although the linearity range is quite narrow ( $0\text{--}5 \cdot 10^{-4} \text{ mol L}^{-1}$ ), this method can be used to determine the concentration of citrate in an unknown sample when a calibration curve is properly built.

We have applied this method to our systems in order to determine the concentration of citrate in the solvent separated from the particles by centrifugation. Since our solvent is EAN, and dilutions are necessary to fit the linearity range of citrate concentration for analysis, we verify the effect of the presence of the IL on the (Fe-5NSA) complex by preparing calibration curves after doping the aqueous complex with a constant quantity of EAN. For EAN volume contents of 5 vol%, 10 vol%, 20 vol% and 30 vol%, the absorption is decreased by the presence of the IL, but the Absorbance *vs.* [Cit] curves remain linear in the same range as in water. As an example of such results, we show the UV-vis absorption spectra for the Fe-5NSA complex in the presence of 5 vol% EAN and growing concentrations of citrate in Figure 4.2. The relative calibration curve obtained by plotting the absorbance at 492 nm as a function of [Cit] is shown in Figure 4.3.

The analysis on the solvent separated from a  $\text{Na}_3\text{Cit-NP/EAN}$  dispersion yields  $0.95 \cdot 10^{-2} \text{ mol L}^{-1}$  free citrate, which is not far from the average value of  $1.3 \cdot 10^{-2} \text{ mol L}^{-1}$  found in similar aqueous dispersion (measured by conductivity). However, this spectrophotometric method presents a few inconveniences. Indeed, when the particles are separated from the solvent, some free iron ions (which can be present if the starting aqueous ferrofluid has not been dialysed) or very small particles may pass through the

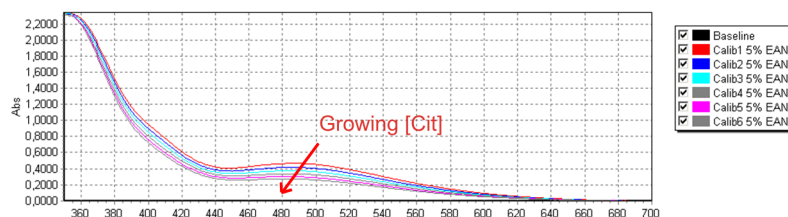


FIGURE 4.2: UV-Vis absorption spectra for the FeNSA-5 complex in the presence of growing citrate concentration and constant 5 vol% EAN. As [Cit] increases (see values in the abscissa of Fig. 4.3), the absorption maximum at 492 nm decreases.

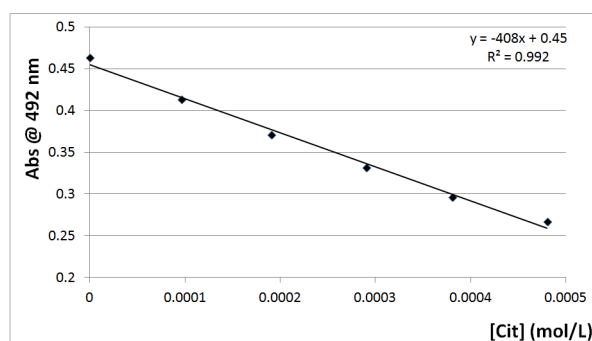


FIGURE 4.3: Calibration curve for the Fe-5NSA complex in the presence of growing citrate concentration and 5 vol% EAN, obtained by plotting the absorbance at 492 nm as a function of the concentration of citrate.

filter and remain in the separated EAN. The iron content in such solvent has been determined to vary between 0 and  $1 \cdot 10^{-3} \text{ mol L}^{-1}$ . Ferric ions displace the Fe-5NSA complex equilibrium and introduce a bias in the measurements, while particles strongly modify the absorption spectra, as shown by the grey trait in Figure 4.4, so that the absorption maximum at 492 nm disappears. This basically means that in our real samples such method, despite its attractiveness, cannot always be applied.

We have recently discovered the existence of an alternative method based on a turn-on fluorescent indicator for citric acid with micromolar sensitivity [106]. This method will be tested on EAN dispersions in the near future.

### Localization of the Counterions

In aqueous dispersions, a fraction of the cationic counterions introduced with citrate (namely  $\text{Na}^+$  and  $\text{Li}^+$ ) are located at the surface of the highly negatively charged particles. On the other hand, after the transfer of the particles to the ionic liquid EAN, there is no *a priori* certitude on whether the counterions will remain next to the surface or, on the contrary, dissolve in the bulk ionic liquid to be replaced by EAN's cation,

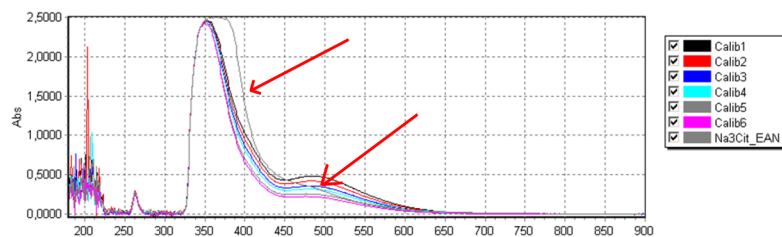


FIGURE 4.4: UV-Vis absorption spectra for the FeNSA-5 complex in the presence of growing citrate concentration, compared to a sample of unknown [Cit] containing nanoparticles. The red arrows point at the modified shape of the absorption curve and the disappearance of the absorption maximum at 492 nm.

ethylammonium, at the NP surface. Indeed,  $\text{EA}^+$  is present in the overwhelming concentration of  $11 \text{ mol L}^{-1}$  in EAN, which makes it about 100 times more concentrated than the  $\text{Li}^+$  and  $\text{Na}^+$  counterions introduced with citrate. Obviously, this uncertainty about the position of the cationic counterions does not exist when  $\text{EA}^+$  is also the initial counterion of citrate. Therefore, we proceed to analyse the distribution of the counterions  $\text{Na}^+$  and  $\text{Li}^+$  in our EAN dispersions.

The concentration of Na and Li elements is determined by Flame Atomic Absorption Spectroscopy after degradation of the particles in acidic medium. Such concentration is measured in the whole starting suspension (denoted  $[\text{X}^+]_{\text{tot}}$ , where  $\text{X}^+$  is  $\text{Na}^+$  or  $\text{Li}^+$ ), in the concentrated NP fraction and in the separated IL fraction. The latter, denoted  $[\text{X}^+]_{\text{free}}$ , yields the concentration of cationic counterions not bound to the NP, and is considered as representative of the concentration of free cation in the dispersion (assuming that the centrifugation procedure did not cause any displacement of the free/bound equilibrium).

The material balance of cations before and after separation is verified to confirm that no ions remain trapped in the centrifugal filter. In the case of large particles, the process of concentration gives place to a phase separation (discussed later in 4.4), that is, the concentrated NP fraction in the filter actually contains two phases: one liquid and dilute, the other more concentrated and very viscous, both black, the volumes of which cannot be measured directly. Therefore, in order to perform the material balance, we first determine the volume fractions of NP in these two phases by SQUID magnetization measurements, which yield the most accurate  $\Phi$  values especially in the case of the viscous phase. Since the total volume of the sum of the two phases is known, we are then able to calculate the volumes of each by applying the lever rule for thermodynamic phase separations, and therefore verify the material balance in these samples.

Finally, the concentration of cationic counterion that remains near the NP surface is obtained by the difference  $[X^+]_{NP} = [X^+]_{tot} - [X^+]_{free}$ ; when this value is related to the surface of the particles (taking into consideration the volume fraction and the size polydispersity), we obtain cation densities of the order of  $1.6 \pm 0.4$  cations/nm<sup>2</sup>. These values are not far from the maximal charge in water for citrated NP dispersions (around 2 charges/nm<sup>2</sup>). This result allows us to state that part of the counterions of citrate do remain at the solid/liquid interface, and we can expect them to play a role in determining the microstructure of the suspensions.

### **Residual Water Content after Lyophilization**

The concentration of residual water in lyophilized EAN dispersions is evaluated by performing a Karl Fischer coulometric titration on the separated EAN. The remaining water content in the final dispersions is estimated in the order of 1 wt%, assuming that the quantity of water determined in the particle-free solvent is representative of that in the whole dispersion.

### 4.3 Evolution During the Preparation of the Samples: the Special Case of Lithium

We are now familiar with the fact that maghemite nanoparticles coated with lithium citrate are never fully redispersed in EAN. In the dilute samples, a dispersed fraction is always in equilibrium with a precipitate, and such equilibrium becomes stable over a few weeks after the preparation of the suspensions. The process had already been studied by means of DLS on a polydisperse product (see 3.4.1).

However, when less polydisperse particles are used, the evolution of the dispersion is not exactly the same for the two NP sizes, since the large particles appear to reach the kinetic equilibrium sooner than the small ones. Therefore, for both NP sizes, the dispersed fraction is sampled repeatedly over a period of several weeks, so that the specimens thereby obtained represent an “arrested” dispersion, capable of taking a “snapshot” of the  $\text{Li}^+$  products during their temporal evolution. Such specimens are studied by means of SAXS experiments, which allow to follow the evolution of these dispersions. Figures 4.5 and 4.6 show the results of these measurements for both the SSC (small) and CC (large) particles in EAN, compared with the form factor  $P(Q)$  (obtained as described in Appendix B, Section B.7) for each size. We can notice indeed that the temporal evolution of the two samples is completely different.

For the 7 nm particles (SSC), the quantity of dispersed NP grows with time, as shown by the increasing volume fraction in the supernatant (from 0.013% to 0.63%). Over the course of two weeks, the supernatant has reached the maximum NP concentration, corresponding to about 70% of all the NP. The scattering curves prove the existence of large NP aggregates in the first days after the preparation of the sample, with  $R_G > 40$  nm (the actual size cannot be calculated in the available Q-range). The size of the clusters becomes smaller over the course of a few weeks. The scattering curve for the final product is never superimposed to the form factor, due to the persistence, in such sample, of small aggregates with  $N_{ag} \approx 1.6$  (as demonstrated in Subsection 4.5.2).

As for what concerns the large particles, their concentration in the supernatant grows more slowly, but to a lesser extent (from 0.046% to 0.16% in 8 weeks), reaching only about 20% of the maximum possible  $\Phi$ . This is in agreement with the fact that the attempt to reach higher concentrations results in phase separation (this is discussed later in 4.4). The scattering curves in Figure 4.6 are all very similar, showing that the

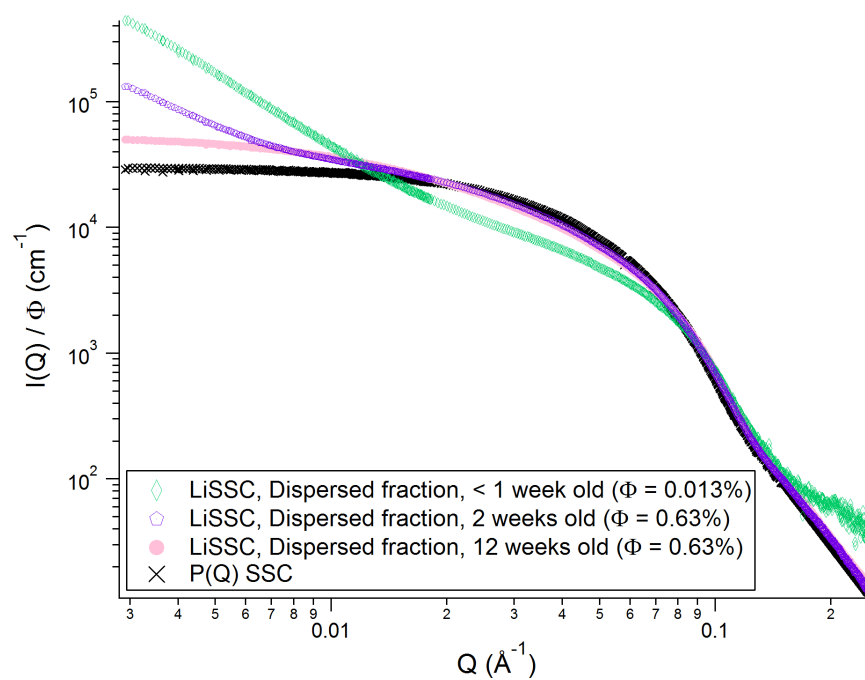


FIGURE 4.5: Effect of ageing on the redispersion equilibrium of  $\text{Li}^+$  dispersions in EAN (small particles).

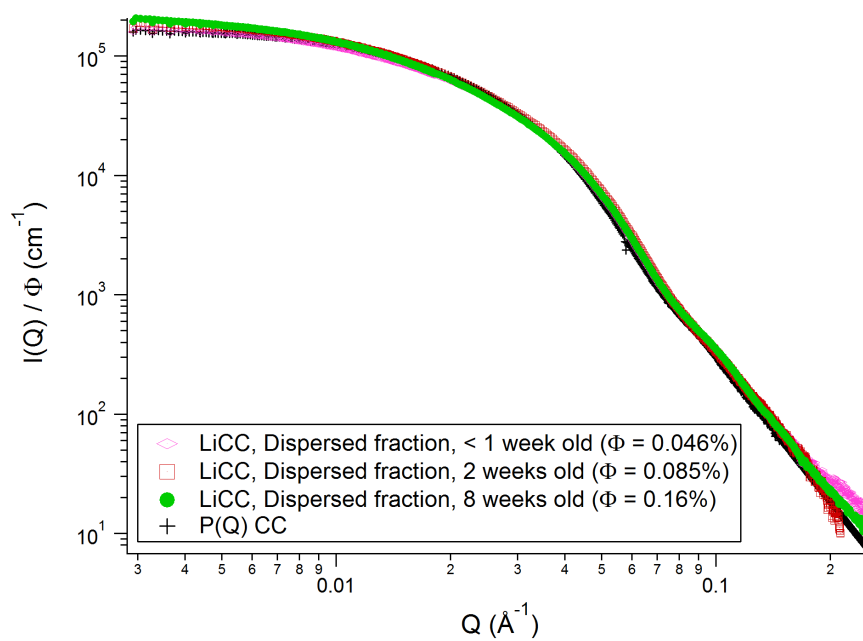


FIGURE 4.6: Effect of ageing on the redispersion equilibrium of  $\text{Li}^+$  dispersions in EAN (large particles).

same type of objects are present during the entire evolution period. The calculation of  $R_G$  from the Guinier plot yields  $14 \pm 1$  nm. For a polydisperse system, we expect  $R_G \approx R_H \approx 2.4 \times R_0$  for  $\sigma = 0.25$  [102, 107]. Hence, the value of  $R_G = 14$  nm is consistent with the redispersion of single nanoparticles having  $R_0 = 5.5$  nm. The final product (8 weeks old) shows a slight increase of the  $I(Q=0, \Phi)$  value with respect to the form factor, due to the attractive interactions between particles. All this suggests that the larger clusters formed in the LiCC samples are too big to return in suspension, and not fragile enough to be broken into smaller, redispersible aggregates; such clusters hence remain in the precipitate.

These results show that the presence of a precipitate in the Li samples is not dependent on the polydispersity of the NP size, since similar effects are observed with both polydisperse (Chapter 3) and quasi-monodisperse samples. It is an ion-dependent effect which reflects the cluster-forming tendency of Li-covered maghemite NP in the ionic liquid EAN (or during the transfer from water to EAN). The type of clusters constituting the precipitate depends on the size of the particles and thus on the attractive (van der Waals and magnetic dipolar) interactions between the particles: small clusters are formed in the case of 7 nm particles, which are also fragile and are broken down into smaller objects over time; while the larger NP, for which the attractive interactions are stronger, give rise to big clusters that precipitate immediately, and only single nanoparticles can be redispersed.

## 4.4 Effect of NP Size and Concentration

In the previous Section, we described the temporal evolution of  $\text{Li}^+$  samples up to reaching their kinetic equilibrium. Such equilibrium represents the moment from which the dispersions can be further investigated since their evolution has stopped. We can then move to characterizing the suspensions in their final state in order to evaluate their colloidal stability.

As explained earlier, for each size and counterion, series of growing NP volume fraction are prepared. For the SSC lot (small particles, 7 nm), most of the samples are constituted by homogeneous, single-phase dispersions, of growing viscosity as the NP content grows higher. Exceptions are the following:



- EA<sup>+</sup> dispersions up to  $\Phi = 2.86\%$  are stable, even though the observation through optical microscopy reveals the presence of very few large objects in suspension. At higher concentrations, though, centrifugation seems to destabilize the samples, since a NP concentration gradient is formed along the vertical axis of the tube. This is not a phase separation, since the samples revert to a normal state without concentration gradient over some days or after stirring. These are the only samples for which this behaviour was observed.
- The entire Li<sup>+</sup> series is stable against centrifugation and in the absence of a magnetic field. However, when a magnetic field is applied, the two most concentrated samples ( $\Phi = 5.07\%$  and  $\Phi = 7.34\%$ ) are destabilized, as evidenced by the formation of elongated needles of liquid concentrated phase (Figure 4.7) which relax and disappear when the field is removed.

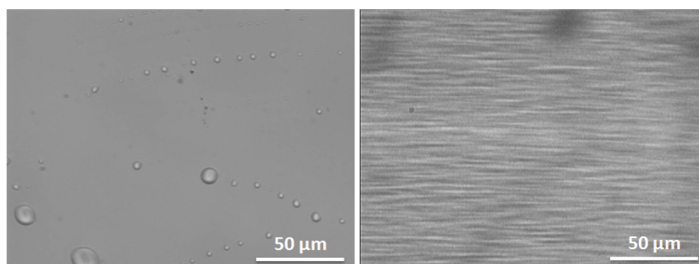


FIGURE 4.7: Optical microscopy image for a dispersion of citrated maghemite NP in EAN (with Li<sup>+</sup> as counterion and  $\Phi = 5.07\%$ ). Left: in the absence of an applied magnetic field, the sample does not show any peculiar features (the drops are air bubbles trapped near the glass surface). Right: with an applied magnetic field ( $H \simeq 160 \text{ kA m}^{-1}$ ), a reversible phase separation is induced, identifiable by the formation of elongated needles of liquid concentrated phase.

Table 4.1 summarizes all the samples prepared for the SSC lot, comparing the volume fraction obtained by FAAS and by SANS (*via* the calculation of the scattering invariant). It can be noticed that the two values are generally in good agreement. The EA<sup>+</sup> samples of  $\Phi > 2.86\%$  (mentioned above) are not included, since the presence of a concentration gradient, sometimes resembling a phase separation, made it difficult to perform reliable FAAS and SAS analyses.

The behaviour of CC samples (large particles, 11 nm) is very different. Upon concentration, these systems encounter a phase separation which is in most cases quite evident even by bare eye observation. The separated fraction in the centrifugal filter is actually split in two parts: the upper part is a dilute suspension (usually with  $\Phi \leq 1\%$  for all

**Concentration of NP/EAN Dispersions: Small Particles (SSC)**

Counterion	$\Phi_{FAAS}\%$	$\Phi_{SANS}\%$
Na <sup>+</sup>	1.00	0.85
Na <sup>+</sup>	4.38	5.50
Na <sup>+</sup>	8.32	7.67
EA <sup>+</sup>	0.50	0.62
EA <sup>+</sup>	3.70	2.86
Li <sup>+</sup>	0.55	0.57
Li <sup>+</sup>	1.88	1.63
Li <sup>+</sup>	5.34	3.91
Li <sup>+</sup>	6.16	5.07
Li <sup>+</sup>	7.44	7.34

TABLE 4.1: Concentration of NP/EAN dispersions: small particles (SSC) with three different counterions.  $\Phi_{FAAS}\%$  = volume fraction obtained by FAAS analysis of Fe;  $\Phi_{SANS}\%$  = volume fraction obtained from SANS data through the calculation of the scattering invariant.

counterions), while the lower one is a very viscous, almost gel-like concentrated dispersion ( $\Phi \geq 15\%$  for all counterions). Figure 4.8 shows a photo of a SANS sample holder containing a CC sample with EA<sup>+</sup> as counterion. If the cell is observed against daylight, the coexistence of a dilute phase (red, upper part of the cell) and a concentrated phase (black, on the bottom) is quite evident. When the concentrated phase is separated from the dilute phase and deposited on a magnet, it shows the typical peaks of concentrated ferrofluids.

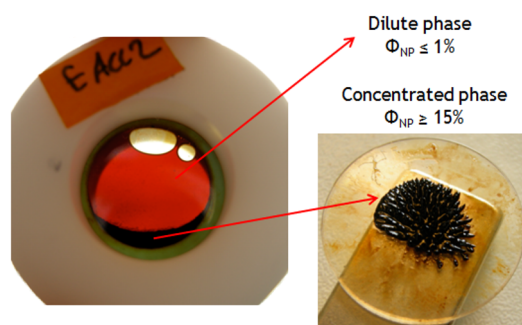


FIGURE 4.8: Photo of a SANS sample holder showing the coexistence of a dilute and a concentrated phase upon gas-liquid phase separation in a EACC sample.

Figure 4.9 shows an optical microscopy photograph of a NaCC sample that underwent such phase transition. In the absence of an external magnetic field, we are able to distinguish the clear dilute phase (in the background) and the large pieces of concentrated phase, coexisting in the same sample. When a magnetic field  $H$  is applied, the

existing concentrated phase aligns along the direction of  $H$ , and new concentrated phase is (reversibly) formed due to the increased attractive interactions.

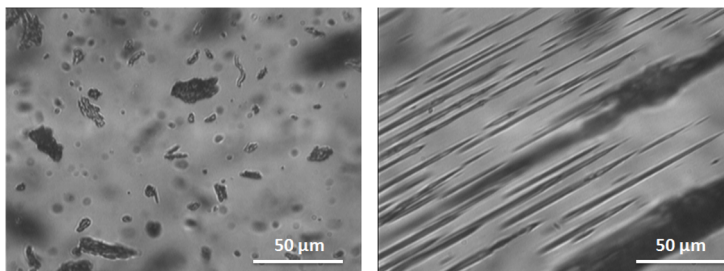


FIGURE 4.9: Optical microscopy photograph showing: (left) the coexistence of dilute and concentrated phases from a phase-separated NaCC/EAN dispersion; (right) the same sample upon application of a magnetic field ( $H \simeq 160 \text{ kA m}^{-1}$ ).

The phenomenon observed in the CC dispersions is a spinodal decomposition due to a colloidal gas-liquid transition, which is typically found in colloids interacting *via* short-range repulsions and long-range attractive forces [40]. Indeed, the larger size of the particles induces more intense attractive forces between them. Figure 4.10 depicts a schematic  $\Pi$  *vs.*  $\Phi$  (osmotic pressure *vs.* NP volume fraction) phase diagram for a colloidal system characterized by the presence of both attractive and repulsive interactions: our CC samples find themselves in the two-phase area corresponding to the coexistence of gas and liquid phases. From now on, we will refer to the dilute and concentrated phases, respectively, as “gas phase” and “liquid phase”.

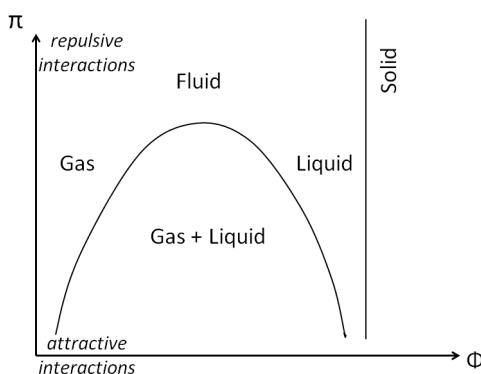


FIGURE 4.10: Schematic  $\Pi$  *vs.*  $\Phi$  (osmotic pressure *vs.* NP volume fraction) phase diagram for a colloidal system characterized by the presence of both attractive and repulsive interactions.

Following the separation of the suspension in two phases, the particles of different sizes (since our samples have low but not zero polydispersity) are supposed to be accommodated in one or the other phase due to different interactions existing between

them [40], hence the “gas” phase contains the fraction of slightly smaller particles and the “liquid” phase contains the fraction of slightly larger particles from the original CC lot. Nevertheless, the size difference between the particles in the two phases is basically negligible: the size distributions obtained from the magnetization curves for a one-phase dispersion (with  $\text{Li}^+$  counterions), and for the colloidal gas phase resulting from its spinodal decomposition, can both be fitted by the same lognormal function with parameters  $d_0 = 11$  nm and  $\sigma = 0.2$ . Such figures are slightly different from the parameters obtained in water, due to the fact that  $\text{Li}^+$  dispersions in EAN always have a precipitate at the bottom. So finally, the gas-liquid phase separation does not alter the size distributions of the particles in the two phases in a significant way.

The independent analysis of each of these two phases is quite challenging, due to the physical difficulty of separating the colloidal gas from the liquid phase without polluting one with the other. They are both black, and it is difficult to sample inside the centrifugal filter; the dilute gas phase can be sampled with a pipette or a syringe (but bits of concentrated phase may remain trapped inside the liquid), while the use of a spatula is mandatory for the concentrated phase. The latter is indeed glue-like, very viscous and difficult to manipulate.

Such technical problems have an impact on several things. For example, two different sets of SAS experiment performed on the CC samples with  $\text{Li}^+$  counterions (LiCC) show a tiny evolution over a period of one year. However, it is not easy to evaluate whether the phases were sampled in the exact same way during the two different experiments, and we are left with the doubt that the (however slight) differences we observe may be due not to temporal evolution, but to different degrees of pollution of one phase with the other. Another point concerns the incertitude on the volume fraction (obtained from FAAS analysis or from the scattering invariant), which varies depending on the degree of purity of the phase in study.

Table 4.2 summarizes all the samples prepared and studied with the respective NP volume fractions (or their range, in the case of multiple samples separating into a colloidal gas and a concentrated liquid phase) obtained by FAAS and SAXS. Large error bars are to be taken into account in the determination of  $\Phi_{\text{SAXS}}\%$ . Indeed, filling a SAXS sample holder with one of these products is not a straightforward task, due to the nature of the SAXS sample cells (with windows made of soft mica sheets, that can be deformed when in contact with a concentrated phase). Therefore, the thickness of the sample may

vary from the nominal thickness indicated by the chosen spacer.

Also, for some of the most concentrated samples, the  $I(Q, \Phi)$  scattering curve rises steeply in the low- $Q$  region (due, for example, to a high degree of aggregation), which makes the calculation of the scattering invariant not possible [108]. The value of  $\Phi$  is then obtained by considering the necessary factor to force the superposition between the  $I(Q, \Phi)$  curve of the sample and the  $I(Q, \Phi)$  curve of a standard product of known, reliable  $\Phi$ . Such  $\Phi$  values are marked by an asterisk in Table 4.2.

<b>Concentration of NP/EAN Dispersions: Large Particles (CC)</b>		
Counterion (type of phase)	$\Phi_{FAAS}\%$	$\Phi_{SAXS}\%$
Na <sup>+</sup> (one-phase)	0.99	0.63
Na <sup>+</sup> (one-phase)	2.27	1.35
Na <sup>+</sup> (gas phase)	0.30–1.23	0.31–0.75
Na <sup>+</sup> (liquid phase)	7.67	13.7–40*
EA <sup>+</sup> (gas phase)	0.28–1.19	0.30–0.44
EA <sup>+</sup> (liquid phase)	0.96–17.8	7.58–55*
Li <sup>+</sup> (one-phase)	0.17	0.16
Li <sup>+</sup> (gas phase)	0.38–0.70	0.14–0.20
Li <sup>+</sup> (liquid phase)	15.9–22.3	18.0–45*

TABLE 4.2: Concentration of NP/EAN dispersions: large particles (CC) with three different counterions.  $\Phi_{FAAS}\%$  = volume fraction obtained by FAAS analysis of Fe;  $\Phi_{SAXS}\%$  = volume fraction obtained from SAXS data through the calculation of the scattering invariant. (\* = values not obtained from the invariant, see text)

## 4.5 Small Particles (7 nm): Effect of the Counterion

### 4.5.1 Dilute Regime

We now focus on the small particles (SSC, 7 nm) and the effect of the three different counterions for citrate on the dilute and concentrated dispersions. A deeper characterization of the suspensions at the nanoscopic scale is performed by means of small angle scattering techniques and magneto-optic birefringence experiments. Due to the slow redispersion process,  $\text{Li}^+$  samples are allowed to rest for at least 4 weeks after their preparation, before any structural analysis is undertaken. First SANS and then SAXS experiments are carried out on these kinetically stable dilute dispersions, with 1 month of distance between the two sets of measurements. The comparison between the results from the two sets of data shows that there was no structural evolution in the dilute samples over 1 month. For this reason, here we show the results from SAXS only; however, the NP volume fractions obtained from the SANS invariant are used throughout the entire Section thanks to their better reliability in the case of concentrated samples. This simply stems from the better controlled thickness in the preparation of SANS samples holders.

Figure 4.11 presents the structure factors  $S(Q, \Phi)$  obtained from SAXS data for the three dilute dispersions corresponding to  $\text{Na}^+$ ,  $\text{Li}^+$  and  $\text{EA}^+$  counterions. The curves are very much alike, and a closer look gives us information on the structure of the dispersions. In all of the three cases,  $S(Q=0, \Phi) > 1$  reflects the existence of attractive interactions, while the peak around  $0.1 \text{ \AA}^{-1}$  corresponds to a characteristic nearest-neighbour distance of 6.3 nm, close to the diameter of the particles, which means that the most probable relative position of two particles is at contact with one another.

The picture that comes along here tells us that the transfer from water to EAN has resulted in a slight aggregation of the particles, with only little difference between the counterions. This result is consistent with our previous study involving highly polydisperse maghemite dispersions (Chapter 3). Indeed, the study of SANS data had shown that all particles (even large ones) were homogeneously dispersed in EAN with a large number of monovalent cationic counterions, except  $\text{Li}^+$  for which only the smaller particles were dispersible. Such different behaviour of  $\text{Li}^+$  is now no longer observed due to the use of smaller and less polydisperse nanoparticles.

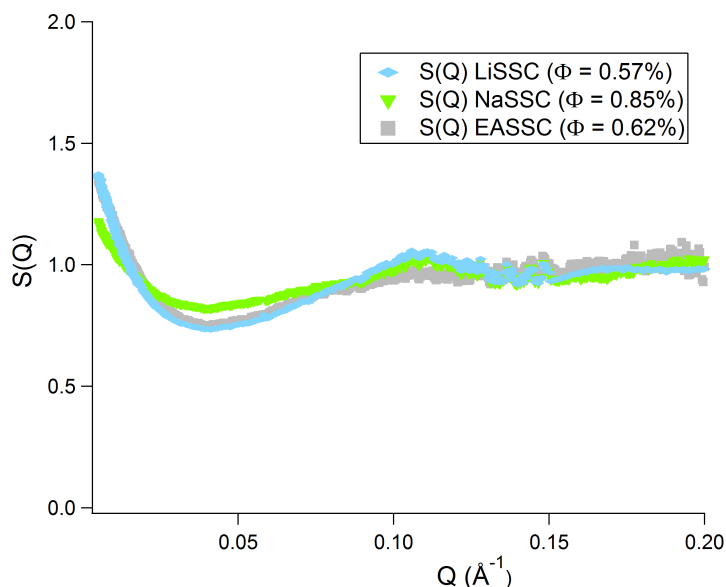


FIGURE 4.11: Structure factors ( $S(Q, \Phi)$ ) obtained for each of the three counterions in the dilute dispersions regime ( $\Phi < 1\%$ ).

#### 4.5.2 Concentrated Regime

Let us now examine the consequences of increasing the nanoparticles concentration. For each counterion, a series of samples of growing NP volume fraction is prepared in the range  $1\% < \Phi < 8\%$ , except in the case of  $\text{EA}^+$ , for which only one sample is prepared with a concentration of  $\Phi = 2.68\%$ . Indeed, when trying to reach higher concentrations, the centrifugation process leads to the formation of a NP concentration gradient resembling a phase separation but reversible. These are the only samples for which this behaviour was observed.

In all of the three cases, *i.e.*,  $\text{Na}^+$ ,  $\text{Li}^+$  and  $\text{EA}^+$ , all the dispersions are homogeneous from a macroscopic and microscopic point of view in zero applied magnetic field, regardless of the concentration. However, as mentioned above, the observation of the two most concentrated  $\text{Li}^+$  samples ( $\Phi = 5.07\%$  and  $\Phi = 7.34\%$ ) by optical microscopy under the effect of an applied magnetic field evidenced the formation of a concentrated phase, meaning that these dispersions are probably near a gas–liquid phase transition boundary. Similarly to the dilute samples, the comparison of SANS and SAXS experiments showed no temporal evolution of these samples over 1 month.

Figures 4.12 and 4.13 show the results respectively from static SAXS and dynamic magneto–optic birefringence experiments for some representative samples for each counterion. The data reinforce the idea of a very different behaviour at the nanoscopic scale

depending on the cationic counterion. Since the three cationic counterions give rise to three distinct situations, we now discuss them one by one.

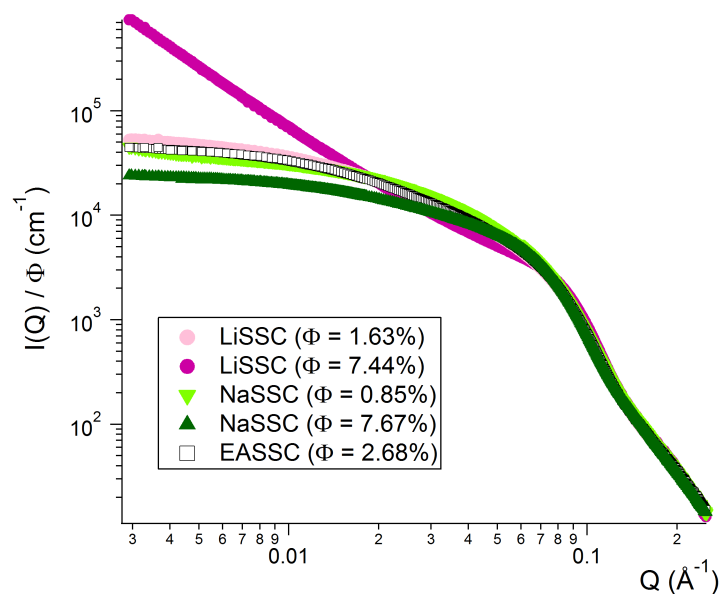


FIGURE 4.12: Absolute scattered intensities (normalized by the NP volume fraction,  $\Phi$ ) for dispersions of 7 nm citrated maghemite NP in EAN with different counterions for citrate.

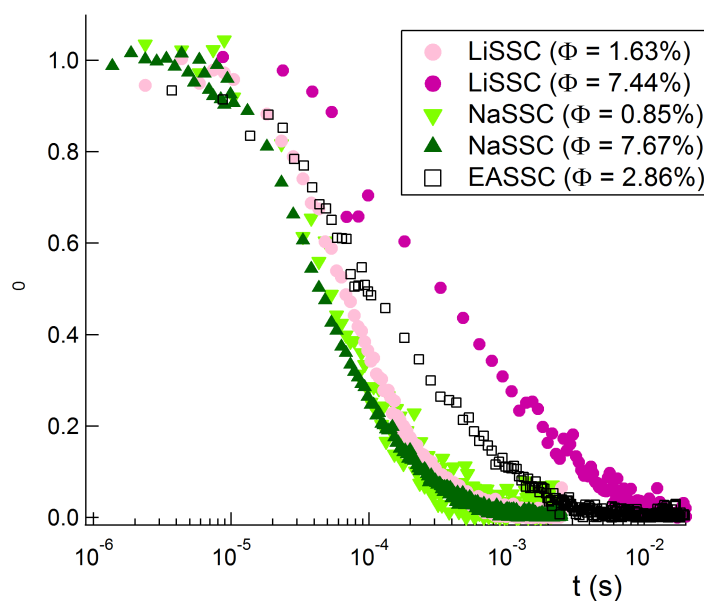


FIGURE 4.13: Normalized intensity *vs.* time plots obtained from magnetic birefringence measurements on the same samples as in Figure 4.12.



## Sodium counterions

In Figure 4.12, it can be noticed that the scattering curves for the two  $\text{Na}^+$  samples decreases with growing concentration in the low- $Q$  regime. This fact could be interpreted in two ways: either the interparticle interactions become more repulsive as  $\Phi$  increases, or the dilute dispersion contains aggregates that are broken down into smaller objects in the more concentrated sample. Although the latter hypothesis seems quite unlikely, we can find an answer in the magneto-optic experiments.

As evidenced by the superimposed curves in Figure 4.13, the characteristic rotation time  $\tau_{rot}$  obtained by the magneto-optic birefringence experiments for the SSC particles coated with sodium citrate does not vary when  $\Phi$  is increased up to  $\sim 8\%$ . This indicates that the same type of dispersed objects exist in the samples. Owing to this fact, the observed diminution of  $I(Q=0, \Phi)$  with growing  $\Phi$  is to be attributed to the existence of repulsive interactions.

The calculation of the radius of gyration  $R_G$  from the SAXS data is performed through the Guinier law (see Appendix B). The  $R_G$  of the most dilute sample is  $9.5 \pm 1.5$  nm. This is coherent with the hydrodynamic radius  $R_H$  inferred from the birefringence experiments, equal to  $12 \pm 0.5$  nm. For a polydisperse system, characterized by the radius  $R_0$  and polydispersity  $\sigma$ , we expect  $R_H \approx R_G$  [107] and  $R_H \approx 2.4 \times R_0$  for  $\sigma = 0.25$  [102]. We observe  $R_H \approx R_G$  but  $R_H \approx 3\text{--}4 \times R_0$ . These numbers clearly hint at the presence of small aggregates of less than 2 particles on average.

In light of these findings, we consider the most dilute  $\text{Na}^+$  sample as the form factor accounting for the presence of small (most probably dimeric) particle aggregates. Therefore, we use the experimental scattered intensity of this dilute sample *in lieu* of a  $P(Q)$  function, and we calculate the structure factors for the two more concentrated dispersions with the same counterion as  $S(Q, \Phi) = [I(Q, \Phi) / \Phi] \times [0.0085 / I(Q, \Phi = 0.85\%)]$ .

The resulting  $S(Q, \Phi)$  curves are shown in Figure 4.14, and they clearly evidence the repulsive interactions ( $S(Q=0, \Phi) < 1$ ) existing between the dispersed objects. Also, the position of the structure peak corresponds to the most probable distance between two neighbouring objects, which can be calculated as  $2\pi/0.08 \text{ \AA}^{-1} = 7.8$  nm. This value is larger than the center-to-center distance of particles at contact, but at least twice smaller than the average distance between particles homogeneously distributed in space ( $> 16$  nm, obtained from the volume fraction of NP). Hence, this result completes the

picture of a system in which weak repulsive forces exist between the particles.

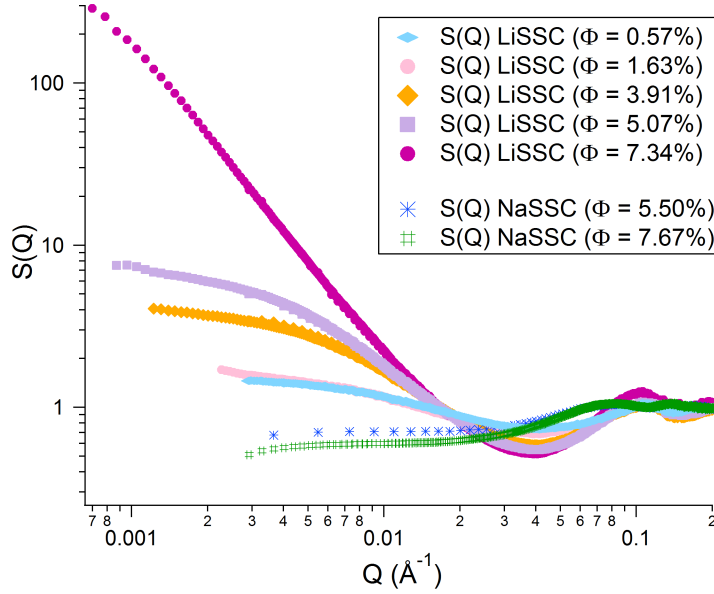


FIGURE 4.14: Effect of NP concentration ( $\Phi$ ) on the structure factors  $S(Q, \Phi)$  of citrated maghemite NP (with  $\text{Li}^+$  and  $\text{Na}^+$  as counterions) dispersed in EAN. For the sake of clarity, only 1 in every 5 experimental points have been traced.

At this point of the analysis, since the origin of the repulsions is unknown, we simulate the appearance of the experimental  $S(Q, \Phi)$  on the basis of a Yukawa repulsive potential, chosen for its simplicity. This is expressed as:

$$\frac{V(d)}{kT} = -A \frac{\exp\left(-\frac{d-2R}{\lambda}\right)}{d/2R} \quad d \geq 2R \quad (4.1)$$

where  $d$  is the center-to-center distance,  $A$  and  $\lambda$  are respectively the amplitude and the range of the interaction, and  $R$  is the radius of the sphere equivalent to the aggregates found in the dilute  $\text{Na}^+$  sample. Using the above potential, the pair correlation function  $g(r)$  and then the structure factor  $S(Q, \Phi)$  are calculated by iterative resolution, using the Ornstein-Zernike equation with the hypernetted chains (HNC) equation [109] (calculations performed with the software kindly provided by Luc Belloni).

In the calculation, the concentration of colloids in the systems is taken as the number of objects in solution by considering the aggregation number. Two parameters,  $A$  and  $\lambda$ , remain to be fixed in order to proceed with the calculation. We are able to catch the main features of the two experimental  $S(Q, \Phi)$  by imposing  $A = 0.32$  and  $\lambda = 3.5$  nm:

this situation represents a system where the interaction energy for the objects at contact amounts to 0.32 kT, and its range is of about the radii of the objects themselves.

These findings explain the observed stability of the Na<sup>+</sup> dispersions in the absence of an external magnetic field. Moreover, as explained above, all the suspensions are found stable even under the influence of an applied field ( $H \simeq 160 \text{ kA m}^{-1}$ ), which has the effect of adding an attractive contribution (in the measure of a fraction of kT) to the total interaction potential. This effect is nevertheless insufficient to induce a reversible destabilization under field, which on the contrary is observed in the most concentrated Li<sup>+</sup> samples.

### Lithium counterions

The characteristic rotation time  $\tau_{rot}$  of the objects dispersed in the Li<sup>+</sup> samples increases with growing  $\Phi$  (Figure 4.13), which is an indication of the formation of particle clusters.

Hence, the structure factors for all the samples in the series are calculated from SAXS data (Figure 4.14) using the form factor  $P(Q)$  of the individual particles (obtained for the aqueous dispersions as explained in Appendix B). The value of  $S(Q=0, \Phi)$  extrapolated for  $Q = 0$  gives the aggregation number  $N_{ag}$ ; the ensemble of the  $N_{ag}$  and  $R_G$  values for the LiSSC series are collected in Table 4.3.

<b>Properties of the LiSSC series</b>					
<i>Sample:</i>	<i>LiSSC 0.6</i>	<i>LiSSC 1.6</i>	<i>LiSSC 3.9</i>	<i>LiSSC 5.1</i>	<i>LiSSC 7.3</i>
$\Phi_{SANS}\%$	0.57	1.63	3.91	5.07	7.34
$N_{ag}$	1.60±0.05	1.7±0.1	4.3±0.5	8±1	> 100
$R_G(\text{nm})$	11±1	12.5±2	18±1	22±1.5	> 170
$R_H(\text{nm})$	< 15	13.5±0.5	35±7	35±7	35±7
$\beta$	—	1	0.5	0.5	0.5

TABLE 4.3: Results for the series of SSC (7 nm) dispersions with Li<sup>+</sup> counterions in EAN.  $\Phi_{SANS}$ : volume fraction determined from the scattering invariant in SANS;  $N_{ag}$ : number of aggregation;  $R_G$ : radius of gyration calculated from SAXS;  $R_H$ : hydrodynamic radius obtained from magneto-optical measurements;  $\beta$ : stretching exponent of the exponential fit of the relaxation of birefringence measurements (Figure 4.13).

For  $\Phi < 5\%$ , the number of aggregation increases up to  $N_{ag} = 8$  with growing NP concentration. The size of the aggregates being quite small, no fractal dimension can reasonably be determined from these data. As for what concerns the sample at the highest concentration,  $\Phi = 7.34\%$ ,  $N_{ag}$  and  $R_G$  cannot be calculated in the available  $Q$  range; therefore only the lower limit values are given in Table 4.3 for this sample [110].

It should be noted that, despite the high  $N_{ag}$ , sample LiSSC 7.3 remains liquid (although quite viscous) and homogeneous as observed by optical microscopy without magnetic field. In the low  $Q$  regime,  $S(Q, \Phi)$  varies as  $Q^{-1.9}$ : this value is consistent with a process of aggregation following either the RLCA (reaction limited aggregation) or DLCA (diffusion limited aggregation) mechanism. In the latter case, the resulting aggregates would be fragile (loosy clusters [110]).

The hydrodynamic radii extracted from the magneto-optic measurements show a rupture in trend between LiSSC 1.6 and LiSSC 3.9 (please note that the birefringence signal of sample LiSSC 0.6 (not shown) was too noisy to be analysed quantitatively, but quite similar to that of LiSSC 1.6). Sample LiSSC 1.6 contains small aggregates ( $R_H = 13.5$  nm), while the three dispersions of higher  $\Phi$  are all characterized by relaxation curves very close to one another (data not shown), suggesting the presence of the same type of objects in the three samples. This would appear, at first glance, inconsistent with the results from SAXS.

Let us examine more closely the values of the hydrodynamic and gyration radii listed in Table 4.3. For a polydisperse magnetic fluid, we expect  $R_H \approx R_G$  [107]. In the present system, we find  $R_H > R_G$  for  $\Phi < 5\%$ , with the ratio of the two radii  $< 1.9$ : this is reasonable once we take into account the size polydispersity  $\sigma$  of the objects (as indicated both by the initial  $\sigma$  and the stretching exponent  $\beta$  value) and the error bars on the calculated values. However, for sample LiSSC 7.3 we have  $R_H < R_G$ . It is worth mentioning that the  $R_G$  and, even more, the  $R_H$  values are determined *via* experimental techniques that are more sensitive to the largest particles and to the presence of particle aggregates [102]: this fact could be at the origin of the different evolution trends followed by the two radii with increasing  $\Phi$ . Anyway, for the most concentrated sample, LiSSC 7.3, the  $R_H$  measured by magneto-optic experiments indicates that the large clusters that were present in the suspension are broken down under the effect of the rotation induced by the magnetic field applied in the experiment. These would thus be fragile aggregates, in a behaviour more in favour of the DLCA hypothesis mentioned above.

The whole set of results concerning the  $\text{Li}^+$  systems hints at a slightly attractive interaction potential at contact, leading to the formation of either small aggregates, the size of which does not evolve over time, or large clusters at high nanoparticles concentration, which may evolve with time as in [110]. Such weak attraction is in agreement with the obtention of suspensions which are homogeneous on the microscopic

scale and stable over at least one year. Also, it can explain the fact that the larger particles are more difficult to disperse in the presence of  $\text{Li}^+$  counterion, as evidenced by the presence of a precipitate in the starting dilute dispersion. Finally, such weak attractions are in agreement with a destabilization under an applied magnetic field as observed by optical microscopy.

### **Ethylammonium counterions**

As mentioned earlier in the text, the case of ethylammonium counterions represents a sort of reference since it only contains one cationic species,  $\text{EA}^+$ , that can be located at the solid/liquid interface. The sample prepared at  $\Phi = 2.86\%$  is stable both in the absence and in the presence of an applied magnetic field, as observed by optical microscopy; the  $\tau_{rot}$  measured through the birefringence relaxation experiments evidences the presence of small aggregates ( $R_H = 20 \pm 5$  nm).

These results delineate the picture of an intermediate behaviour compared to those of the systems containing  $\text{Na}^+$  and  $\text{Li}^+$  counterions, whose behaviours are opposite.

Indeed, in the case of  $\text{Na}^+$  counterions, as  $\Phi$  grows, the SAXS scattered intensity  $I(Q=0, \Phi)$  decreases. At the same time, the characteristic relaxation time  $\tau_{rot}$  deduced by the magneto-optic birefringence experiments is independent from the NP concentration: this means that the dispersed objects do not aggregate and remain in repulsive interaction.

On the contrary, with  $\text{Li}^+$  counterions the trend is exactly the opposite compared to sodium: now, the SAXS curves show a strongly increasing value of  $I(Q=0, \Phi)$  for growing NP volume fraction. At the same time, the birefringence relaxation time for the more concentrated sample is one order of magnitude larger than for the dilute one: the NP are agglomerating.

In conclusion, the results confirm the presence of  $\text{Na}^+$  and  $\text{Li}^+$  cationic counterions close to the nanoparticles surface after the transfer of the NP from aqueous medium to the ionic liquid, as well as their role in the interactions between particles. Moreover, the presence of these counterions at the interface modifies the interaction potential between the colloids, which is tuned from slightly attractive (for lithium) to slightly repulsive (for sodium). This fact is rendered by the existence of different microstructures in the three systems, all of which are nevertheless macroscopically homogeneous.

## 4.6 Large Particles (11 nm): Effect of the Counterion

### 4.6.1 Dilute Regime

Dispersions of 11 nm (CC) citrate-coated nanoparticles in EAN behave quite differently from their 7 nm counterparts. Only a few single-phase dilute dispersions have been obtained at low  $\Phi$  for  $\text{Na}^+$  and  $\text{Li}^+$  counterions, but all these samples are (reversibly) destabilized under the application of a magnetic field. For  $\text{EA}^+$ , there is just no one-phase sample in the  $\Phi$  interval we explored: all dispersions of large NP with  $\text{EA}^+$  counterions phase-separate immediately.

Figure 4.15 shows the structure factors of two dilute, one-phase dispersions for  $\text{Na}^+$  and  $\text{Li}^+$  counterions, along with the  $S(Q, \Phi)$  for the gas phase (dilute phase resulting from a gas-liquid spinodal decomposition, as explained above in Section 4.4) of an  $\text{EA}^+$  dispersion. The structure factors are obtained by dividing the  $\Phi$ -normalized experimental scattering curves by the experimental form factor  $P(Q)$  for large particles, derived from the aqueous dilute dispersions as described in Appendix B. As mentioned in Section 4.4, despite the fact that the phase separation may determine a kind of “size-sorting”, as particles of different sizes are preferentially accommodated in one of the two phases, in our case such effect appears negligible. The use of the same  $P(Q)$  curve is then justified for the one-phase samples as well as both of the phases deriving from the spinodal decomposition.

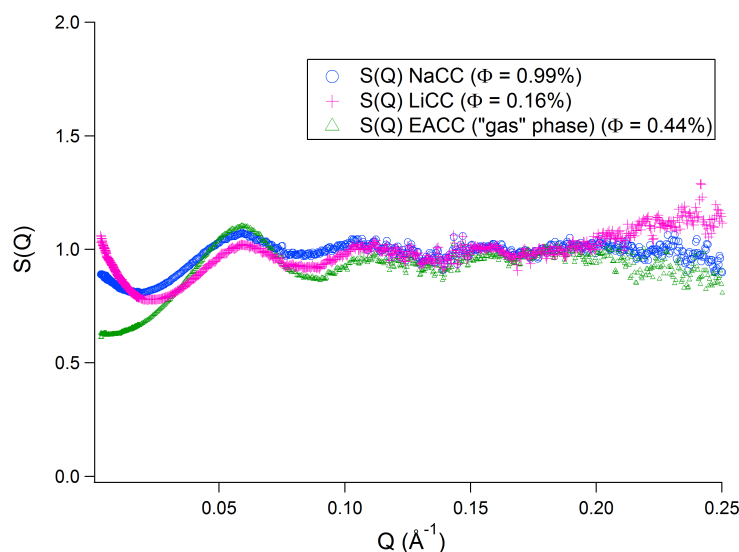


FIGURE 4.15: Structure factors for dilute suspensions of large particles in EAN, with different counterions for citrate. See text for details.

All of the three curves in Figure 4.15 have a structure peak at  $0.06 \text{ \AA}^{-1}$ , translating into a contact distance between neighbouring particles. The structure factors of the  $\text{Na}^+$  and  $\text{Li}^+$  samples are very close to each other, although the  $S(0, \Phi)$  values are slightly dissimilar (repulsive interactions for  $\text{Na}^+$ , attractive for  $\text{Li}^+$  counterions). Also, the  $\text{Na}^+$  and  $\text{Li}^+$  samples have a different temporal stability: indeed, contrary to  $\text{Na}^+$ , the  $\text{Li}^+$  dispersion is unstable over time, since it slowly phase-separates over several months. For the  $\text{EA}^+$  gas phase,  $S(0, \Phi)$  being inferior to 1, the interparticle forces are globally repulsive; however, the ageing of such  $\text{EA}^+$  gas phases, as seen from repeated SAS experiments after 1 month, has shown the tendency of the interparticle potential to turn towards globally attractive forces, while the structure peak at  $0.06 \text{ \AA}^{-1}$  becomes less pronounced. It should be always kept in mind, though, that this sample is already resulting from a phase separation process, and thus characterized by a state of equilibrium that does not really allow for comparison to the two other samples.

Stable dilute samples for the three counterions have been investigated by means of magneto-optic birefringence measurements, the results of which are shown in Figure 4.16. From the exponential fits of the curves, we can obtain the following values of hydrodynamic radii: 15 nm and 17 nm for the  $\text{Na}^+$  samples of, respectively,  $\Phi = 0.99\%$  and  $2.27\%$ ; 16 nm for the  $\text{Li}^+$  sample; 17 nm for the  $\text{EA}^+$  gas phase. These values are slightly larger than the expected  $R_H \approx 2.4 \times R_0$  [102, 107], where  $R_0$  is 5.5 nm for our particles, therefore hinting at the presence of some small aggregates of less than 2 particles.

#### 4.6.2 Concentrated Regime

The dilute dispersions described in the previous Subsection are concentrated by centrifugation in order to obtain suspensions with higher NP volume fraction. For each of citrate's cationic counterions, a gas-liquid phase separation is observed, at different concentration thresholds depending on the ion. The gas phase is a dilute dispersion of quite low  $\Phi$  ( $\leq 1\%$ ) while the liquid phase is more concentrated and dense, attaining volume fractions of a few tens%. Let us remind that, as a consequence of this phase separation, several technical problems are encountered in the manipulation of the samples and in the determination of the volume fractions. The reader is referred to Subsection 4.4 for more details.

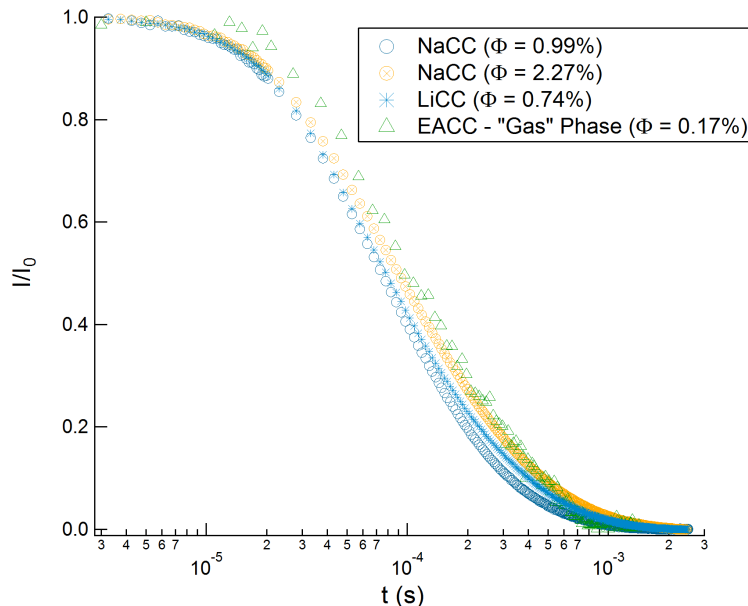


FIGURE 4.16: Magneto-optic birefringence experiments for dilute suspensions of large particles in EAN, with different counterions for citrate. See text for details.

The gas phases are all very dilute, and if they are correctly separated from the concentrated phases, they are not destabilized by a magnetic field. The  $S(Q, \Phi)$  curves obtained from SAXS experiments for these samples (data not shown) are similar to the one-phase dispersions, presenting a correlation peak at  $Q = 0.06 \text{ \AA}^{-1}$  (corresponding to  $d \approx 11 \text{ nm}$ ), which indicates that for each counterion the gas phases are made of particles whose most probable relative position is at contact. The  $S(0, \Phi)$  values depend on the cationic counterion present on the NP surface.

The structure factors of the liquid phases (Fig. 4.17) have in common the presence of a contact peak. Once again, the behaviour at  $S(0, \Phi)$  is extremely different, showing the existence of ion-specific interactions.

### Sodium counterions

When sodium is used as a counterion for citrate, one-phase dispersions of large maghemite NP can be obtained in EAN with concentrations up to  $\sim 1.5\%$ . This is the highest phase separation threshold observed, since with other counterions the phase transition is found at lower NP volume fractions. Despite the fact that they are constituted of a single phase, though, these dispersions are destabilized by the application of a magnetic field, as indicated by the formation of a concentrated phase which disappears very slowly (several hours) upon removal of the field (Fig. 4.18).



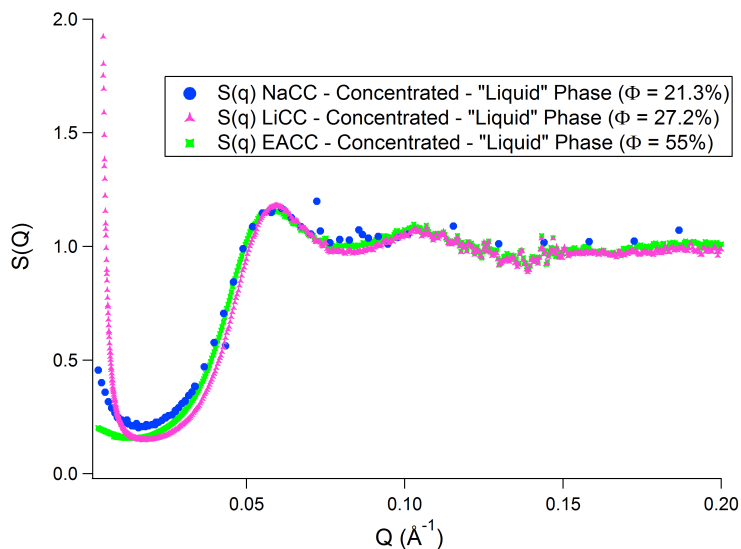


FIGURE 4.17: Structure factors obtained from SAXS experiments for the liquid phases of concentrated CC nanoparticles dispersed in EAN, with three different counterions.

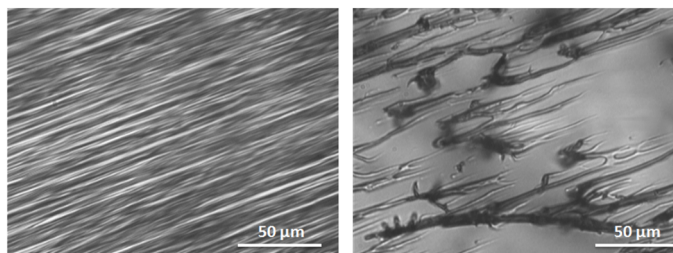


FIGURE 4.18: Optical microscopy under applied magnetic field ( $H \simeq 160 \text{ kA m}^{-1}$ ). Left: NaCC one-phase dispersion with a concentrated phase formed due to the presence of the magnetic field. Right: snapshot of the same sample showing the slow relaxation of the concentrated phase upon removal of the field.

When attempting to reach  $\Phi \geq 1.5\%$ , the dispersions with  $\text{Na}^+$  counterions separate into colloidal gas and liquid phases. Figure 4.19 shows the SAXS scattered intensities for a one-phase NaCC sample and the two phases obtained after the spinodal decomposition. In this case the NP volume fraction of the colloidal gas phase is lower than that of the one-phase stable dispersion: this is not logical, since the phase separation is observed when attempting to increase the volume fraction and while keeping the other parameters constant (basically, moving along an horizontal line in the phase diagram of Fig. 4.10). However, due to the complexities of the dynamics of phase transitions, predictions of phase diagrams are not straightforward. In many cases the products deriving from colloidal phase separations strongly depend on the starting position in the phase diagram, and discrepancies may exist between predictions and actual observations

[111]. In our case, the one-phase dispersions with  $\text{Na}^+$  counterions (used to obtain the more concentrated samples which later phase-separate) could be only metastable, and this would explain why the gas phase resulting from the spinodal decomposition has a lower  $\Phi$  than expected.

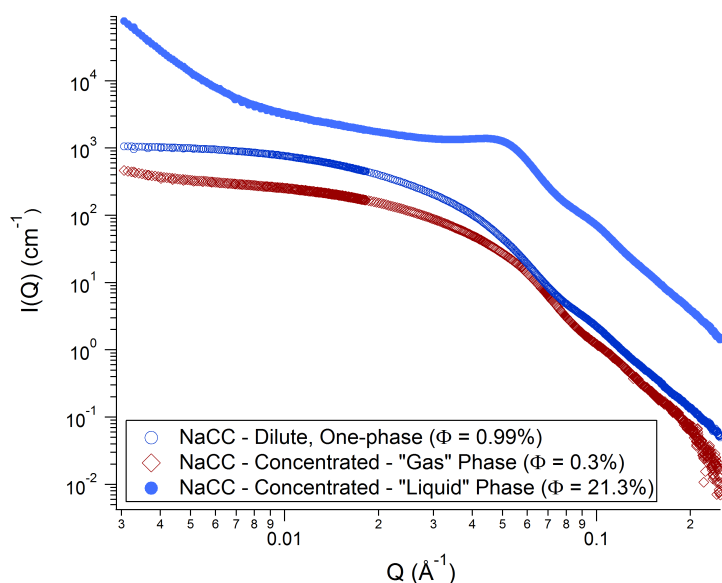


FIGURE 4.19: SAXS scattered intensities of NaCC samples: one-phase dispersion, and the two phases resulting from spinodal decomposition.

Both the gas and the liquid phases evolve over time. The dilute phase, studied by SANS, and by SAXS (shown in Fig. 4.19) one month later, shows the existence of more repulsive interactions as it ages. On the contrary, the global potential in the concentrated phase becomes more attractive. For both, the structure factors show the presence of a structure peak corresponding to the contact distance between neighbouring particles.

### Lithium counterions

Dispersions of large maghemite NP with lithium counterions have a different behaviour compared to those with  $\text{Na}^+$ . The phase separation is encountered at a lower threshold ( $\Phi < 1\%$ ). The two phases resulting from the spinodal decomposition are stable over time, as proven by the SAXS curves obtained with a 1 year interval, shown in Figures 4.20 and 4.21. In particular, the two curves for the gas phase (aged 2 and 14 months) are perfectly superimposed; the two curves for the concentrated phase, on the other hand, are slightly different, but this could be due to the presence of a small amount of dilute phase trapped during the sampling in one of the two cases.

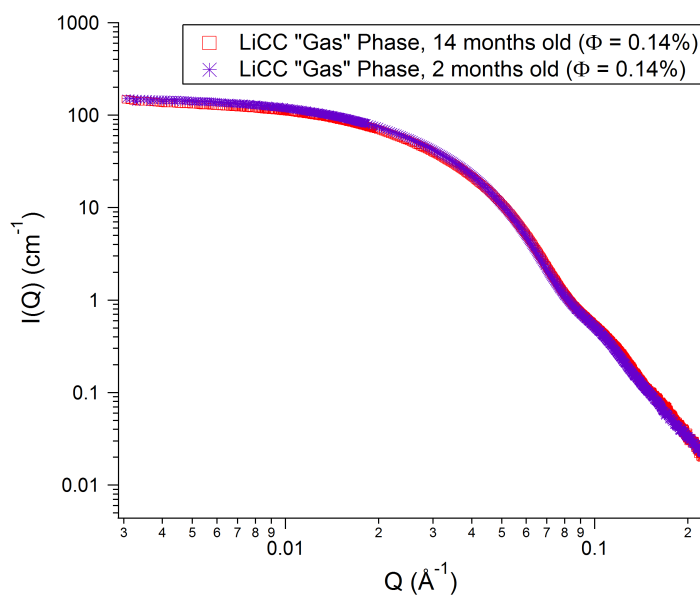


FIGURE 4.20: SAXS  $I(Q, \Phi)$  curves for LiCC gas phases, showing no time evolution over one year. The  $\Phi$  values result from the calculation of the scattering invariant.

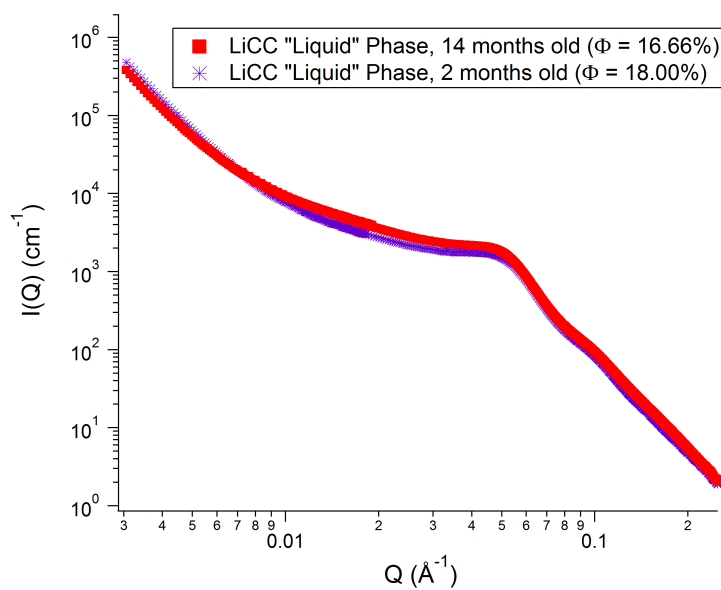


FIGURE 4.21: SAXS  $I(Q, \Phi)$  curves for LiCC liquid phases, showing no time evolution over one year. The  $\Phi$  values result from the calculation of the scattering invariant.

Figures 4.22, 4.23 and 4.24 show the results of three types of experiments (SAXS, SQUID magnetization, and magneto-optical birefringence, respectively) for a one-phase LiCC sample, compared to those for the gas and liquid phases obtained while trying to reach higher  $\Phi$ . The volume fractions indicated in the figures are those acquired from the SQUID experiments, where the values corresponding to the dilute dispersion and the gas phase are in perfect agreement with the results of FAAS analysis.

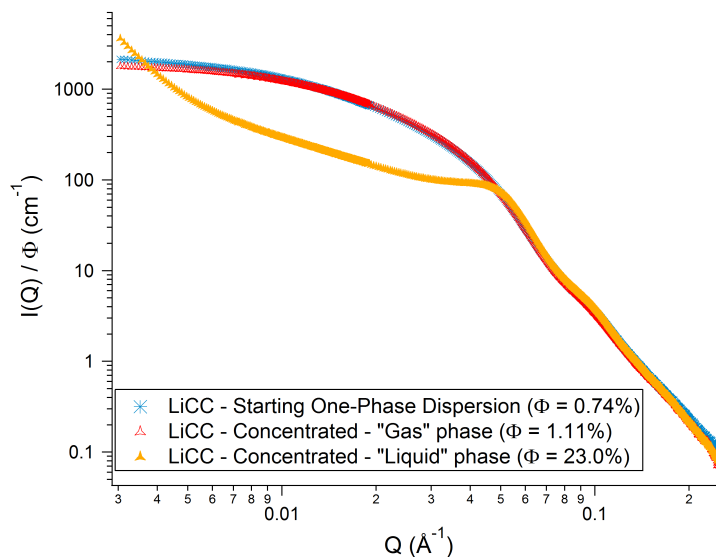


FIGURE 4.22: SAXS results for LiCC one-phase and phase-separated samples. The volume fractions  $\Phi$  are obtained from SQUID measurements.

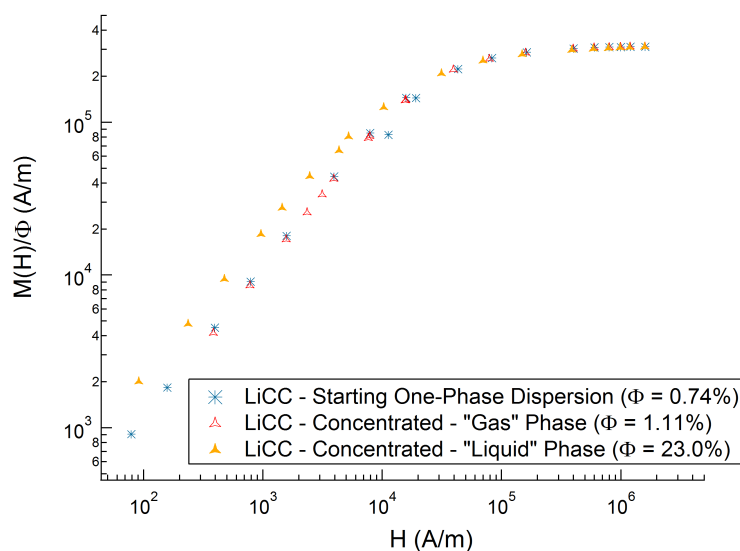


FIGURE 4.23: SQUID magnetization results for LiCC one-phase and phase-separated samples, and the volume fractions  $\Phi$  obtained by the fit of the magnetization curves.

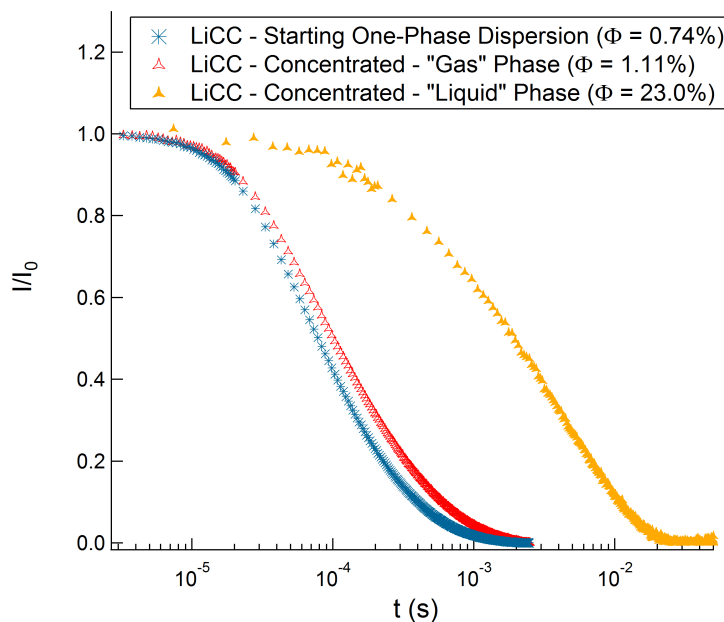


FIGURE 4.24: Magneto-optic birefringence results for LiCC one-phase and phase-separated samples. The volume fractions  $\Phi$  are obtained from SQUID measurements.

The magnetization curves for the one-phase sample and the gas phase are superimposed: both are fitted by the same lognormal function with parameters  $d_0 = 11$  nm and  $\sigma = 0.2$ , confirming that the gas-liquid phase separation does not alter the size distributions of the particles in the two phases in a significant way. However, SAXS experiments show that the scattering curves of two samples, although similar, diverge in the low- $Q$  regime. The linear fit of a Guinier plot gives  $R_G = 16 \pm 0.5$  nm for the starting dilute sample and  $13 \pm 0.5$  nm for the gas phase after separation. The values indicate a slight degree of aggregation in the starting one-phase dispersion, while the gas phase contains a suspension of isolated nanoparticles.

Similarly, the fit of the magneto-optic birefringence curves yields close characteristic relaxation times  $\tau_{rot}$  for the two products. From such times we obtain the hydrodynamic radii of the objects in both samples, corresponding to 16 and 19 nm for, respectively, the one-phase dispersion and the gas phase. The trend of the  $R_H$  though is opposed to that of  $R_G$  in the two samples, that is, the birefringence measurements seem to hint at a higher degree of aggregation in the gas phase. The results from SAXS and magneto-optic birefringence experiments seem thus to be in contradiction, but the differences between the one-phase sample and the gas phase remain quite thin.

All of the experiments reported in Figures 4.22, 4.24 and 4.23 attest the difference of

the liquid phase compared to the other two samples. Despite the high volume fraction and the very viscous appearance, this phase is indeed a liquid, as shown by the magneto-optic birefringence measurements. The relaxation time  $\tau_{rot} = 4$  ms, much longer than the usual  $\tau_{rot}$  values measured for dilute samples, is consistent with the local dynamics of aggregates having a hydrodynamic radius of 48 nm. However, the present situation is different from the one described for the small particles (4.5.2), where suspensions of  $\Phi \approx 5\text{-}7\%$  formed aggregates that relaxed slowly after the extinction of the magnetic field. In the case of the liquid phase formed by large particles, the volume fraction is much more elevated ( $\Phi = 23\%$ ), and the rotational dynamics are slowed down by several contributions [112]: dipolar interactions (we are now in the high-coupling regime, and this interaction approaches  $kT$ ); hydrodynamic interactions; physical rubbing of the particles against each other due to the contact; interpenetration of the layers of molecules adsorbed on the surface. In our case, we should add the possible interaction between ionic liquid layers surrounding the surface of the nanoparticles. Although the microscopic mechanism of the relaxation is not well understood, it has been proven [112] that the first two contributions (dipolar and hydrodynamic interactions) are too weak to explain the observed slowing down of the local dynamics; the origin of the phenomenon must then lie in the sum of all the contributions listed above. In particular, the contact between particles is proven by the interaction peak at  $0.06 \text{ \AA}^{-1}$  in the  $S(Q, \Phi)$  curve extracted from SAXS experiments, which translates an average nearest-neighbour distance equivalent to the diameter of one particle.

### **Ethylammonium counterions**

The  $EA^+$  samples are the least stable. They are always split in two phases in the whole  $\Phi$  range we examined, and such phases in turn are not stable over time. As the samples become older, the value of  $S(0, \Phi)$  increases, as shown in Figures 4.25 (for the gas phase) and 4.26 (for the liquid phase). In both cases, newer samples show repulsive interactions and a well-defined structure peak corresponding to the contact between particles; older samples are characterized by growing attractive interactions while the structure peak becomes smeared out.

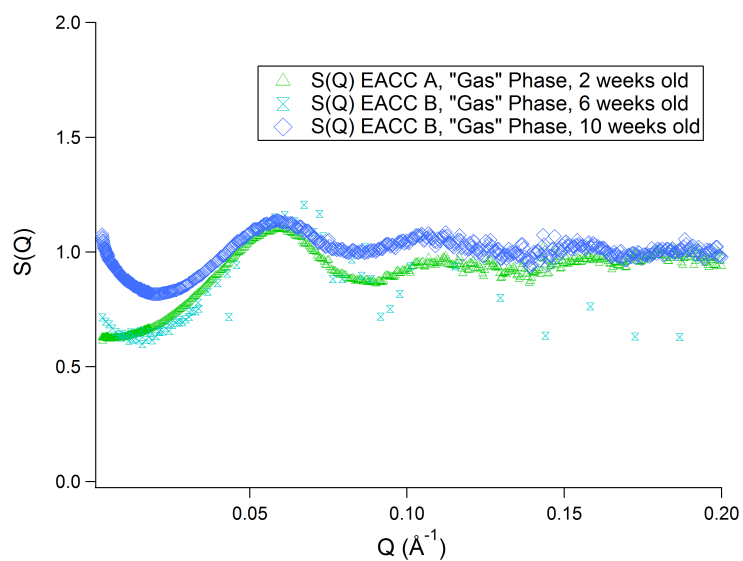


FIGURE 4.25: Effect of ageing on EACC gas phases with  $\Phi \approx 0.5\%$ . Curves referred to as A and B are different samples; sample B was analysed by SANS first and by SAXS 1 month later

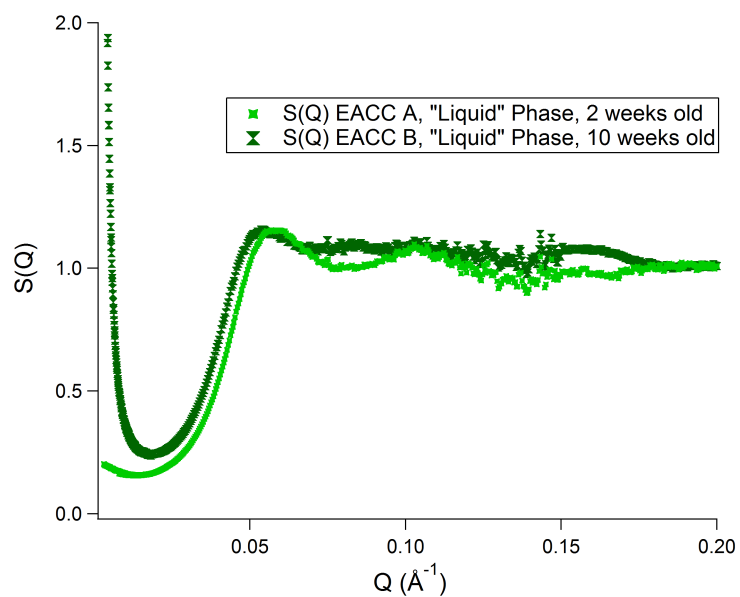


FIGURE 4.26: Effect of ageing on EACC liquid phases with  $\Phi \approx 30\%$ . Curves referred to as A and B are different samples.

## 4.7 Discussion on the Effect of the Counterions on Both Sizes

The results described in the previous Sections evidence a strongly counterion-dependent behaviour of the maghemite/EAN dispersions. The question arising spontaneously concerns the very origin of such effects. We are therefore led to consider the forces typically existing between maghemite nanoparticles in a colloidal system. Regardless of the solvent, two types of attractive interactions are always present: van der Waals and dipolar forces. Regarding the magnetic dipolar force, for dilute dispersions the interaction energy  $U_{dip}/kT$  is of the order of  $-6 \cdot 10^{-6} kT$  for small particles and  $-9 \cdot 10^{-5} kT$  for large particles, which is negligible at room temperature. The magnetic interaction becomes important for very concentrated systems with large particles at contact, where the interaction energy in the high coupling regime overcomes  $kT$ .

The van der Waals interaction between maghemite spheres in EAN can be estimated by a rough calculation based on the Lifschitz theory [22] and on corrections due to the presence of citrate [32]. Such calculation shows that the order of magnitude of this interaction is the same as in water.

As for what concerns the repulsive forces between the nanoparticles in common solvents, they are usually of electrostatic or steric origin. In our case, despite the fact that the surface of the particles is charged, the classic models describing the electrostatic repulsion in water cannot be applied, since they are unable to take into account such a high ionic concentration as that characterizing an ionic liquid (namely,  $11.2 \text{ mol L}^{-1}$  for EAN). At the same time, interactions of electrostatic type do exist between all the charged species present in the system (anions, cations and the surface of the particles), and they are responsible for the organization of the structure at the nanoscopic level. In particular, such interactions lie at the origin of the structuration of IL layers near surfaces, as determined in numerous experimental works [20, 21] and by numerical simulations (for example in [92]). The precise organization of the interface depends on several parameters, such as the chemical nature of the species involved (size, polarizability...), the surface charge and its rugosity, precluding at present any predictions or general laws when it comes to the interfacial behaviour of ILs.

Surface force studies on ILs at an interface, carried out by atomic force microscopy, show in most cases the presence of a repulsive force between the AFM tip and a given



surface separated by an IL, and the organization of the ionic liquid in one to a few layers at the interface [21]. In the case of EAN in contact with mica, for example, the observed structuration covers the length of 3–4 layers of ion pairs, corresponding to a range of about 2 nm. This value is of the same order of magnitude as the range of the interaction potential we determined for the counterion  $\text{Na}^+$  in the present system. Also, it should be noted that, in the aforementioned work, the authors observe attractive interactions between the AFM tip and a graphite surface separated by EAN, but unfortunately no further commentary is available on this matter. It can be said, however, that the change of surface material seems to strongly affect the organization of this IL.

The comparison of our results with the literature on dispersions of magnetic nanoparticles in ILs is rather difficult. Indeed, the surface of the NP has been varied, and different cases involve bare NP or coatings such as polymers of various ligands [11, 14, 16], with different and sometimes contradictory results. However, the interface is seldom precisely described, therefore the effect of the counterion's nature on the interaction potential is never addressed. In the present study,  $\text{Na}^+$  and  $\text{Li}^+$  seem to modify the repulsion generated by the IL's layer-by-layer organization. Indeed, if these ions do remain close to the surface, as suggested by our FAAS analysis, they most probably participate to the formation of the very first cationic layer in order to compensate the negative charge of citrate at the surface. Such compensation may be more or less effective, depending on the nature of the counterion (its size, the interaction between like cations and with the surface, the possible solvation of the ion). As a consequence, the organization of the IL around the nanoparticle would be modified accordingly, as well as the long-range interactions between the various objects in suspension. Unfortunately, at present only a few works have focused on the effect of added salt in NP/IL colloidal systems [85, 90, 91]: the modification of the interface is only indirectly evidenced, and the consequences of such modification are sometimes contradictory. For example, the authors of the surface force studies [85] and [90] report a destabilizing effect of added lithium salt on their systems: the  $\text{Li}^+$  would modify the interface leading to a weakening of the IL's structuration as layers. However, in [91], the presence of  $\text{Li}^+$  seems to stabilize a dispersion of silica particles in IL; the authors propose a model in which the  $\text{Li}^+$  cations interact with other species at the interface helping to form ordered solvation layers. In the present work, in the case of  $\text{Li}^+$ , the counterion seems to play a similar role to that found in [85] and [90], since it is more difficult to stabilise the particles than

with the other counterions ( $\text{Li}^+$  samples always have a precipitate at the bottom) and the structure factors of these samples always show the existence of attractive forces.

Due to the many intervening factors, it appears quite difficult to predict *a priori* the colloidal stability of such systems or to explain its ion-dependency in a straightforward manner. We can, however, describe our systems by classing them according to the strength of the attractive interactions that characterize them. Figure 4.27 summarizes the observations on the stability of all the SSC samples (the volume fraction used in the abscissa is the one issuing from SANS).

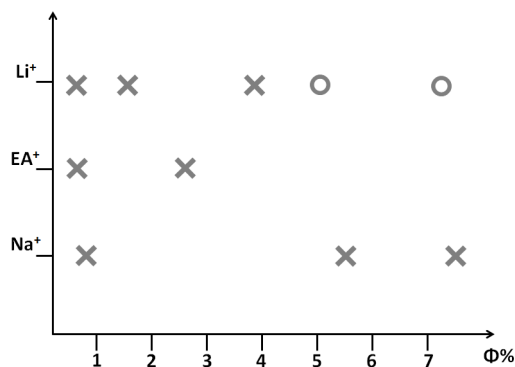


FIGURE 4.27: Diagram showing the different behaviours of NP/EAN dispersions of small particles, depending on the counterion of citrate, either  $\text{Na}^+$ ,  $\text{EA}^+$  or  $\text{Li}^+$ . Crosses = stable one-phase samples whatever the magnetic field; circles = samples showing reversible phase separation under magnetic field (observed by optical microscopy, with  $H \simeq 160 \text{ kA m}^{-1}$ ).

Figure 4.28 gives an overview of all the samples prepared from the CC lot. Only the two least concentrated  $\text{Na}^+$  samples and the one least concentrated  $\text{Li}^+$  sample are one-phase suspensions; however, all three of them are destabilized under the effect of a magnetic field, meaning that they are not far from the destabilization threshold. In all of the other cases, a phase separation occurs when trying to attain higher  $\Phi$ .

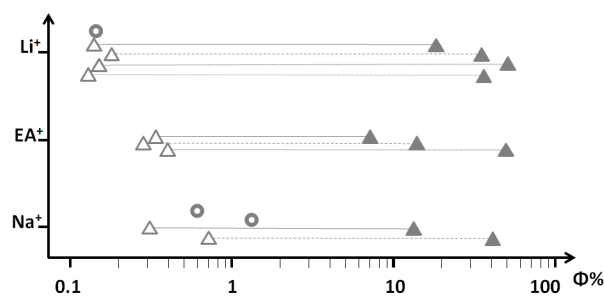


FIGURE 4.28: Diagram showing the different behaviours of NP/EAN dispersions of large particles, depending on the counterion of citrate, either  $\text{Na}^+$ ,  $\text{EA}^+$  or  $\text{Li}^+$ . Circles = one-phase samples without magnetic field, destabilized in the presence of a magnetic field; empty triangles = dilute (colloidal gas) phases; full triangles = concentrated (colloidal liquid) phases; horizontal lines = guide for the eye to retrieve the phases that originated from the same sample.

## 4.8 Effect of Water Content

In Chapter 1 we discussed the fact that the presence of water can greatly affect the properties of ionic liquids and the colloidal systems based on these solvents. According to some authors [11, 16, 27, 66], water has a disruptive effect on the solvation layers formed by ILs when in contact with a surface, which is regarded to as the cause of the loss of colloidal stability in NP/IL dispersions. Another effect that must be taken into account is the dramatic change in viscosity for an IL/water system compared to the neat IL, which affects the transport properties of the medium.

In order to look deeper into this matter, we add known quantities of water to dilute dispersions of maghemite NP in the ionic liquid EAN. Starting from a lyophilized dispersion, we prepare samples containing 5%, 10% and 20% of water (volume percent). The nanoparticles are covered with citrate, with sodium or ethylammonium as cationic counterions. For both cations, the two NP sizes are examined (7 nm and 11 nm). All samples are studied by means of small angle X-ray scattering, and the structure factors thereby obtained are shown in the following figures.

The results for small particles are summarized in Figures 4.30 for  $\text{Na}^+$  and 4.29 for  $\text{EA}^+$ . Surprisingly, the behaviour is exactly opposite for the two. When the counterion is ethylammonium, the same cation as the IL, the interactions are initially slightly repulsive (the structure factor is quasi non-existent, actually, since the entire curve is almost flat and lying around the value of 1) in the lyophilized dispersion. Here, the water content is estimated in the order of 1 wt%. The interactions become gradually more attractive as the water content grows to 5 vol% (corresponding to 4 wt%) and up

to 20 vol% water (about 16 wt%). This is quite consistent with the behaviours observed by other authors in EAN/water mixtures without nanoparticles [15, 20] and in colloidal dispersions [11, 16, 27, 66], where the presence of water reduces the repulsion due to the IL layers and destabilizes the colloidal systems. On the other hand, in the case in which sodium is used as a counterion for citrate, the interactions are attractive in the 100% EAN dispersion (which actually contains about 1 wt% water), but they become repulsive with the addition of more water and they remain unchanged from 5 vol% up to 20 vol%.

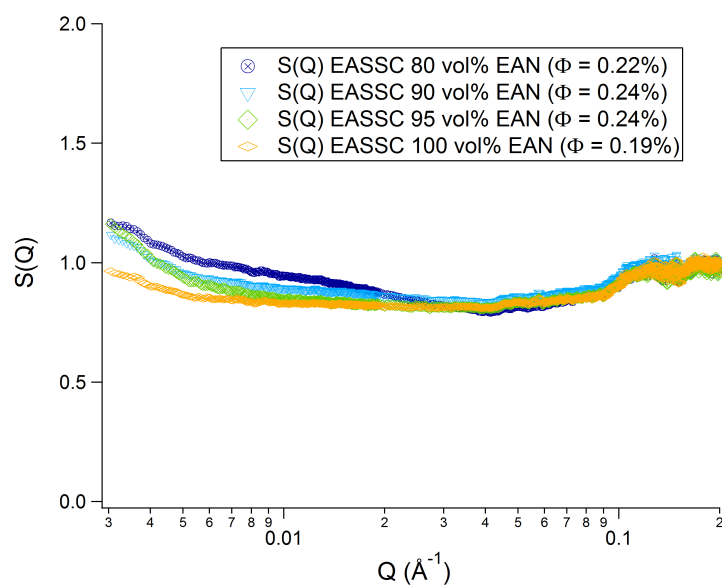


FIGURE 4.29: Structure factors for EAN/W dispersions. Small particles, EA<sup>+</sup> counterions.

The trends observed are the same for large particles. In this case, it should be noted that the starting EAN dispersions used to prepare the EAN/water mixed suspension were actually gas phases from phase-separated products. The structure factors are reported in Figures 4.32 and 4.31.

The value of  $S(0, \Phi)$  grows with growing water content in the case of EA<sup>+</sup> counterions, indicating increasingly attractive interactions; the sample with 20 vol% water is completely flocculated and is therefore not studied by SAXS. The samples with 10 vol% and 5 vol% water are apparently stable by naked-eye observation, but optical microscopy reveals the presence of two phases. For Na<sup>+</sup> counterions,  $S(0, \Phi)$  decreases with water content, indicating more repulsive interactions, and remains pretty much unchanged for the higher water percentages. However the samples are not perfectly stable since

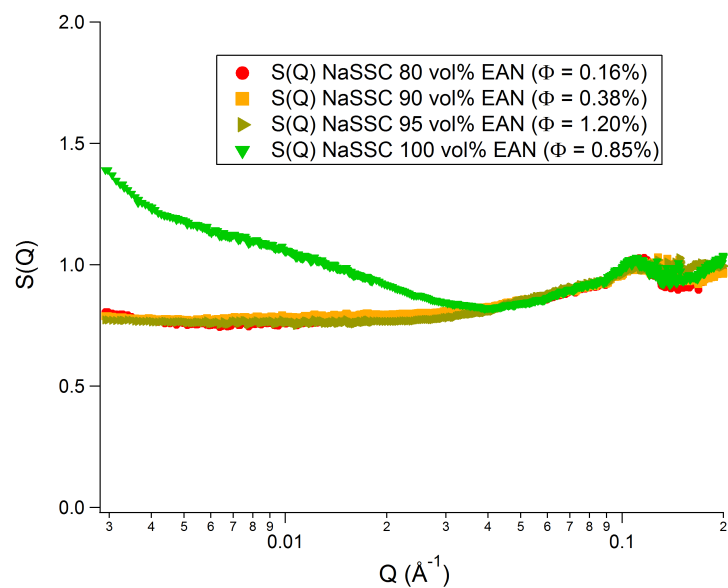


FIGURE 4.30: Structure factors for EAN/W dispersions. Small particles,  $\text{Na}^+$  counterions.

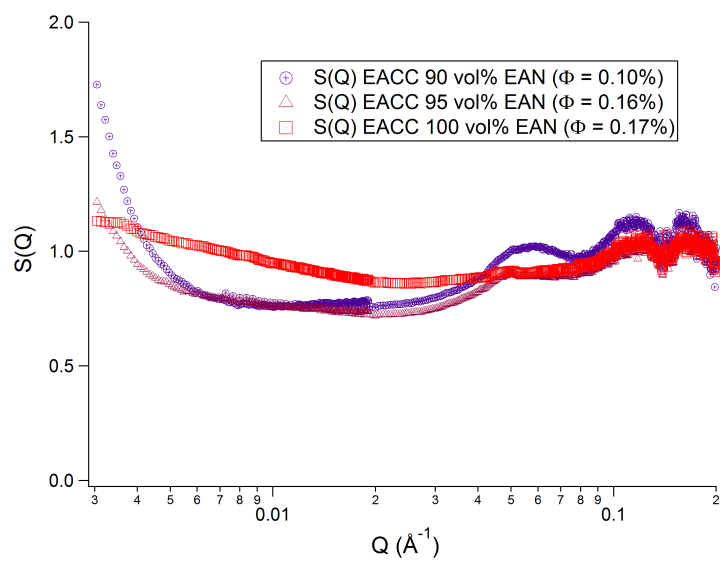


FIGURE 4.31: Structure factors for EAN/W dispersions. Large particles,  $\text{EA}^+$  counterions.

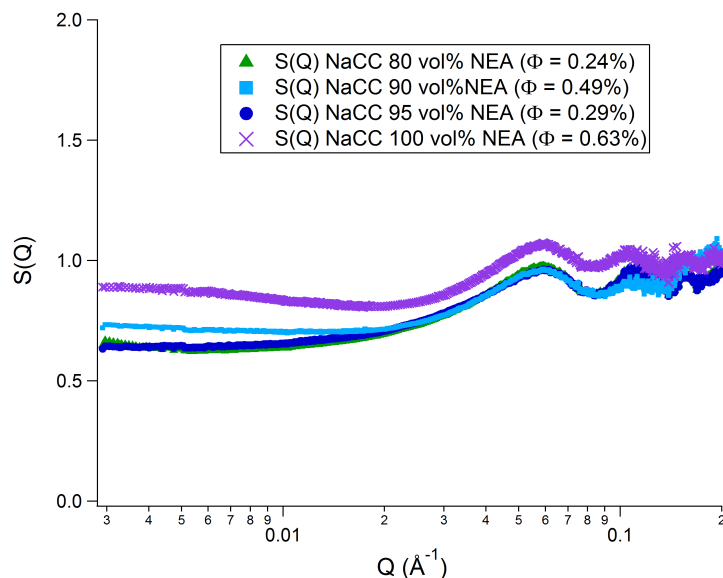


FIGURE 4.32: Structure factors for EAN/W dispersions. Large particles,  $\text{Na}^+$  counterions.

the formation of a concentrated phase is induced when a magnetic field is applied (the suspensions are otherwise one-phase).

These results show that the nature of the counterion of citrate is essential for the colloidal stability of maghemite dispersions in EAN/water mixtures, with a stabilizing mechanism that may lie in the different degree of hydration of each ion. In the case of sodium, the change in behaviour of the dispersions is quite evident with the addition of 5 vol% water, that is, going from 1 wt% to 4 wt%. We then wonder what the role is of that 1 wt% water in the starting sample. If we take the hydration number of sodium to be 4, and we consider a typical dilute suspension (10 mL,  $\Phi = 1\%$ ) of small particles with 1.6 charges/nm<sup>2</sup>, we have roughly 500  $\text{Na}^+$  ions surrounding each of the about  $3 \cdot 10^{17}$  particles in the sample. Considering only the first hydration shell of the cations, a rapid calculation shows that approximately 0.02 g of water are necessary to hydrate the surface  $\text{Na}^+$  ions of the particles. We then need to take into account the quantity of water necessary to hydrate the carboxylate groups of citrate on the NP, which are present in the same number as the compensating sodium cations; we thus add another 0.02 g of water, making a total of 0.04 g H<sub>2</sub>O needed to hydrate the surface of the NP. In a typical sample, 1 wt% water equals 0.12 g. If water interacts preferentially with the ions on the particles, it is evident that in our samples the whole surface is already completely hydrated even in the starting dispersion that we denominate “100%

EAN". It is then not clear why such a striking variation in the interparticle potential would occur when adding more water, and why the effect would be stabilizing instead of disrupting, as observed in the case of ethylammonium and by other authors as mentioned above. However, the possibility of a stronger interaction of water with EAN (thanks to hydrogen-bonding), rather than with the NP or the other ions, should be taken into account. At present, we do not have more detailed information on the localization of water molecules in our dispersions.

Finally, we consider the symmetrically opposite side of the water/EAN mixture ratios and investigate the effect of added EAN in an aqueous dispersion of citrated maghemite NP with sodium counterions. Based on the observations of other authors [15, 20], we treat EAN as any other salt and add typical quantities expressed in molar concentration: 0.5 M, 1 M and 2 M. This is done for both particle sizes, and the resulting structure factors obtained from SAXS experiments are presented in Figures 4.33 and 4.34 for, respectively, small and large NP.

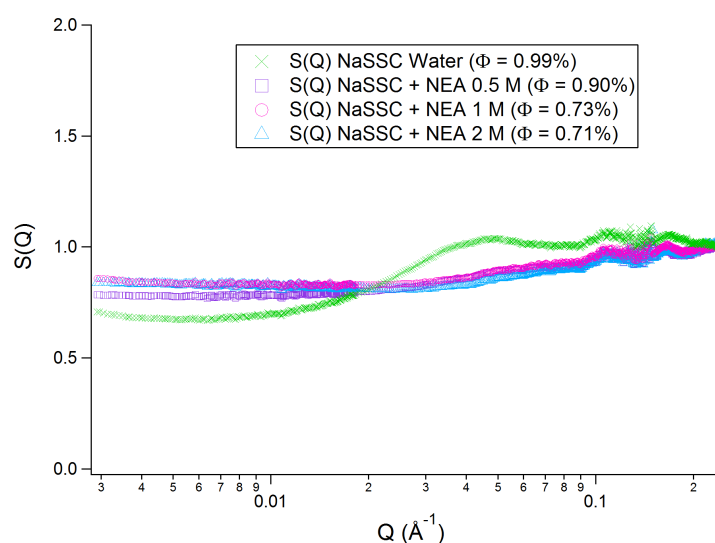


FIGURE 4.33: Structure factors for aqueous maghemite dispersions with added EAN. Small particles.

The aqueous dispersion of small particles remains remarkably stable up to the addition of 2 M ethylammonium nitrate, while usually much lower concentrations of other salts suffice to lead to its destabilisation (for example, NaCl in concentration  $< 0.5$  M [39]). The peak in the structure factor of the aqueous dispersion (Fig. 4.33) disappears when 0.5 M EAN is added, a sign that the interparticle repulsions are reduced, as well as the fact that the value of  $S(0, \Phi)$  increases. However, the interactions in the dispersions

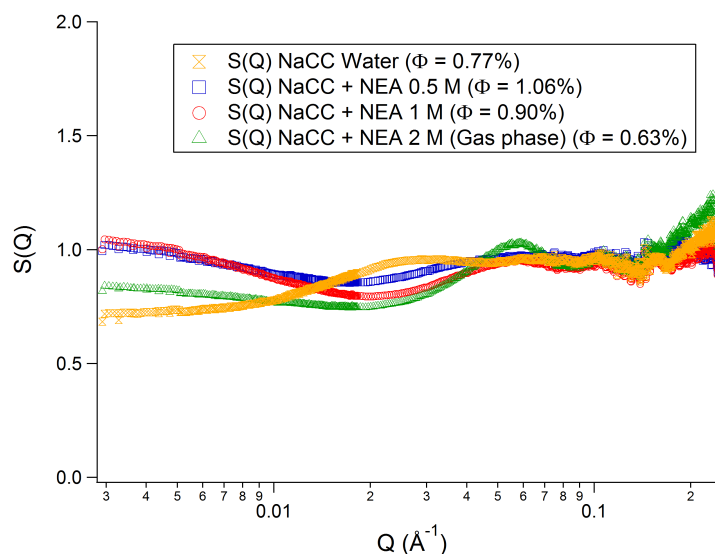


FIGURE 4.34: Structure factors for aqueous maghemite dispersions with added EAN. Large particles.

with added IL never switch into the attractive regime. The stability of these samples is confirmed by the observation of the samples by optical microscopy, with and without magnetic field.

In the case of large particles, the structure factor of the aqueous dispersion (Fig. 4.34) shows a change from globally repulsive ( $S(0, \Phi) < 1$ ) to slightly attractive ( $S(0, \Phi) > 1$ ) already at 0.5 M EAN. Once again, the stability of the sample is remarkable considered the quantity of added salt (the destabilization threshold by NaCl is even lower for large particles than for the small ones). With the addition of more IL, the interactions grow a little more attractive, and at 2 M EAN we encounter a phase separation, indicating that the destabilization threshold has been reached. The structure factor shown in Fig. 4.34 is relative to the gas phase (dilute phase) of such sample, which shows again repulsive interactions and a structure peak corresponding to the contact between particles.

Once again, the difference between the two particle sizes is evidenced in their different stability. The large particles are more easily destabilized when salt is added, since the attractive (van der Waals and magnetic dipolar) interactions are stronger than for the smaller NP. Ethylammonium nitrate, added in small quantities to the aqueous dispersions, behaves like a classic electrolyte by screening the NP surface charges and destabilising the suspensions; however, its behaviour is not exactly the same as a typical 1:1 salt such as NaCl, since both small and large particles remain stable in the presence of unusually high concentrations of added EAN. The reason is not easy to evaluate; it



may be found, for example, in the more diffuse charge density on the ethylammonium cation, which may lead to a less effective screening.

## 4.9 Conclusion

In this Chapter we investigated the behaviour of small (7 nm) and large (11 nm) citrate-covered maghemite nanoparticles with low polydispersity, dispersed in the ionic liquid EAN. The two different sizes allowed us to tune the attractive part of the interparticle potential. We also varied the concentration  $\Phi$  of the particles, the nature of the cationic counterion of citrate, and we looked into the effect of using mixed water and EAN in different proportions as a dispersing phase.

The results enlighten the presence, in our systems, of weak repulsive forces that are dominating in the case of  $\text{Na}^+$  counterions for small particles; such repulsions have been estimated in the order of about 0.3 kT. For the other counterions, the systems are characterized by globally attractive interparticle interactions, that are exacerbated by the concentration and in the case of the large particles. The latter form less stable dispersions, that encounter phase separation at a low  $\Phi$  threshold. Such threshold, together with the intensity of the attractions between NP, allows us to class the counterions according to their effect for both NP sizes.  $\text{Li}^+$  is the one generating the most intense attractions, since its samples always present a precipitate (in equilibrium with a dispersed phase) even at low  $\Phi$ ; such destabilizing role of  $\text{Li}^+$  is in agreement with the results of other authors [85, 90], however the exact mechanism lying at the origin of these ion-specific interactions is not clear.  $\text{EA}^+$ , the same cation as the IL, has an intermediate behaviour and, although its dilute samples appear stable, they are easily destabilized by the addition of water (in agreement with other works [11, 16, 27, 66]), the application of a magnetic field, and by centrifugation. Finally,  $\text{Na}^+$  imparts the suspensions with the best colloidal stability, evidenced by the repulsive interactions between small particles (even in the presence of moderate quantities of water) and a higher threshold to spinodal decomposition for the large ones. Once again, the mechanism giving place to such microstructure and interparticle potential is unclear. It is difficult to compare our work to the literature since there have been very few studies investigating the effect of added salt in NP/IL colloidal systems, most of which deal with lithium due to its importance for electrochemical applications.

The case of  $\text{Li}^+$  being quite peculiar, it was investigated during its temporal evolution after preparation, to learn more about the partial redispersion process that characterized its precipitates and their equilibrium with the dispersed phases. Once again, the size of the particles tunes the attractions and gives place to different microstructures. On one hand, small particles form fragile clusters that break down over time, leaving dispersed aggregates of a few particles; on the other hand, large NP (characterized by stronger attractions) form big, dense aggregates that precipitate irreversibly, leaving only single NP in the dispersed fraction.

In conclusion, the results presented here show the huge importance of the composition of the interface on the interaction potential between nanoparticles dispersed in an ionic liquid, and prove the existence of repulsive forces (probably of electro-steric/solvation origin) in ILs even in the absence of large stabilizing molecules such as surfactants, despite the alleged annihilation of electrostatic interactions often cited in the literature.

## Chapter 5

# Tests with Cholinium-based Ionic Liquids

### Contents

---

<b>5.1 Introduction</b> . . . . .	<b>139</b>
<b>5.2 Dispersion of Maghemite Nanoparticles in Cholinium-Aminoacid ILs</b> . . . . .	<b>142</b>
<b>5.3 Dispersions of Maghemite in Water/[Cho][Gly] Media</b> . . . . .	<b>144</b>
<b>5.4 Conclusion</b> . . . . .	<b>145</b>

---

### 5.1 Introduction

The final step of the work described in this Thesis is to use the knowledge acquired in the study of the EAN model for the preparation of greener systems, using biocompatible ILs as a dispersing medium for maghemite nanoparticles. Indeed, ionic liquids are renowned “green solvents”, but their real impact on the environment and on living organisms is not always that clear [41]. One of the main principles of green chemistry pleads to “design synthetic methods to use and generate substances that minimize toxicity to human health and the environment” [113]. Therefore, for ILs to be truly “green” compounds, their toxicity should be low, and their preparation should start from renewable natural sources, possibly proceeding *via* simple routes (for example, acid-base reactions, of which the only by-product is water).

Attempts at obtaining eco-friendly ionic liquids were made, among others, by Carter *et al.* [114] and by Fukumoto *et al.* [115]. The authors of [114] obtained salts melting

below 100 °C by combining *onium* cations (among which the classic substituted imidazoliums and pyridiniums) with the anions of the sweeteners saccharin and acesulfame: these are of widespread use in foodstuffs as non-nutritive sweeteners, and thus possess well established toxicological profile. In [115], Room-Temperature ILs are prepared from 20 natural amino acids *via* acid-base reactions, using as a neutralizing agent 1-ethyl-3-methylimidazolium hydroxide. The ILs obtained in these works surely have interesting physico-chemical properties, and the chosen anions are bound to reduce their possible toxicity and environmental impact, but often it is the head group of IL cations that has a deciding role in toxicity [116]; in this case, due to the presence of the rather suspect imidazolium cation, and in the absence of complete cytotoxicity studies, nothing certain can be said beyond hypotheses. What is known about imidazolium ILs is that they have low biodegradability, as shown by the results of a work by Gathergood *et al.* [117] on a large number of ILs based on the imidazolium cation, most of them liquid at room temperature. In this work, none of the studied ILs show higher biodegradability than the common surfactant SDS (sodium dodecyl sulfate). The authors found a higher biodegradability for the ILs incorporating an ester group, which is a cleavage site for enzymatic attack, as confirmed by a similar study on ionic liquids with a substituted pyridinium cation [118]. On the other hand, in [117] the [BMIM]-derived ILs containing an amide in the side chain show poor biodegradation. Finally, the most widely used methylimidazolium ionic liquids, [BMIM][BF<sub>4</sub>] and [BMIM][PF<sub>6</sub>] are found to show no biodegradation at all.

It becomes evident that, among the available *onium* cations, imidazolium and pyridinium are not always the best choice for the production of eco-friendly chemical systems. In 2003, Abbott *et al.* first reported [119] the preparation of eutectic solvents from mixtures of hydroxyethyltrimethylammonium (cholinium, Fig. 5.1) chloride with urea. In fact, room-temperature molten salts have been obtained for a long time from eutectic mixtures (for example, by mixing quaternary ammonium salts with metal salts): the decrease in the freezing point of these systems derives from a deep eutectic, resulting from the formation of complex ions and a subsequent decrease in the lattice energy. In [119], a whole variety of amide compounds, among which urea, are mixed with cholinium chloride in a 2:1 mole ratio. As a result, only those compounds capable of forming hydrogen bonds with chloride ions result in the formation of a homogeneous liquid, with a significant decrease in the freezing point compared to the pure amide.

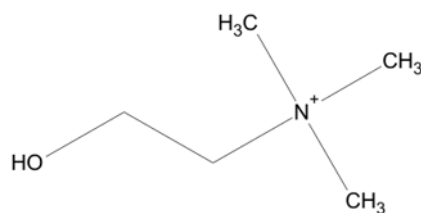


FIGURE 5.1: The cholinium cation.

Besides eutectic mixtures, biodegradable ILs have been obtained by coupling the cation of choline with different anions. Yu *et al.* [120] prepared Room-Temperatures ILs by the association of cholinium with naphthenic acids, which show excellent biodegradability. With phosphate anions [121], low toxicity ILs are obtained, that could be used as co-formulation stabilizers within slow-release pharmaceutical preparations. Petkovic *et al.* [116] prepared ILs from choline and alkanooates, and verified their toxicity and biodegradability on penicillin-derived fungal isolates: the anion toxicity depends on the length of the linear chain (ethanoate < propanoate < ... < decanoate), and the biodegradability appears to be strongly concentration-dependent. The association of choline with the sweeteners acesulfame and saccharine also yields low-toxicity ILs [122]. Some of these ILs have already been employed as co-substrates in the biodegradation of an azo dye in aqueous solution [123]. Choline has also been used to obtain an IL with the photosensitizer Purpurin-18 [124], used as a stabilizer for gold nanoparticles to be employed in photodynamic and photothermal therapy against cancer.

All the cholinium-based ILs mentioned above could be good candidates to be used in this work due to their low toxicity; however, some of them present inconveniences. For example, cholinium saccharinate and acesulfamate are extremely viscous: 328 mPa s (at 70 °C) for cholinium saccharinate (which is not liquid at room temperature) and 1072 mPa s (at 25 °C) for cholinium acesulfamate [122]. Also, since the most readily available source of acesulfamate is the commercial product AcesulfameK (potassium salt), the reaction medium is polluted with alkali salts and the synthesized IL needs to be purified through a costly and long procedure involving ion-exchange resins. High viscosity is a property also shared by cholinium alkanooate ILs, and is assumed to derive from a strong hydrogen bonding characteristic of many choline-based ILs [125].

In the framework of this Thesis, we choose to associate the benign cholinium cation with natural aminoacids. These ILs have already been employed as solvents for the

selective extraction of lignin in rice straw [126]. They are also characterized by high viscosities; however, in the case of the compounds obtained with glycine and alanine (respectively: [Cho][Gly] and [Cho][Ala]) such viscosity is acceptable (respectively 121 mPa s and 163 mPa s at 25 °C) and the ILs are indeed liquid at room temperature [127]. Both products show good thermal stability (respective degradation temperatures are 150 °C and 159 °C). Most importantly, the synthesis of [Cho][Gly] and [Cho][Ala] can proceed *via* a simple route involving the neutralization of choline hydroxide with the amino acid, which are renewable biomaterials, leaving only water as by-product: this clearly classifies as a *green* procedure. We report here the synthesis and the first results on the dispersion of maghemite nanoparticles in these new media.

## 5.2 Dispersion of Maghemite Nanoparticles in Cholinium-Aminoacid ILs

The ionic liquids [Cho][Gly] and [Cho][Ala] are synthesized and purified as described in Subsection 2.2.6. They are characterized by means of <sup>1</sup>H-NMR and FT-IR spectra to assess their purity. The density measurements give 1.14 g cm<sup>-3</sup> for [Cho][Gly] and 1.12 g cm<sup>-3</sup> for [Cho][Ala] at 25 °C. Karl Fischer titrations allow us to evaluate the hygroscopicity of these ILs: right after preparation they contain about 1 wt% water, a content which increases slowly over time for the IL left in contact with ambient air, reaching 5 wt% after 2 days.

The neat ILs, lyophilized, are used as dispersing media for maghemite nanoparticles. The dispersions are prepared according to process 1 (see Subsection 2.2.7) by mixing an aqueous ferrofluid with [Cho][Gly] or [Cho][Ala] in a 10:90 weight ratio, in order to have  $\Phi \approx 0.1\%$ . For this scope, both acidic (positively charged surface, nitrate counterions) and citrated (with sodium counterions) particles are used, and with both sizes, *i.e.*, 7 and 11 nm. As a result, all types of particles flocculate more or less rapidly in [Cho][Ala]. On the other hand, stable dispersions are obtained in [Cho][Gly], especially in the case of small particles; therefore, we attempt the preparation of dispersions 10 times more concentrated ( $\Phi \approx 1\%$ , obtained by mixing the aqueous ferrofluid and the IL in a 1:1 weight ratio). The colloidal stability of the samples is assessed by visual observation, and the results are summarized in Table 5.1.

<b>Dispersions of maghemite NP in [Cho][Gly]</b>		
Type of particles:	Acidic	Citrated
Small (7 nm), $\Phi \approx 0.1\%$	stable	stable
Small (7 nm), $\Phi \approx 1\%$	stable	stable
Large (11 nm), $\Phi \approx 0.1\%$	partial	partial
Large (11 nm), $\Phi \approx 1\%$	partial	partial

TABLE 5.1: Dispersions of maghemite NP in [Cho][Gly], acidic and covered with sodium citrate, with two different particle sizes. Observations recorded 4 days after preparation.

Dispersions of small particles are stable in [Cho][Gly] for both types of surface functionalization and both concentrations. This result stands out in comparison to what we found for the ionic liquid EAN, since in the latter IL acidic particles always ended up flocculating. On the other hand, 11 nm NP are only partially stable in [Cho][Gly] (*i.e.*, a precipitate coexists with a dispersed fraction). Probably, in the case of large particles the dipolar interactions become too strong to ensure good colloidal stability.

### SAXS Analysis of Small NP Dispersions in [Cho][Gly]

SAXS experiments are performed on the two stable suspensions of acidic and citrated maghemite nanoparticles dispersed in [Cho][Gly] with  $\Phi \approx 1\%$ . The measurements are carried out at the LIONS laboratory (CEA Saclay, France) on a home-made SAXS apparatus. The samples are enclosed in quartz capillaries with a thickness of 1 mm. Lupolen polymer is used as a reference to obtain the intensity in absolute unit. The scattering curves are therefore presented in Figure 5.2.

The curve relative to the citrated NP in Figure 5.2 is fitted by a form factor of spheres with lognormal size distribution, characterized by the radius  $R_0 = 2.7$  nm and the polydispersity  $\sigma = 0.29$ . Such distribution is very similar to the one found for  $\text{Na}_3\text{Cit-NP}$  dispersed in water ( $R = 3.0$  nm,  $\sigma = 0.28$ ), showing that these particles are homogeneously dispersed in [Cho][Gly]. The sample was also analysed in the wide-angle (WAXS) range, where we can observe a correlation peak at  $1.5 \text{ \AA}^{-1}$  pertaining to the solvent. The characteristic distance of this peak corresponds to  $4.5 \text{ \AA}$ , indicating the existence of a nanoscale organization of the ionic liquid.

The scattering curve of the acidic particles, evidently, cannot be fitted by the same function as the citrated NP. In the present case, we use a form factor of cylinders with polydisperse radius, which yields  $R_0 = 2.4$  nm,  $\sigma = 0.25$  for the circular section, and  $L = 24.0$  nm as the length of the cylinder. It appears that acidic particles in

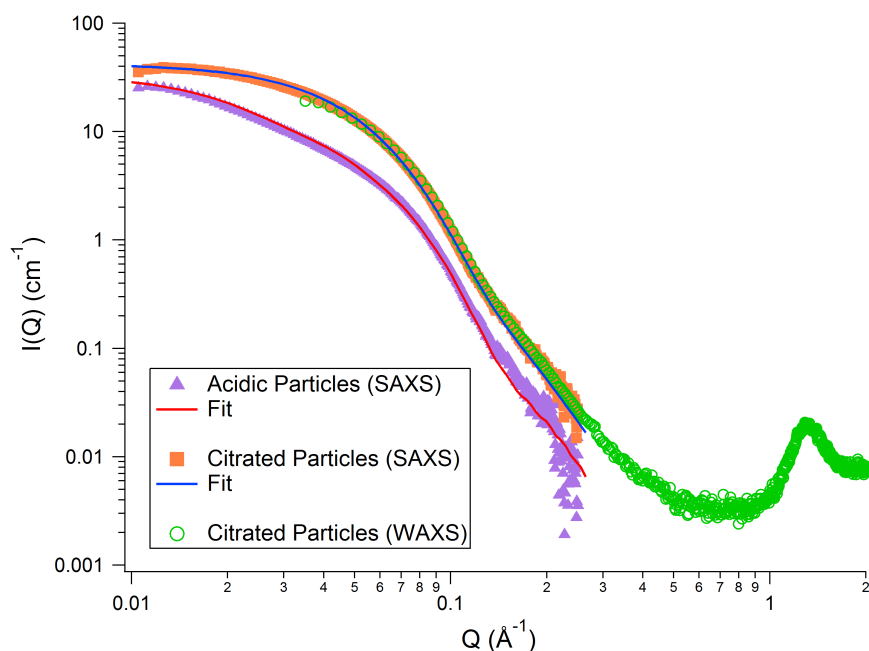


FIGURE 5.2: SAXS scattered intensities for small NP (acidic and citrated) dispersions in [Cho][Gly]. The samples have  $\Phi \approx 1\%$ .

[Cho][Gly] actually form aggregates of finite size, with a length corresponding to about 4 nanoparticles. Despite the aggregation, the suspension does not show any precipitate.

### 5.3 Dispersions of Maghemite in Water/[Cho][Gly] Media

For the sake of comparison with the previous results obtained with EAN, we now focus on the suspensions of NP covered with sodium citrate, and verify the effect of the water/IL ratio on the colloidal stability. The results of the visual observations 4 days after the preparation of the samples are summarized in Table 5.2.

**Dispersions of maghemite NP in [Cho][Gly] and its aqueous mixtures**

Particle Size:	Small	Large
[Cho][Gly] = 0 wt%	stable	stable
[Cho][Gly] = 20 wt%	partial	partial
[Cho][Gly] = 50 wt%	stable	partial
[Cho][Gly] = 70 wt%	stable	partial
[Cho][Gly] = 90 wt%	stable	partial
[Cho][Gly] = 100 wt%	stable	partial

TABLE 5.2: Dispersions of small and large citrated maghemite NP in [Cho][Gly] and its aqueous mixtures, as observed 4 days after preparation. All samples have a NP volume fraction of  $\Phi \approx 0.1\%$ .



Large particles are homogeneously dispersed only in water, while the suspensions in pure [Cho][Gly] and all its mixtures with water present a certain amount of precipitate. This is once again associated to the size, leading to stronger dipolar interactions between particles and the formation of non-dispersible aggregates.

The results for small particles evidence a destabilization of the aqueous suspension as the IL is added in low quantity. This behaviour is as expected, since the dilute IL simply behaves as any electrolyte by screening the surface charges of the particles and destabilizing their dispersions. However, as the [Cho][Gly] content increases, the dispersions are stabilized again. This is reminiscent of the behaviour in EAN, therefore we cannot exclude the possibility that the repulsive forces recorded in Na<sub>3</sub>Cit-NP/EAN samples (see 4.5.2) may exist here as well. Among the dispersions of small particles, those with low enough viscosities could be studied by means of DLS. The viscosities were measured in the neat IL/water mixtures (without particles). The NP suspension containing 50 wt% IL ( $\eta = 7.73$  mPa s at 20 °C, measured in our laboratory) is characterized by two populations of objects: one has an average hydrodynamic diameter of 10 nm, and is also found in the pure water sample, while the other is centred around 60 nm, indicating the presence of aggregates in the suspension. Indeed, a few weeks later the observation of vial reveals a precipitate on the bottom. The sample with 70 wt% IL ( $\eta = 31.2$  mPa s at 20 °C, also measured in our laboratory) has only one population of dispersed objects, with an average size of 10 nm; no large aggregates are present anymore. The dispersions with a higher content of [Cho][Gly] could not be analysed, since their viscosity was too high to perform a DLS experiment. Nevertheless, the present DLS results confirm the visual observations of Table 5.2, while the SAXS curve for the sample at 100 wt% [Cho][Gly] (described in the precedent Section) shows a very good and homogeneous dispersion in the pure IL. Also, two months after their preparation the samples are still unchanged and no precipitation has occurred in the suspensions with high [Cho][Gly] content.

## 5.4 Conclusion

In this final Chapter, we attempted to adapt the methods and the knowledge acquired previously with EAN to new, “greener” ionic liquids. Our choice has fallen on cholinium glycinate, [Cho][Gly], and cholinium alaninate, [Cho][Ala], which are biocompatible ILs produced from renewable natural sources and synthesized *via* a simple route that yields

only water as secondary product. These ILs are endowed with acceptable viscosities and good thermal stability. Moreover, cholinium-based ILs have already been used as stabilizers for nanoparticles to be employed in anti-cancer therapy [124].

Between the two, [Cho][Gly] has proven easier to purify and manipulate, and a much better dispersant for maghemite nanoparticles. In particular, NP of small size (7 nm) yield stable dispersions in [Cho][Gly] at  $\Phi \approx 0.1\%$  and  $\Phi \approx 1\%$ , and in most of its mixtures with water. The homogeneous state of dispersions could be proven, in different samples, by SAXS and DLS experiments. This ionic liquid is therefore a good candidate for eco-friendly applications in which homogeneous maghemite dispersions are required.

There is, however, a lot left to do. The systems need a more complete characterization, especially from a rheological point of view. Prospective work includes verification of the long-term stability of the samples (since choline is biodegradable, its solution are quickly spoiled, especially if stored at ambient conditions), investigations on the possible existence of a pH scale, characterization of the free/bound equilibrium of citrate and the distribution of its counterion, verification of the effects of different counterions for citrate, study of the interparticle interactions... Also, at present the synthesis of this IL is followed by its purification using a mixture of methanol and acetonitrile, of which the first is especially well-known for its toxicity. One step to be taken in the future will then be the replacement of this solvent with another of low or no toxicity, in order for these systems to fully deserve the “green” appellation.

# Conclusions and Perspectives

The goal of this Thesis was to study the mechanisms leading to colloidal stability in ionic liquids, in order to understand which parameters control the microstructure of such systems, whether the classical theories and equations used to describe typical colloids can be applied to ILs, and how to tune these systems depending on their desired final application. In order to answer these questions, we focused on a model system made of two components that have been thoroughly characterized separately. The IL chosen as a dispersing phase was ethylammonium nitrate (EAN), one of the oldest ILs, known for its similarity with water. The nanoparticles were magnetic iron oxide in the maghemite form, synthesized in water *via* a coprecipitation method, which offer the opportunity to study the interparticle interactions in different media. Once their surface properties were adequately tuned in water, the solvent in which we are able to control their stability, we transferred the particles to the ionic liquid EAN.

In the first part of this work, we established the protocol for the successful transfer of the NP from water to EAN, starting from aqueous dispersions with a high polydispersity of the particles' size. Chapter 3 describes the tests we performed to understand the behaviour of the particles with different types of surface functionalization: the systems we probed were characterized by different signs and densities of NP surface charge, adsorption of citrate anions, different counterions. These particles were mixed not only with the neat IL but also its mixtures with water. The colloidal stability was first assessed by simple visual observation and by FAAS analysis of iron, yielding the quantity of dispersed particles in the samples. As a result, the impossibility of dispersing uncharged particles (at the PZC) demonstrated the necessity of a charged surface in order to stabilize maghemite NP in EAN. However, acidic (positively charged) and basic (negatively charged) NP were not very stable in EAN or EAN/water mixtures, while citrated NP showed the best colloidal stability in such media. The microscopic investigation (by means of SANS and DLS) of the suspensions obtained in neat EAN evidenced a peculiar behaviour (redispersion of aggregates over time) of those particles for which lithium had been introduced as a counterion for citrate.

In Chapter 4, we moved on to a more detailed investigation of the maghemite/NP

systems. We chose to use two different sizes of NP, each with low size polydispersity: this enabled us to tune the interparticle attractions, due to the van der Waals and magnetic dipolar forces, which are stronger for large NP. We also studied the effect of increasing the NP volume fraction  $\Phi$ , and used three different counterions for citrate: sodium because of its extensive use in water, lithium for its particular behaviour, and ethylammonium as the same cation as the IL solvent. The samples were characterized by means of SAXS and magneto-optic birefringence experiments.

The effect of the counterion is already evident in the aforementioned peculiar behaviour of lithium, which turned out to vary with the size of the particles. We studied the temporal evolution of these samples by SAXS, in order to better understand why their precipitate would redisperse. In the case of small NP, we could observe the formation of large clusters, but fragile, which were broken down over time, allowing for the redispersion of small (dimeric) aggregates. On the other hand, large particles, thanks to the stronger attractive interactions between them, formed more solid aggregates that could not be redispersed; the observed increase of  $\Phi$  in the supernatant was, in this case, due to the redispersion of single NP. This points out the fundamental role of the attractive interactions in our media.

However, the other two counterions,  $\text{Na}^+$  and  $\text{EA}^+$ , also had each a different behaviour, depending on the size and the concentration of the NP. Small particles gave place to stable dispersions in EAN even at high concentration ( $\Phi \approx 8\%$ ), which enlightened striking differences between the counterions of citrate. Indeed, when increasing  $\Phi$ , the interparticle interactions became more repulsive with  $\text{Na}^+$ , more attractive with  $\text{EA}^+$  and strongly attractive with  $\text{Li}^+$ . In the latter case, we could observe the formation of aggregates of non-finite size, but fragile and easily broken by a magnetic field, probably built through the DLCA process. Concerning the repulsions taking place in the presence of sodium, they were estimated to be in the order of magnitude of  $0.3 kT$ . In the case of large particles, something different was found: as we tried to concentrate them, the dispersions gave place to a phase separation into a colloidal gas (dilute dispersion) and a colloidal liquid (concentrated and very viscous suspension). This behaviour is typical of colloidal systems governed by long-range attractions, which is consistent with the larger size of the NP and the stronger attractive forces existing between them. Such phase separation was encountered at different  $\Phi$  thresholds, following the order  $\text{Na}^+ > \text{EA}^+ > \text{Li}^+$ . Therefore, dispersions with sodium counterions were once again the

most stable, and those with lithium the least stable. It must be said that the difference between  $\text{Na}^+$  and  $\text{EA}^+$  had not been ascertained in the previous experiments involving polydisperse NP, in which only lithium appeared to behave differently from the other counterions. Indeed, such difference was not evident in the dilute samples. This suggests that more types of behaviours could be observed by concentrating the dispersions with other counterions (for example  $\text{K}^+$ ,  $\text{Cs}^+$  and  $\text{Ca}^{2+}$ ), maybe evidencing a sort of Hofmeister series of cations, and it would be interesting to pursue the investigations in this direction.

The question arising spontaneously concerns the origin of such different effects. In order to shed more light on the matter, we analysed the composition of the interface. We were able to determine the amount of citrate's counterions at the NP surface, which turns out to be of the same order of magnitude as the typical surface charge density in aqueous dispersions ( $1.6$  cations/ $\text{nm}^2$ ). The concentration of free citrate is also consistent with the one typically found in water (in the order of  $0.01$  mol  $\text{L}^{-1}$ ), hinting at the fact that the interface of maghemite nanoparticles is not (or only slightly) modified during the transfer from water to EAN. Therefore, since the cations introduced with citrate do stay close to the NP surface, the different behaviours observed in the colloidal systems must be related to the specific counterion located at the interface. However, at present we do not know exactly which properties of each counterion are linked to the different interparticle interactions arising in our systems. For example, the existence of repulsive forces in the  $\text{Na}_3\text{Cit-NP}$  samples is a fact, but we do not have any further information on their origin. We can suppose that they arise from the structuration of EAN in layers at the interface, as proven by many surface force studies involving ILs in contact with flat surfaces.

The interactions between particles are also influenced by the presence of water in the samples. Dispersions in EAN with growing water content were analysed by SAXS for both particle sizes and with the counterions sodium and ethylammonium. As a result, with growing  $\text{H}_2\text{O}$  concentration the interactions became more repulsive in the presence of  $\text{Na}^+$  and more attractive when  $\text{EA}^+$  is present. Once again, the effect observed is strongly ion-specific. However, considering the initial water content (about 1 wt%) of our "pure EAN" dispersions, assuming a preferential interaction of water with the surface of the particles, a rapid calculation showed that the surface would be already completely covered by one layer of water molecules. Therefore, if the interactions depend on the

composition of the interface, we cannot explain why they vary in such a striking manner when more water is added.

As the last step, in Chapter 5 we adapted the methods and the knowledge acquired with EAN to new, “greener” ionic liquids. We focused on cholinium glycinate, [Cho][Gly], a biocompatible IL produced from renewable natural sources and synthesized *via* a simple route that yields only water as secondary product. Maghemite nanoparticles of small size (7 nm) yielded stable dispersions in [Cho][Gly] at  $\Phi \approx 0.1\%$  and  $\Phi \approx 1\%$ , and in most of its mixtures with water. The homogeneous state of dispersion could be proven, in different samples, by SAXS and DLS experiments. This ionic liquid is therefore a good candidate for eco-friendly applications in which homogeneous maghemite dispersions are required. Perspective work involves a more complete characterization of the systems, verification of the long-term stability of the samples, and the replacement of methanol (used during the purification stage) with a different solvent of low or no toxicity, in order for these systems to fully deserve the “green” appellation.

## Appendix A

# Dispersions of Different Nanoparticles in Ionic Liquids

This table aims to resume, in a schematic fashion, the dispersions of nanoparticles in ionic liquids described in Section [1.4.2](#), and it is meant as a supporting document for the reader who may wish to rapidly retrieve a particular NP/IL system in the literature. For each material, all the ionic liquids in which such nanoparticles have been dispersed are listed, along with the NP size and surface composition. Finally, the state of dispersion is noted (unstable: the particles flocculate immediately or almost so; bad: the dispersion is only partially stable, with a coexisting precipitate, or it is stable only on a short period of time; good: the particles are completely dispersed and stable over time; gel: a physical gel is formed). In every single case, the paper reporting the system described is referred to.

Dispersions of Metal and Oxide Particles in Ionic Liquids

Material	Dispersing IL	Surface Functionalization	NP Diameter	Stability	Reference
Gold, Au <sup>0</sup>	[BMIM][PF <sub>6</sub> ]	bare	~ 50 nm	unstable	[12]
	[BMIM][PF <sub>6</sub> ]	bare	2 nm	unstable	[27]
	[BMIM][PF <sub>6</sub> ]	IL homopolymer	8-12 nm	good	[9]
	[BMIM][NTf <sub>2</sub> ]	IL homopolymer	8-12 nm	good	[9]
	[BMIM][NTf <sub>2</sub> ]	bare	2 nm	unstable	[27]
	[BMIM][BF <sub>4</sub> ]	bare	2 nm	unstable	[27]
Platinum, Pt <sup>0</sup>	[BMIM][N(CN) <sub>2</sub> ]	bare	2 nm	unstable	[27]
	[BMIM][PF <sub>6</sub> ]	IL homopolymer	1.5-4 nm	good	[9]
Palladium, Pd <sup>0</sup>	[BMIM][NTf <sub>2</sub> ]	IL homopolymer	1.5-4 nm	good	[9]
	[BMIM][PF <sub>6</sub> ]	IL homopolymer	1.5-3.5 nm	good	[9]
	[BMIM][NTf <sub>2</sub> ]	IL homopolymer	1.5-3.5 nm	good	[9]
Iron, Fe <sup>0</sup>	[EMIM][EtSO <sub>4</sub> ]	bare	1.0 μm	bad	[70]
	[EMIM][EtSO <sub>4</sub> ]	silica	1.4 μm	good	[70]
	[EMIM][Et <sub>2</sub> PO <sub>4</sub> ]	bare	1.0 μm	bad	[70]
	[EMIM][Et <sub>2</sub> PO <sub>4</sub> ]	silica	1.4 μm	good	[70]
Maghemite, γ-Fe <sub>2</sub> O <sub>3</sub>	[EMIM][Ac]	bare	8-12 nm	good	[11]
	[EMIM][Ac]	AA <sub>10-b</sub> -AM <sub>14</sub>	8-12 nm	good	[11]
	[EMIM][SCN]	AA <sub>10-b</sub> -AM <sub>14</sub>	8-12 nm	good	[11]

Maghemite, γ-Fe<sub>2</sub>O<sub>3</sub>



Dispersions of Metal and Oxide Particles in Ionic Liquids

Material	Dispersing IL	Surface Functionalization	NP Diameter	Stability	Reference
	[EMIM][SCN]	AA <sub>10-b</sub> -AM <sub>14</sub>	8-12 nm	unstable	[11]
	[BMIM][BF <sub>4</sub> ]	bare	10 nm	good	[16]
	[BMIM][BF <sub>4</sub> ]	bare	8-12 nm	bad	[11]
	[BMIM][BF <sub>4</sub> ]	AA <sub>10-b</sub> -AM <sub>14</sub>	8-12 nm	unstable	[11]
	[BMIM][NTf <sub>2</sub> ]	IL ion	10 nm	good	[67]
	EAN	AA <sub>10-b</sub> -AM <sub>14</sub>	8-12 nm	unstable	[11]
	EAN	AA <sub>10-b</sub> -AM <sub>14</sub>	8-12 nm	good	[11]
	[EMIM][EtSO <sub>4</sub> ]	bare	9 nm	unstable	[14]
	[EMIM][EtSO <sub>4</sub> ]	bare	~ 1 μm	bad	[69]
	[EMIM][EtSO <sub>4</sub> ]	oleate	9 nm	good	[14]
	[EMIM][Et <sub>2</sub> PO <sub>4</sub> ]	bare	~ 1 μm	bad	[69]
	[BMIM][NTf <sub>2</sub> ]	bare	~ 1 μm	bad	[69]
	[BMIM][NTf <sub>2</sub> ]	IL ion	10 nm	good	[67]
Magnetite, Fe <sub>3</sub> O <sub>4</sub>	[BMIM][PF <sub>6</sub> ]	bare	~ 1 μm	good	[69]
	[BMIM][BF <sub>4</sub> ]	bare	~ 1 μm	bad	[69]
	[HMIM][Cl]	bare	~ 1 μm	bad	[69]
	[P <sub>14,6,6,6</sub> ][Cl]	bare	~ 1 μm	good	[69]
	[P <sub>14,6,6,6</sub> ][N(CN) <sub>2</sub> ]	bare	~ 40 nm (DLS)	soft gel	[78]

Dispersions of Metal and Oxide Particles in Ionic Liquids

Material	Dispersing IL	Surface Functionalization	NP Diameter	Stability	Reference
	$[P_{14,6,6,6}][N(CN)_2]$	allyltrimethoxysilane	162 nm	hard gel	[78]
	$[P_{14,6,6,6}][N(CN)_2]$	3-mercaptopropyl trimethoxysilane	188 nm	hard gel	[78]
	[EMIM][EtSO <sub>4</sub> ]	bare	20 nm	unstable	[68]
Cobalt Ferrite, CoFe <sub>2</sub> O <sub>4</sub>	[EMIM][EtSO <sub>4</sub> ]	oleate	20 nm	good	[68]
	[BMIM][NTf <sub>2</sub> ]	IL ion	10 nm	good	[14]
	[EMIM][NTf <sub>2</sub> ]	bare	5 nm	bad	[71]
	[EMIM][NTf <sub>2</sub> ]	bare	6 nm	good	[71]
	[EMIM][NTf <sub>2</sub> ]	bare	8 nm	bad	[71]
	[EMIM][NTf <sub>2</sub> ]	bare	13 nm	unstable	[71]
	[EMIM][NTf <sub>2</sub> ]	bare	25 nm	unstable	[71]
	[EMIM][BF <sub>4</sub> ]	bare	5 nm	bad	[71]
	[EMIM][BF <sub>4</sub> ]	bare	6 nm	good	[71]
	[EMIM][BF <sub>4</sub> ]	bare	8 nm	bad	[71]
	[EMIM][BF <sub>4</sub> ]	bare	13 nm	unstable	[71]
	[EMIM][BF <sub>4</sub> ]	bare	25 nm	unstable	[71]
	[BMPy][NTf <sub>2</sub> ]	IL ion	~ 5 nm	gel $\xrightarrow{wt\%}$ glass	[77]
	[EMIM][NTf <sub>2</sub> ]	-OH	12 nm	gel	[72]
	[EMIM][NTf <sub>2</sub> ]	-OH	12 nm	gel	[73]
Titania, TiO <sub>2</sub>					
Silica (Ludox)					

Dispersions of Metal and Oxide Particles in Ionic Liquids

Material	Dispersing IL	Surface Functionalization	NP Diameter	Stability	Reference
	[EMIM][NTf <sub>2</sub> ]	-CH <sub>3</sub>	12 nm	gel	[73]
	[EMIM][EtSO <sub>4</sub> ]	-OH	12 nm	gel	[73]
	[EMIM][EtSO <sub>4</sub> ]	-CH <sub>3</sub>	12 nm	gel	[73]
	[E-OH-MIM][NTf <sub>2</sub> ]	-OH	12 nm	sol	[73]
	[E-OH-MIM][NTf <sub>2</sub> ]	-CH <sub>3</sub>	12 nm	gel	[73]
	[EMIM][BF <sub>4</sub> ]	-OH	12 nm	gel	[73]
	[EMIM][BF <sub>4</sub> ]	-CH <sub>3</sub>	12 nm	gel	[73]
	[BMIM][BF <sub>4</sub> ]	-OH	12 nm	sol	[73]
	[BMIM][BF <sub>4</sub> ]	-CH <sub>3</sub>	12 nm	gel	[73]
	[BMIM][PF <sub>6</sub> ]	-OH	12 nm	gel	[73]
	[BMIM][PF <sub>6</sub> ]	-CH <sub>3</sub>	12 nm	gel	[73]
	[BMIM][SCN]	-OH	12 nm	gel	[73]
	[BMIM][SCN]	-CH <sub>3</sub>	12 nm	gel	[73]
	[BMIM][N(CN) <sub>2</sub> ]	-OH	12 nm	gel	[73]
	[BMIM][N(CN) <sub>2</sub> ]	-CH <sub>3</sub>	12 nm	gel	[73]
	[BMIM][CF <sub>3</sub> SO <sub>3</sub> ]	-OH	12 nm	gel	[73]
	[BMIM][CF <sub>3</sub> SO <sub>3</sub> ]	-CH <sub>3</sub>	12 nm	gel	[73]
	[BMIM][CF <sub>3</sub> CO <sub>2</sub> ]	-OH	12 nm	gel	[73]

Dispersions of Metal and Oxide Particles in Ionic Liquids

Material	Dispersing IL	Surface Functionalization	NP Diameter	Stability	Reference
	[BMIM][CF <sub>3</sub> CO <sub>2</sub> ]	-CH <sub>3</sub>	12 nm	gel	[73]
	[DEME][BF <sub>4</sub> ]	-OH	12 nm	gel	[73]
	[DEME][BF <sub>4</sub> ]	-CH <sub>3</sub>	12 nm	gel	[73]
	[EMIM][NTf <sub>2</sub> ]	-OH	62 nm	unstable	[10]
	[EMIM][NTf <sub>2</sub> ]	PMMA	62 nm	good	[10]
	[EMIM][NTf <sub>2</sub> ]	PMMA	120 nm	sol $\xrightarrow{wt\%}$ gel	[74]
	[EMIM][NTf <sub>2</sub> ]	PBnMA	120 nm	sol $\xrightarrow{wt\%}$ gel	[75]
	[BMIM][NTf <sub>2</sub> ]	-OH	62 nm	unstable	[10]
	[BMIM][NTf <sub>2</sub> ]	PMMA	62 nm	good	[10]
	[BMIM][BF <sub>4</sub> ]	-OH	62 nm	unstable	[10]
	[BMIM][BF <sub>4</sub> ]	PMMA	62 nm	unstable	[10]
	[BMIM][PF <sub>6</sub> ]	-OH	62 nm	unstable	[10]
	[BMIM][PF <sub>6</sub> ]	PMMA	62 nm	good	[10]
	[OMIM][NTf <sub>2</sub> ]	-OH	62 nm	unstable	[10]
	[OMIM][NTf <sub>2</sub> ]	PMMA	62 nm	good	[10]

Silica (amorphous)

TABLE A.1

# Appendix B

## Small Angle Scattering Techniques

### B.1 Theoretical Principles

Small Angle Scattering is a technique that allows the retrieval of information on the nanoscale structure of a sample, based on the scattering of a neutron or X-ray beam. The theoretical principle is the same for both SANS and SAXS [98]:

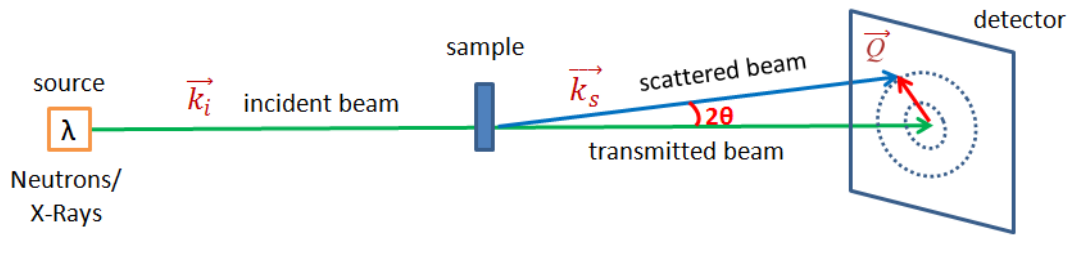


FIGURE B.1: The principle of small angle scattering.

an incident beam of radiation, described by the wave vector  $\vec{K}_i$  whose module is  $2\pi/\lambda$ , travels across the sample and interacts with the matter that constitutes it; in particular, X-rays interact with the electrons in the sample, while neutrons interact with the nuclei. Such interaction is followed by several phenomena, but the one in which we are interested here is scattering. The scattered intensity is represented by the vector  $\vec{K}_s$ . The angle formed between these two vectors is  $2\theta$ ; the difference vector,  $\vec{S}$ , is defined as  $\vec{K}_s - \vec{K}_i$ , its module being equal to  $S = 2 \sin \theta / \lambda$ . The vector  $\vec{Q}$ , more commonly used, is defined from  $\vec{S}$ , and its module is

$$Q = 2\pi S = \frac{4\pi \sin \theta}{\lambda} \quad (\text{B.1})$$

The differential scattering cross section,  $d\sigma/d\Omega$ , corresponds to the scattered intensity in the solid angle  $d\Omega$ . The total scattering cross section will then be:

$$\sigma_T = \int \frac{d\sigma}{d\Omega} d\Omega \quad (\text{B.2})$$

The scattered intensity in the direction of the scattering vector  $\vec{Q}$ , in the solid angle  $d\Omega$ , is proportional to the differential scattering cross section through the photons flux  $\Phi_0$ :

$$dI \approx \Phi_0 \frac{d\sigma}{d\Omega} d\Omega \quad (\text{B.3})$$

In the case of X-rays, the incident beam is a wave, characterised by a wavelength  $\lambda$  of the order of the ångström; as an electromagnetic wave, the X-ray beam will interact more strongly with charged particles at the atomic scale, *i.e.*, electrons and protons. However, the differential scattering cross section depending on the inverse square power of the mass, the interaction of x-rays with protons is negligible, and the only effective contribution to the scattered intensity comes from the interaction with electrons. For an isolated atom, the differential scattering cross section will be proportional to the electron cloud polarizability  $\alpha$ , as evidenced in the following equation, often referred to as the Rayleigh ratio:

$$\frac{d\sigma}{d\Omega} = \frac{\pi^2 \alpha^2}{\lambda^4} \left( \frac{1 + \cos^2 2\theta}{2} \right) \quad (\text{B.4})$$

Neutrons, on the other hand, are particles of non-negligible mass, characterized by their kinetic energy; their wavelength can then be defined by the De Broglie equation:

$$\lambda = \frac{h}{m\nu} = \frac{h}{\sqrt{2mE}} \quad (\text{B.5})$$

So for example, for a neutron possessing a kinetic energy of 10 meV, the associated wavelength will be equal to 2.86 Å. An incident beam of neutrons will interact with the nuclei of the atoms in the sample; the differential scattering cross section for an isolated atom will be equal to the square of the scattering length  $b$ , which is a specific parameter

for each element.

The different dependence of the scattered intensity for X-ray and neutron beams on the atomic parameters is exemplified by Fig. B.2.

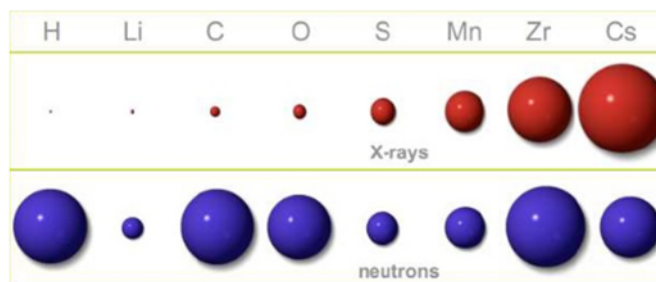


FIGURE B.2: The dependence of the scattered intensity for X-ray and neutron beams on the different atomic parameters. The larger the sphere for each atom, the higher the scattering intensity. Reproduced from: J. M. Carpenter, “Introduction to Theory of Neutron Scattering”, Presentation at Argonne National Laboratory, 2006

When a photon- or neutron beam hits a sample volume  $V$  having portions of matter with different electronic densities (or nuclear properties), the waves scattered in different spots will not necessarily have the same paths, and they may interact in a constructive or destructive way. Bragg’s law,

$$n\lambda = 2d \sin \theta \quad (\text{B.6})$$

with  $d$  being the distance between the paths of the waves, tells us that the amplitude of the interference wave will be maximum for a multiple of the wavelength. This equation also shows the proper angle needed for a constructive interference in a system where the scatterers are separated by a given distance  $d$ : since in colloidal systems  $d$  is large (10–1000 nm) and the wavelength of the radiation is low, small detection angles are needed.

## B.2 Experimental Intensity and Absolute Intensity

During a small angle scattering experiment, it is customary to measure the intensity of a reference pure solvent or compound whose absolute scattering intensity (measured in  $\text{cm}^{-1}$ ) is known. This solvent is generally water, but others can be used, such as toluene or lupolen resin. The absolute intensity is then obtained by normalizing the

experimentally measured intensity of a sample (in arbitrary units, *a.u.*) to the standard's experimental and tabulated intensities as follows:

$$I_{sample}(\text{cm}^{-1}) = \frac{I_{sample}(\text{a.u.})}{I_{standard}(\text{exp, a.u.})} \times I_{standard}(\text{tab, cm}^{-1}) \quad (\text{B.7})$$

### B.3 Form Factor and Structure Factor

For scatterers of spherical symmetry, such as the nanoparticles studied in this work, the absolute scattered intensity  $I(Q)$  is given (in accordance with the “decoupling approximation” for polydisperse systems [128]) by:

$$I(Q, \Phi) = (\Delta\rho)^2 \cdot \Phi \cdot V_P \cdot P(Q) \cdot S(Q, \Phi) \quad (\text{B.8})$$

where  $\Delta\rho$  is the difference of scattering length density (SLD) between the scatterers (*i.e.*, the particles) and the solvent (the quantity  $(\Delta\rho)^2$  is commonly referred to as “contrast”),  $\Phi$  is the particles volume fraction, and  $V_P$  is the volume of one particle.  $P(Q)$  and  $S(Q, \Phi)$  are two functions, respectively the *form factor* and the *structure factor*, both depending on  $Q$ .

The form factor is given by  $P(Q) = \langle |F(Q)|^2 \rangle$ , where  $F(Q)$  is a function describing the size and geometry of the scatterers. In the case of spherical symmetry, it has the following form:

$$F(Q) = \int_0^\infty 4\pi x^2 \gamma_0(x) \frac{\sin Qx}{Qx} dx \quad (\text{B.9})$$

where  $\gamma_0(x)$  is the normalized Patterson function, or autocorrelation function (see Section B.5). For  $Q = 0$ ,  $F(Q)$  is equal to the volume  $V$  of the scatterer.

The structure factor,  $S(Q, \Phi)$ , is the Fourier transform of the pair correlation function  $g(r)$ . It describes the interactions between scatterers, and it is equal to 1 in the case of non-interacting particles (*i.e.*, very dilute or charge-screened). At  $Q = 0$ ,  $S(Q, \Phi)$  gives the isothermal compressibility of the system,  $\chi$ :

$$S(Q = 0, \Phi) = \chi = \frac{kT}{V_P} \frac{\partial \Phi}{\partial \Pi} \quad (\text{B.10})$$



where  $k$  is Boltzmann's constant and  $\Pi$  is the osmotic pressure. In the case of sufficiently dilute colloidal suspensions, the virial development of the osmotic pressure as a function of the colloids' volume fraction ( $\Phi = nV_P$ ) yields:

$$\Pi \simeq nkT \left[ 1 + \frac{A_2}{V_P} \Phi + \frac{A_3}{V_P^2} \Phi^2 + \dots \right] \quad (\text{B.11})$$

$S(Q, \Phi)$  is thus related to the second virial coefficient  $A_2$  and its analysis at  $S(0, \Phi)$  allows to extract information on the interparticle potential of the system. When  $S(0, \Phi)$  deviates from unit, it is an indication of the interactions between particles, whose general trend can be repulsive ( $S(0, \Phi) < 1$ ) or attractive ( $S(0, \Phi) > 1$ ).

In the case of polydisperse systems, the experimental structure factor,  $S'(Q, \Phi)$ , is related to the actual structure factor  $S(Q, \Phi)$  by [129]:

$$S'(Q, \Phi) = 1 + \beta(Q)[S(Q, \Phi) - 1] \quad (\text{B.12})$$

$$\beta(Q) = |\langle F(Q) \rangle|^2 / \langle |F(Q)|^2 \rangle \quad (\text{B.13})$$

$S'(Q, \Phi)$  is only equal to  $S(Q, \Phi)$  in the case of monodisperse particles. In the case of the present work, the size polydispersity of the nanoparticles is low enough to allow the assumption  $S'(Q, \Phi) \approx S(Q, \Phi)$ . Experimentally,  $S(Q, \Phi)$  is obtained from the ratio of the absolute scattered intensity of the sample (normalized by the volume fraction  $\Phi$ ) and the form factor:

$$S(Q, \Phi) = I_{exp, norm}(Q, \Phi) / P(Q) \quad (\text{B.14})$$

Figure B.3 shows schematically the contributions of  $P(Q)$  and  $S(Q, \Phi)$  to the total scattered intensity function,  $I(Q, \Phi)$ . Figure B.4 resumes the information that can be extracted from the  $I(Q, \Phi)$  curve depending on the selected  $Q$  range.

## B.4 Calculation of Scattering Length Densities and Contrast

The SAXS scattering length density (SLD or  $\rho$ ) for any given material is calculated according to Equation B.15:

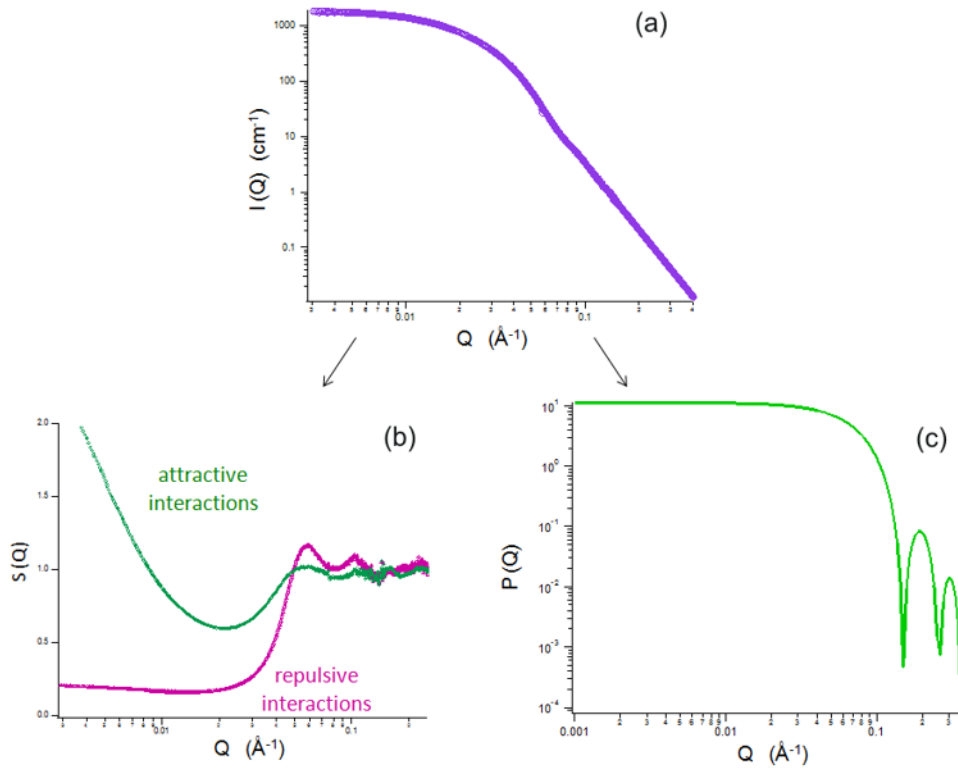


FIGURE B.3: (a) Example of experimental SAXS spectrum for a polydisperse sample, where the scattered intensity  $I(Q, \Phi)$  is expressed in absolute unity,  $\text{cm}^{-1}$ . (b) Typical structure factors,  $S(Q, \Phi)$ , that can be extracted from a SAXS spectrum. Depending on whether  $S(Q=0, \Phi)$  is superior or inferior to 1, the trend of the interparticle interaction is, respectively, attractive or repulsive. (c) Example of form factor,  $P(Q)$ , corresponding to monodisperse spheres.

$$\rho_{SAXS} = r_e \frac{\sum_i (n \cdot e^-)_i}{V_{molec}} \quad (\text{B.15})$$

where  $r_e$  is the Rayleigh constant, equal to  $2.80 \cdot 10^{-10}$  cm, the fraction numerator is the total number of electrons for each atom  $i$  of one molecule of the material, and  $V_{molec}$  is the molecular volume. In SANS,  $\rho$  is calculated according to Equation B.16:

$$\rho_{SANS} = \frac{\sum_i b_i}{V_{molec}} \quad (\text{B.16})$$

where now the fraction shows the sum of the nuclear property  $b_i$  for all the atoms  $i$  in the molecule.

A SAXS or SANS signal can be recorded from a sample only if a difference of SLD exists between the solvent and the particles. The higher the contrast between such SLD values, the higher the scattered intensity from the sample. Such contrast between

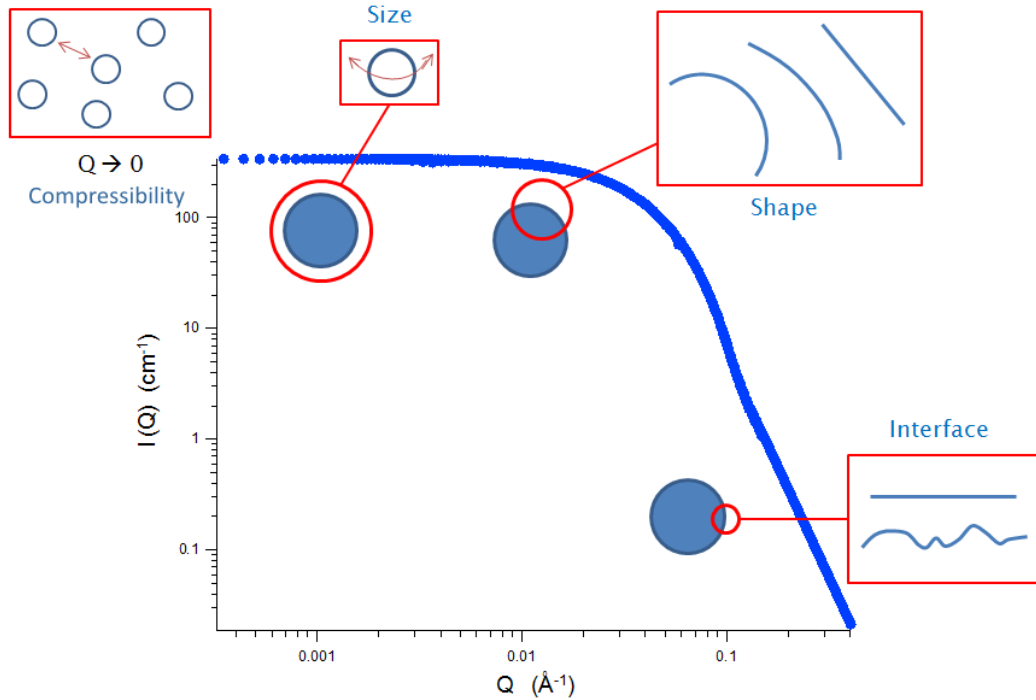


FIGURE B.4: Schematic example of scattered intensity  $I(Q, \Phi)$  as a function of  $Q$ . Depending on  $Q$ , different spatial scales  $2\pi/Q$  are probed and different information can be extracted concerning the system in study.

particles and solvent is simply calculated as  $\Delta\rho^2$ . Table B.1 shows the SLD values for the materials used in this work, while Table B.2 shows the contrast values for the dispersions studied by SAXS and SANS.

Material	SLD (SAXS, $\text{cm}^{-2}$ )	SLD (SANS, $\text{cm}^{-2}$ )
Maghemite	$4.06 \cdot 10^{11}$	$6.96 \cdot 10^{10}$
Water	$9.36 \cdot 10^{10}$	$-5.61 \cdot 10^9$
Ethylammonium Nitrate	$1.10 \cdot 10^{11}$	$1.32 \cdot 10^{10}$
Choline-Glycine	$1.02 \cdot 10^{11}$	$5.72 \cdot 10^9$

TABLE B.1: Scattering Length Densities (SLD) for SAXS and SANS.

System	$\Delta\rho^2$ (SAXS, $\text{cm}^{-4}$ )	$\Delta\rho^2$ (SANS, $\text{cm}^{-4}$ )
Maghemite/Water	$9.76 \cdot 10^{22}$	$5.66 \cdot 10^{21}$
Maghemite/EAN	$8.78 \cdot 10^{22}$	$3.19 \cdot 10^{21}$
Maghemite/[Cho][Gly]	$9.25 \cdot 10^{22}$	$4.09 \cdot 10^{21}$

TABLE B.2: Scattering Length Contrasts ( $\Delta\rho^2$ ) for SAXS and SANS.

## B.5 The Scattering Invariant. Calculation of $\Phi$

It can be shown [98] that the integral of the function  $Q^2 \cdot d\sigma/d\Omega(Q)$  is a constant of the system, thereby also called *invariant*. Its most current form is the following:

$$\int_0^{\infty} IQ^2 dQ = \Phi(1 - \Phi)2\pi^2(\Delta\rho)^2 \quad (\text{B.17})$$

For an isotropic system of two phases only [108], this relation allows to calculate the volume fraction  $\Phi$  of the scatterers from the scattering invariant. However, we do not have access to the entire  $Q$  range from 0 to infinity: the experimental range is limited to  $[Q_{min}, Q_{max}]$ . For this reason, the integral is calculated by parts by extrapolating the function in the lower and higher limits (first and third integrals in Eq. B.19). This is especially important for the high- $Q$  regime, which has a great contribution to the invariant even if the experimental intensity is low. In the high- $Q$  regime, the scattered intensity  $I(Q, \Phi)$  has an asymptotic behaviour described by Porod's law [130]:

$$\lim_{Q \rightarrow \infty} I(Q, \Phi) = \frac{(\Delta\rho)^2 2\pi S}{Q^4 V} \quad (\text{B.18})$$

where  $S$  is the surface of the particle and  $V$  the volume. A plot of  $IQ^4$  vs.  $Q$  allows to obtain Porod's constant  $C_{Porod}$ . So, integrating by parts, it follows:

$$\int_0^{\infty} IQ^2 dQ = \int_0^{Q_{min}} IQ^2 dQ + \int_{Q_{min}}^{Q_{max}} IQ^2 dQ + \int_{Q_{max}}^{\infty} IQ^2 dQ \quad (\text{B.19})$$

where  $Q_{min}$  and  $Q_{max}$  are, respectively, the lowest and the highest  $Q$ -limits in the experimental curve. Approximations lead to replace the integrals with the following expressions:

$$\int_0^{\infty} IQ^2 dQ = \left( I(0) \frac{1}{3} Q_{min}^3 \right) + \left( \sum_{Q=Q_{min}}^{Q=Q_{max}} IQ^2 \Delta Q \right) + \left( \frac{C_{Porod}}{Q_{max}} \right) = Inv \quad (\text{B.20})$$

This way, the second degree equation in Eqn. B.17 can be solved to retrieve  $\Phi$ . If the hypothesis  $\Phi \ll 1 \Rightarrow 1 - \Phi \simeq 1$  stands, the volume fraction is calculated from the simplified formula:

$$\Phi = \frac{I_{nv}}{2\pi^2(\Delta\rho)^2} \quad (\text{B.21})$$

## B.6 Guinier Plot

A Guinier plot is based on the Guinier approximation for the behaviour of the scattered intensity when  $Q$  tends to zero. One can show that for dilute suspensions ( $S(Q, \Phi) = 1$ ) the scattering intensity decreases around the central beam as [108]:

$$I(Q) \approx \Phi V_P e^{-(qR_G^2/3)} \quad (\text{B.22})$$

where  $R_G$  is the radius of gyration of the scatterers. This approximation is only valid if the condition  $QR_G < 1$  is verified. The Guinier plot,  $\ln I(Q)$  *vs.*  $Q^2$ , is a common tool used to extract  $R_G$  from the slope  $R_G^2/3$ .

## B.7 Experimental Form Factors, $P(Q)$

In this work, the form factors for both small (7 nm) and large (11 nm) particles are obtained experimentally from aqueous dilute dispersions after extrapolation for  $\Phi = 0$ . Indeed, when  $\Phi \rightarrow 0$ ,  $S(Q, \Phi) \rightarrow 1$ , so that only the form factor contributes to the scattered intensity.

Briefly, for each particle size, four dilute dispersions ( $\Phi = 0.01\%$ ,  $0.03\%$ ,  $0.06\%$  and  $0.1\%$ ) of  $\text{Na}_3\text{Cit}$ -covered maghemite NPs are prepared; for each of these, three different saline concentrations (as free sodium citrate: 5 mM, 30 mM and 100 mM) are fixed. The presence of salt is needed to screen the NP surface charge, so that the interparticle interactions are negligible.

Based on Eqn. B.8, the quantity  $V_P P(Q)$  can be obtained by calculating the quantity  $I(Q)/((\Delta\rho)^2\Phi)$ . In order to extrapolate such quantity at null volume fraction, for each  $Q$  value the quantity  $I(Q)/((\Delta\rho)^2\Phi)$  is plotted as a function of  $\Phi$ , and the value of  $I(Q)/((\Delta\rho)^2\Phi)$  at  $\Phi = 0$  can then be extrapolated. This is done for each of the three salinities, and leads to the obtention of three curves  $I(Q)/((\Delta\rho)^2\Phi)$  as a function of  $Q$ , which are superimposed. These are shown in Figures B.5 and B.6 for each particle size.

The extrapolated form factors of Figures B.5 and B.6 are fitted with a lognormal function for spheres, yielding a radius  $R = 30 \text{ \AA}$  and polydispersity  $\sigma = 0.28$  for the

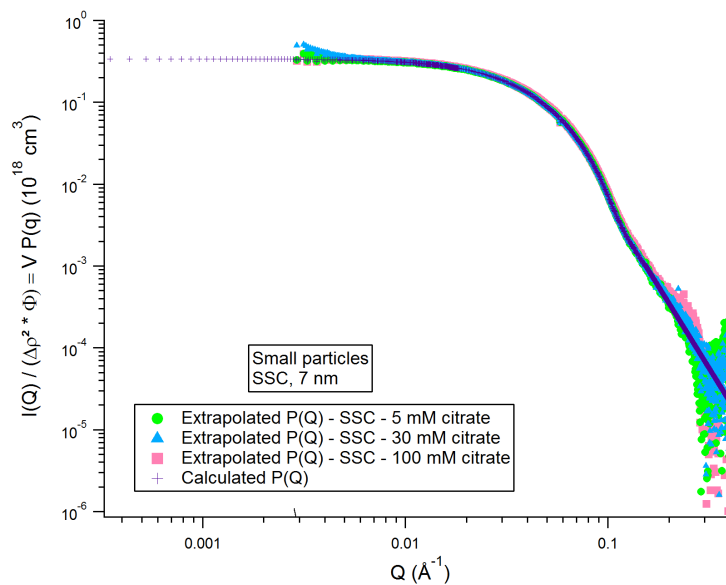


FIGURE B.5: Obtention of an experimental form factor  $P(Q)$  for the small NP. See text for details.

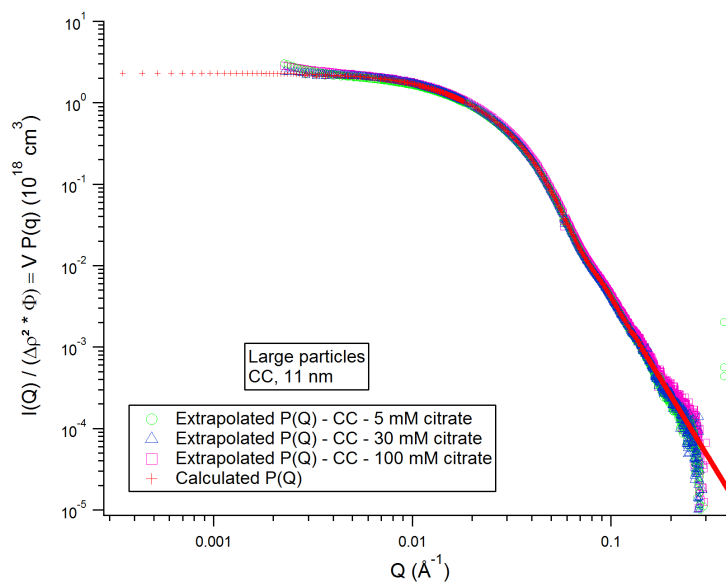


FIGURE B.6: Obtention of an experimental form factor  $P(Q)$  for the large NP. See text for details.

small particles (SSC, 7 nm); for the large particles (CC, 11 nm), the fit yields  $R = 55 \text{ \AA}$ ,  $\sigma = 0.30$ . Due to technical difficulties in the high-Q (signal affected by high noise level) and in the low-Q (signal affected by scattering from the sample holder) regimes, only the central part of the experimental form factor is considered, while the two extremes are completed by calculated data. At low Q values, a Guinier law B.22 is used. A Porod law B.18 is used in the high-Q limit to complete the experimental curve with a  $Q^{-4}$  law. The resulting curves for each NP size, combining experimental data and theoretical points, are shown in Figures B.5 and B.6, superposed to the experimental intensities, and singularly in Figure B.7.

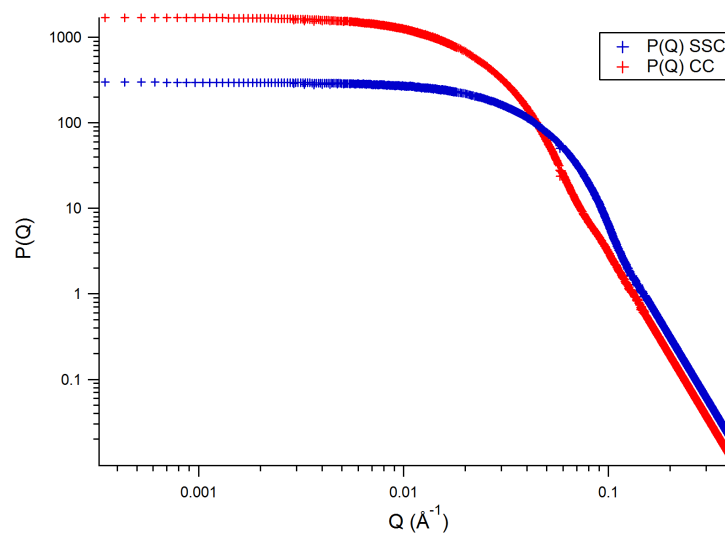


FIGURE B.7: Experimental  $P(Q)$  curves for small (SSC) and large (CC) particles, normalized to the maghemite/EAN contrast and to  $\Phi = 1\%$ .

The experimental form factors  $P(Q)$  obtained by the procedure described above, normalized to the maghemite/EAN contrast, are then used throughout this work to obtain the structure factors  $S(Q)$  of more concentrated dispersions.





# Bibliography

- [1] Tsukasa Torimoto, Tetsuya Tsuda, Ken-ichi Okazaki, and Susumu Kuwabata. New frontiers in materials science opened by ionic liquids. *Advanced Materials*, 22(11): 1196–1221, 2010. doi: 10.1002/adma.200902184.
- [2] Zhonghao Li, Zhen Jia, Yuxia Luan, and Tiancheng Mu. Ionic liquids for synthesis of inorganic nanomaterials. *Current Opinion in Solid State and Materials Science*, 12(1):1–8, 2008. doi: 10.1016/j.cossms.2009.01.002.
- [3] Qinghua Zhang, Shiguo Zhang, and Youquan Deng. Recent advances in ionic liquid catalysis. *Green Chemistry*, 13(10):2619–2637, 2011. doi: 10.1039/c1gc15334j.
- [4] Elise B. Fox, Ann E. Visser, Nicholas J. Bridges, and Jake W. Amoroso. Thermophysical properties of nanoparticle-enhanced ionic liquids (NEILs) heat-transfer fluids. *Energy & Fuels*, 27(6):3385–3393, 2013. doi: 10.1021/ef4002617.
- [5] Jean Le Bideau, Lydie Viau, and André Vioux. Ionogels, ionic liquid based hybrid materials. *Chemical Society Reviews*, 40(2):907–925, 2011. doi: 10.1039/c0cs00059k.
- [6] Hong Yang, Chengzhong Yu, Qunliang Song, Yongyao Xia, Fuyou Li, Zhigang Chen, Xianghong Li, Tao Yi, and Chunhui Huang. High-temperature and long-term stable solid-state electrolyte for Dye-Sensitized solar cells by self-assembly. *Chemistry of Materials*, 18(22):5173–5177, 2006. doi: 10.1021/cm061112d.
- [7] David S. Jacob, Avner Rothschild, Harry L. Tuller, and Aharon Gedanken. In situ sonochemical hydrolysis and deposition of composite layers of ionic liquid entrapped in colloidal silica network and their application as sensors for various gases. *Ultrasonics Sonochemistry*, 17(4):726–729, 2010. doi: 10.1016/j.ultsonch.2009.12.015.

- [8] E. J. Verwey, J. Th. G. Overbeek, and K. van Nes. *Theory of the Stability of Lyophobic Colloids*. 1948 edition.
- [9] Dongbin Zhao, Zhaofu Fei, Wee Han Ang, and Paul J. Dyson. A strategy for the synthesis of transition-metal nanoparticles and their transfer between liquid phases. *Small*, 2(7):879–883, 2006. doi: 10.1002/sml.200500317.
- [10] Kazuhide Ueno, Aya Inaba, Masashi Kondoh, and Masayoshi Watanabe. Colloidal stability of bare and polymer-grafted silica nanoparticles in ionic liquids. *Langmuir*, 24(10):5253–5259, 2008. doi: 10.1021/la704066v.
- [11] Nirmesh Jain, Xiaoli Zhang, Brian S. Hawkett, and Gregory G. Warr. Stable and water-tolerant ionic liquid ferrofluids. *ACS Applied Materials & Interfaces*, 3(3):662–667, 2011. doi: 10.1021/am1012112.
- [12] Guor-Tzo Wei, Zusing Yang, Chia-Ying Lee, Hsiao-Yen Yang, and C. R. Chris Wang. Aqueous-Organic phase transfer of gold nanoparticles and gold nanorods using an ionic liquid. *Journal of the American Chemical Society*, 126(16):5036–5037, 2004. doi: 10.1021/ja039874m.
- [13] Ryouta Tatumi and Hisashi Fujihara. Remarkably stable gold nanoparticles functionalized with a zwitterionic liquid based on imidazolium sulfonate in a high concentration of aqueous electrolyte and ionic liquid. *Chemical Communications*, (1):83–85, 2005. doi: 10.1039/b413385d.
- [14] Laura Rodríguez-Arco, Modesto T. López-López, Fernando González-Caballero, and Juan D.G. Durán. Steric repulsion as a way to achieve the required stability for the preparation of ionic liquid-based ferrofluids. *Journal of Colloid and Interface Science*, 357(1):252–254, 2011. doi: 10.1016/j.jcis.2011.01.083.
- [15] Jacob A. Smith, Oliver Werzer, Grant B. Webber, Gregory G. Warr, and Rob Atkin. Surprising particle stability and rapid sedimentation rates in an ionic liquid. *The Journal of Physical Chemistry Letters*, 1(1):64–68, 2010. doi: 10.1021/jz9000642.
- [16] Flavia C. C. Oliveira, Liane M. Rossi, Renato F. Jardim, and Joel C. Rubim. Magnetic fluids based on  $\gamma\text{-Fe}_2\text{O}_3$  and  $\text{CoFe}_2\text{O}_4$  nanoparticles dispersed in ionic liquids. *The Journal of Physical Chemistry C*, 113(20):8566–8572, 2009. doi: 10.1021/jp810501m.

- [17] Marie-Alexandra Neouze. About the interactions between nanoparticles and imidazolium moieties: emergence of original hybrid materials. *Journal of Materials Chemistry*, 20(43):9593–9607, 2010. doi: 10.1039/c0jm00616e.
- [18] Ryo Kanzaki, Kuniaki Uchida, Shota Hara, Yasuhiro Umebayashi, Shin-ichi Ishiguro, and Satoshi Nomura. Acid–Base property of ethylammonium nitrate ionic liquid directly obtained using ion-selective field effect transistor electrode. *Chemistry Letters*, 36(5):684–685, 2007. doi: 10.1246/cl.2007.684.
- [19] Koichi Fumino, Alexander Wulf, and Ralf Ludwig. Hydrogen bonding in protic ionic liquids: Reminiscent of water. *Angewandte Chemie International Edition*, 48(17):3184–3186, 2009. doi: 10.1002/anie.200806224.
- [20] R. G. Horn, D. F. Evans, and B. W. Ninham. Double-layer and solvation forces measured in a molten salt and its mixtures with water. *Journal of Physical Chemistry*, 92:3531–3537, 1988.
- [21] Robert Hayes, Gregory G. Warr, and Rob Atkin. At the interface: Solvation and designing ionic liquids. *Physical Chemistry Chemical Physics*, 12(8):1709–1723, 2010. doi: 10.1039/b920393a.
- [22] Jacob N. Israelachvili. *Intermolecular and Surface Forces*. 2001, third edition.
- [23] Ali Naji, Matej Kanduc, Roland R Netz, and Rudolf Podgornik. Exotic electrostatics: Unusual features of electrostatic interactions between macroions. *arXiv preprint arXiv:1008.0357*, 2010.
- [24] Vincent Dahirel and Marie Jardat. Effective interactions between charged nanoparticles in water: what is left from the DLVO theory? *Current Opinion in Colloid & Interface Science*, 15:2–7, 2010. doi: 10.1016/j.cocis.2009.05.006.
- [25] Pierre Bonhote, Ana-Paula Dias, Nicholas Papageorgiou, Kuppuswamy Kalyanasundaram, and Michael Grätzel. Hydrophobic, highly conductive ambient-temperature molten salts. *Inorganic Chemistry*, 35(5):1168–1178, 1996.
- [26] Laura Rodríguez-Arco, Modesto T López-López, Juan D G Durán, Andrey Zubarev, and Dmitriy Chirikov. Stability and magnetorheological behaviour of magnetic fluids based on ionic liquids. *Journal of Physics: Condensed Matter*, 23(45):455101, 2011. doi: 10.1088/0953-8984/23/45/455101.

- [27] Evert Vanecht, Koen Binnemans, Sergiy Patskovsky, Michel Meunier, Jin Won Seo, Linda Stappers, and Jan Fransaer. Stability of sputter-deposited gold nanoparticles in imidazolium ionic liquids. *Phys. Chem. Chem. Phys.*, 14:5662–5671, 2012. doi: 10.1039/c2cp23677j.
- [28] B. W. Ninham. On progress in forces since the DLVO theory. *Advances in Colloid and Interface Science*, 83:1–17, 1999.
- [29] Herrmann Weingärtner. Understanding ionic liquids at the molecular level: Facts, problems, and controversies. *Angewandte Chemie International Edition*, 47:654–670, 2008. doi: 10.1002/anie.200604951.
- [30] Kazuhide Ueno, Hiroyuki Tokuda, and Masayoshi Watanabe. Ionicity in ionic liquids: correlation with ionic structure and physicochemical properties. *Physical Chemistry Chemical Physics*, 12(8):1649–1658, 2010. doi: 10.1039/b921462n.
- [31] Matthew A. Gebbie, Markus Valtinerb, Xavier Banquyc, Eric T. Foxd, Wesley A. Henderson, and Jacob N. Israelachvili. Ionic liquids behave as dilute electrolyte solutions. *PNAS*, 110(24):9674–9679, 2013. doi: 10.1073/pnas.1307871110.
- [32] F. Cousin, E. Dubois, and V. Cabuil. Tuning the interactions of a magnetic colloidal suspension. *Physical Review E*, 68(2):021405, 2003. doi: 10.1103/PhysRevE.68.021405.
- [33] R. Massart. Preparation of aqueous magnetic liquids in alkaline and acidic media. *I.E.E.E., Transactions on Magnetism*, 2:1247–1248, 1981.
- [34] J.-C. Bacri, R. Perzynski, D. Salin, V. Cabuil, and R. Massart. Magnetic colloidal properties of ionic ferrofluids. *Journal of Magnetism and Magnetic Materials*, 62:36–46, 1986.
- [35] S. Odenbach. *Colloidal Magnetic Fluids: Basics, Development and Application of Ferrofluids*. Lecture Notes in Physics 763. Springer-Verlag Berlin Heidelberg, 2009.
- [36] I.T. Lucas, S. Durand-Vidal, E. Dubois, J. Chevalet, and P. Turq. Surface charge density of maghemite nanoparticles: Role of electrostatics in the proton exchange. *Journal of Physical Chemistry C*, 111(50):18568–18576, 2007. doi: 10.1021/jp0743119.

- [37] Emmanuelle Dubois. *PhD Thesis, 1997*.
- [38] N. Fauconnier, A. Bée, J. Roger, and J. N. Pons. Synthesis of aqueous magnetic liquids by surface complexation of maghemite nanoparticles. *Progress in Colloid and Polymer Science*, 83:233–242, 1996.
- [39] E. Dubois, V. Cabuil, F. Boué, and R. Perzynski. Structural analogy between aqueous and oily magnetic fluids. *Journal of Chemical Physics*, 111(15):7147–7160, 1999. doi: 10.1063/1.480007.
- [40] N.A.M. Verhaegh and H.N.W. Lekkerkerker. Phase transitions in colloidal suspensions. *IOS Press*, 134:347–381, 1997.
- [41] Thi Phuong Thuy Pham, Chul-Woong Cho, and Yeung-Sang Yun. Environmental fate and toxicity of ionic liquids: A review. *Water Research*, 44(2):352–372, 2010. doi: 10.1016/j.watres.2009.09.030.
- [42] Y. Guangren, D. Zhao, W. Lu, S. Yang, and X. Chen. Viscosity of ionic liquids: Database, observation, and quantitative structure-property relationship analysis. *AIChE Journal*, 58(9):2885–2899, 2012. doi: 10.1002/aic.12786.
- [43] Jairton Dupont and Jackson D. Scholten. On the structural and surface properties of transition-metal nanoparticles in ionic liquids. *Chemical Society Reviews*, 39:1780–1804, 2010. doi: 10.1039/b822551f.
- [44] S. Aparicio, M. Atilhan, and F. Karadas. Thermophysical properties of pure ionic liquids: Review of present situation. *Industrial & Engineering Chemistry Research*, 49(20):9580–9595, 2010. doi: 10.1021/ie101441s.
- [45] Hiroshi Usui, Hiroshi Matsui, Nobuo Tanabe, and Shozo Yanagida. Improved Dye-Sensitized solar cells using ionic nanocomposite gel electrolytes. *Journal of Photochemistry and Photobiology A: Chemistry*, 164(1-3):97–101, 2004. doi: 10.1016/j.jphotochem.2003.12.020.
- [46] Chuan-Pei Lee, Kun-Mu Lee, Po-Yen Chen, and Kuo-Chuan Ho. On the addition of conducting ceramic nanoparticles in solvent-free ionic liquid electrolyte for dye-sensitized solar cells. *Solar Energy Materials and Solar Cells*, 93(8):1411–1416, 2009. doi: 10.1016/j.solmat.2009.03.010.

- [47] Nicholas J. Bridges, Ann E. Visser, and Elise B. Fox. Potential of nanoparticle-enhanced ionic liquids (NEILs) as advanced heat-transfer fluids. *Energy & Fuels*, 25(10):4862–4864, 2011. doi: 10.1021/ef2012084.
- [48] M.-D. Bermudez, A.-E. Jimenez, J. Sanes, and F.-J. Carrion. Ionic liquids as advanced lubricant fluids. *Molecules*, 14(8):2888–2908, 2009. doi: 10.3390/molecules14082888.
- [49] Yeny C. Hudiono, Trevor K. Carlisle, Jason E. Bara, Yanfeng Zhang, Douglas L. Gin, and Richard D. Noble. A three-component mixed-matrix membrane with enhanced CO<sub>2</sub> separation properties based on zeolites and ionic liquid materials. *Journal of Membrane Science*, 350(1-2):117–123, 2010. doi: 10.1016/j.memsci.2009.12.018.
- [50] P. Walden. Über die molekulargröße und elektrische leitfähigkeit einiger geschmolzener salze. *Bull. Acad. Imp. Sci.*, 1800, 1914.
- [51] Gerald Perron, Alain Hardy, Jean-Claude Justice, and Jacques E. Desnoyers. Model system for concentrated electrolyte solutions: Thermodynamic and transport properties of ethylammonium nitrate in acetonitrile and in water. *Journal of Solution Chemistry*, 22(12):1159–1178, 1993.
- [52] N. Benhlima, M. Turmine, P. Letellier, R. Naejus, and D. Lemordant. Etude électrochimique du nitrate d'éthylammonium fondu à 298 K: établissement d'une échelle de potentiel redox. *Journal de Chimie Physique*, 95:25–44, 1998.
- [53] D. F. Evans, A. Yamauchi, R. Roman, and E. Z. Casassa. Micelle formation in ethylammonium nitrate, a low-melting fused salt. *Journal of Colloid and Interface Science*, 88(1):89–96, 1982.
- [54] M. Haddad, H. Bahri, and P. Letellier. Tensions superficielles des mélanges binaires eau-nitrate d'éthylammonium à 298 K. *Journal de Chimie Physique*, 83(6):419–426, 1986.
- [55] Martin Allen, Fennell D. Evans, and Rufus Lumry. Thermodynamic properties of ethylammonium nitrate + water system: partial molar volumes, heat capacities and expansivities. *Journal of Solution Chemistry*, 14(8):549–560, 1995.

- [56] H. Weingärtner, A. Knocks, W. Schrader, and U. Kaatze. Dielectric spectroscopy of the room temperature molten salt ethylammonium nitrate. *Journal of Physical Chemistry*, 105(38):8646–8650, 2001. doi: 10.1021/jp0114586.
- [57] N. Benhlima, D. Lemordant, and P. Letellier. Propriétés physicochimiques des mélanges eau-nitrate d'éthylammonium fondu, à 298 K. Echelles d'acidité - solubilités. *Journal de Chimie Physique*, pages 1919–1939, 1989.
- [58] Rob Atkin and Gregory G. Warr. The smallest amphiphiles: Nanostructure in protic room-temperature ionic liquids with short alkyl groups. *The Journal of Physical Chemistry B*, 112(14):4164–4166, 2008. doi: 10.1021/jp801190u.
- [59] Robert Hayes, Silvia Imberti, Gregory Warr, and Rob Atkin. The nature of hydrogen bonding in protic ionic liquids. *Angewandte Chemie International Edition*, 52:4623–4627, 2013. doi: 10.1002/anie.201209273.
- [60] Jingcheng Hao and Thomas Zemb. Self-assembled structures and chemical reactions in room-temperature ionic liquids. *Current Opinion in Colloid & Interface Science*, 12(3):129–137, 2007. doi: 10.1016/j.cocis.2006.11.004.
- [61] Pedro Migowski, Giovanna Machado, Sergio R. Texeira, Maria C. M. Alves, Jonder Morais, Agnès Traverse, and Jairton Dupont. Synthesis and characterization of nickel nanoparticles dispersed in imidazolium ionic liquids. *Physical Chemistry Chemical Physics*, 9(34):4814–4821, 2007. doi: 10.1039/b703979d.
- [62] Markus Antonietti, Daibin Kuang, Bernd Smarsly, and Yong Zhou. Ionic liquids for the convenient synthesis of functional nanoparticles and other inorganic nanostructures. *Angewandte Chemie International Edition*, 43(38):4988–4992, 2004. doi: 10.1002/anie.200460091.
- [63] Flavia C. C. Oliveira, Fernando B. Effenberger, Marcelo H. Sousa, Renato F. Jardim, Pedro K. Kiyohara, Jairton Dupont, Joel C. Rubim, and Liane M. Rossi. Ionic liquids as recycling solvents for the synthesis of magnetic nanoparticles. *Physical Chemistry Chemical Physics*, 13(30):13558–13564, 2011. doi: 10.1039/c1cp21518c.
- [64] Hideaki Itoh, Kensuke Naka, and Yoshiki Chujo. Synthesis of gold nanoparticles modified with ionic liquid based on the imidazolium cation. *Journal of the American Chemical Society*, 126(10):3026–3027, 2004. doi: 10.1021/ja039895g.

- [65] Li Wang, Lixian Chang, Bin Zhao, Zhongyong Yuan, Gaosong Shao, and Wenjun Zheng. Systematic investigation on morphologies, forming mechanism, photocatalytic and photoluminescent properties of ZnO nanostructures constructed in ionic liquids. *Inorganic Chemistry*, 47(5):1443–1452, 2008. doi: 10.1021/ic701094a.
- [66] Joel C. Rubim, Flavio A. Trindade, Marcos A. Gelesky, Ricardo F. Aroca, and Jairton Dupont. Surface-enhanced vibrational spectroscopy of tetrafluoroborate 1-*n*-butyl-3-methylimidazolium (BMIBF<sub>4</sub>) ionic liquid on silver surfaces. *Journal of Physical Chemistry C*, 112:19670–19675, 2008. doi: 10.1021/jp808101g.
- [67] Anderson M. M. S. Medeiros, Alexandre L. Parize, Vanda M. Oliveira, Brenno A. D. Neto, Andris F. Bakuzis, Marcelo H. Sousa, Liane M. Rossi, and Joel C. Rubim. Magnetic ionic liquids produced by the dispersion of magnetic nanoparticles in 1-*n*-butyl-3-methylimidazolium bis(trifluoromethanesulfonyl)imide (BMI.NTf<sub>2</sub>). *Applied Materials & Interfaces*, 4:5458–5465, 2012. doi: 10.1021/am301367d.
- [68] Wei Huang and Xiaolei Wang. Study on the properties and stability of ionic liquid-based ferrofluids. *Colloid and Polymer Science*, 290(16):1695–1702, 2012.
- [69] C. Guerrero-Sanchez, T. Lara-Ceniceros, E. Jimenez-Regalado, M. Raša, and U. S. Schubert. Magnetorheological fluids based on ionic liquids. *Advanced Materials*, 19(13):1740–1747, 2007. doi: 10.1002/adma.200700302.
- [70] A. Gómez-Ramírez, M. T. López-López, F. González-Caballero, and J. D. G. Durán. Stability of magnetorheological fluids in ionic liquids. *Smart Materials and Structures*, 20(4):045001, 2011. doi: 10.1088/0964-1726/20/4/045001.
- [71] Alexandra Wittmar and Mathias Ulbricht. Dispersions of various titania nanoparticles in two different ionic liquids. *Industrial & Engineering Chemistry Research*, 51(25):8425–8433, 2012. doi: 10.1021/ie203010x.
- [72] Kazuhide Ueno, Kenji Hata, Toru Katakabe, Masashi Kondoh, and Masayoshi Watanabe. Nanocomposite ion gels based on silica nanoparticles and an ionic liquid: Ionic transport, viscoelastic properties, and microstructure. *The Journal of Physical Chemistry B*, 112(30):9013–9019, 2008.
- [73] Kazuhide Ueno, Satoru Imaizumi, Kenji Hata, and Masayoshi Watanabe. Colloidal interaction in ionic liquids: Effects of ionic structures and surface chemistry on



- rheology of silica colloidal dispersions. *Langmuir*, 25(2):825–831, 2009. doi: 10.1021/la803124m.
- [74] Kazuhide Ueno, Yuta Sano, Aya Inaba, Masashi Kondoh, and Masayoshi Watanabe. Soft glassy colloidal arrays in an ionic liquid: Colloidal glass transition, ionic transport, and structural color in relation to microstructure. *The Journal of Physical Chemistry B*, 114(41):13095–13103, 2010. doi: 10.1021/jp106872w.
- [75] Kazuhide Ueno, Aya Inaba, Takeshi Ueki, Masashi Kondoh, and Masayoshi Watanabe. Thermosensitive, soft glassy and structural colored colloidal array in ionic liquid: Colloidal glass to gel transition. *Langmuir*, 26(23):18031–18038, 2010. doi: 10.1021/la103716q.
- [76] André Vioux, Lydie Viau, Sabrina Volland, and Jean Le Bideau. Use of ionic liquids in sol-gel; ionogels and applications. *Comptes Rendus Chimie*, 13(1-2):242–255, 2010. doi: 10.1016/j.crci.2009.07.002.
- [77] Surya S. Moganty, Samanvaya Srivastava, Yingying Lu, Jennifer L. Schaefer, Salmaan A. Rizvi, and Lynden A. Archer. Ionic liquid-tethered nanoparticle suspensions: A novel class of ionogels. *Chemistry of Materials*, 24(7):1386–1392, 2012. doi: 10.1021/cm300424v.
- [78] Bartosz Ziólkowski, Katrin Bleek, Brendan Twamley, Kevin J. Fraser, Robert Byrne, Dermot Diamond, and Andreas Taubert. Magnetic ionogels (MagIGs) based on iron oxide nanoparticles, poly(N-isopropylacrylamide), and the ionic liquid trihexyl(tetradecyl)phosphonium dicyanamide. *European Journal of Inorganic Chemistry*, pages 5245–5251, 2012. doi: 10.1002/ejic.201200597.
- [79] Meltem Tunckol, Jérôme Durand, and Philippe Serp. Carbon nanomaterial–ionic liquid hybrids. *Carbon*, 50(12):4303–4334, 2012. doi: 10.1016/j.carbon.2012.05.017.
- [80] Varsha Khare, Alexander Kraupner, Alexandre Manton, Aleksandra Jelicic, Andreas F. Thunemann, Cristina Giordano, and Andreas Taubert. Stable iron carbide nanoparticle dispersions in [Emim][SCN] and [Emim][N(CN)<sub>2</sub>] ionic liquids. *Langmuir*, 26(13):10600–10605, 2010. doi: 10.1021/la100775m.

- [81] Hans-Jürgen Butt, Brunero Cappella, and Michael Kappl. Force measurements with the atomic force microscope: Technique, interpretation and applications. *Surface Science Reports*, 59:1–152, 2005. doi: 10.1016/j.surfrep.2005.08.003.
- [82] Aaron Elbourne, James Sweeney, Grant B. Webber, Erica J. Wanless, Gregory G. Warr, Mark W. Rutland, and Rob Atkin. Adsorbed and near-surface structure of ionic liquids determines nanoscale friction. *Chemical Communication*, 49(60): 6797–6799, 2013. doi: 10.1039/c3cc42844c.
- [83] Rob Atkin and Gregory G. Warr. Self-assembly of a nonionic surfactant at the Graphite/Ionic Liquid interface. *Journal of the American Chemical Society*, 127(34):11940–11941, 2005. doi: 10.1021/ja053904z.
- [84] Brian D. Fitchett and John C. Conboy. Structure of the room-temperature ionic liquid/SiO<sub>2</sub> interface studied by sum-frequency vibrational spectroscopy. *Journal of Physical Chemistry B*, 108:20255–20262, 2004. doi: 10.1021/jp0471251.
- [85] Frank Endres, Natalia Borisenko, Sherif Zein El Abedin, Robert Hayes, and Rob Atkin. The interface ionic liquid(s)/electrode(s): In situ STM and AFM measurements. *Faraday Discussions*, 154:221–233, 2012. doi: 10.1039/c1fd00050k.
- [86] Jenel Vatamanu, Oleg Borodin, and Grant D. Smith. Molecular insights into the potential and temperature dependences of the differential capacitance of a room-temperature ionic liquid at graphite electrodes. *Journal of the American Chemical Society*, 132(42):14825–14833, 2010. doi: 10.1021/ja104273r.
- [87] M. Mezger, H. Schroder, H. Reichert, S. Schramm, J. S. Okasinski, S. Schoder, V. Honkimaki, M. Deutsch, B. M. Ocko, J. Ralston, M. Rohwerder, M. Stratmann, and H. Dosch. Molecular layering of fluorinated ionic liquids at a charged sapphire (0001) surface. *Science*, 322(5900):424–428, 2008. doi: 10.1126/science.1164502.
- [88] Kazuhide Ueno, Motohiro Kasuya, Masayoshi Watanabe, Masashi Mizukami, and Kazue Kurihara. Resonance shear measurement of nanoconfined ionic liquids. *Physical Chemistry Chemical Physics*, 12(16):4066–4071, 2010. doi: 10.1039/b923571j.
- [89] S Bovio, A Podestà, P Milani, P Ballone, and M G Del Pópolo. Nanometric ionic-liquid films on silica: a joint experimental and computational study. *Journal of*

- Physics: Condensed Matter*, 21(42):424118, 2009. doi: 10.1088/0953-8984/21/42/424118.
- [90] R. Hayes, N. Borisenko, B. Corr, G. B. Webber, F. Endres, and R. Atkin. Effect of dissolved LiCl on the ionic liquid–Au(111) electrical double layer structure. *Chem. Commun.*, 48:10246–10248, 2012. doi: 10.1039/c2cc35737b.
- [91] Jonas Nordström, Luis Aguilera, and Aleksandar Matic. Effect of lithium salt on the stability of dispersions of fumed silica in the ionic liquid BMImBF<sub>4</sub>. *Langmuir*, 28(9):4080–4085, 2012. doi: 10.1021/la204555g.
- [92] Guang Feng, Rui Qiao, Jingsong Huang, Sheng Dai, Bobby G. Sumpter, and Vincent Meunier. The importance of ion size and electrode curvature on electrical double layers in ionic liquids. *Physical Chemistry Chemical Physics*, 13(3):1152–1161, 2011. doi: 10.1039/c0cp02077j.
- [93] F. Bernardi, J. D. Scholten, G. H. Fecher, J. Dupont, and J. Morais. Probing the chemical interaction between iridium nanoparticles and ionic liquid by XPS analysis. *Chemical Physics Letters*, 479:113–116, 2009. doi: 10.1016/j.cplett.2009.07.110.
- [94] Susan Perkin. Ionic liquids in confined geometries. *Physical Chemistry Chemical Physics*, 14(15):5052–5062, 2012. doi: 10.1039/c2cp23814d.
- [95] R. M. Lynden-Bell. Screening of pairs of ions dissolved in ionic liquids. *Phys. Chem. Chem. Phys.*, 12:1733–1740, 2009. doi: 10.1039/B916987C.
- [96] Susan Perkin, Mathieu Salanne, Paul Madden, and Ruth Lynden-Bell. Is a Stern and diffuse layer model appropriate to ionic liquids at surfaces? *Proceedings of the National Academy of Sciences*, 110(44):E4121–E4121, 2013. doi: 10.1073/pnas.1314188110.
- [97] P. Moriel, E.J. García-Suárez, M. Martínez, A.B. García, M.A. Montes-Morán, V. Calvino-Casilda, and M.A. Bañares. Synthesis, characterization, and catalytic activity of ionic liquids based on biosources. *Tetrahedron Letters*, 51(37):4877–4881, 2010. doi: 10.1016/j.tetlet.2010.07.060.

- [98] D. Espinat. Application des techniques de diffusion de la lumière, des rayons x et des neutrons à l'Étude des systèmes colloïdaux. *Révue de l'Institut Français du Pétrole*, 45(6):1–131, 1990.
- [99] Edward H. Hellen. Padé–Laplace analysis of signal averaged voltage decays obtained from a simple circuit. *American Journal of Physics*, 73(9):871–875, 2005. doi: 10.1119/1.1927551.
- [100] Simon Foner. Versatile and sensitive vibrating-sample magnetometer. *The Review of Scientific Instruments*, 30(7):548–557, 1959.
- [101] E. Hasmonay, E. Dubois, J.C. Bacri, R. Perzynski, Yu.L. Raikher, and V.I. Stepanov. Static magneto-optical birefringence of size-sorted  $\gamma$ -Fe<sub>2</sub>O<sub>3</sub> nanoparticles. *Eur. Phys. J. B*, 5:859–867, 1998.
- [102] J.-C. Bacri, R. Perzynski, D. Salin, and J. Servais. Magnetic transient birefringence of ferrofluids: particle size determination. *Journal de Physique*, 48:1385–1391, 1987.
- [103] *CRC Handbook of Chemistry and Physics*. CRC Press, 57th edition.
- [104] Steven R. Kline. Reduction and analysis of SANS and USANS data using IGOR pro. *Journal of Applied Crystallography*, 39(6):895–900, 2006. doi: 10.1107/S0021889806035059.
- [105] Kil Sang Lee, Dai Woon Lee, and Jae Young Hwang. Spectrophotometric determination of some organic acids with ferric 5-nitrosalicylate complex. *Analytical Chemistry*, 40(13):2049–2052, 1968.
- [106] M. Isabel Burguete, Francisco Galindo, Santiago V. Luis, and Laura Vígara. A turn-on fluorescent indicator for citrate with micromolar sensitivity. *Dalton Transactions*, (36):4027–4033, 2007. doi: 10.1039/B711139H.
- [107] B. Berkovski, editor. *Magnetic Fluids and Applications Handbook*. Begell House Inc. Publ. New York, 1996.
- [108] O. Spalla. General theorems in small-angle scattering. In *Neutrons, X-Rays and Light: Scattering Methods Applied to Soft Condensed Matter*. Lindner and Zemb, North-Holland, Elsevier edition, 2002.

- [109] R. Klein. Interacting colloidal suspensions. In *Neutrons, X-Rays and Light: Scattering Methods Applied to Soft Condensed Matter*. Lindner and Zemb, North-Holland, Elsevier edition, 2002.
- [110] G. Mériguet, E. Wandersman, E. Dubois, A. Cebers, J. de Andrade Gomes, G. Demouchy, J. Depeyrot, A. Robert, and R. Perzynski. Magnetic fluids with tunable interparticle interaction: monitoring the under-field local structure. *Magnetohydrodynamics*, 49:191–201, 2013.
- [111] Valerie J. Anderson and Henk N. W. Lekkerkerker. Insights into phase transition kinetics from colloid science. *Nature*, 416:811–815, 2002.
- [112] Guillaume Mériguet. *PhD Thesis, 2005*.
- [113] Paul T. Anastas and John C. Warner. *Green Chemistry: Theory and Practice*. 1998 edition.
- [114] Elke B. Carter, Stephanie L. Culver, Phillip A. Fox, Russell D. Goode, Ioanna Ntai, Morgan D. Tickell, Rachel K. Traylor, Norris W. Hoffman, and James H. Davis, Jr. Sweet success: Ionic liquids derived from non-nutritive sweeteners. *Chemical Communications*, (6):630–631, 2004. doi: 10.1039/b313068a.
- [115] Kenta Fukumoto, Masahiro Yoshizawa, and Hiroyuki Ohno. Room temperature ionic liquids from 20 natural amino acids. *Journal of the American Chemical Society*, 127(8):2398–2399, 2005. doi: 10.1021/ja043451i.
- [116] Marija Petkovic, Jamie L. Ferguson, H. Q. Nimal Gunaratne, Rui Ferreira, Maria C. Leitão, Kenneth R. Seddon, Luís Paulo N. Rebelo, and Cristina Silva Pereira. Novel biocompatible cholinium-based ionic liquids — toxicity and biodegradability. *Green Chemistry*, 12(4):643–649, 2010. doi: 10.1039/b922247b.
- [117] Nicholas Gathergood, M. Teresa Garcia, and Peter J. Scammells. Biodegradable ionic liquids: Part I. Concept, preliminary targets and evaluation. *Green Chemistry*, 6(3):166–175, 2004. doi: 10.1039/b315270g.
- [118] Jitendra R. Harjani, Robert D. Singer, M. Teresa Garcia, and Peter J. Scammells. Biodegradable pyridinium ionic liquids: design, synthesis and evaluation. *Green Chemistry*, 11(1):83–90, 2009. doi: 10.1039/b811814k.

- [119] Andrew P. Abbott, Glen Capper, David L. Davies, Raymond K. Rasheed, and Vasuki Tambyrajah. Novel solvent properties of choline chloride/urea mixtures. *Chemical Communications*, (1):70–71, 2003. doi: 10.1039/b210714g.
- [120] Yinghao Yu, Xingmei Lu, Qing Zhou, Kun Dong, Hongwei Yao, and Suojiang Zhang. Biodegradable naphthenic acid ionic liquids: Synthesis, characterization, and quantitative structure–biodegradation relationship. *Chemistry, A European Journal*, 14:11174–11182, 2008. doi: 10.1002/chem.200800620.
- [121] Katherine D. Weaver, Hye Jin Kim, Jiazeng Sun, Douglas R. MacFarlane, and Gloria D. Elliott. Cyto-toxicity and biocompatibility of a family of choline phosphate ionic liquids designed for pharmaceutical applications. *Green Chemistry*, 12(3):507–513, 2010. doi: 10.1039/b918726j.
- [122] Peter Nockemann, Ben Thijs, Kris Driesen, Colin R. Janssen, Kristof Van Hecke, Luc Van Meervelt, Simone Kossmann, Barbara Kirchner, and Koen Binnemans. Choline saccharinate and choline acesulfamate: Ionic liquids with low toxicities. *The Journal of Physical Chemistry B*, 111(19):5254–5263, 2007. doi: 10.1021/jp068446a.
- [123] Sudharshan Sekar, Mahadevan Surianarayanan, Vijayaraghavan Ranganathan, Douglas R. MacFarlane, and Asit Baran Mandal. Choline-based ionic liquids-enhanced biodegradation of azo dyes. *Environmental Science & Technology*, 46(9):4902–4908, 2012. doi: 10.1021/es204489h.
- [124] Dorjnamjin Demberelnyamba, Mama Ariunaa, and Young Key Shim. Newly synthesized water soluble cholinium-purpurin photosensitizers and their stabilized gold nanoparticles as promising anticancer agents. *International Journal of Molecular Sciences*, 9(5):864–871, 2008. doi: 10.3390/ijms9050864.
- [125] José Restolho, José L. Mata, and Benilde Saramago. Choline based ionic liquids: Interfacial properties of RTILs with strong hydrogen bonding. *Fluid Phase Equilibria*, 322-323:142–147, 2012. doi: 10.1016/j.fluid.2012.03.016.
- [126] Xue-Dan Hou, Thomas J. Smith, Ning Li, and Min-Hua Zong. Novel renewable ionic liquids as highly effective solvents for pretreatment of rice straw biomass by selective removal of lignin. *Biotechnology and Bioengineering*, 109(10):2484–2493, 2012. doi: 10.1002/bit.24522.

- 
- [127] Qiu-Ping Liu, Xue-Dan Hou, Ning Li, and Min-Hua Zong. Ionic liquids from renewable biomaterials: synthesis, characterization and application in the pretreatment of biomass. *Green Chemistry*, 14(2):304–307, 2012. doi: 10.1039/c2gc16128a.
- [128] Jan Skov Pedersen. Modelling of small-angle scattering data from colloids and polymer systems. In *Neutrons, X-Rays and Light: Scattering Methods Applied to Soft Condensed Matter*. Lindner and Zemb, North-Holland, Elsevier edition, 2002.
- [129] Michael Kotlarchyk and Sow-Hsin Chen. Analysis of Small Angle Neutron Scattering spectra from polydisperse interacting colloids. *The Journal of Chemical Physics*, 79(5):2461–2470, 1983. doi: 10.1063/1.446055.
- [130] G. Porod. Die Röntgenkleinwinkelstreuung von dichtgepackten kolloiden Systemen. *Colloid & Polymer Science*, 124(2):83–114, 1951.